



UNIVERSITÄT  
LEIPZIG



---

# Elucidation of the Role of Paramagnetic Valence States of High Spin Transition Metal Ions in MOF Catalysts by EPR Spectroscopy

---

Joint DOCTORAL DISSERTATION

by

**Kavipriya Thangavel., M.Sc.**

Supervisors:

**Prof. Andreas Pöpl**

**Prof. Damien M. Murphy**

**University of Leipzig**

Fakultät für Physik und Geowissenschaften

&

**Cardiff University**

School of Chemistry

June 2023



---

## Bibliographische Beschreibung:

Thangavel, Kavipriya

Elucidation of the Role of Paramagnetic Valence States of High Spin Transition Metal Ions in MOF Catalysts by EPR Spectroscopy

Universität Leipzig, Dissertation, 2023

192 S.<sup>1</sup>, 265 Lit.<sup>2</sup>, 18 Tab., 83 Abb

### ABSTRACT

In this thesis, the CW and pulse EPR techniques are employed to understand several information, such as the local and electronic structure and magnetic interactions of metal ions in metal-organic frameworks as well as the guest-host framework interaction upon gas adsorption. Other characterization techniques, such as PXRD, SQUID, and quantum chemical calculation, are also outlined, which are complementary to the information provided by EPR. *In situ* EPR studies give valuable details on structural transition, which can't be attained by other techniques always. EPR spectroscopy confirms that post-synthetic modification is possible in paddle wheel-based MOFs through the magnetic coupling of metal centers and also gives information about magnetic mixed paddle wheel units, which is often complicated to understand. The quite challenging divalent nickel-based MOF is studied along with NO adsorption, and the result highlights the capabilities of sophisticated EPR techniques in combination with quantum chemical calculations to provide fundamental insights into the non-obvious electronic structure of open-shell species docked in metal-organic frameworks. Finally, the inter- and intra-trimer interactions of high-spin chromium-based trimers are discussed in detail in combination with SQUID magnetometry.

---

<sup>1</sup>S. (Seitenzahl insgesamt)

<sup>2</sup>Lit. (Anzahl der im Literaturverzeichnis ausgewiesenen Literaturangaben)

# Acknowledgements

I am deeply grateful to **Prof. Dr. Andreas Pöpl** for his exceptional guidance, unwavering support, and valuable insights throughout my entire PhD project. His patience, persistence, and dedication have been instrumental in shaping my research journey. I am truly thankful for the remarkable platform he provided me to explore my ideas and for his prompt and constructive feedback. I would also like to express my sincere appreciation to my second leading supervisor, **Prof. Dr. Damien M. Murphy**, for his invaluable support and fruitful suggestions during my time at Cardiff University. His expertise and mentorship have greatly contributed to the success of my research endeavours. I am immensely thankful to both Prof. Pöpl and Prof. Murphy for their belief in me and for giving me the opportunity to be a part of the PARACAT project. Their trust and encouragement have been pivotal in my academic and personal growth.

I am grateful to PARACAT (813209), the Marie Curie Horizon 2020 ITN network EU, for funding this PhD. I extend my thanks to **Prof. Dr. Mario Chiesa** for designing and coordinating PARACAT. I also appreciate the financial support provided by the Deutsche Forschungsgemeinschaft (DFG) within the research unit FOR2433 (MOF Switches). Additionally, I would like to thank **Prof. Dr. Sabine Van Doorslaer** and **Prof. Dr. Inés García-Rubio** for their fruitful cooperation within the PARACAT project.

I sincerely thank **Dr. Matthias Mendt** (Leipzig University) for his valuable time, effort, and assistance with the experiments, concepts, and analysis. I extend my gratitude to **Dr. Andrea Folli** (Cardiff University) for his support, guidance, and fruitful suggestions throughout my doctoral work. I would also like to express my thanks to **Dr. Paolo Cleto Bruzzese** for his contributions to experiments, computations, and dedication to my project. Also, I appreciate the assistance and knowledge sharing from my colleague **Muhammad Fernadi Lukman** in the laboratory.

I wish to express my sincere thanks to faculty members at the Felix Bloch Institute for Solid state physics, University of Leipzig, for their support and help throughout my course. In particular, **Prof. Dr. Jürgen Haase** for the opportunity to work on my PhD in his group at the Felix Bloch Institute of Solid-State Physics, **Dr. Winfried Böhlman** for the sample synthesis and activation processes, **Stefan Schlayer** for the liquid helium supply and assistance with instruments, **Anastasia Kultraeva** for teaching EPR in the very beginning, **Niklas Vetter** and **Lisa Marie Tauche** for the pleasant assistance with the EPR measurements.

I would like to extend my thanks to our collaborators **Prof. Dr. Stefan Kaskel** and group, **Prof. Dr. Martin Hartmann** and group, **Prof. Dr. Dirk Volkmer** and group for providing MOF samples and for the fruitful collaborations.

---

I express my sincere gratitude to my previous project guides in India, Associate Prof. **Dr. R. Kalaiselvan** (Bharathiar University, India), **Prof. Dr. C. Venkateswaran** (University of Madras, India), and Associate **Prof. Dr. Nirmala** (IIT Madras, India), for their guidance, support, and the opportunity to work in the field of magnetism in their research groups. Their resources and the experiences gained from my previous projects have greatly contributed to my PhD work.

I would like to extend my special thanks to my friends **Dr. Jinu Kurian**, **Pranab Kumar Roy** and **S. Gajendhiran** for their invaluable support throughout my academic journey. Whether it was discussing research ideas, providing feedback on my work, or offering moral support during challenging times, their presence has made a significant difference. I am grateful for their friendship and the unwavering support they have shown me.

I extend my gratitude to my fellow PARACAT ESRs fellows, **Dr. Leonora Podvorica**, **Dr. Maruan Alberto Bracci**, **Andrea Guidetti**, **Fardokht Rezayi**, **Antonino Famulari**, **David Fiaco**, **Dr. Ilenia Serra**, and **Dr. Yu-Kai Liao**. Our collective journey throughout the PARACAT program has been invaluable. The collaboration and knowledge exchange with each of them has significantly contributed to my scientific understanding in the field of metal-organic frameworks and EPR spectroscopy. I appreciate their support and camaraderie during this memorable experience.

I extend my heartfelt gratitude to my mother, **Maragatham Thangavel**, for her unwavering belief in education and constant support throughout my journey, starting from kindergarten. Her unwavering presence has been invaluable, and I am truly grateful for her unwavering commitment. My heartfelt thanks go to my uncle, **Shanmuga Sundaram Periyasamy**, for his continuous encouragement throughout my journey from kindergarten to my doctoral program. To my beloved grandparents, **Saraswathy Periyasamy** and **Periyasamy Pongiyannan**, as well as my uncles, **Sakthivel Periyasamy** and **Vetrivel Periyasamy**, though no longer with us, I want to express my deep gratitude. You made my childhood days joyful and memorable. I cherish the love and influence these special individuals have had on my life.

*Dedicated to my **Mom**, Maragatham Thangavel ...*

---

# Preface

An outline of the Thesis structure is briefly consolidated, featuring authored and peer-reviewed publications/submissions associated with the content of the thesis chapters.<sup>3</sup>

1. **Chapter 1** presents an extensive introduction to the MOF materials and the significance of utilizing the EPR technique on the MOFs.

2. **Chapter 2** reports a brief overview of MOF materials used in this thesis along with the EPR theory and techniques employed. Part of this chapter is adapted from a book chapter:

M. Bracci, P. C. Bruzzese, A. Famulari, D. Fioco, A. Guidetti, Y-K. Liao, L. Podvorica, S. F. Rezayi, I. Serra, **K. Thangavel**, D. M. Murphy, "Paramagnetic species in catalysis research: A unified approach towards (the role of EPR in) heterogeneous, homogeneous and enzyme catalysis", *RSC: Electron Paramagn. Reson.* **2020**, *27*, 1-46. (all authors are equally contributed to the book chapter and alphabetically arranged - copyright @ 2021 RSC<sup>4</sup>).

3. **Chapter 3** presents *in situ* xenon and ethylene gas adsorption studies on DUT-49(Cu) MOF and EPR investigations of the physisorption and chemisorption properties of this material. This chapter has been published as an article:

**K. Thangavel et al.**, "Monitoring the local structure and magnetic properties of the dinuclear Cu<sub>2</sub>-paddle wheel nodes in the mesoporous metal-organic framework DUT-49(Cu) upon adsorption-induced breathing transitions", *J. Phys. Chem. C*, **2023**, *127*, *17*, 82178234. (copyright @ 2023 ACS<sup>5</sup>.)

4. **Chapter 4** reports magnetic interaction of mixed metals in post synthetically modified DUT-49(M,M) (M - Cu, Zn, Mn) MOFs and has been published as an article:

**K. Thangavel et al.**, "Magnetic coupling of divalent metal centers in post-synthetic metal exchanged bimetallic DUT-49 MOFs by EPR spectroscopy", *AIP Adv.*, **2023**, *13*, 015019. (CC BY 4.0 copyright @ 2023, Authors)

Also discussed bimetallic Fe and Zn-based HKUST-1 MOF, and part of this chapter is adapted from the article:

J. Bitzer, S. Otterbach, **K. Thangavel**, A. Kultaeva, Prof. Dr. R. Schmid, A. Pöpl, W. Kleist, "Experimental Evidence for the Incorporation of Two Metals at Equivalent Lattice Positions in Mixed-Metal MetalOrganic Frameworks", *Chem. Eur. J.* **2020**, *26*, 5667-5675. (CC BY 4.0 copyright @ 2019, Authors)

---

<sup>3</sup>The contribution of the author of this thesis and other authors are summarized in Chapter 8.

<sup>4</sup>Permission granted from the RSC to reuse the content in the thesis from the article

<sup>5</sup>Permission granted from the ACS to reuse the content in the thesis from the article

---

5. **Chapter 5** highlights the capabilities of sophisticated EPR techniques in combination with quantum chemical calculations in providing fundamental insights into the non-obvious electronic structure of open-shell species docked in MOFs and accepted as an article:

**K. Thangavel** *et al.*, "Unveiling the atomistic and electronic structure of Ni(II)NO adduct in MOF-based catalyst by EPR spectroscopy and quantum chemical modelling", *Phys. Chem. Chem. Phys.*, **2023**, 25, 15702-15714 (CC BY 3.0 copyright @ 2023, Authors)

6. **Chapter 6** reports the magnetic interaction of Cr(III) trimers complexes in the MIL-101(Cr) and bimetallic MIL-100(Al/Cr) MOFs, and the article corresponds to this chapter is accepted in

**K. Thangavel** *et al.*, "EPR and SQUID interrogations of Cr(III) trimer complexes in the MIL-101(Cr) and bimetallic MIL-100(AlCr) MOFs" - *Scipost Physics Proc.*, **2023**, 11, 016 (CC BY 4.0 copyright @ 2023, Authors)

7. **Chapter 7** presents the overall conclusion of the thesis mentioning how successfully the EPR spectroscopic technique has been used potentially on MOF catalyst materials and how the paramagnetic transition metal ions were used to interrogate the local structure in several MOFs.



# Contents

<b>1</b>	<b>Introduction</b>	<b>1</b>
<b>2</b>	<b>Materials and Methods</b>	<b>9</b>
2.1	The choice of MOFs . . . . .	9
2.1.1	DUT-49(Cu) MOF . . . . .	9
2.1.2	HKUST-1 MOF . . . . .	10
2.1.3	Ni:MFU-4l:NO <sub>2</sub> MOF . . . . .	11
2.1.4	Bimetallic MIL-100(Al/Cr) and MIL-101(Cr) . . . . .	13
2.1.5	Post synthetically ion exchanged MOFs (Bimetallic DUT-49 and HKUST-1) . . . . .	14
2.2	EPR spectroscopy . . . . .	15
2.2.1	Principles of electron paramagnetic resonance . . . . .	15
2.2.2	The spin Hamiltonian parameters . . . . .	18
2.2.3	Spin relaxation and line shapes . . . . .	22
2.2.4	Pulsed EPR methods . . . . .	28
2.2.4.1	Electron Spin Echo Envelope Modulation (ESEEM) . . . . .	29
2.2.4.2	Hyperfine Sublevel Correlation (HYSCORE) spectroscopy . . . . .	30
2.2.4.3	Electron Nuclear Double Resonance (ENDOR) spectroscopy . . . . .	31
2.2.5	Review of EPR technique on MOF science . . . . .	33
2.3	Magnetization measurement: SQUID . . . . .	37
<b>3</b>	<b>Adsorption-Induced Breathing Transitions in DUT-49(Cu) MOF</b>	<b>44</b>
3.1	Introduction . . . . .	44
3.2	EPR of the virgin state of DUT-49(Cu) . . . . .	46
3.3	<i>In situ</i> EPR gas adsorption studies . . . . .	49
3.3.1	<i>In situ</i> EPR in parallel to xenon sorption . . . . .	49
3.3.2	<i>In situ</i> EPR in parallel to ethylene sorption . . . . .	56
3.4	<i>In situ</i> PXRD in parallel to ethylene sorption at 165 K . . . . .	62
3.5	Discussions . . . . .	64
3.6	Conclusion . . . . .	69

---

3.7	Experimental section . . . . .	70
3.8	Supplementary material for chapter 3 . . . . .	73
<b>4</b>	<b>Post-Synthetically Modified Paddle Wheel-Based Bimetallic MOFs</b>	<b>89</b>
4.1	Introduction . . . . .	89
4.2	Magnetic coupling of divalent metal centers in bimetallic DUT-49 MOFs . . . . .	89
4.3	HKUST-1 MOFs . . . . .	95
4.3.1	Zinc incorporated CuBTC MOF . . . . .	95
4.3.2	Iron incorporated CuBTC MOF . . . . .	98
4.4	Conclusion . . . . .	101
4.5	Experimental Details . . . . .	102
<b>5</b>	<b>Atomistic and electronic structure of Ni(II)-NO adduct in a MFU-4l(Ni):NO<sub>2</sub> MOF</b>	<b>106</b>
5.1	Introduction . . . . .	106
5.2	EPR investigations of Ni-MFU-4l-NO <sub>2</sub> . . . . .	108
5.2.1	CW-EPR spectroscopy and coordination geometry of Ni(II) in Ni-MFU-4l-NO <sub>2</sub>	108
5.2.2	CW and pulsed EPR investigations of the Ni(II)NO adduct in Ni-MFU-4l-NO <sub>2</sub>	112
5.3	Geometric and electronic structure of Ni(II)NO in MFU-4l-NO <sub>2</sub> . . . . .	118
5.4	Conclusion . . . . .	122
5.5	Experimental techniques and methods . . . . .	123
5.6	Supplimentary material for Chapter 5 . . . . .	127
<b>6</b>	<b>Cr(III) trimer complexes in the MIL-101(Cr) and bimetallic MIL-100(Al/Cr) MOFs</b>	<b>143</b>
6.1	Introduction . . . . .	143
6.2	SQUID magnetometry results . . . . .	145
6.3	EPR spectroscopy results . . . . .	148
6.4	Conclusion . . . . .	152
6.5	Experimental Details . . . . .	153
<b>7</b>	<b>Conclusion</b>	<b>156</b>
<b>8</b>	<b>Publications and Miscellaneous</b>	<b>159</b>
<b>9</b>	<b>CV and Miscellaneous</b>	<b>162</b>

# List of Figures

2.1	Metal-organic polyhedra built up of (a) paddle-wheel units containing metal and (b) crystal structure of DUT-49(M). . . . .	9
2.2	Structure of the secondary building unit (Cu(II)-Cu(II) PW) of activated HKUST-1. The water molecules are removed from the axial centres and represent the CUS PW Units. . . . .	11
2.3	(a) Post-synthetic metal- and side-ligand exchange reactions in MFU-4l at peripheral sites (a part of the SBU is shown, t - tetrahedral, o - octahedral), (b) schematic representation of the Kuratowski unit in MFU-4l and synthesis of MFU-4l-NO <sub>2</sub> (an idealized composition is shown, in the following schemes only one peripheral Ni-center is shown)(Reproduced from Ref [17]. with permission from the Royal Society of Chemistry.) . . . . .	12
2.4	Cr(III)/Al(III) ions are in the octahedral trimer units and four trimers, forming a supertetrahedra (Modified from [26, 27] with permission from the Royal Society of Chemistry.) showing MIL-101(Cr) and MIL-100(Al <sub>0.8</sub> Cr <sub>0.2</sub> ) frameworks with different pore sizes . . . . .	13
2.5	The pathways of PSM in MOFs: a) metal exchange, b) metal incorporation, c) ligand exchange, d) ligand installation, e) ligand removal, and e) guest incorporation inside the pores. Adapted from [34] copyright @ 2019 The Authors. . . . .	14
2.6	EPR Energy level diagram depicting the relationship between the absorbed energy, first derivative signal, and magnetic field for the $S = 1/2$ system[40] . . . . .	17
2.7	Terms in spin Hamiltonian parameters[43] . . . . .	19
2.8	Scheme of $g$ -tensor and the consequential EPR spectra for (a) isotropic, (b-c) axial and (c) orthorhombic symmetry. (adapted from ref. [44]). . . . .	20
2.9	Chart showing the relation between exchange interaction and zero-field splitting interaction for a $S = 1$ dimeric system[47, 48] . . . . .	26
2.10	Dysonian EPR signal and the characteristic points and parameters are shown and adapted from [57] copyright @ 2009, Springer-Verlag . . . . .	28
2.11	Pulse sequence of (a)2-pulse ESE and (b) 3-pulse ESE . . . . .	29

2.12	Pulse sequence of HYSCORE . . . . .	30
2.13	a) HYSCORE powder patterns for an $S = 1/2, I = 1/2$ spin system with an isotropic hf tensor $A$ . b) HYSCORE powder patterns for an $S = 1/2, I = 1/2$ spin system with an axial hf tensor which contains isotropic ( $a_{iso}$ ) and dipolar ( $T$ ) contributions. Blue correlation ridges represent the strong coupling case ( $ A  >  2\nu_I $ ); red correlation ridges represent the weak coupling case ( $ A  <  2\nu_I $ ). The image is adapted from [60] Copyright @ 2020 American Chemical Society . . . . .	31
2.14	ENDOR pulse sequence . . . . .	32
2.15	EPR as a tool to interrogate different properties of MOFs . . . . .	34
2.16	Schematic setup of a SQUID magnetometer with 2nd order gradiometer. The inset shows the SQUID response $V_{SQUID}$ versus sample position (x-pos.) [81] . . . . .	37
3.1	Crystal structures of DUT-49(Cu) and guest-induced framework dynamics: a) building blocks used in the construction of DUT-49(Cu); b) Pore size of contracted pore ( $cp$ ) phase of DUT-49(Cu); c) Pore system of open pore ( $op$ ) phase of DUT-49(Cu); d) Guest-induced breathing in DUT-49(Cu) including NGA and Gate Opening (GO). [2]	45
3.2	Energy level plots of $S = 1$ Cu(II) - Cu(II) dimer in its antiferromagnetically coupled excited triplet state as a function of the applied magnetic field. (a) $B \parallel xy$ , (b) $B \parallel z$ . Here $D = 8985$ MHz and (c) experimental EPR spectra of activated DUT-49(Cu) at $T = 290$ K (top) and $T = 7$ K (bottom) show the labelling of the different transitions of the $S = 1$ signal of species $A_{cp}$ according to Wassermann <i>et al.</i> [30] ( $B_{xy}$ and $B_z$ ) and the labelling of the Cu(II) monomer species M (purple). $B_{min}$ is a forbidden transition superpositioned with the $B_{z1}$ transition. . . . .	47

- 3.3 The low field part of the *in situ* EPR spectra of the  $S = 1$  state of the Cu(II) - Cu(II) dimers in DUT-49(Cu) during (a) xenon adsorption and (b) xenon desorption at 156 K temperature in a first cycle starting with an activated sample. Furthermore, spectra are shown, which were measured in a second cycle at 158 K during (c) adsorption and (d) desorption starting with a sample which went through a full initial xenon ad/desorption cycle after activation. The EPR spectra are labelled with the relative xenon pressures  $p/p_0$  ( $p_0 = 51$  kPa in (a) and (b) and  $p_0 = 55$  kPa in (c) and (d)) at which they were measured. Orange spectra indicate the dominant presence of the *op* phase, green spectra that of the *cp* phase, olive spectra indicate the coexistence of both phases, and the red spectrum corresponds to *op* phase of the gas-free activated sample. The assignment of the various phases is based on correlating the *in situ* EPR spectra with sorption isotherms measured by Krause *et al.*[3] . . . . . 49
- 3.4 ZFS parameter  $D$  of the  $S = 1$  state determined for five different Cu PW species  $A_{op}$  (up-pointing triangle)  $X_{op}$  (squares),  $X_{cp1}$  (down-pointing triangles),  $X_{cp2}$  (circles) and  $X_{cp}$  (stars) during xenon adsorption (blue), and subsequent desorption (red) at a) the first ad/desorption cycle at  $T = 156$  K and b) the second ad/desorption cycle at  $T = 158$  K. Regions where the occurrence of structural phase transitions are indicated by the *in situ* EPR data are highlighted in blue during adsorption and in red during desorption. Lines are added as guides for the eyes. (closed symbols adsorption, opened symbols desorption) . . . . . 50
- 3.5 Schematic phase diagram for DUT-49(Cu) during the first adsorption and desorption cycle of (a) xenon and (b) ethylene, as derived from EPR experiments. . . . . 52
- 3.6 The low field part of the *in situ* EPR spectra of the  $S = 1$  state of the Cu(II) - Cu(II) dimers in DUT-49(Cu) during (a) ethylene adsorption and (b) ethylene desorption at 165 K temperature in a first cycle starting with an activated sample (red). The EPR spectra are labelled with the relative ethylene pressures  $p/p_0$  ( $p = 82$  kPa). Orange spectra indicate the dominant presence of the *op* phase, green spectra that of the *cp* phase, and the red spectrum corresponds to the *op* phase of the gas-free activated sample. . . . . 57
- 3.7 ZFS parameter  $D$  of the  $S = 1$  state of the PW species  $A_{op}$  and  $A_{cp}$ (triangles), as well as  $E_{op}$  (squares) and  $E_{cp}$  (circles), determined at different relative pressures  $pp_0$  ( $p_0=82$ ) by *in situ* EPR on DUT-49(Cu) during ethylene adsorption (blue) and subsequent desorption (red) at the temperature  $T = 165$  K. Lines are added as a guide for the eyes. (closed symbols adsorption, opened symbols desorption) . . . . 58

3.8	Parameter $g_z$ of the $S = 1$ state of different PW species (labels defined in the legends) as determined by <i>in situ</i> EPR for a) the first xenon ad/desorption cycle and b) the ethylene ad/desorption cycle. Note that in a) during adsorption, the values for $X_{cp1}$ and $X_{cp2}$ have large errors due to the huge systematic error which arises from an interpretation of the single line of the $B_{z2}$ transition by a superposition of $X_{cp1}$ , $X_{cp2}$ , and for some pressures, even $X_{op}$ . During desorption in a), the $B_{z2}$ line was simulated by a single $S = 1$ species with the $D$ parameter of species $X_{cp1}$ and the $g_z$ parameter was determined in that way. (closed symbols adsorption, opened symbols desorption) . . . . .	60
3.9	Peak-to-peak line width $\Delta B_{pp}$ ( $B_{xy2}$ ) of the $S = 1$ state of the Cu(II) - Cu(II) dimers as determined during a) the first xenon ad/desorption cycle and b) the ethylene ad/desorption cycle from the <i>in situ</i> EPR spectra. (closed symbols adsorption, opened symbols desorption) . . . . .	61
3.10	(a,c) PXRD patterns were measured in parallel to (b) adsorption and (d) desorption of ethylene on DUT-49(Cu). The right axis shows the evolution of unit cell parameter $a$ , and the inset visualizes the structural transformations in the system. . . . .	62
3.11	Adsorption and desorption isotherms of ethylene on DUT-49(Cu) at $T = 165$ K, shown at a (a) linear and (b) logarithmic pressure scale. Zoomed low-pressure range of the (c) adsorption isotherm and the (d) PXRD patterns measured on DUT-49(Cu) sample in vacuum (black) and adsorption point 7 (red). PW unit (e) and projection of unit cell along (110) direction (f) showing the adsorption sites of ethylene molecules. . . . .	63
3.12	Characterization of DUT-49(Cu) sample: (a) PXRD patterns, (b) nitrogen physisorption at 77 K, and (c) SEM images. . . . .	73
3.13	Adsorption and desorption isotherms of xenon on DUT-49(Cu) at $T = 165$ K . . . . .	73
3.14	(a) Temperature-dependent EPR data of DUT-49(Cu), and (b) Bleaney Bowers fit on the EPR intensity of the $S = 1$ state of the Cu(II) - Cu(II) dimers extracted from temperature-dependent EPR data. . . . .	74
3.15	EPR spectra of activated DUT-49(Cu) showing (a) the $S = 1/2$ Cu(II) monomer species (M) at 7 K & 290 K, and (b) the thermally populated $S = 1$ Cu(II) pair species ( $A_{op}$ ) in the PW units at 290 K (* corresponds to M). Redline simulated spectrum. . .	74
3.16	Schematic phase diagram for DUT-49(Cu) during the adsorption and desorption cycle of (a) xenon cycle 1, (b) xenon cycle 2 and (c) ethylene cycle 1 as derived from EPR experiments. . . . .	75

3.17 *In situ* EPR spectra of DUT-49(Cu) during (a) xenon adsorption and (b) xenon desorption at 156 K temperature in a first cycle starting with an activated sample. Furthermore, spectra are shown, which were measured in a second cycle at 158 K during (c) adsorption and (d) desorption starting with a sample which went through a full initial xenon ad/desorption cycle after activation. The EPR spectra are labelled with the relative xenon pressures  $p/p_0$  ( $p_0 = 51$  kPa in (a) and (b) and  $p_0 = 55$  kPa in (c) and (d)) at which they were measured. Orange spectra indicate the dominant presence of the *op* phase, green spectra that of the *cp* phase, olive spectra indicate the coexistence of both phases, and the red spectrum corresponds to *op* phase of the gas-free activated sample. The assignment of the various phases are based by correlating the *in situ* EPR spectra with sorption isotherm measured by Krause *et al*[3]. . . . . 76

3.18 Selected experimental (solid lines) and simulated (dotted lines) EPR spectra of (a) xenon adsorption and (b) xenon desorption over DUT-49(Cu) at 156 K temperature in a first cycle starting with an activated sample. Furthermore, spectra are shown, which were measured in a second cycle at 158 K during (c) adsorption and (d) desorption starting with a sample which went through a full initial xenon ad/desorption cycle after activation. Special focus in the simulations were given in reproducing the line shape of the  $B_{xy1}$  transition as this very sensitive to variations in the parameter  $D$  whereas the  $B_{z1}$  transition at  $B < 50$  mT with its multiple HF splitting is difficult to simulate correctly. The EPR spectra are labelled with the relative xenon pressures  $p/p_0$  ( $p_0 = 51$  kPa in (a) and (b) at which they were measured. Orange spectra indicate the dominant presence of the *op* phase, green spectra that of the *cp* phase, olive spectra indicate the coexistence of both phases, and the red spectrum corresponds to *op* phase of the gas-free activated sample as we derive in this work by *in situ* EPR correlated to a sorption isotherm measured by Krause *et al*[3] . . . . . 77

3.19 Simulation of (a)  $\Delta D$  variation and (b)  $E/D$  ratio variation for fixed  $D$  values. . . . . 77

3.20 Enlarged X-band *in situ* EPR spectra of (a & b)  $B_z$  and  $B_{xy1}$  transition, (c & d)  $B_{xy2}$  and, (e & f)  $B_{z2}$  transitions measured during the first cycle of xenon adsorption and desorption respectively, recorded at 156 K. . . . . 79

- 
- 3.21 *In situ* EPR spectra of DUT-49(Cu) during (a) ethylene adsorption and (b) ethylene desorption at 165 K temperature in a first cycle starting with an activated sample (red). The EPR spectra are labelled with the relative ethylene pressures  $p/p_0$  ( $p_0 = 82$  kPa), orange spectra indicate the dominant presence of the *op* phase, green spectra that of the *cp* phase, olive spectra indicate the coexistence of both phases, and the red spectrum corresponds to the *op* phase of the gas-free activated sample. . . . . 80
- 3.22 Selected EPR simulations of (a) Ethylene adsorption and (b) ethylene desorption at 165 K temperature in a first cycle starting with an activated sample (red). The EPR spectra are labelled with the relative ethylene pressures  $p/p_0$  ( $p_0 = 82$  kPa) Orange spectra indicate the dominant presence of the *op* phase, green spectra that of the *cp* phase, olive spectra indicate the coexistence of both phases, and the red spectrum corresponds to the *op* phase of the gas-free activated sample. . . . . 80
- 3.23 Enlarged X-band *in situ* EPR spectra of (a & b)  $B_{z1}$  and  $B_{xy1}$  transition, (c & d)  $B_{xy2}$  and (e & f)  $B_{z2}$  transition measured during cycle1 ethylene adsorption and desorption, respectively, recorded at 165(1) K. . . . . 81
- 3.24 Parameters  $g_{x,y}$  of the  $S = 1$  state of different PW species (labels defined in the legends) as determined by *in situ* EPR for a) the first xenon ad/desorption cycle and b) the ethylene ad/desorption cycle. . . . . 82
- 3.25  $A_z$  parameters of the  $S = 1$  state of different PW species (labels defined in the legends) as determined by *in situ* EPR for a) the first xenon ad/desorption cycle and b) the ethylene ad/desorption cycle. . . . . 82
- 3.26 Cu(II) monomer species during a) xenon adsorption and (b) xenon desorption at 156 K temperature in the first cycle, starting with an activated sample. The EPR spectra are labelled with the relative xenon pressures  $p/p_0$  ( $p_0 = 51$  kPa) at which they were measured. Orange spectra indicate the dominant presence of the *op* phase, green spectra that of the *cp* phase, olive spectra indicate the coexistence of both phases, and the red spectrum corresponds to *op* phase of the activated sample. 84
- 3.27 *In situ* EPR spectra the  $S = 1/2$  Cu(II) monomer species M during (a) ethylene adsorption and (b) ethylene desorption at 165 K temperature of an activated sample. The EPR spectra are labelled with the relative ethylene pressures  $p/p_0$  at which they were measured. (yellow spectra indicate the dominant presence of the *op* phase, green spectra that of the *cp* phase, and red spectra indicate the gas-free *op* phase.) . . 84



3.28	<i>In situ</i> EPR spectra the $S = 1/2$ Cu(II) monomer species M for cycle 1 (a) xenon at 156 K and (b) ethylene at 165 K during sorption process (red line corresponding simulation). The EPR spectra are labelled with the relative ethylene pressures $p/p_0$ .	85
4.1	Temperature-dependent X-band EPR experiments from $T = 7$ K to $T = 170$ K for (a) DUT-49(Cu), (b) DUT-49(Cu <sub>0.7</sub> Zn <sub>0.3</sub> ), (c) DUT-49(Mn), (d) DUT-49(Cu <sub>0.5</sub> Mn <sub>0.5</sub> ) ( a weak signal at $\sim 150$ mT indicates the minor Co impurity species, a violet bar in (a) & (b) $S = 1/2$ Cu(II) monomer, gray bar in (c) a mixture of $S = 1/2$ Cu(II) & $S = 5/2$ Mn(II) monomers, and yellow bar in (d) $S = 5/2$ Mn(II) monomer).	90
4.2	Experimental (black) and simulated (red) spectra of (a) the $S = 1/2$ spin state of the Cu(II) monomer, (b) the $S = 1$ spin state of the Cu(II) - Cu(II) dimer of DUT-49(Cu) and DUT-49(Cu <sub>0.7</sub> Zn <sub>0.3</sub> ) at X-band frequency, (c) the $S = 1$ spin state of the Cu(II) - Cu(II) dimer of DUT-49(Cu) at Q-band frequency (for the spin Hamiltonian parameters, see the text, * signals in (b) & (c) indicate $S = 1/2$ Cu(II) monomer) and (d) The intensity extracted from the temperature-dependent X-band EPR data of DUT-49(M, M) fitted using Bleaney Bowers susceptibility equations for the coupled $S = 1/2$ dimer species. (Blue points - DUT-49(Cu), black points - DUT-49(Cu <sub>0.7</sub> Zn <sub>0.3</sub> ), green points - DUT-49(Cu <sub>0.5</sub> Mn <sub>0.5</sub> ), and red line Bleaney Bowers susceptibility fit)	91
4.3	Comparison of X-band EPR experiments of DUT-49(M <sub>x</sub> M <sub>1-x</sub> ) MOFs recorded at (a) low and (b) 160 K temperatures ( a weak signal at $\sim 150$ mT indicates the minor Co(II) impurity species).	93
4.4	Temperature-dependent Q-band EPR spectra of (a) DUT-49(Mn) and (b) DUT-49(Cu <sub>0.5</sub> Mn <sub>0.5</sub> ) MOFs	94
4.5	Bimetallic Zn incorporated CuBTC PW structure	95
4.6	(a) Temperature-dependent X-band EPR spectra and (b) The intensity extracted from the temperature-dependent X-band EPR data of activated PSM ZnCuBTC fitted using Bleaney Bowers susceptibility equations for the coupled $S = 1/2$ dimer species	96
4.7	Experimental (black) and simulated (red) spectra of (a) hydrated and (b) activated PSM ZnCuBTC MOFs (# - additional feature due to NQI)	97
4.8	Experimental orientation selective CW X-band <sup>1</sup> H ENDOR spectra of (a) PSM ZnCuBTC (this work) and (b) SOL ZnCuBTC[12]	98
4.9	EPR spectra of (a) CuBTC, (b) CuBTC/ $\alpha$ -Fe <sub>2</sub> O <sub>3</sub> , (c) CuBTC/MIL-100(Fe) and (d) FeCuBTC measured at 15 K, 100 K, and 300 K temperatures.	100

---

4.10	PXRD of Post synthetically modified ZnCuBTC confirming the formation . . . . .	103
4.11	SEM images of PSM ZnCuBTC MOF in different magnifications . . . . .	103
5.1	View along the (-1 -1 -1) face of Ni-MFU-4l-NO <sub>2</sub> space-filling periodic model. An inset of the main subunit of the material is shown on the right. C, N, O, Ni, Zn and H are green, blue, red, yellow, violet, and white colour, respectively. . . . .	107
5.2	Experimental (black line) and simulated (red line) CW EPR W-band spectrum of Ni(II) ions having $S = 1$ in Ni-MFU-4l-NO <sub>2</sub> obtained at 20 K. . . . .	110
5.3	Geometry optimized periodic structures at B3LYP-D3/pob-TZVP-rev2 of Ni-MFU-4l-NO <sub>2</sub> . The computed $g$ - and $D$ -tensor frames are also reported. . . . .	111
5.4	Experimental (black lines) and simulated (red lines) X-band CW EPR spectra of the Ni(II)-NO adduct in Ni-MFU-4l-NO <sub>2</sub> formed upon NO adsorption and recorded at (a) 10 K and (b) 288 K. The simulation is composed of the sum of two different species A (dotted green line) and B (dotted blue line). The small signal around $\sim 340$ mT corresponds to the radical. . . . .	112
5.5	Experimental (black) and simulated (red) X-band <sup>14</sup> N ENDOR spectra of Ni(II)NO adduct in Ni-MFU-4l-NO <sub>2</sub> recorded at different magnetic field settings. The simulation of the <sup>14</sup> N(2) signal was obtained by using one of the DFT-computed sets of Euler angles for the triazole <sup>14</sup> N. The ESE spectrum with the corresponding field positions at which the ENDOR spectra were taken is plotted on the left-hand side. All spectra were recorded at 10 K. . . . .	115
5.6	Simulation (in red) of the X-band <sup>14</sup> N HYSCORE spectrum (in black) of Ni(II)-NO adduct in Ni-MFU-4l-NO <sub>2</sub> recorded at a) 325.0 mT, b) 320.8 mT, and c) 309.0 mT. The ESE detected EPR signal of Ni(II)NO is reported on the left side. Spectra were recorded at 10 K. . . . .	117
5.7	Atomistic structure of Ni(II)NO species in Ni-MFU-4l-NO <sub>2</sub> as obtained after the geometry optimization of the periodic model. The labels of the significant nuclei are reported. The relevant bond lengths are given in nm. The computed $g$ -tensor orientations are shown in red. . . . .	118

- 5.8 Contour plots of the most important natural orbitals (with predominant Ni 3d and NO  $\pi^*$  character) optimized with the CASSCF(11e,11o) calculation and spin density map. Indicated qualitative nature and fractional occupation number (n) are reported. Contour values:  $\leq 0.03$  a.u. for the orbitals and  $\pm 0.003$  electrons/ $a_0$  for the spin density (the positive sign is shown in cyan, the negative sign in dark blue). N, O, Ni, C and H atoms are reported in blue, red, yellow, green and white, respectively . . . . . 119
- 5.9 (a) PXRD and SEM image (inset: scale bar - 4  $\mu\text{m}$ ) of Ni-MFU-4l:NO<sub>2</sub> and (b) IR spectra comparison of various MFU-4l materials . . . . . 127
- 5.10 (a) W-band and (b) Q-band EPR spectra (black) and simulation (red) of the spin  $S = 1$  of Ni(II) in Ni-MFU-4l:NO<sub>2</sub> with the spin Hamiltonian parameters  $g_{xx} = 2.050(5)$ ,  $g_{yy} = 2.055(6)$ ,  $g_{zz} = 2.060(5)$ ,  $D = 35.5(5)$  GHz and  $E = 0.5$  GHz. (the extra signals of Q-band data are from the EPR cavity and the radical from the MOF sample.) . . . . . 128
- 5.11 Angular dependent road map for the  $S = 1$  Ni(II) species at (a) W-band and (b) Q-band frequency (Blue - simulated EPR spectra with spin Hamiltonian parameters  $g_{iso} = 2.05$ ,  $D = 35500$  MHz and  $E = 5000$  MHz; Red - A road map of the expected spectral position). . . . . 128
- 5.12 Geometry optimized periodic structures at B3LYP-D3/pob-TZVP-rev2 of (a) Ni-MFU-4l:NO<sub>2</sub> and (b) Ni-MFU-4l:Cl. The computed  $g$ - and  $D$ -frames are also reported. Nitrogen and oxygen atoms are shown in blue and red, respectively. The other atoms are labelled in the figures. . . . . 129
- 5.13 (a) Temperature-dependent X-band EPR spectra of NO adsorbed over Ni-MFU-4l:NO<sub>2</sub> ranging from temperature 10 K to 288 K (solid line - experimental data and dotted line - simulation of the sum of two different species A and B) and (b) Intensity corresponds to magnetic susceptibility as a function of temperature, extracted from double integration of full range temperature dependent EPR data (fit - red: paramagnetic susceptibility fit). The small signal around 340 mT corresponds to the radical. . . . . 130
- 5.14 The temperature-dependent trend of  $g$ -tensor parameters (a)  $g_{xx}$ , (b)  $g_{yy}$ , (c)  $g_{zz}$  and (d) Gaussian (blue) and Lorentzian (black) linewidth for NO adsorbed MFU-4l(Ni):NO<sub>2</sub> system (species A). . . . . 131

- 5.15 Arrhenius plot of the homogeneous (a) EPR linewidths,  $\delta B_L^{hom}$  and (b)  $\ln(\delta B_L^{hom})$  of Ni(II)-NO adduct in Ni-MFU-4l:NO<sub>2</sub>. The activation energies were found to be  $E_{A1} = 1.1(2)$  kJ/mol for the lower temperature range (75 K–250 K) and  $E_{A2} = 23(1)$  kJ/mol for the higher temperature range (250 K–288 K).  $\delta B_L^{hom}(T) = \delta^{total} B_i(T) - \delta^{total} B_i(50\text{ K})$  . . . . . 131
- 5.16 Atomistic structure of Ni-MFU-4l:NO<sub>2</sub>-NO adduct. (a) Ni(II)-NO and (b) Zn(II)-NO binding sites. The metal-nitrosyl bond distances are reported in nm together with the computed relative electronic energy for the two configurations. . . . . 133
- 5.17 X-band <sup>14</sup>N ENDOR spectra simulation of the Ni(II)-NO species in Ni-MFU-4l:NO<sub>2</sub> highlighting the contribution of each <sup>14</sup>N species. The black lines are the experimental spectra. The ESE spectrum with the corresponding field position sampled is plotted on the left. The blue, green and yellow lines represent the simulation obtained with the spin Hamiltonian of <sup>14</sup>N(2) by using the orientation computed from  $N_{f1}$ ,  $N_{f2}$  and  $N_{f3}$ , respectively. The red line is obtained by using the spin Hamiltonian parameters of <sup>14</sup>N(1). . . . . 134
- 5.18 Calculated (at B3LYP-D3(ABC)/pob-TZVP-rev2 level of theory) and experimental comparison of IR spectra for the Ni-MFU-4l:NO<sub>2</sub> (blue spectra) and Ni-MFU-4l:Cl (red spectra) samples. . . . . 135
- 5.19 Contour plots ( $\pm 0.03$  a.u.) of natural CASSCF(11e,11o) orbitals with indicated qualitative character and fractional occupation number ( $n$ ). N, O, Ni, C, Zn and H atoms are reported in blue, red, yellow, green, violet and white, respectively. . . . 136
- 5.20 Temperature-dependent X-band EPR spectra of NO adsorbed over Ni-MFU-4l:NO<sub>2</sub> (a) with 0.2 and (b) 120 mbar . . . . . 136
- 6.1 (a) Cr(III)/Al(III) ions are in the octahedral trimer units and four trimers, forming a supertetrahedra (Modified from rivera *et al.*[27] with permission from the Royal Society of Chemistry.) showing MIL-101(Cr) and MIL-100(Al<sub>0.8</sub>Cr<sub>0.2</sub>) frameworks, and (b) Scheme of the trimer unit contains three  $S = 3/2$  Cr(III) spins shows the situation of spin 'frustration' ( $J_0$  and  $J_1$  are the exchange coupling parameters). . . . 144
- 6.2 ZFC, FCC and FCW  $M-T$  curves of (a) MIL-101(Cr), and (b) MIL-100(Al<sub>0.8</sub>Cr<sub>0.2</sub>) with an applied field of 0.5 T. (Insets: The temperature-dependence of the reciprocal of the magnetic susceptibility of its corresponding ZFC curves.) . . . . . 146
- 6.3  $M-H$  curves recorded at 5 K, 25 K and 100 K for (a) MIL-101(Cr) and, 5 K and 35 K for (b) MIL-100(Al<sub>0.8</sub>Cr<sub>0.2</sub>). . . . . 147

6.4	C-W fit on the temperature-dependent reciprocal of the magnetic susceptibility of (a) MIL-101(Cr) and (b) MIL-100( $\text{Al}_{0.8}\text{Cr}_{0.2}$ ) below $T < 15$ K. . . . .	148
6.5	Temperature-dependent X-band EPR data of (a) MIL-101(Cr) and (b) MIL-100( $\text{Al}_{0.8}\text{Cr}_{0.2}$ ) at temperature ranging from $T = 7$ K to $T = 290$ K(*-corresponds to the gaseous oxygen in the cryostat). . . . .	149
6.6	EPR Intensities ( $I_{EPR}$ ) belong to Cr(III) spectra of (a) MIL-101(Cr), and (b) MIL-100( $\text{Al}_{0.8}\text{Cr}_{0.2}$ ) extracted from temperature-dependent X-band EPR data. (Inset: Corresponding C-W fit of $I_{EPR}^{-1}$ as a function of temperature.) . . . . .	149
6.7	(a & b) X-band, (c & d) Q-band and (e & f) W-band EPR spectra of MIL-101(Cr) and MIL-100( $\text{Al}_{0.8}\text{Cr}_{0.2}$ ) MOFs, respectively. ( $g$ -values of the corresponding signals: $g_A = 1.979$ , $g_B = 1.779$ , $g_C = 5.5 - 4.0$ , $g_D = 1.973$ and $g_E = 1.945$ ) . . . . .	150
6.8	Temperature-dependent (a) $g_{iso}$ trend, and (b) peak to peak width ( $\Delta B_{pp}$ ) of MIL-101(Cr) and MIL-100( $\text{Al}_{0.8}\text{Cr}_{0.2}$ ) extracted from the X-band temperature-dependent spectra. . . . .	151
9.1	It is the SEM image (polygon shaped) of a paddle wheel-based bimetallic ZnCuBTC metal-organic framework containing an antiferromagnetically coupled $S = 1$ spin state Cu(II)-Cu(II) dimers - portrayed as a <b>Coral reef - Underwater artwork</b> . . . . .	162

# List of Tables

1.1	The list of MOF materials investigated in this thesis . . . . .	3
2.1	Pore sizes of MFU-1, MFU-4, MFU-4l MOFs . . . . .	12
2.2	The difference between spin-lattice and spin-spin relaxation[38, 39]. . . . .	23
3.1	Experimentally derived spin Hamiltonian parameters of different $S = 1$ species assigned to copper PW units in DUT-49 (Cu) under different conditions. ( $T$ temperature, $p/p_0$ relative pressure) . . . . .	48
3.2	Experimentally derived spin Hamiltonian parameters of $S = 1/2$ species M assigned to Cu(II) monomer measured at 7 K and 290 K and $S = 1$ assigned to Cu(II)-Cu(II) dimer at 290 K. (Quadrupole coupling of Cu(II) monomer, $Q_{xx,yy} = -5(2)$ MHz, $Q_{zz} = 10(2)$ MHz) . . . . .	75
3.3	Experimentally derived spin Hamiltonian parameters of different $S = 1$ species assigned to PW units in DUT-49 (Cu) during xenon sorption recorded at 156 K in the first cycle. ( $A_{x,y} < 60$ MHz and $E/D < 0.008$ , $p_0 = 51$ kPa) . . . . .	78
3.4	Experimentally derived spin Hamiltonian parameters of different $S = 1$ species assigned to PW units in DUT-49 (Cu) during ethylene sorption recorded at 165 K. ( $A_{x,y} < 58$ MHz and $E/D < 0.006$ ) . . . . .	83
3.5	Spin Hamiltonian parameters $g$ , $A$ , $Q$ of $S = 1/2$ Cu(II) monomer for the xenon (156 K) and ethylene (165K) during the sorption process for the selected conditions. ( $Q_{xx,yy} = 5(2)$ MHz, $Q_{zz} = 10(2)$ MHz) . . . . .	85
4.1	Total spin ( $S$ ) states of metal dimers in the PW units of DUT-49(M,M) MOFs at a temperature of 7 K and 160 K as derived from EPR experiments. . . . .	93
4.2	Spin Hamiltonian parameter of $S = 1/2$ Cu(II) monomer species in PSM ZnCuBTC MOF measured at $T = 7$ K . . . . .	97
4.3	Comparison of intensity/mass, relative total EPR signal intensity, isotropic $g'$ -value and line width $\Delta B_{pp}$ (mT) at $T = 300$ K temperature. . . . .	101

---

5.1	Experimental and computed spin Hamiltonian parameters for spin $S = 1$ Ni(II) incorporated in different Ni-MFU-4l-X framework variants. Uncertainty values for the $g_{ii}$ , $D$ , and $E/D$ parameters of 0.006, 0.01 $\text{cm}^{-1}$ and 0.01 were estimated for the experimental values, respectively. . . . .	111
5.2	Computed and experimental spin Hamiltonian parameters for the prevalent Ni(II)NO species in Ni-MFU-4l-NO <sub>2</sub> . The labels of the nuclei refer to the ones reported in Figure 5.7. Hyperfine and quadrupole couplings are given in MHz. Uncertainty values for the $g$ -, $A$ -tensors, $e^2qQ/h$ and $\eta$ of 0.005, 0.5 MHz, 1.5 MHz and 0.4 were estimated for the experimental values, respectively. For the simulation of the spectra, the computed $g$ -frame and Euler angles for $A$ - and quadrupole tensors were adopted.	116
5.3	Calculated bond length ( $d$ in nm), computed spin populations (%) at Ni ( $\rho_{\text{Ni}}$ ) and NO ligand ( $\rho_{\text{NO}}$ ) and experimental maximum <sup>14</sup> N hyperfine couplings ( $A_{\text{max}} =  a_{\text{iso}} + 2T $ , in MHz) of Ni(II)NO moieties detected in this work and in Ni-doped ZSM-5 system. The data relative to ZSM-5 are taken from Pietrzyk <i>et al.</i> [14] . . . . .	121
5.4	Experimental spin Hamiltonian parameters for the Ni(II)-NO adduct in Ni-MFU-4l:NO <sub>2</sub> of species A recorded at several temperatures. (Gaussian ( $\Delta B_G^{pp}$ ) and Lorentzian ( $\Delta B_L^{pp}$ ) broadening) . . . . .	130
5.5	Computed Euler rotation of hyperfine ( $\alpha, \beta, \gamma$ ) and quadrupolar tensors ( $\alpha', \beta', \gamma'$ ) to the $g$ -tensor. First rotation by $\alpha$ around $z$ ; second rotation by $\beta$ around $y'$ ; third rotation by $\gamma$ around $z''$ . A positive sign corresponds to a clockwise rotation, a negative sign to a counterclockwise rotation. The tensor values (calculated at CASSCF level of theory) are in MHz, while angles (calculated at DFT level of theory) are in degrees. $g$ - tensor = [2.226 2.255 2.276] . . . . .	135
6.1	Paramagnetic Curie temperature ( $\theta_p$ ), effective magnetic moment ( $\mu_{\text{eff}}$ ) and Curie constant values of MIL-100(Cr) and MIL-101(Al <sub>0.8</sub> Cr <sub>0.2</sub> ) from SQUID and EPR measurements. . . . .	147
6.2	Comparison of magnetization values for the MIL-101(Cr) and MIL-100(Al <sub>0.8</sub> Cr <sub>0.2</sub> ) MOFs found from $M$ - $T$ and $M$ - $H$ curves at the 5 K, 25 K, 35 K and 100 K temperatures	147

## Chapter 1

# Introduction

In recent years, Metal-Organic Frameworks (MOFs) have started to gain considerable attention as the most prominent class of microporous materials for applications such as gas storage and separation, liquid purification, catalysis, sensing, electrochemical energy, super-capacitors, and heat storage owing to their unique structural diversity and tunability [1–6]. Recently, NuMAT technologies first commercialized a MOF product for toxic gas storage[7]. The ultrahigh porosity, tuneable pore nature, enormous internal surface area and volume, very low density and crystal integrity are just some of the bespoke properties of MOFs which provide a pathway towards a potentially unique role in the field of heterogeneous catalysis[3–5]. The high surface area of MOFs also creates large accessible volume space with a large number and variety of active sites for catalysis[3].

In addition, another important property of MOFs is the so-called ‘breathing effect’, where the porous nature of the MOFs can be manipulated to reversibly change from narrow to large pore transformations without any topological framework distortion[1, 8]. Furthermore, MOF materials can also be functionalised for bespoke catalytic applications via the modification of coordinatively unsaturated active sites, the encapsulation of guest species in pores, or by coating with functional materials[3, 9, 10].

Although MOFs are essentially based on a cage-like complex structure, they are composed of two simple hybrid building blocks through ion-covalent bonds. The first is the metal clusters, or secondary building units (SBU), and the second is the organic linkers[1, 4, 11]. The appropriate choice of MOF components dictates the physical and chemical properties of the resulting material, including porosity, chemical and thermal stability, magnetic susceptibility, conductivity, etc[1, 4, 11]. The first MOF, developed by Yaghi *et al.*[12], was namely MOF-5, with a relatively simple structure. Later developments expanded the complexity of the chemical composition to include more than one-liner and/ or hetero bimetallic species using a variety of synthesis techniques, including hydrothermal, solvothermal, and microwave-assisted techniques, along with other post-synthesis modification methods adopted by several groups[11, 13]. Furthermore, chemists have



also successfully synthesized highly complex and interesting multi-component MOFs, which contain multiple SBU and organic linkers within a single framework[13–17].

So far, more than 20,000 MOF materials have been synthesized, and it has been believed that MOFs are purely synthetic materials and don't exist naturally. In 2016, the perception was shaken by the discovery of two minerals having some MOF structural properties named '*Stepanovite*' and '*Zhemchuzhnikovite*'. Fast forward to the amazing discovery, single crystal XRD established their structure to be MOFs. The metal constituents are iron and aluminium coordinated by three oxalate ligands[18].

There are many experimental techniques, including spectroscopic methods, that have been utilized on MOF materials to investigate the structural, physical and chemical properties[4, 19–27]. Among all of them, electron paramagnetic resonance (EPR) spectroscopy is one of the inevitable tools when it comes to the local structure of MOF as it provides structural, electronic, magnetic and dynamic properties of MOFs when it contains a paramagnetic metal ion[8, 28–37]. More frequent utilization of EPR in the field of MOFs is, therefore, highly desirable. At the same time, the electronic configuration, coordination number, and amount of paramagnetic species matter a lot for the EPR technique to get qualitative and quantitative information about the material[14]. Table 1.1 summarizes the paramagnetic species from the SBU of different MOFs serves as a tool to interrogate the several properties discussed in this thesis.

For some instances where there are no magnetic ions in MOFs, and it is diamagnetic, incorporating a feeble amount of paramagnetic species at desired metal sites as a probe could be beneficial for the EPR investigations[8, 15, 38]. In the case of such magnetically diluted MOFs, one can prevent undesired magnetic interactions, which may cause a broadening of the EPR spectrum. For instance, Mendt *et al.*[8] scrutinized the structural phase transition as a function of temperature and upon CO<sub>2</sub> gas adsorption of a magnetically diluted MIL-53(Al<sub>1-x</sub>Cr<sub>x</sub>) MOF (MIL - Materials of Institute Lavoisier,  $x = 0.01 \dots 0.02$ ) where diamagnetic Al(III) sites are substituted by 1% and 2% of paramagnetic spin  $S = 3/2$  Cr(III) ions. As another example of paramagnetic dilution, recently, we reported MIL-100(Al<sub>1-x</sub>Cr<sub>x</sub>) MOF in which 20% Cr(III) ions are incorporated on Al(III) sites where EPR spectroscopy at X- (9.4 GHz), Q- (34 GHz) and W-band (95 GHz), and superconducting quantum interference device (SQUID) measurements on antiferromagnetically (AFM) coupled metal trimers in MIL100(Al<sub>0.8</sub>Cr<sub>0.2</sub>) MOFs were investigated (See Chapter 6).

In recent years, the magnetic properties of MOFs have been getting attention in the field of molecular magnetism since they can be tuned by paramagnetic SBU units[39]. Superconducting quantum interference device (SQUID) magnetometry and vibrating sample magnetometer (VSM) are used to study the temperature and field-dependent magnetic properties of various magnetic

materials[29, 40–42], including MOFs, and EPR can be utilized as a complementary tool to extract the magnetic properties of certain MOF systems from the local structure view[16, 17, 29]. In this regard, AFM inter- and intramolecular interaction of Cr(III) trimers in the MIL-100(Al/Cr) and MIL-101(Cr) MOFs, AFM intermolecular interaction of Cu(II) pairs in DUT-49(Cu) MOF and coupling of mixed metal ions in bimetallic DUT-49(M,M) (M - Zn, Cu, Mn) are investigated in this thesis work.

Along with several features, coordinatively unsaturated(CUS) SBU of MOF materials plays a critical role in gas adsorption (chemisorption), and the guest molecules interact with the CUS results in altering the local structure[8, 15, 16, 33] without affecting the framework topology. The interaction of guest molecules with the framework can be monitored by both *in situ*[8, 15, 16, 26, 33, 35, 43] and *ex situ*[15, 30, 32, 35] EPR techniques where the CUS or the absorbed molecules are paramagnetic. In some cases, where there is no chemical interaction between the framework and guest molecules (e.g: inert gases), there will still be a change in the local structure due to the Van der Waals( London dispersion) interaction and hydrogen bonding, which can be detected by monitoring the stimulated change of SBU via the modification of their magnetic signature[16, 33, 44]. In this aspect, the *in situ* xenon (physisorption) and ethylene (chemisorption) gas adsorption on Cu(II) pair-based DUT-49(Cu) MOF and *ex situ* NO (chemisorption) adsorption on Ni(II) based MFU-4l(Ni):NO<sub>2</sub> MOFs are examined in this thesis work.

TABLE 1.1: The list of MOF materials investigated in this thesis

No.	MOFs	Paramagnetic species	Focused on (in thesis)	Chapter
1	DUT-49(Cu)[16]	Cu(II)	<i>In situ</i> xenon and ethylene gas adsorption	3
2	DUT-49(M,M)[17] HKUST-1(M)	Cu(II), Mn(II), Zn(II) Zn(II), Cu(II)	post ion exchange modification	4
3	FeCuBTC[24]	Cu(II), Fe(III)	confirmation of mixed PWs	4
4	MFU-4l:NO <sub>2</sub> [42]	Ni(II)	NO gas adsorption	5
5	MIL-101(Al/Cr)[45], MIL-101(Cr)	Cr(III)	magnetic coupling	6

An intriguing aspect of MOF materials is their ability to undergo post-synthetic modification (PSM), allowing for structural alterations even after the synthesis is complete. This entails the partial or complete substitution of metal ions in the secondary building units (SBUs) with desired paramagnetic ions and the modification of linkers. PSM of MOFs has been achieved through various methods, including linker and/or metal ion modification, as well as adsorption or exchange of guest species, to enhance their physical and chemical properties[17, 27, 46, 47]. PSM serves as a

promising and widely utilized strategy for creating novel scaffolds with improved properties compared to their parent frameworks[24, 46, 48]. In many cases, the properties of the parent framework are enhanced in the resulting MOF after modification. While verifying the successful incorporation/metal exchange and characterizing the magnetic properties of resulting mixed metal clusters in PSM MOFs can be challenging, EPR spectroscopy serves as a unique and powerful complementary tool to elucidate such properties, especially when paramagnetic ions are involved[17, 24]. In this context, our research focused on studying both ion and side linker-modified MFU-4l:NO<sub>2</sub> MOF (described in Chapter 5) and ion-exchanged MOFs DUT-49(M,M) and HKUST-1(M) (discussed in Chapter 4) using continuous-wave (CW) and pulse EPR spectroscopic techniques, wherever applicable, to gain insights into their structural and magnetic characteristics.

During my doctoral journey, I delved into the fields of magnetism, magnetochemistry, quantum chemistry, spin chemistry, and molecular spectroscopy, all of which revolve around the study of spin systems. It is intriguing to observe that different fields use their own traditional terms to describe the same phenomena; for instance, uniaxial magnetic anisotropy in magnetism is referred to as axial zero-field splitting (ZFS) in EPR science[49]. By employing EPR as a complementary and alternative tool, alongside other experimental techniques, a comprehensive understanding of various aspects can be attained, including magnetic properties, structural characteristics, local geometry, spin dynamics, and the response to external influences. As part of my PhD work within the PARACAT project (Paramagnetic species in catalysis research) focusing on heterogeneous catalysis, we extensively investigated the MOF catalyst materials. Our approach involved employing EPR spectroscopy in conjunction with SQUID magnetometry, powder X-ray diffraction, and quantum chemical modelling as necessary, enabling us to explore multiple dimensions of these materials.

# Bibliography

- (1) Serre, C.; Millange, F.; Thouvenot, C.; Nogues, M.; Marsolier, G.; Louër, D.; Férey, G. *Journal of the American chemical society* **2002**, *124*, 13519–13526.
- (2) Huang, A.; He, Y.; Zhou, Y.; Zhou, Y.; Yang, Y.; Zhang, J.; Luo, L.; Mao, Q.; Hou, D.; Yang, J. *Journal of Materials Science* **2019**, *54*, 949–973.
- (3) Doonan, C. J.; Sumbly, C. J. *CrystEngComm* **2017**, *19*, 4044–4048.
- (4) Furukawa, H.; Cordova, K. E.; O’Keeffe, M.; Yaghi, O. M. *Science* **2013**, *341*, 1230444.
- (5) Jeremias, F.; Lozan, V.; Henninger, S. K.; Janiak, C. *Dalton transactions* **2013**, *42*, 15967–15973.
- (6) Zhao, Y.; Song, Z.; Li, X.; Sun, Q.; Cheng, N.; Lawes, S.; Sun, X. *Energy storage materials* **2016**, *2*, 35–62.
- (7) *NuMat Technologies*.
- (8) Mendt, M.; Jee, B.; Himsl, D.; Moschkowitz, L.; Ahnfeldt, T.; Stock, N.; Hartmann, M.; Pöppl, A. *Applied Magnetic Resonance* **2014**, *45*, 269–285.
- (9) Xu, C.; Fang, R.; Luque, R.; Chen, L.; Li, Y. *Coordination chemistry reviews* **2019**, *388*, 268–292.
- (10) Long, J.; Wang, S.; Ding, Z.; Wang, S.; Zhou, Y.; Huang, L.; Wang, X. *Chemical Communications* **2012**, *48*, 11656–11658.
- (11) Remya, V.; Kurian, M. *International Nano Letters* **2019**, *9*, 17–29.
- (12) Li, H.; Eddaoudi, M.; O’Keeffe, M.; Yaghi, O. M. *nature* **1999**, *402*, 276–279.
- (13) Yuan, S.; Qin, J.-S.; Li, J.; Huang, L.; Feng, L.; Fang, Y.; Lollar, C.; Pang, J.; Zhang, L.; Sun, D., et al. *Nature communications* **2018**, *9*, 808.
- (14) Bracci, M.; Bruzzese, P. C.; Famulari, A.; Fioco, D.; Guidetti, A.; Liao, Y.-K.; Podvorica, L.; Rezayi, S. F.; Serra, I.; Thangavel, K.; Murphy, D. M. *Electron Paramag. Reson.* **2021**, *27*, 1–46.
- (15) Mendt, M.; Vervoorts, P.; Schneemann, A.; Fischer, R. A.; Pöppl, A. *J. Phys. Chem. C* **2019**, *123*, 2940–2952.
- (16) Thangavel, K.; Walenszus, F.; Mendt, M.; Bon, V.; Kaskel, S.; Pöppl, A. *The Journal of Physical Chemistry C* **2023**, DOI: 10.1021/acs.jpcc.2c08905.

- 
- (17) Thangavel, K.; Mendt, M.; Garai, B.; Folli, A.; Bon, V.; Murphy, D. M.; Kaskel, S.; Pöppl, A. *AIP Advances* **2023**, *13*, 015019.
- (18) Huski, I.; Pekov, I. V.; Krivovichev, S. V.; Frii, T. *Science advances* **2016**, *2*, e1600621.
- (19) Krause, S.; Bon, V.; Senkovska, I.; Stoeck, U.; Wallacher, D.; Többens, D. M.; Zander, S.; Pillai, R. S.; Maurin, G.; Coudert, F.-X., et al. *Nature* **2016**, *532*, 348–352.
- (20) Krause, S.; Bon, V.; Senkovska, I.; Többens, D. M.; Wallacher, D.; Pillai, R. S.; Maurin, G.; Kaskel, S. *Nature communications* **2018**, *9*, 1–8.
- (21) Mali, G.; Mazaj, M.; Aron, I.; Hanel, D.; Aron, D.; Jaglii, Z. k. *J. Phys. Chem. Lett.* **2019**, *10*, 1464–1470.
- (22) Krause, S.; Evans, J. D.; Bon, V.; Senkovska, I.; Ehrling, S.; Stoeck, U.; Yot, P. G.; Iacomi, P.; Llewellyn, P.; Maurin, G., et al. *The Journal of Physical Chemistry C* **2018**, *122*, 19171–19179.
- (23) Bon, V.; Brunner, E.; Pöppl, A.; Kaskel, S. *Advanced Functional Materials* **2020**, *30*, 1907847.
- (24) Bitzer, J.; Otterbach, S.; Thangavel, K.; Kultaeva, A.; Schmid, R.; Pöppl, A.; Kleist, W. *Chem. Eur. J.* **2020**, *26*, 5667–5675.
- (25) Falcaro, P.; Ricco, R.; Doherty, C. M.; Liang, K.; Hill, A. J.; Styles, M. J. *Chem. Soc. Rev.* **2014**, *43*, 5513–5560.
- (26) Ehrling, S.; Mendt, M.; Senkovska, I.; Evans, J. D.; Bon, V.; Petkov, P.; Ehrling, C.; Walenszus, F.; Pöppl, A.; Kaskel, S. *Chemistry of Materials* **2020**, *32*, 5670–5681.
- (27) Garai, B.; Bon, V.; Krause, S.; Schwotzer, F.; Gerlach, M.; Senkovska, I.; Kaskel, S. *Chemistry of Materials* **2020**, *32*, 889–896.
- (28) Mendt, M.; Gutt, F.; Kavooosi, N.; Bon, V.; Senkovska, I.; Kaskel, S.; Pöppl, A. *The Journal of Physical Chemistry C* **2016**, *120*, 14246–14259.
- (29) Kultaeva, A.; Biktagirov, T.; Neugebauer, P.; Bamberger, H.; Bergmann, J.; van Slageren, J.; Krautscheid, H.; Pöppl, A. *J. Phys. Chem. C* **2018**, *122*, 26642–26651.
- (30) Kultaeva, A.; Böhlmann, W.; Hartmann, M.; Biktagirov, T.; Pöppl, A. *The journal of physical chemistry letters* **2019**, *10*, 7657–7664.
- (31) Jee, B.; Eisinger, K.; Gul-E-Noor, F.; Bertmer, M.; Hartmann, M.; Himsl, D.; Pöppl, A. *The Journal of Physical Chemistry C* **2010**, *114*, 16630–16639.
- (32) Jee, B.; Koch, K.; Moschkowitz, L.; Himsl, D.; Hartman, M.; Pöppl, A. *The Journal of Physical Chemistry Letters* **2011**, *2*, 357–361.

- (33) Polyukhov, D. M.; Krause, S.; Bon, V.; Poryvaev, A. S.; Kaskel, S.; Fedin, M. V. *J. Phys. Chem. Lett.* **2020**, *11*, 5856–5862.
- (34) Friedländer, S.; Petkov, P. S.; Bolling, F.; Kultaeva, A.; Böhlmann, W.; Ovchar, O.; Belous, A. G.; Heine, T.; Pöppl, A. *The Journal of Physical Chemistry C* **2016**, *120*, 27399–27411.
- (35) imnas, M.; Jee, B.; Hartmann, M.; Banys, J.; Pöppl, A. *The Journal of Physical Chemistry C* **2015**, *119*, 28530–28535.
- (36) imnas, M.; Ciupa, A.; Maczka, M.; Pöppl, A.; Banys, J. *The Journal of Physical Chemistry C* **2015**, *119*, 24522–24528.
- (37) Friedländer, S.; Simenas, M.; Kobalz, M.; Eckold, P.; Ovchar, O.; Belous, A. G.; Banys, J.; Krautscheid, H.; Pöppl, A. *The Journal of Physical Chemistry C* **2015**, *119*, 19171–19179.
- (38) Nevjestic, I.; Depauw, H.; Leus, K.; Rampelberg, G.; Murray, C. A.; Detavernier, C.; Van Der Voort, P.; Callens, F.; Vrielinck, H. *The Journal of Physical Chemistry C* **2016**, *120*, 17400–17407.
- (39) Espallargas, G. M.; Coronado, E. *Chem. Soc. Rev.* **2018**, *47*, 533–557.
- (40) Son, K.; Kim, R. K.; Kim, S.; Schütz, G.; Choi, K. M.; Oh, H. *physica status solidi (a)* **2020**, *217*, 1901000.
- (41) Zhao, X.; Liu, S.; Tang, Z.; Niu, H.; Cai, Y.; Meng, W.; Wu, F.; Giesy, J. P. *Scientific reports* **2015**, *5*, 11849.
- (42) Thangavel, K.; Bruzzese, P. C.; Mendt, M.; Folli, A.; Knippen, K.; Volkmer, D.; Murphy, D. M.; Pöppl, A. *Physical Chemistry Chemical Physics* **2023**, DOI: 10.1039/D3CP01449E.
- (43) Jee, B.; Hartmann, M.; Pöppl, A. *Molecular Physics* **2013**, *111*, 2950–2966.
- (44) Aquilanti, V.; Cornicchi, E.; Moix Teixidor, M.; Saendig, N.; Pirani, F.; Cappelletti, D. *Angewandte Chemie International Edition* **2005**, *44*, 2356–2360.
- (45) Thangavel, K.; Folli, A.; Ziese, M.; Hausdorf, S.; Kaskel, S.; Murphy, M. D.; Pöppl, A. *Scipost Physics Proc.* **2023**, *11*, 016.
- (46) Mandal, S.; Natarajan, S.; Mani, P.; Pankajakshan, A. *Advanced Functional Materials* **2021**, *31*, 2006291.
- (47) Koeberl, M.; Cokoja, M.; Herrmann, W. A.; Kuehn, F. E. *Dalton Transactions* **2011**, *40*, 6834–6859.
- (48) Denysenko, D.; Volkmer, D. *Faraday Discussions* **2017**, *201*, 101–112.

- (49) Chilton, N. F., *Single-Molecule Magnets: Design, Measurement, and Theory - IVEM International EPR Seminars*; URL-<https://www.youtube.com/watch?v=0qjfavhp4rwab> channel = IVEMInternationalEPRSeminars: 2022.

## Chapter 2

# Materials and Methods

### 2.1 The choice of MOFs

In this thesis work, flexible and rigid MOF materials are investigated by means of EPR techniques with and without external stimuli (gas adsorption). The details of the MOF materials and the motivation for work are discussed in this Chapter. The SBU containing transition metal ions are the EPR active sites and the behaviour of the local structure upon gas adsorption, the way local structure interacts with the guest molecules, and inter and intra molecular interaction were analysed. The choice of our MOF materials are DUT-49(Cu), MFU-4l(Ni):NO<sub>2</sub>, MIL-100(Al/Cr), MIL-101(Cr), Zn- and Fe- based HKUST-1. Among all these, DUT-49 MOF has a flexible nature and is also known as breathing effect[1, 2].

#### 2.1.1 DUT-49(Cu) MOF

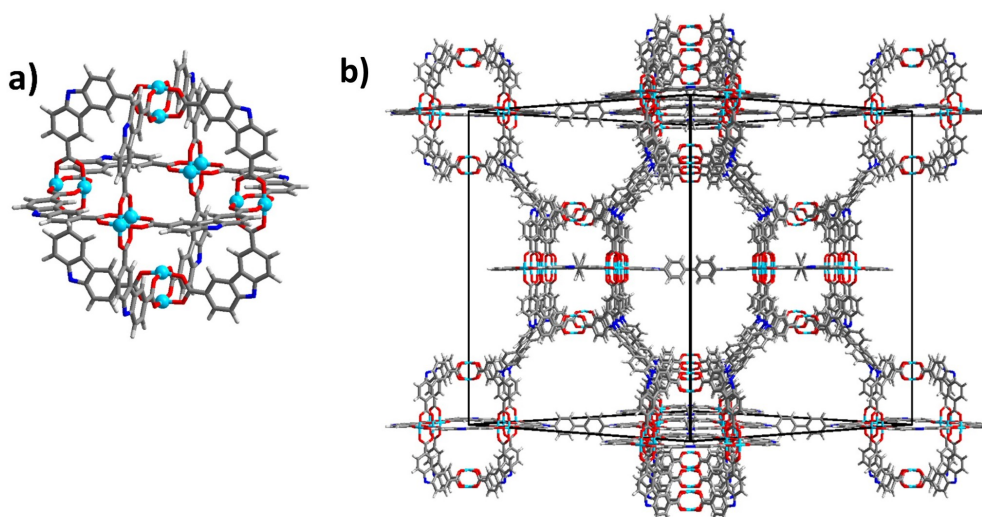


FIGURE 2.1: Metal-organic polyhedra built up of (a) paddle-wheel units containing metal and (b) crystal structure of DUT-49(M).

DUT stands for the Dresden University of Technology, and the MOF DUT family were synthesized by Prof. Stefan Kaskel's group, Dresden, for our EPR studies. We worked on a paddle



wheel (PW) based DUT-49(M) MOFs with the composition  $[\text{Cu}_2(\text{C}_{40}\text{H}_{20}\text{N}_2\text{O}_8)]$  (Figure 2.1) where metal ions in a PW unit connected through a  $\text{H}_4\text{BBCDC}$  linker ( $[[1,1'\text{-biphenyl}]-4,4'\text{-diyl}]\text{bis}(9\text{H-carbazole-3,6-dicarboxylic acid})$ ). DUT-49(Cu) material has pores in three different sizes, i.e: cuboctahedral (12 Å), tetrahedral (21 Å), and octahedral (26 Å) pores. This material exhibits a unique and novel counterintuitive feature called negative gas adsorption (NGA) for the first time reported in 2016 by Krause *et al.*[3], and was originally synthesized for methane storage applications[4]. Normal porous MOFs take up gas for the increased pressure, whereas NGA materials instead release gas upon applied external pressure for a certain pressure range, leading to an overall pressure amplification in a closed system. DUT-49(Cu) is a well-studied representative of flexible mesoporous frameworks, in particular, also famous for long-lived overloaded metastable states in the presence of a variety of gases at defined temperatures, leading to NGA transitions[2, 5]. As of 2019, DUT-49 has been the only known MOF showing NGA transition, and then DUT-50, with the systematic linker expansion, was also reported as a second NGA material[3]. The combined experimental and computational studies confirm NGA to be a general phenomenon observable for highly porous materials satisfying specific structural design rules (pore size > 2 nm, particle size, framework softness, permeability of adsorption-induced structural contraction)[3].

Herein, on this material, the pore transformation ( $op \leftrightarrow cp$ ) upon xenon and ethylene gas adsorption and the mechanistic insights into these transitions were investigated by means of *in situ* X-band CW - EPR spectroscopy along with *in situ* XRD studies (see Chapter 3) on DUT-49(Cu) MOF. The antiferromagnetically coupled Cu(II) - Cu(II) dimers in the PW units of this pillared layer MOF serve as local magnetic probes in the *in situ* EPR measurement[5]. In addition, post-synthetic metal ion exchange on bimetallic DUT-49(M,M)(M-Cu, Zn, Mn) was examined using X-, Q- and W-band CW - EPR (see Chapter 4)[6].

### 2.1.2 HKUST-1 MOF

HKUST-1 (Hong Kong University of Science and Technology), also referred to as CuBTC, MOF-199, or  $\text{Cu}_3\text{BTC}_2$ , is an extensively studied copper-based MOF material. Its structure consists of dimeric copper paddlewheel (PW) units connected by benzene-1,3,5-tricarboxylate (BTC) linkers (Figure 2.2)[7–9]. HKUST-1 exhibits a cubic crystal structure, belonging to the space group  $\text{Fm}\bar{3}\text{m}$ , and possesses a high surface area ranging from 1500 to 2000  $\text{m}^2/\text{g}$ [10]. The unique characteristics of HKUST-1, such as the presence of coordinatively unsaturated sites (CUS), Lewis acid properties, large surface area, and the benzene ring structure, make it an excellent adsorbent for gases like  $\text{CO}_2$ ,  $\text{CH}_4$ , and volatile organic compounds. These features contribute to its applications in

gas storage, separation, and catalysis, making HKUST-1 a highly versatile and valuable MOF material.

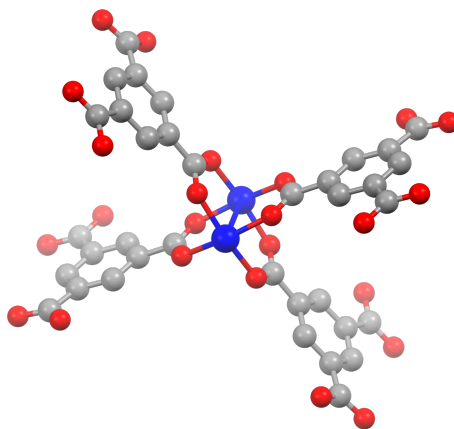


FIGURE 2.2: Structure of the secondary building unit (Cu(II)-Cu(II) PW) of activated HKUST-1. The water molecules are removed from the axial centres and represent the CUS PW Units.

In addition to its gas adsorption capabilities, HKUST-1 is also utilized for the removal of metal ion impurities from water due to its ionic and electrical conductivity, commercial availability, ease of operation, and economic feasibility. However, the hydrolytic instability of HKUST-1, attributed to its open structure, imposes limitations on its applications[8, 9]. To overcome this limitation, researchers have explored PSM of HKUST-1 by modifying the ligands and/or metal ions, which has shown promising results in enhancing its adsorption capacities for polluted gases[9]. Several research groups have successfully synthesized bimetallic paddlewheel units within the HKUST-1 framework using different combinations of transition metal ions, employing various synthesis routes. This exploration of modified HKUST-1 materials aims to harness the exceptional properties of the building units for diverse applications such as catalysis, selective gas adsorption, and storage[7, 9–15].

In this regard, using CW and pulse EPR spectroscopic techniques, we discussed the formation of mixed PW units in zinc and iron-incorporated HKUST-1 MOFs in Chapter 4, and our results are in good agreement with the other structural characterizations as well.

### 2.1.3 Ni:MFU-4l:NO<sub>2</sub> MOF

The Ni-MFU-4l-NO<sub>2</sub> ([Zn<sub>4</sub>Ni<sub>1</sub>(NO<sub>2</sub>)<sub>3</sub>Cl<sub>1</sub>(BTDD)<sub>3</sub>], H<sub>2</sub>-BTDD = bis(1H-1,2,3-triazolo[4,5-b],[4,5-i])dibenzo[1,4]dioxin)) MOF in a cubic structure we received from Prof. D. Volkmer group (University of Augsburg) stands for 'Metal-Organic framework Ulm University'. This MOF is synthesized by post-ion exchange and linker modification by substituting a certain amount of Ni(II) and

NO<sub>2</sub> on Zn(II) and Cl sites, respectively, from the parent MFU-4l ([Zn<sub>5</sub>Cl<sub>4</sub>(BTDD)<sub>3</sub>], H<sub>2</sub>-BTDD = bis(1H-1,2,3-triazolo[4,5-b],[4,5-i])dibenzo[1,4]dioxin) MOF(Figure 2.3)[16, 17]. After the post-exchange modification, the paramagnetic Ni(II) is in a five-fold coordinated environment which is our key interest from the EPR perspective.

The MFU MOF family have been extensively studied in confinement effects for supercooled liquids[18], highly effective gas separation[19], in cyclic gas-phase heterogeneous process[17], stereoselective heterogeneous diene polymerization[20], as a catalyst for the reversible gas-phase redox process[21] and gating effects for hydrogen Sorption[22]. The size of the pore for the different MOFs in the MFU family is given in Table 2.1[18]

TABLE 2.1: Pore sizes of MFU-1, MFU-4, MFU-4l MOFs

MOF	Composition	Pore size (Å)
MFU -1	C <sub>48</sub> H <sub>48</sub> N <sub>12</sub> OCo <sub>4</sub>	18
MFU -4	C <sub>48</sub> H <sub>6</sub> Cl <sub>4</sub> N <sub>18</sub> Zn <sub>5</sub>	11
MFU -4l	C <sub>36</sub> H <sub>12</sub> Cl <sub>4</sub> N <sub>18</sub> O <sub>6</sub> Zn <sub>5</sub>	12/18

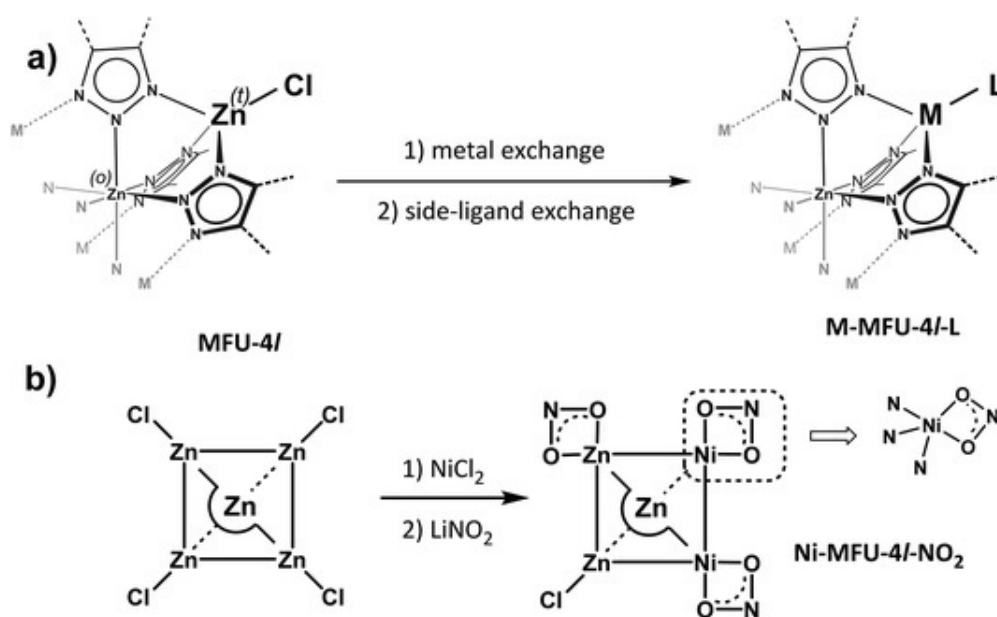


FIGURE 2.3: (a) Post-synthetic metal- and side-ligand exchange reactions in MFU-4l at peripheral sites (a part of the SBU is shown, t - tetrahedral, o - octahedral), (b) schematic representation of the Kuratowski unit in MFU-4l and synthesis of MFU-4l-NO<sub>2</sub> (an idealized composition is shown, in the following schemes only one peripheral Ni-center is shown)(Reproduced from Ref [17]. with permission from the Royal Society of Chemistry.)

Herein, we performed NO adsorption on MFU-4l(Ni):NO<sub>2</sub> and the nature of the chemical bonding between NO and open-shell Ni(II) ions docked in a metalorganic framework is fully characterized by EPR spectroscopy and computational methods. High-frequency EPR experiments reveal the presence of unsaturated Ni(II) ions displaying fivefold coordination. Upon NO

adsorption, in conjunction with advanced EPR methodologies and DFT/CASSCF modelling, the covalency of the metal-NO and metal-framework bonds is directly quantified. This enables unravelling the complex electronic structure of NiII/NO species and retrieving their microscopic structure (see Chapter 5).

#### 2.1.4 Bimetallic MIL-100(Al/Cr) and MIL-101(Cr)

MIL-100 and MIL-101 MOF materials are made up of BTC and 1,4-benzenedicarboxylate (BDC) linkers, respectively, connected with  $\mu_3$ -O-centered trinuclear inorganic clusters  $[M_3(\mu_3-O)(O_2C-R)_6]$  (Figure 2.4)[23]. Each metal centre is situated in an octahedral environment coordinated by one  $\mu_3$  atom, which is shared with two other metallic centres and makes trimers. MIL-101 and MIL-100 MOFs possess two different mesopore cages. i.e: 25 Å and 29 Å for MIL-100, and 29 Å and 34 Å for MIL-101[23–25].

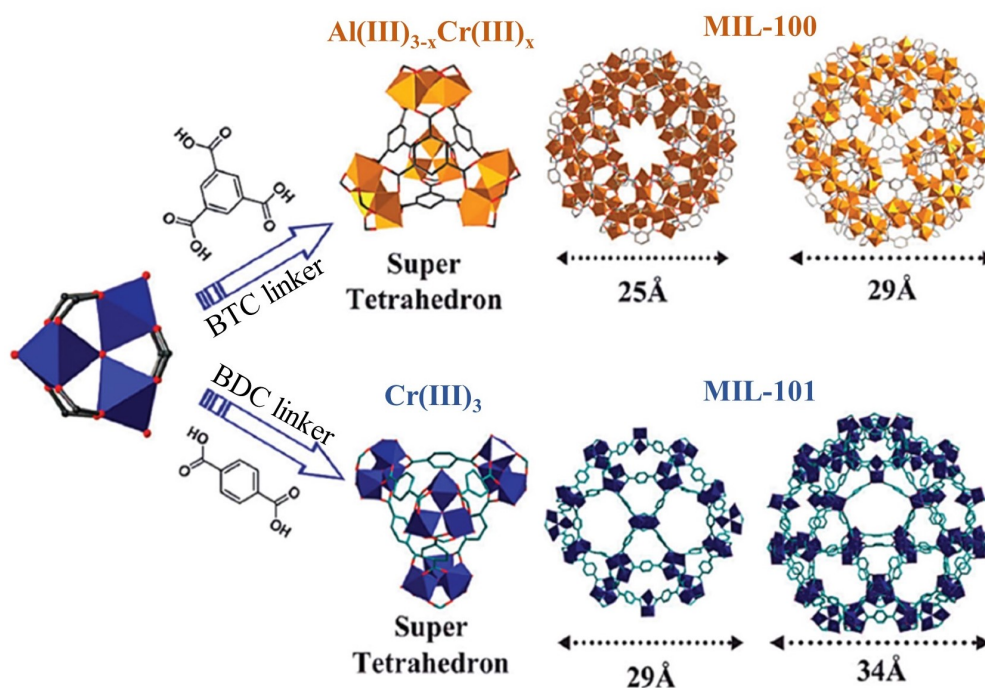


FIGURE 2.4: Cr(III)/Al(III) ions are in the octahedral trimer units and four trimers, forming a supertetrahedra (Modified from [26, 27] with permission from the Royal Society of Chemistry.) showing MIL-101(Cr) and MIL-100( $Al_{0.8}Cr_{0.2}$ ) frameworks with different pore sizes

MIL-100(Al) and MIL-101(Al) MOFs have been investigated for the sorption and separation of gases, adsorption of liquids[28], upon high-pressure effect[29], ethylene polymerization[30] and encapsulation of chemical species[28]. In addition, Mali *et al.*[31] investigated the magnetism of Al(III) and Fe(III) mixed metals in MIL-100 MOF by means of  $^{27}Al$  NMR and spectroscopy and reported the arrangement of those metal ions (3Fe and/or 2Fe1Al units, 1Fe2Al units) within the

framework. Such bimetal-organic MIL-100 and MIL-101 frameworks with coordinatively unsaturated metal sites may serve as Lewis acid sites for highly efficient catalytic processes[32, 33].

In this regard, we utilized magnetically diluted MIL-100( $\text{Al}_{0.8}\text{Cr}_{0.2}$ ) MOF by incorporating 20% Cr(III) on Al(III) sites and pure MIL-101(Cr) MOF for comparison. Further, we examined the inter- and intra-magnetic interaction between Cr(III) trimers in the SBU of these MOFs by means of multi-frequency EPR spectroscopic techniques and magnetization measurements using a superconducting quantum interference device(SQUID).

### 2.1.5 Post synthetically ion exchanged MOFs (Bimetallic DUT-49 and HKUST-1)

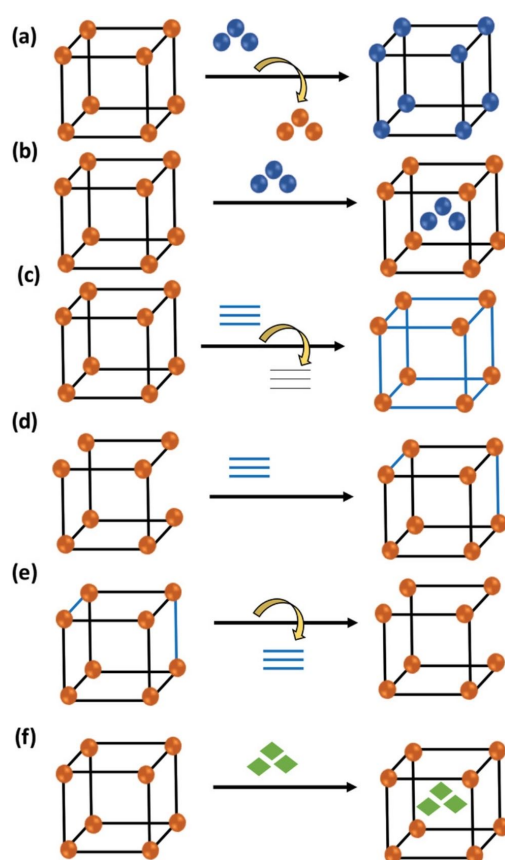


FIGURE 2.5: The pathways of PSM in MOFs: a) metal exchange, b) metal incorporation, c) ligand exchange, d) ligand installation, e) ligand removal, and e) guest incorporation inside the pores. Adapted from [34] copyright @ 2019 The Authors.

Post-synthetic modification (PSM) of MOF materials offers versatile routes for enhancing their properties without altering the network topology. PSM can be achieved through the modification of linkers (ligands) and/or metal ions, as well as the adsorption or exchange of guest species. Figure 2.5 illustrates the potential pathways for PSM in the SBUs and linker components of MOF materials. This strategy is widely employed and holds great promise for generating novel scaffolds with improved physical and chemical properties compared to the parent frameworks[11,

17, 34–37]. In many cases, the properties of interest in the parent framework are significantly enhanced in the resulting MOF after modification. Mandal *et al.* recently discussed the applications of PSM-MOFs across various fields, including ferroelectrics, gas adsorption, magnetism, electrical conductivity, dye encapsulation, surface alteration, chemical sensing, and catalysis[34]. PSM represents a powerful strategy for tailoring MOF materials to meet specific requirements and expand their potential applications.

While PSM of MOF materials offers great potential, verifying the successful incorporation or metal exchange, as well as understanding the magnetic properties of resulting mixed metal clusters, can pose challenges. However, EPR spectroscopy emerges as a unique and powerful complementary tool for elucidating such properties in PSM MOFs, particularly when paramagnetic ions are involved[6]. In our study, we focused on investigating both ion and side linker-modified MFU-4l:NO<sub>2</sub> MOF, as described in Section 2.1.3, as well as ion-exchanged MOFs DUT-49(M,M) and Zn-incorporated HKUST-1. We employed both continuous-wave (CW) and pulse EPR spectroscopic techniques to analyze these materials and gain valuable insights into their characteristics, whenever applicable. The utilization of EPR spectroscopy enhances our understanding of the structural and magnetic properties of PSM MOFs, facilitating their potential applications in various fields.

## 2.2 EPR spectroscopy

### 2.2.1 Principles of electron paramagnetic resonance

EPR spectroscopy, also known as EPR, operates on the principle of electromagnetic radiation interacting with unpaired electrons in paramagnetic species within a static magnetic field[38, 39]. This spectroscopic technique shares similarities with nuclear magnetic resonance (NMR), as both methods involve the interaction of electromagnetic radiation with a magnetic moment. However, while EPR focuses on unpaired electrons, NMR is concerned with the nucleus possessing a non-zero nuclear spin. By subjecting paramagnetic species to microwave radiation, EPR spectroscopy enables the resonance absorption of the unpaired electrons, providing valuable information about the electron spin dynamics, molecular structure, and magnetic properties. With its ability to probe the behavior of unpaired electrons, EPR spectroscopy plays a crucial role in the investigation of diverse fields, including chemistry, materials science, biology, and physics.

The electric field ( $\vec{E}_1$ ) and magnetic field ( $\vec{B}_1$ ) of EM waves are coupled perpendicular in the direction of propagation and the stream of particles of EM radiation is known as 'photons'. The energy of any microwave photon is given by the quantity  $h\nu_{mw}$  ( $h$  - Planck's constant and  $\nu_{mw}$  -

mw frequency). In most spectroscopic techniques, the oscillating electric field ( $\vec{E}_1$ ) component of the EM radiation interacts with an oscillating electric dipole of the molecule. Whereas, in magnetic resonance, the oscillating magnetic dipole of the molecule interacts with the oscillating magnetic field component ( $\vec{B}_1$ ) of the EM radiation. Nevertheless, in magnetic resonance experiments, a static magnetic field  $\vec{B}$  is applied in addition to the oscillating magnetic field component ( $\vec{B}_1$ ) to align the magnetic moments and to shift the energy levels to attain splitting. Every single electron in the molecule possesses an intrinsic magnetic-dipole moment resulting from its spin. Thus, the net moment is zero when its paired with another electron in a singlet state (or paired electrons in a triplet state with spin  $S = 1$ ). Therefore, in the case of EPR, it is necessary that the molecule should contain one or more unpaired electrons for the interaction with an EM field.

The energy of interaction between a paramagnetic species containing an unpaired electron, with the magnetic moment  $\mu$ , and a magnetic field  $B$  is given by [38]

$$U = -\vec{\mu} \cdot \vec{B} \quad (2.1)$$

In the concept of paramagnetism, it is assumed that the magnetic moment of paramagnetic centres is weakly coupled, and hence, it can be considered that the paramagnetic species are isolated from one another. In such cases, the paramagnetic susceptibility  $\chi$ , obeys Curie's law [38]

$$\chi = \frac{C}{T} \quad (2.2)$$

where  $C$  - Curie constant and  $T$  - temperature. Further, the magnetic moment  $\vec{\mu}$  associated with electron spins  $S$ , both are considered to be quantum operators and can be related by [38]

$$\hat{\mu} = -g\mu_B\hat{S} \quad (2.3)$$

where  $\mu_B$  - electron Bohr magneton and  $g$  - Zeeman factor or so-called electron  $g$ -factor. Now, the potential energy of the dipole in the magnetic field can be expressed as a Hamiltonian operator [38]

$$\hat{H} = g\mu_B\hat{S} \cdot \vec{B} \quad (2.4)$$

By EPR science, it is also known as spin Hamiltonian operator or Hamiltonian. For a  $S = 1/2$  two-level system, the energies obtained as solutions to eqn. 2.4 are [38]

$$E_{\pm} = \pm \frac{1}{2}g\mu_B B \quad (2.5)$$

## 2.2. EPR spectroscopy

Under resonance conditions, for a fixed microwave frequency,  $\nu_{MW}$ , an EPR transition occurs when the magnetic field is varied until the resonance value of  $\vec{B}$  is reached. Hence,

$$\Delta E = h\nu_{mw} = E_+ - E_- = g\mu_B B \quad (2.6)$$

According to the transition probability theory in quantum mechanics, a transition rate for the induced transitions ( $1/2 \rightarrow -1/2$  and  $-1/2 \rightarrow 1/2$ ) can be expected. For both the transitions, it requires that the sample needs to be placed in a magnetic field,  $\vec{B}$ , perpendicular to the microwave oscillating magnetic field,  $\vec{B}_1$ . The transitions which give rise to EPR spectra are originated from the magnetic dipole and the selection rule for the magnetic quantum number ( $M_s$ ), which has the allowed values  $S, S-1, \dots, -S$ , is [38]

$$|\Delta M_s| = 1 \quad (2.7)$$

For instance, the illustration of  $S = 1/2$  system is given in Figure 2.6[40]. Furthermore, eqn. 2.7 is no longer strictly valid when  $S > 1/2$  or when hyperfine, quadrupole and nuclear Zeeman interactions are present, which will be discussed in the proceeding sections 2.2.2.

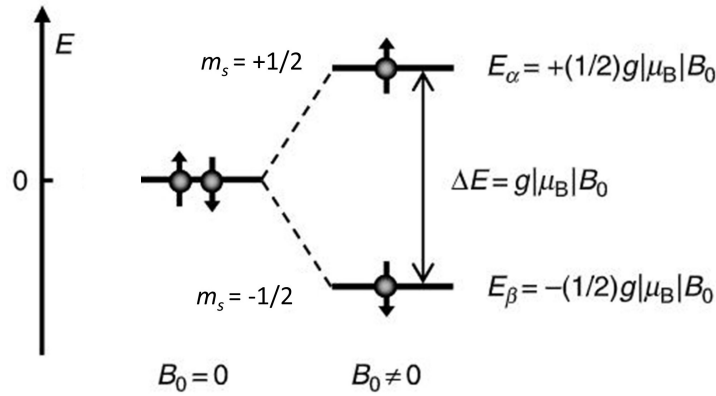


FIGURE 2.6: EPR Energy level diagram depicting the relationship between the absorbed energy, first derivative signal, and magnetic field for the  $S = 1/2$  system[40]

In the absence of  $\vec{B}$ , for the ensemble of electron spins with  $S = 1/2$  populated in the two states, namely,  $m_s = +1/2$  and  $m_s = -1/2$  will be equally populated. This situation changes when the external field,  $\vec{B}$ , is applied if the spin ensemble is allowed to interact with its environment (*lattice*). When  $\vec{B} \neq 0$ , the states  $m_s = +1/2$  and  $m_s = -1/2$  will not have the same energy and the ratio between the number ( $N$ ) of spins in these states can be given by the Boltzmann distribution law[40]

$$\frac{N_{+1/2}}{N_{-1/2}} = \exp\left(\frac{-g\mu_B \vec{B}}{k_B T}\right) \quad (2.8)$$



where  $k_B$  is the Boltzmann constant, and  $T$  is the absolute temperature of the lattice. At room temperature,  $g\mu_B\vec{B} \ll k_B T$ , and only the linear term is present from the expanded exponential series. Here, the approximate populate ratio becomes[40]

$$\frac{N_{+1/2}}{N_{-1/2}} = 1 - \frac{g\mu_B\vec{B}}{k_B T} \quad (2.9)$$

This approximation is valid unless the spin system is at a very high field or very low temperature. The relaxation processes between these energy levels when the spin interacts with its neighbouring spins and the lattice are discussed in the proceeding section 2.2.3

EPR spectroscopy can be operated at several MW frequencies, which requires a corresponding applied magnetic field for the electron spin resonance. The MW frequencies start from S-band (2-4 GHz), X-band (8-10 GHz), Q-band ( 34 GHz), and W-band ( 94 GHz), and expand upto Terahertz region. Upto Q-band, EPR spectroscopy can be operated using an electromagnet which produces a magnetic field around 1.6 - 2 T and above Q-band MW region, EPR needs to be operated using a superconducting magnet. Herein, we used X-, Q- and W- band EPR spectroscopies to examine several paramagnetic centers containing MOF materials.

In general, CW EPR spectra are recorded by maintaining an MW irradiation field of constant frequency ( $\nu$ ) and sweeping the applied magnetic field ( $B$ ). During the experiment, the sample is mounted in a microwave cavity (resonator), and the microwave irradiation is provided by the klystron source. The waveguide transfers the MW to the cavity. Afterwards, the transferred MW should be critically coupled by adsorbing the incident MW power completely. The modulation amplitude, modulation frequency, microwave power, sweep time, conversion time, and time constant are the important parameters to get good quality EPR spectra with a high signal-to-noise ratio, and one needs to ensure a good combination of these values during the experiments.

### 2.2.2 The spin Hamiltonian parameters

The energy terms describing the interactions of the electron and nuclear spins among themselves and with their environment in a molecule (or a solid) can be described by the complete spin Hamiltonian eqn.2.10[41, 42]. The presence of spin Hamiltonian terms can be eliminated based on the spin quantum numbers of the interacting ions and their relative magnitudes.

$$\hat{H}_{spin} = \hat{H}_{EZ} + \hat{H}_{ZFS} + \hat{H}_{HF} + \hat{H}_{NZ} + \hat{H}_{NQ} \quad (2.10)$$

This could be explicitly expanded as

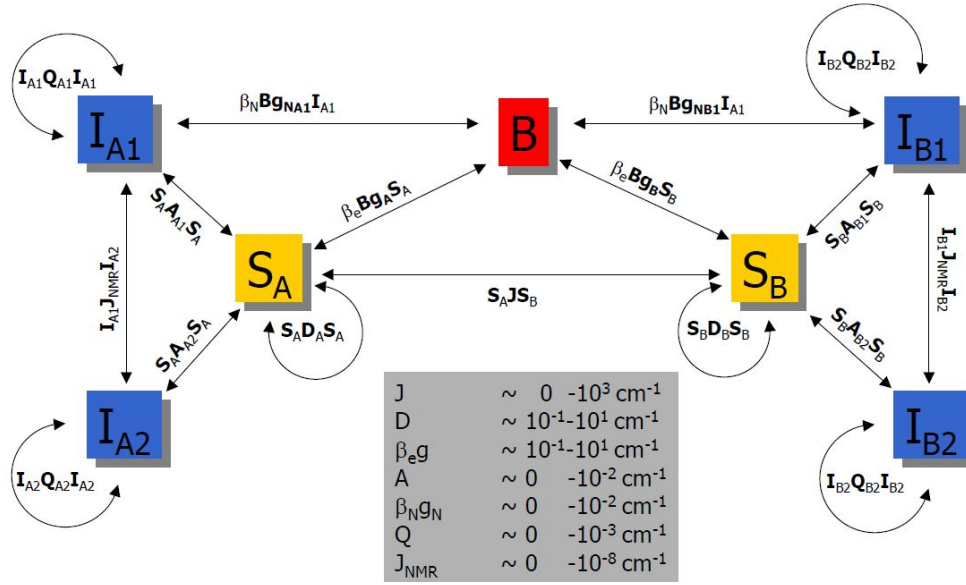


FIGURE 2.7: Terms in spin Hamiltonian parameters[43]

$$\hat{H}_{spin} = \mu_B \vec{B}^T \cdot \mathbf{g} \cdot \hat{S} + \hat{S}^T \mathbf{D} \hat{S} + \sum_{j=1}^N \hat{S}^T \mathbf{A}^j \hat{I}^j - \mu_n \sum_{j=1}^N \mathbf{g}_{N,j} \vec{B}^T \hat{I}^j + \sum_{i=1}^M \hat{I}^{k_i T} \mathbf{Q}^{k_i} \hat{S}^{k_i} \quad (2.11)$$

The detailed description of eqn.2.11 is given below.

### Electron Zeeman interaction

The first term  $\hat{H}_{EZ}$  is an electron Zeeman (EZ) interaction (eqn. 2.12) term that describes the interaction between the applied magnetic field,  $B$  and the electron spin  $S$ . The matrix  $g$  is the  $g$ -tensor with the principal values  $g_{xx}, g_{yy}, g_{zz}$ .

$$\hat{H}_{EZ} = \mu_B \vec{B}^T \cdot \mathbf{g} \cdot \hat{S} \quad (2.12)$$

In general, all spatial information is accommodated in the  $g$ -tensor, which can be anisotropic or reduced to isotropic based on the local symmetry of the paramagnetic metal ion or molecule. If the symmetry is low,  $g$ -tensor will be  $g_{xx} \neq g_{yy} \neq g_{zz}$  and referred to be orthorhombic. It will be axial when two principle  $g$ -values are equal ( $g_{xx} = g_{yy} \neq g_{zz}$ ) and when all principle values are equal, the  $g$ -tensor is referred to be isotropic or cubic ( $g_{xx} = g_{yy} = g_{zz}$ ) (Figure 2.8).

### Zero Field splitting

The second term  $\hat{H}_{ZFS}$  (eqn. 2.14) corresponds to the zero-field splitting (ZFS) interaction and, which manifests only when there is more than one unpaired electron in the spin system ( $S > 1/2$ ).

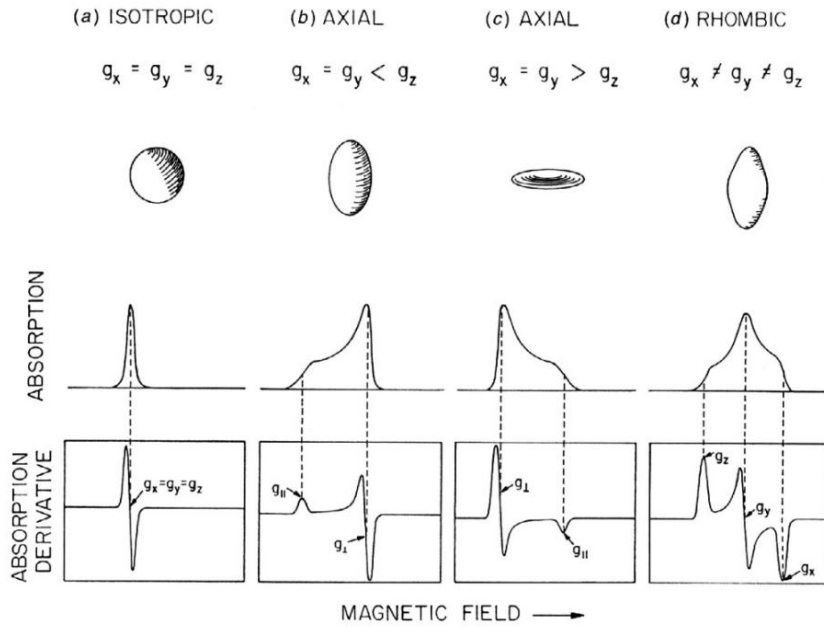


FIGURE 2.8: Scheme of  $g$ -tensor and the consequential EPR spectra for (a) isotropic, (b-c) axial and (d) rhombic symmetry. (adapted from ref. [44]).

The ZFS term leads to splitting even in the absence of an external magnetic field (if  $S > 1/2$ ). In principle, ZFS arises from i) spin-spin coupling (direct dipolar interaction among pairs of unpaired electrons) and ii) spin-orbit coupling (the interaction of unpaired electron spin angular momentum with its electron orbital momentum).

$$\hat{H}_{ZFS} = \hat{S}^T \mathbf{D} \hat{S} \quad (2.13)$$

For  $S \leq 5/2$ ,

$$\hat{H}_{ZFS} = D[\hat{S}_z^2 - \frac{1}{3}S(S+1)] + E(\hat{S}_x^2 - \hat{S}_y^2) \quad (2.14)$$

where,  $D$  can be presented as a traceless ZFS tensor and defined by two parameters  $D$  and  $E$  in its principle axes frame. In general, the limitation between the  $D$  and  $E$  parameters is  $|E| \leq \frac{|D|}{3}$ . The ZFS can be much greater than the EZ interaction on the basis of ligand field symmetry and electron coupling. Here  $D$  is the axial (uniaxial) ZFS parameter, and  $E$  is the rhombic ZFS parameter.

### Hyperfine interaction

The third term  $\hat{H}_{HF}$  in eqn. 2.15 describes hyperfine interaction (HFI) arising from the magnetic interaction of an electron spin with nuclear spins in its close surrounding ( $< 1$  nm). The HFI

interaction could be further split into isotropic and anisotropic interactions eqn. 2.17.

$$\hat{H}_{HF} = \sum_{j=1}^N \hat{S}^T \mathbf{A}^j \hat{I}^j = \hat{H}_F + \hat{H}_{DD} \quad (2.15)$$

where the vector operator  $\hat{I}^j$  describes the nuclear spin  $I^j$  of the  $j^{th}$  nucleus and the matrices  $\mathbf{A}^j$  are the corresponding HFI tensors. Considering the HFI with a single nucleus, the isotropic and anisotropic operators can be written as

$$\hat{H}_F = a_{iso} \hat{S}^T \hat{I} \quad (2.16)$$

$$\hat{H}_{DD} = \hat{S}^T \mathbf{T} \hat{I} \quad (2.17)$$

where  $\hat{H}_F$  and  $\hat{H}_{DD}$  are the Fermi contact (isotropic) and dipole-dipole (anisotropic) interaction parts. Further,  $T$ -tensor matrix can be written as

$$\mathbf{T} = T \begin{pmatrix} -(1 + \rho) & 0 & 0 \\ 0 & -(1 - \rho) & 0 \\ 0 & 0 & 2 \end{pmatrix} \quad (2.18)$$

with the dipolar constant  $T$  and the asymmetry parameter  $\rho$ . Moreover, the  $\mathbf{A}$ -tensor can be calculated by

$$\mathbf{A} = a_{iso} \mathbf{1} + \mathbf{T} \quad (2.19)$$

Further,  $a_{iso}$  related to the electron spin density  $|\psi(0)|^2$  at the nucleus and  $T$  assuming that the electronic and nuclear magnetic moments can be considered as point-dipoles will be elaborated as

$$a_{iso} = \frac{2}{3} \frac{\mu_0}{h} \mu_B \mu_n g_e g_n |\psi(0)|^2; \mathbf{T} = \frac{\mu_0}{4} \mu_B \mu_n g_e g_n r^{-3} \quad (2.20)$$

where  $\mu$  being the permeability of free space,  $h$  the Planck constant,  $\mu_n$  the nuclear magneton,  $g_e = 2.0023$  the  $g$ -factor of the free electron and  $g_n$  the nuclear  $g$ -factor.  $T$  could be estimated from the distance between the electron and nucleus.

### Nuclear Zeeman interaction

The fourth term  $\hat{H}_{NZ}$ , nuclear Zeeman (NZ) interaction arises from the interaction between the applied magnetic field and the nuclear spins ( $I \neq 0$ ), which in general, doesn't affect the continuous wave EPR spectrum prominently.

$$\hat{H}_{NZ} = -\mu_n \sum_{j=1}^N g_{n,j} \vec{B}^T \hat{I}^j \quad (2.21)$$

where  $g_n$  is the nuclear  $g$ -factor and  $\mu_n$  is the nuclear magneton. Similar to the EZ interaction, the  $m_I$  moments are non-degenerate in an applied magnetic field relative to its orientation, which leads to a splitting of the electronic states by  $2I+1$ . The order of magnitude of the NZ interaction is considerably smaller than the EZ interaction ( $\frac{\mu_B}{\mu_n} > 1800$ )

### Nuclear Quadrupole interaction

In general, the fifth term,  $\hat{H}_{NQ}$  interaction is analogous to the  $\hat{H}_{ZFS}$  situation.

$$\hat{H}_{NQ} = \sum_{i=1}^m \hat{I}^{k_i T} Q^{k_i} \hat{I}^{k_i} \quad (2.22)$$

The  $M$  nuclei with nuclear spins  $I^{k_i} > 1/2$ ,  $i = 1, \dots, m$ , where the  $k_i \in 1, \dots, N$ , have an electric quadrupole moment that interacts with the electric field gradient at the site of the corresponding nucleus. The  $Q^{k_i}$  is the quadrupole interaction tensor, and for the single nucleus with spin  $I$ , its quadrupole interaction tensor can be expressed in its principle axis system as

$$\mathbf{Q} = \frac{e^2 q Q / h}{4I(2I-1)} \begin{pmatrix} -(1+\eta) & 0 & 0 \\ 0 & -(1-\eta) & 0 \\ 0 & 0 & 2 \end{pmatrix} \quad (2.23)$$

where  $e$  is the proton charge,  $eq$  is the largest principle value of the electric field gradient tensor at the nucleus site,  $Q$  is the quadrupole moment and  $\eta$  the biaxiality of the electric field gradient tensor. More often, the term ( $Q_C = e^2 q Q / h$ ) is called quadrupole coupling constant.

## 2.2.3 Spin relaxation and line shapes

### (I) Spin relaxation

The individual resonance line, sometimes referred to as a spin packet, has a width determined by two effects: 1) spin-lattice ( $T_1$ ) relaxation and ii) spin-spin ( $T_2$ ) relaxation. A purely spin-lattice relaxation broadening line has a Lorentzian shape, and spin-spin relaxation is concerned with

mutual spin flips caused by dipolar and exchange interactions between the assembly of spins. The spin-spin broadening dominated lineshape tends to be more Gaussian-like[38].

The following table 2.2 distinguishes the  $T_1$  and  $T_2$  relaxations[38, 39].

TABLE 2.2: The difference between spin-lattice and spin-spin relaxation[38, 39].

No.	Spin - lattice relaxation ( $T_1$ )	Spin - spin relaxation ( $T_2$ )
Also known as	Longitudinal relaxation	Transverse relaxation
Broadening	A purely a spin-lattice relaxation has a Lorentzian shape (homogeneous)	tends to be Gaussian shape If dominated by spin-spin broadening (inhomogeneous)
Temperature	Very temperature dependent	largely temperature independent (but concentration-dependent)
Interactions	Relaxes via lattice phonon	Via dipolar and exchange interaction
Definition	$T_1$ describes how quickly magnetization returns to alignment with the z-axis	$T_2$ describes how quickly magnetization in the x-y plane rotating plane dephases
Phonons	$T_1$ involve real phonons	$T_2$ involve virtual phonons, which leave total energy unaltered

### Spin-lattice relaxation time, $T_1$ (Longitudinal relaxation)

Spin-lattice relaxation ( $T_1$ ) is about how quickly the non-equilibrium transverse magnetization goes back to the longitudinal magnetization aligned parallel to the applied field and is also called 'longitudinal relaxation'. In solids,  $T_1$  is usually small because it can easily lose its energy via the thermal vibrations of the nearby lattice ( $T_1$  relaxation rate -  $T_1^{-1}$ ). Whereas in liquids, it is comparatively more since there are no closed-packed lattices to lose its energy.  $T_1$  depends on the composition, surroundings and structure of the species and temperature.

### Spin-spin relaxation time, $T_2$ ((Transverse relaxation)

Due to spin-spin relaxation ( $T_2$ ), transverse magnetization dephases or defocuses as non-equilibrium magnetization perpendicular to the external magnetic field and is also called 'transverse relaxation' ( $T_2$  relaxation rate -  $T_2^{-1}$ ).

## (II) Line shapes

The shape of the EPR spectra can be affected by homogeneous (Lorentzian) and inhomogeneous (Gaussian) broadening, electron spin exchange for a bi-nuclear reaction, electron transfer between a radical and diamagnetic species, proton transfer, fluxional motion (internal motions of unpaired electrons), dynamic hyperfine coupling, based on single nucleus or multiple nuclei, molecular tumbling effects in liquid samples (isotropic and anisotropic), dipolar effects, spin rotation interaction in the gas phase, saturation-transfer via spin diffusion, change in concentration in chemical reactions, chemically induced dynamic electron polarization (CIDEP) and conductivity (Dysonian broadening) of the material[39]. A few of the above-mentioned cases were encountered during this PhD work for different MOF systems and are described below. Such a change in line shape as a function of temperature from the Ni(II)-NO adduct was discussed in Chapter 5.6 (SI).<sup>1</sup>

### Homogeneous and Inhomogeneous broadening

Homogeneous broadening occurs for the set of species (spins) when all these have the same spin Hamiltonian parameter and the same net magnetic field. In such cases, the local fields of the dipoles need not be identical, but still, the line shape is the same for each dipole (Lorentzian line shapes are common)[39]. In other words, in this case, the EPR spectrum is the sum of a large number of spectra each having the same shift, and the linewidth is determined by the relaxation times.

In general, effective spin-spin relaxation time is often defined by

$$T_{2eff} = |\kappa \gamma_e \Gamma|^{-1} \quad (2.24)$$

under non-saturation conditions, and one can visualize the possible contribution of Lorentzian broadening to  $T_2$ . Where  $\kappa$  is line shape factor (for Lorentzian  $\kappa = 1$  and for Gaussian  $\kappa = (\pi \ln 2)^{1/2}$ ),  $\Gamma$  is a full width at half maximum of Lorentzian,  $\gamma_e$  is a gyro-magnetic ratio of electron[39].

In the case of inhomogeneous broadening, a number of individual spin packets have different resonance frequencies and the broadening results from the unresolved EPR spectrum due to the superposition of different species. The resultant spectrum often has a Gaussian line shape[39]. In other words, the EPR spectrum is the sum of a large number of narrower spectra; each shifted with respect to the other. In such cases,  $B_1$  component of the MW can be chosen to power saturate some selected portion of the EPR line, decreasing its intensity there (known as hole burning)[39].

<sup>1</sup>A weak temperature dependence of  $g_{ij}$  and homogeneous line broadening has been observed in the case of Ni-MFU-4l:NO<sub>2</sub> MOF with adsorbed NO. The Arrhenius-type behavior has been observed.

In addition, the source of inhomogeneous broadening can be a) an inhomogeneous magnetic field, b) unresolved hyperfine splittings, (c) anisotropic interactions in randomly oriented spin systems in the solid, and (d) dipolar interactions between paramagnetic centers[39]. However, the values of  $J_1$  and  $J_2$  can be the same for all spin packets, or they may differ. In some of the above cases, the local magnetic fields can be averaged out via rapid dynamic effects such as tumbling, collisions and exchange, yielding homogeneously broadened lines[39].

### Dipolar effects: isotropic exchange interaction

For the exchange coupled two spin systems, the exchange spin Hamiltonian can be written as[39]

$$\hat{H}_{Ex} = -2J_{ij}\hat{S}_{1i}\hat{S}_{2j} = \frac{1}{2}(\hat{\mathbf{S}}_1^T \cdot \mathbf{J} \cdot \hat{\mathbf{S}}_2 + \hat{\mathbf{S}}_2^T \cdot \mathbf{J} \cdot \hat{\mathbf{S}}_1) \quad (2.25)$$

where  $\hat{\mathbf{S}}$  and  $\hat{\mathbf{S}}$  are the spin operators, indices  $i$  and  $j$  label spatial coordinates,  $\mathbf{J}$  is the  $3 \times 3$  matrix which takes into account the electric coulombic interaction between two unpaired electrons[39]. In our case, we only consider the most important part, the exchange operator, i.e. the isotropic part[39].

$$(\hat{H}_{Ex})_{iso} = -2J\hat{\mathbf{S}}_1^T \cdot \hat{\mathbf{S}}_2 \quad (2.26)$$

where  $2J = \frac{tr(\mathbf{J})}{3}$  is the isotropic exchange coupling constant which can be written as[39]

$$2J = -2\langle \phi_a(1)\phi_b(2) | \frac{e^2}{4\pi\epsilon_0 r} | \phi_a(2)\phi_b(1) \rangle \quad (2.27)$$

Here  $\phi_a(1)$  and  $\phi_a(1)$  are different normalized spatial molecular-orbital wave functions considered for the non-interacting electrons.  $\epsilon_0$  is the permittivity of the vacuum, and  $r$  is the inter-electron distance. For  $2J < 0$ , singlet state lies lowest (the ground state) stays lower (antiferromagnetic), and for  $2J > 0$ , triplet state lies lowest (ferromagnetic)[39].

In a similar manner, the exchange interaction between more complicated three spin systems can be written as[45, 46]

$$\hat{H}_{Ex} = -2[J_{12}(\hat{S}_1\hat{S}_2) + J_{23}(\hat{S}_2\hat{S}_3) + J_{31}(\hat{S}_3\hat{S}_1)] \quad (2.28)$$

If all magnetic ions are equivalent  $J_{12} = J_{21} = J_{31} = J$ . Such complicated Cr(III) based trimeric spin systems in MIL-100( $(Al_{1-x})Cr_x$ ) and MIL-101 MOFs are discussed elaborately in Chapter 6.



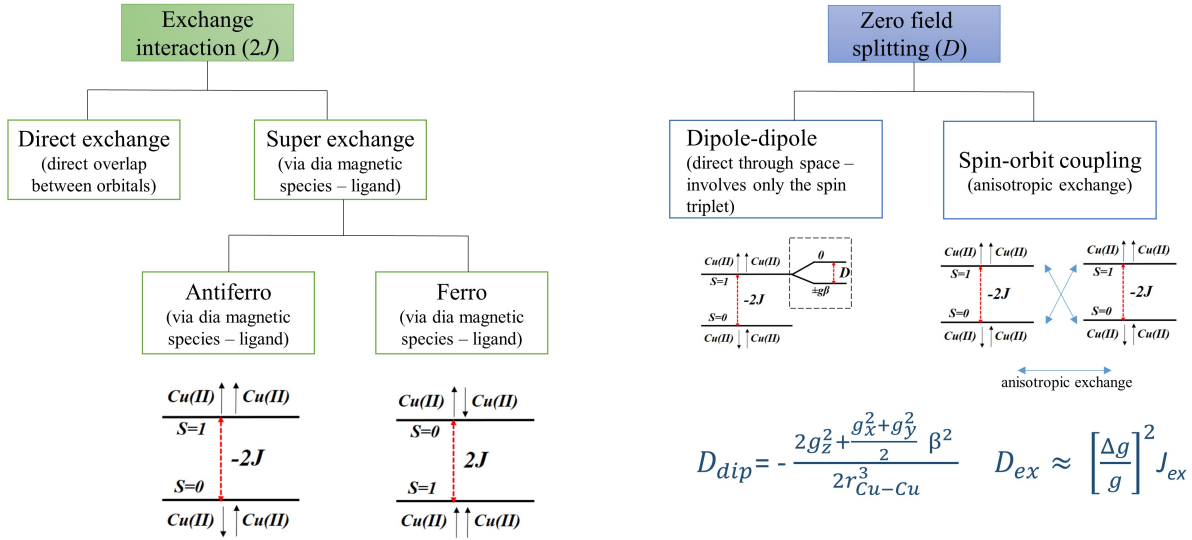


FIGURE 2.9: Chart showing the relation between exchange interaction and zero-field splitting interaction for a  $S = 1$  dimeric system[47, 48]

Moreover, the isotopic exchange coupling constant can be estimated through simple EPR measurements as a function of temperature for the coupled homonuclear species. For instance, for the two spin systems, the Bleaney Bowers equation can be derived by substituting the Hamiltonian  $\hat{H}_{EZ}$  and  $\hat{H}_{Ex}$  part in a magnetic field into van Vleck eqn 2.29[49, 50].

$$\chi = N \frac{\sum_n \left[ \frac{(-E_n^{(1)})^2}{kT} - 2E_n^{(2)} \right] \exp\left(\frac{-E_n^{(0)}}{kT}\right)}{\sum_n \exp\left(\frac{-E_n^{(0)}}{kT}\right)} \quad (2.29)$$

where  $\chi$  is the magnetic susceptibility,  $N$  is Avogadro's constant,  $\mu_B$  is the Bohr magneton,  $k_B$  is the Boltzmann constant,  $n$  corresponds to the energy levels ( $n = 1, 2, 3, 4$ , one singlet state and three excited triplet state) and  $E_n^i$  ( $i = 0, 1, 2$ ) represents the order of Zeeman term. And the simplified form of this equation can be written as

$$\chi = \frac{2N\mu_B^2 g^2}{k_B T} \frac{2 \exp\left(\frac{-2J}{k_B T}\right)}{1 + 3 \exp\left(\frac{-2J}{k_B T}\right)} \quad (2.30)$$

Further, the intensity extracted from the temperature-dependent EPR data ( $I_{EPR}$ ) can be fitted using the Bleaney-Bowers equation 2.31 estimated from eqn. 2.30 for the magnetic susceptibility which is proportional to the ( $I_{EPR}$ )[5, 51]

$$I_{EPR} \propto \chi = \frac{2N\mu_B^2 g^2}{k_B T} \left[ 3 + \exp\left(\frac{-2J}{k_B T}\right) \right]^{-1} \quad (2.31)$$

equation is valid only for the two identical spin  $S = 1/2$  species. In this way, we estimated  $2J$  value for the coupled Cu(II)-Cu(II) dimers(see Sec.3.8). In general, super-exchange occurs between partly occupied orbitals of two magnetic ions because of the Pauli principle (If between partly occupied and unoccupied, it could be a weakly ferromagnetic interaction owing to Hund's rule)[48].

### Dipolar effects: anisotropic interaction

Along with the isotropic exchange interaction, there is an additional quadratic electron spin interaction (when  $S > 1/2$ ), namely, the anisotropic magnetic dipole-dipole interaction. This interaction removes the degeneracy of the spin states even in the absence of a magnetic field and splits them further ( $2S+1$ ), known as *zero field splitting*[39].

The ZFS parameter  $D$  in dimers ( $D = D_{dip} + D_{ex}$ ) is contributed by dipole-dipole interaction ( $D_{dip}$ ) and anisotropic exchange interaction ( $D_{ex}$ ), which can be approximated as[47, 51, 52]

$$D_{dip} = -\frac{2g_z^2 + \frac{g_x^2 + g_y^2}{2}\beta^2}{2r_{Cu-Cu}^3} \quad (2.32)$$

$$D_{ex} \approx \left[ \frac{\Delta g}{g} \right]^2 2J \quad (2.33)$$

where  $g_{x,y,z}$  are the  $g$ -tensor component,  $\beta$  is characteristic deviation of the  $g_i$  values,  $g = (g_x + g_y + g_z)/3$ ,  $r_{Cu-Cu}$  is the distance between two copper ions, and  $2J$  is the isotropic exchange interaction between two copper ions.

### Dysonian broadening

The EPR spectra of concentrated magnetic systems often show a single, broad, unresolved, and featureless signal[53, 54]. Unresolved  $g$ -anisotropy could be due to the short spin-spin relaxation resulting from the magnetic exchange and dipole-dipole interactions. Whereas Dysonian broadening occurs when the microwave interacts with the conduction electrons inside the skin depth ( $\delta$ ) of the material. This type of broadening happens in the conducting material, and one obtains an asymmetric signal of a Dysonian lineshape. The ratio of the amplitude of the left peak (a) to the right peak (b) in Figure 2.10 (or ' $\alpha'$ ' - the symmetry parameter) in the EPR derivative signal is important to describe the asymmetric nature of the EPR signal. There are two conditions taken

into account for the type of broadening i) when particle size is greater than the skin depth of the material and ii) spin-spin relaxation time ( $T_2$ ) is greater than the diffusion time of the charge carriers[53–56].

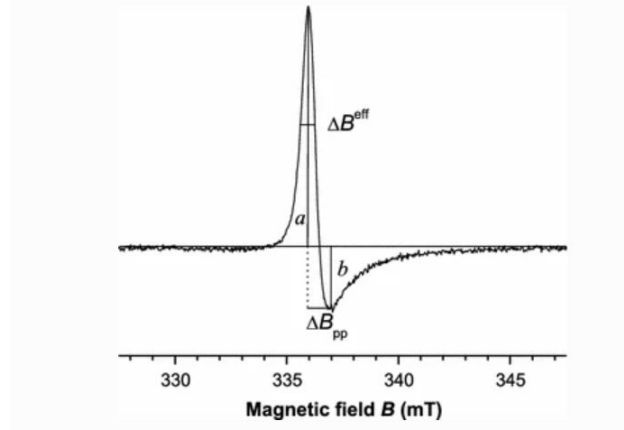


FIGURE 2.10: Dysonian EPR signal and the characteristic points and parameters are shown and adapted from [57] copyright @ 2009, Springer-Verlag

The relation between skin depth and microwave frequency can be written as

$$\delta = \sqrt{\frac{\rho}{\mu_0 \pi \nu_{mw}}} \quad (2.34)$$

Where  $\delta$  is the skin depth,  $\rho$  is the resistivity,  $\mu_0$  is the permeability of free space, and  $\nu_{mw}$  is the MW frequency.

Such behaviour has been studied in the rare-earth-based manganite material  $\text{Pr}_{0.15}\text{Ca}_{0.85}\text{MnO}_3$  during this doctoral period [58]. However, it is not the main work of this thesis.<sup>2</sup>

## 2.2.4 Pulsed EPR methods

In this thesis work, different pulse EPR methods such as ESEEM (electron echo envelope modulation), HYSCORE (hyperfine sublevel correlation) and ENDOR (electron nuclear double resonance) were employed on NO adsorbed MFU-4l(Ni):NO<sub>2</sub> (Chapter 5 and Zn(II) doped HKUST-1 (Chapter 4)MOFs, to extract the HF coupling between the <sup>1</sup>H and <sup>14</sup>N nuclei from the framework linker and the magnetic ions in the SBU. Most of the time, such information is buried in the broadening of CW EPR spectra, and a more detailed description of these techniques can be understood from the ref.[41].

<sup>2</sup>On the  $\text{Pr}_{0.15}\text{Ca}_{0.85}\text{MnO}_3$  work, we used CW EPR as a complimentary technique to investigate the mixed non-Kramer Mn(III) with  $S = 2$  and Kramer Mn(IV) with  $S = 3/2$  ions. The result was in accordance with the electron hopping transport observed in the temperature dependence of electrical resistivity. The material was investigated for the magnetic refrigeration (magnetocaloric effect) application.

### 2.2.4.1 Electron Spin Echo Envelope Modulation (ESEEM)

ESEEM is a pulsed EPR technique that monitors NMR transitions indirectly through EPR transitions, and echo envelope modulation arises when there is a state mixing of the hyperfine levels. The simplest ESEEM is the 2-pulse (primary echo or Hahn echo) ESE given Figure 2.11. The first  $\pi/2$  MW pulse flips the longitudinal magnetization to the x-y plane and generates electron coherence (EC). Then, the second MW  $\pi$  - pulse mixes the EC, which is detectable via the ESE, and the intensity of the ESE is measured as a function of  $\tau$ , whereby the echo signal decays with the  $\tau$  due to the relaxation effects ( $T_m$  - phase memory time of the electron spin) and also be modulated with the nuclear frequencies of the nuclei hf coupled to the unpaired electron[59].

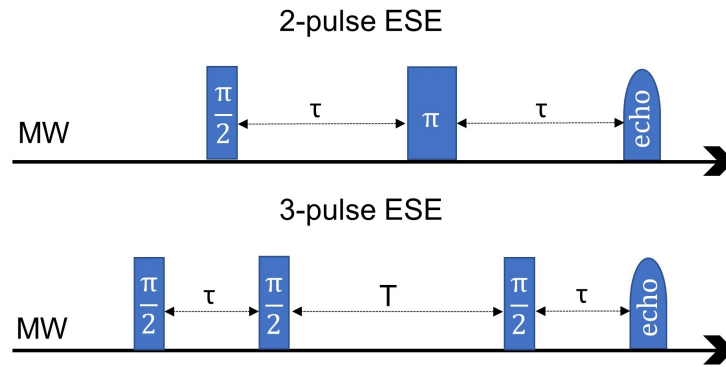


FIGURE 2.11: Pulse sequence of (a) 2-pulse ESE and (b) 3-pulse ESE

For a simple  $S = 1/2$  and  $I = 1/2$  spin systems, the signed nuclear frequencies are

$$\omega_{12} = \omega_{\alpha} = \left[ \left( \omega_I + \frac{A}{2} \right)^2 + \frac{B^2}{4} \right]^{1/2} \quad (2.35)$$

$$\omega_{34} = \omega_{\beta} = \left[ \left( \omega_I - \frac{A}{2} \right)^2 + \frac{B^2}{4} \right]^{1/2} \quad (2.36)$$

where  $A = A_{zz}$  and  $B = \sqrt{A_{zx}^2 + A_{zy}^2}$  are the secular and pseudo-secular HF coupling constants, respectively.  $\omega = 2\pi\nu$ ,  $\omega_{\alpha}$  and  $\omega_{\beta}$  are the nuclear transition angular frequencies,  $\omega_- = \omega_{\alpha} - \omega_{\beta}$  and  $\omega_+ = \omega_{\alpha} + \omega_{\beta}$ .

Further, the echo modulation for the 2p ESEEM can be written as[59]

$$V_{2p}(\tau) = 1 - \frac{k}{4} \left[ 2 - 2\cos(\omega_{12}\tau) - 2\cos(\omega_{34}\tau) + \cos(\omega_-\tau) + \cos(\omega_+\tau) \right] \quad (2.37)$$

where  $k$  is the modulation depth parameter. 3p ESEEM experiments are the better alternatives of 2p ESEEM techniques. The first step is the same as 2p-ESEEM in that  $\pi/2$  MW pulse generates

EC and the next  $\pi/2$  MW pulse creates  $EC \rightarrow NC$ . The NC evolves over the pulse delay  $T$ , and the third  $\pi/2$  MW pulse turns the NC into detectable EC.

### 2.2.4.2 Hyperfine Sublevel Correlation (HYSCORE) spectroscopy

HYSCORE experiment is an extension of the 3p ESEEM experiment. One can easily turn the one-dimensional 3p-ESEEM experiment into a two-dimensional experiment (HYSCORE), and the Fourier transformation along both dimensions lead to similar spectral information that can be obtained by HYSCORE. In this thesis, HYSCORE experiments were done to recover the missing couplings arising from  $^{14}N$  ( $I = 1$ ) in the CW EPR experiments.

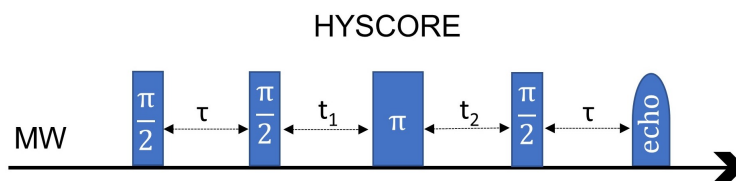


FIGURE 2.12: Pulse sequence of HYSCORE

The pulse sequence of the HYSCORE technique is given in Figure 2.12. In the technique, one more MW  $\pi$ -pulse is inserted in the 3p ESEEM (Figure 2.14), which transfers the NC created by the first two MW  $\pi/2$ -pulses from one  $m_s$  manifold to another and the 2D version of this experiment is so-called HYSCORE experiment. Then, two dimensional Fourier transformation with respect to  $t_1$  and  $t_2$  of the two-dimensional time domain spectrum featuring cross peaks linking the nuclear frequencies of the different  $m_s$  manifolds.

In HYSCORE data, the hyperfine and quadrupole interaction signals from eqns. 2.38 and 2.39 manifest as cross-peaks or ridges in the two-dimensional frequency, which are symmetric about the diagonal of the given quadrant. The (+,+) and (-,+) quadrants of these frequency spectra are symmetric to the (-,-) and (+,-) quadrants. Thus only (-,+) and (+,+) quadrants are typically displaced in literature (Figure 2.13). The HYSCORE technique separates features from hyperfine coupling constants ( $A$ ) in the weak-coupling regime ( $|A| < 2|v_l|$ ) in the (+,+) quadrant from the strong coupling regime ( $|A| > 2|v_l|$ ) in the (-,+) quadrant, as well as this technique allows hyperfine levels corresponding to the same electron-nuclear submanifold to be differentiated. The length of the curvature of these correlation ridges given in Figure 2.13 corresponds to the magnitude of the isotropic and dipolar components of the hyperfine tensor.

The presence of  $\tau$  dependent nuclear frequency "blind spots" represents the loss in intensity of frequencies corresponding to  $n/\tau$  ( $n$ - integer) due to the polarization grating generated by the

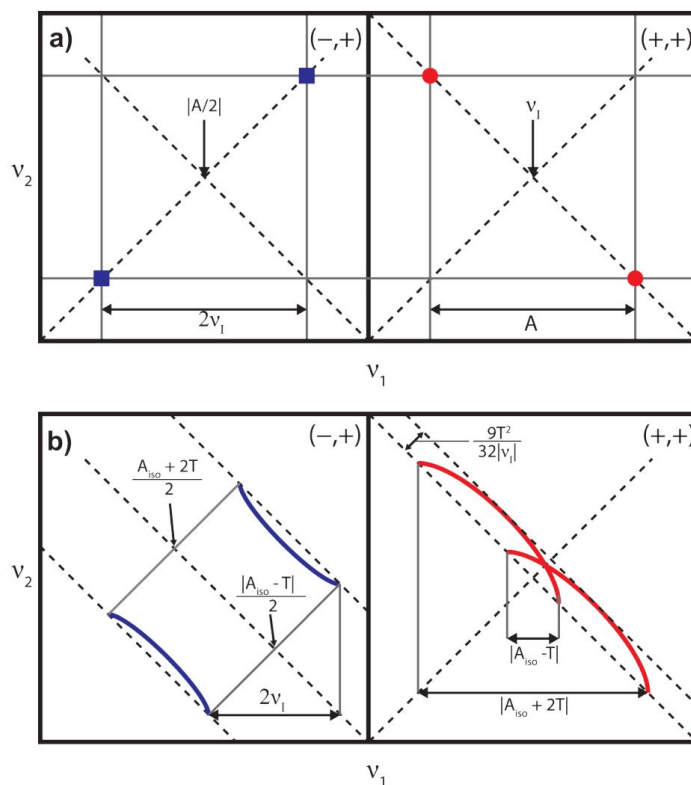


FIGURE 2.13: a) HYSORE powder patterns for an  $S = 1/2$ ,  $I = 1/2$  spin system with an isotropic hf tensor  $A$ . b) HYSORE powder patterns for an  $S = 1/2$ ,  $I = 1/2$  spin system with an axial hf tensor which contains isotropic ( $a_{iso}$ ) and dipolar ( $T$ ) contributions. Blue correlation ridges represent the strong coupling case ( $|A| > |2v_1|$ ); red correlation ridges represent the weak coupling case ( $|A| < |2v_1|$ ). The image is adapted from [60] Copyright @ 2020 American Chemical Society

initial two  $\pi/2$  MW pulses of the stimulated echo pulse sequenced and this requires the collection of HYSORE spectra using multiple values of  $\tau$  to avoid the suppression of peaks[59, 60].

### 2.2.4.3 Electron Nuclear Double Resonance (ENDOR) spectroscopy

In 1956, Feher[61] introduced and demonstrated the technique of ENDOR, which provides the loss of details of hyperfine interaction wealth of detail about the wavefunction of the unpaired electron. By an ENDOR experiment, even a distinctive interaction of an unpaired electron with the 23rd nearest-neighbour set of nuclei was established[39, 62]. The additional NMR dimension enhances the resolution of ENDOR in comparison with typical EPR and makes it the method of choice for the investigation of a large number of magnetic nuclei with a complex paramagnetic system. In ENDOR experiments, there are no observations of direct absorption of NMR (radio frequency) transitions; instead, one observes the change in the EPR transition intensity resulting from the redistribution of the populations of the various states. Both CW and pulse-based ENDOR techniques can be performed, and in this thesis work, we used pulsed ENDOR techniques. When  $I > 1$ , the nuclear quadrupole interaction experienced by nuclei can be tested by ENDOR in

favourable cases. The ENDOR requires use of the complete spin Hamiltonian including  $\hat{H}_{NZ}$  term (when  $I > 1$ )[39].

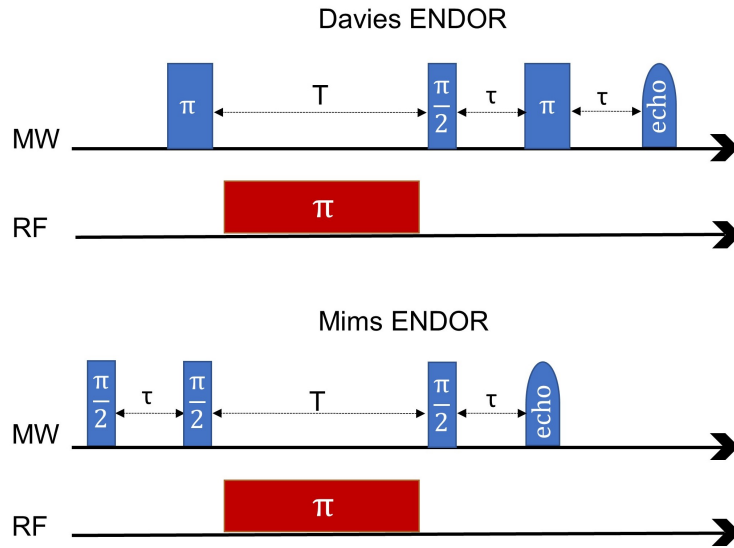


FIGURE 2.14: ENDOR pulse sequence

The pulse sequence of Davies (Davies 1974[63]) and Mims (Mims 1965[64]) ENDOR is given in Figure 2.14. The ENDOR experiments consist of a combination of selective MW and one selective RF pulse. Davies ENDOR is useful for systems with large HFIs. In Davies ENDOR, the first MW  $\pi$  - pulse (so-called preparation pulse,  $B_1 \leq A$  should hold) inverse the electron polarization selectivity for one allowed EPR transition and the following RF pulse inverses selectively nuclear polarization, which modulates the electron polarization of the transition. A further step is read out by a regular echo pulse sequence, and the intensity of the resulting echo is measured as a function of the RF frequency. In ENDOR experiments, since the RF pulse modulates the NMR transitions, the selection rule can be written as  $\Delta m_s = 0$  and  $\Delta m_I = \pm 1$ . The frequencies of the transitions are

$$\nu^\pm = \left| \nu_I \pm \frac{A}{2} \right| \quad (2.38)$$

where  $\nu_n$  is the nuclear Larmor frequency, and  $a$  is the hf coupling constant. For nuclei with  $I \geq 1$ , an additional splitting of the  $\nu_\pm$  manifolds is produced by the NQI ( $Q$ ) which is described in Sec 2.2.2

$$\nu_{m_I}^\pm = \left| \nu_I \pm \frac{3Q(2m_I - 1)}{2} \right| \quad (2.39)$$

The magnitude of echo is maximum when the RF is off-resonant with a nuclear frequency and minimum when the  $\nu_{RF}$  is on-resonant with such a nuclear transition. In such a way, one can

obtain the nuclear frequency spectrum with Davies ENDOR, and the absence of any blind spots is the superiority of Davies ENDOR over ESEEM techniques. At times, for transition metal ions with large hfi/ligand nuclei with a small gyromagnetic ratio, the nuclear transition amplitudes as measured with ENDOR modulated by the so-called hfi enhancement factor[41]. The electron spin follows the oscillating RF field ( $B_{RF}(t)$ ) adiabatically due to the large Larmor frequency, which modulates the magnetic field  $B_{hf}(t)$  generated by the electron spin at the nucleus. Hence, the effective RF field at the nucleus is the sum of  $B_{RF}(t)$  and  $B_{hf}(t)$  fields which may lead to an enhancement or attenuation of the nuclear transition amplitude [41]. As a consequence, the amplitude of the nuclear transition with small frequencies might become barely detectable, with ENDOR high-frequency transition might be enhanced.

In Mims ENDOR, the applied stimulated MW pulse sequence stimulates both EPR transitions, which limits this technique to the relatively small HFI constants ( $B_1 \geq A$ ). Mims ENDOR can be explained as a partial defocusing of the ESE if the RF pulse inverts the nuclear transition leading to a decrease in the intensity of stimulated echo, which in turn modulates the frequency of the electron spin Larmor precession. Hence, the frequency of the precession during the first and second  $\tau$  interval differs by the  $a$  value. The processing magnetization acquires the additional phase  $\Delta\phi = a\tau$  at the moment of the formation of echo, and therefore, the echo intensity is proportional to

$$S_y = \cos(a\tau) \quad (2.40)$$

From eqn. 2.40, no ENDOR effect will be observed when  $a\tau = 2\pi n$  (n- an integer) and therefore, for the given  $\tau$  value 'blindspots' or regions with severely decreased sensitivity appear in the Mims ENDOR which is a major limitation of Mims technique [65].

### 2.2.5 Review of EPR technique on MOF science

Once again, owing to the likely presence of paramagnetic centres in these MOFs, unsurprisingly, EPR has played an important role in the characterisation of such materials (as summarised in Figure 2.15).

#### (i) Magnetic coupling

Most notably, Kultaeva *et al.*, correlated the magnetic properties of a copper-based MOF, labelled [Cu(prz-trz-ia)], through the temperature-dependent magnetisation results of SQUID magnetometry along with multi-frequency EPR results. It is interesting to note that, the temperature-dependent



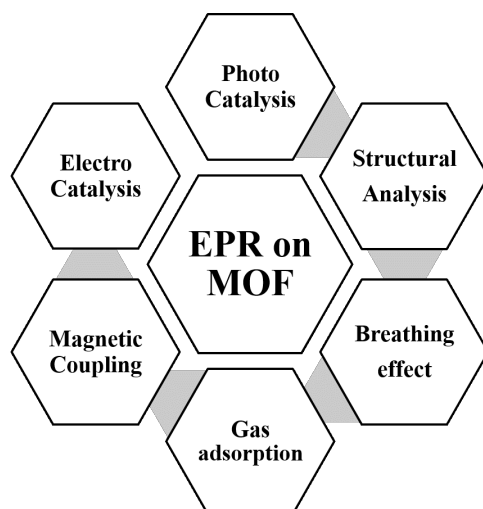


FIGURE 2.15: EPR as a tool to interrogate different properties of MOFs

magnetic behaviour extracted from the EPR results and the magnetic susceptibility data from the SQUID experiments provided a negative value of the paramagnetic Curie temperature ( $\theta_p$ ) due to the antiferromagnetic interaction between the cupric ions. An isotropic exchange coupling constant,  $J_1$ , of antiferromagnetically coupled cupric ions was extracted from the SQUID ( $26 \text{ cm}^{-1}$ ) and EPR ( $23 \text{ cm}^{-1}$ ) results, which agreed well with the DFT calculations[66].

### (ii) Structural analysis

Recently, Bitzer *et al.*[7], used EPR along with the X-ray diffraction and X-ray absorption spectroscopy to study the incorporation of  $\text{Fe}^{3+}$  ions into another copper-based MOF, labelled CuBTC, with paddlewheel units. The presence of  $\text{Fe}^{3+}$   $\text{Cu}^{2+}$  paddlewheels have been successfully confirmed from the strong magnetic interactions among the  $\text{Fe}^{3+}$   $\text{Cu}^{2+}$  species with a  $g$  value of 2.023[66]. imnas *et al.*[67] investigated mixed valent MOF containing  $\text{Cu}_2$  ions in the paddle wheel units and their temperature-dependent X- and Q-band CW EPR spectra reveal that Cu(II) ions in the investigated MOF are present in two different magnetic states. The structural phase transition of Mn incorporated  $[(\text{CH}_3)_2\text{NH}_2][\text{Zn}(\text{HCOO})_3]$  Metal-Organic Framework was presented by imnas *et al.*[68] and the EPR measurements indicate a successful incorporation of local Mn(II) probes into the structure allowing to detect and investigate an orderdisorder structural phase transition in the MOF.

### (iii) Gas adsorption

Using a variety of EPR methods, Mendt *et al.*[69], also explored the structural phase transition of MIL-53(Al/Cr), adsorption of  $\text{CO}_2$  over the MIL-53(Al/Cr) under pressure[69], and the low

temperature NO binding in the MIL-100(Al)[70]. Moreover, Friedländer *et al.* [71] interrogated the bimetallic ZnCuBTC upon adsorption of gases by means of CW single crystal EPR, Polyukhov *et al.*[52] reported the adsorption of n-butane and Et<sub>2</sub>O on the flexible DUT-49 MOF by means of EPR spectroscopy. There are several gas adsorptions, such as HD[72], H-2, D-2 [73], CO<sub>2</sub>[74] on HKUST-1 MOF were explored by CW and pulse EPR spectroscopy techniques. Sheveleva *et al.*[75] reported the CO<sub>2</sub>, N<sub>2</sub> and O<sub>2</sub> gas adsorption on ZIF-8 MOF using stable nitroxide radicals as multifunctional agents embedded into the pores of a MOF prior to the gas sorption.

### (v) Photocatalysis

Although several excellent literature reviews and papers have been published that deal with the catalytic applications of MOF for a varied host of reactions, and whilst many EPR publications have focused on heterogeneous catalysis, there are fewer articles devoted to the combined EPR study of catalytic applications in MOFs. Currently, EPR is finding considerable success in the studies of charge generation, pathways to charge transfer, broad band absorption in photocatalytic activity, and mechanistic origins of electrocatalysts in MOF materials[66].

For example, Nasalevich *et al.*[76] investigated the photocatalytic potential of NH<sub>2</sub> functionalized, *d*<sup>0</sup> metal based MIL-125(Ti), UiO-66(Zr) and UiO-66(Hf) MOFs through X-band EPR under UV illumination. The Ti<sup>3+</sup> (S = 1/2) ions were generated in the photoexcited state, only in the NH<sub>2</sub>-MIL-125(Ti) material upon UV illumination as a result of ligand-metal charge transfer(LCMT). Also, a transient weak signal found in the NH<sub>2</sub>-UiO-66(Zr) and NH<sub>2</sub>-UiO66(Hf) materials, was attributed to the highest occupied crystalline orbital (HOCO) lowest unoccupied crystalline orbital (LUCO) transition of a radical in the framework and no LCMT was observed. The EPR results were also in accordance with the computational results. Horiuchi *et al.*[77], also performed X-band *in situ* EPR studies on amino functionalised Ti-MOF under the visible light irradiation. Once again, paramagnetic Ti<sup>3+</sup> ions were produced from the diamagnetic Ti<sup>4+</sup> centres via LCMT with reported spin Hamiltonian parameters  $g_{yy} = 1.980$ ,  $g_{yy} = 1.953$ ,  $g_{yy} = 1.889$ . The presence of Ti<sup>3+</sup> ions was confirmed by exposure of the material to air, at which point the paramagnetic Ti<sup>3+</sup> centres were immediately oxidised back to the original Ti<sup>4+</sup> centres.

In another study, Chen *et al.*[78], investigated the NNU-28(Zr) MOF under the continuous visible light illumination using *in situ* X-band EPR to study the photocatalytic activity of CO<sub>2</sub> reduction with formate formation. Firstly, the anthracene-based ligand in the NNU-28 material was found to act as a photo-reducing component of CO<sub>2</sub>, which was confirmed by the strong EPR signal of an anionic radical (g = 2.003) under visible light irradiation, whereas the ligand itself in the absence of any irradiation, gave a weak signal with the same g value. The authors found two

more additional signals at  $g = 2.009$  and  $g = 2.030$  during the *in situ* EPR measurements of NNU-28(Zr) upon continuous visible light illumination, which were not related to the ligand. These new signals were attributed to the LCMT process of  $Zr_6$  oxo clusters, thereby revealing the existence of a dual catalytic pathway as confirmed by the EPR[66].

#### (vi) Electrocatalysis

Zhao *et al.*[79], investigated the electrocatalytic performance of mixed  $Co_{0.6}Fe_{0.4}$ -MOF-74 and compared their results with Co-MOF-74 ( $Co^{2+}$ ,  $S = 3/2$ ) and Fe-MOF-74 ( $Fe^{2+}$ ,  $S = 2$ ) materials for the oxygen evolution reaction (OER) by means of X-band EPR. The EPR data revealed that the  $Co_{0.6}Fe_{0.4}$ -MOF-74 has more open metal clusters compared to the single metal counterparts. Ji *et al.* have also investigated the Lewis acidic nature of MOFs, including ZrOHBTC and ZrOTf-BTC, to better understand the catalytic performance of the materials. The difference between the  $g_{zz}$  values from the  $Zr(O^-)$  active species of ZrOH-BTC and ZrOTf-BTC, was revealed by EPR owing to the difference in Lewis acidity of those MOFs. The  $g_{zz}$  value of 2.0310 for ZrOTf-BTC was shown to arise from the energy splitting ( $\Delta = 0.99$  eV) between the  $\pi_x^*$  and  $\pi_y^*$  orbitals which is comparable to the  $\Delta$  (1 eV) of benchmark homogeneous Lewis acid catalyst  $Sc(OTf)_3$ [66].

#### (vii) Photochromic effect

Photochromism on MOF can be observed when a structural change of the framework is induced by the absorption of light, which results in colour change. In some cases, a ligand of the MOF itself is photochromic after and before the incorporation into a MOF (Eg: Spiropyrans, azobenzenes, naphthalenediimides, diarylethenes). Secondly, there are some examples of non-photochromic to photochromic ligands upon incorporation into a MOF. The third case is the ligand of the MOF generates radicals in response to the absorption of light, which leads to photo-induced electron transfer. J. Cornelio *et al.*[80], investigated the third type of photo-induced ligand-to-ligand charge transfer in the Zn-based MUF-7 and MUF-77 MOFs. DMF dissolved MOFs exposed to 405 nm UV laser (1 mW) irradiation, which results in a colour change from yellow to red. Electron transfer through space from truxene - based hmtt ligand to bdc - quin ligand generates a truxene radical cation and a pyrazine radical anion (captodative effect). X-band EPR studies at 100 K confirm the generation of radical upon UV laser irradiation, and  $g = 2.0037$  could be attributed to the pyrazine radical anion. Such an EPR signal was not observed before irradiation. Moreover, the radical generation stays in the dark for 80 min, and after exposing it to visible light, there is a loss of signal  $g = 2.0037$  due to the reversible process triggered photochemically by visible light, not thermally[80].

## 2.3 Magnetization measurement: SQUID

In this thesis work, a Superconducting Quantum Interference Device (SQUID) is used as a complementary technique along with EPR spectroscopy on MIL-100 and MIL-101 MOFs. A magnetometer is used to measure the extrinsic material quantity of magnetic dipole moment as a function of external parameters, typically applied magnetic field or temperature. In SQUID magnetometry, the superconducting magnet is used and which relies on superconductivity and the Josephson effect, intrinsically requires cryogenic temperature.

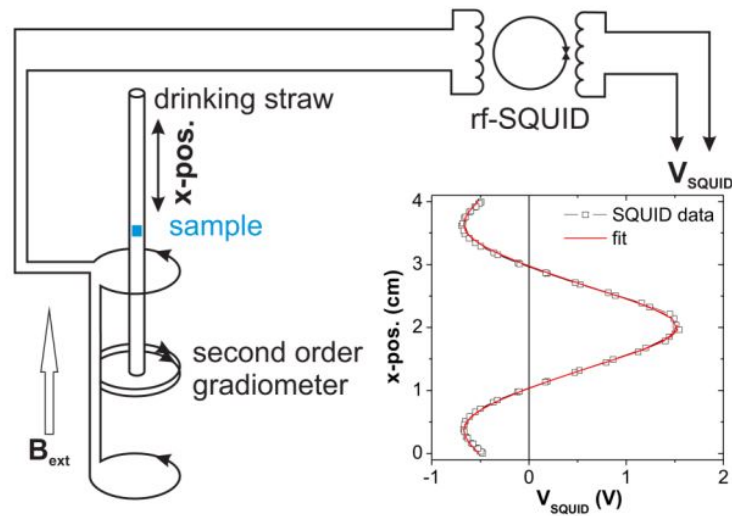


FIGURE 2.16: Schematic setup of a SQUID magnetometer with 2nd order gradiometer. The inset shows the SQUID response  $V_{SQUID}$  versus sample position (x-pos.)[81]

SQUID consists of two Josephson junctions connected in parallel on a closed superconducting loop and a fundamental property of superconducting rings is that they can enclose magnetic flux only in multiples of a universal constant called flux quantum  $\phi_0$ . i.e: an external magnetic field can penetrate a superconductive loop only if the applied magnetic field is an integer multiple of the magnetic flux quantum  $\phi_0$

$$\phi_0 = \frac{h}{2e} = 2 \times 10^{-15} \text{Wb} \quad (2.41)$$

Since the  $\phi_0$  is the smallest quantity of the magnetic flux, this physical effect can be used to produce an extraordinarily sensitive magnetic detector known as SQUID, which actually functions as magnetic flux-to-voltage transducers because they convert the magnetic flux, which is difficult to measure, into voltage ( $V_{SQUID}$ ), which is easy to measure (with no direct measurement of the magnetic field at the location of the sample).

The fundamental principle of operating an induction-based magnetometer is to move a sample of the unknown moment near a set of the pickup coil. According to Faraday's law, a change in magnetic flux with the induced electric fields causes charge flow in a conductor. The motion can be controlled by knowing the pickup coil construction, and the task then becomes to quantify the results of this induction, from which the moment can be determined. The pick-up coil is made up of a closed loop of superconducting wire as a second-order gradiometer to reliably suppress the influence of all kinds of external magnetic fields[82].

# Bibliography

- (1) Krause, S.; Bon, V.; Senkovska, I.; Stoeck, U.; Wallacher, D.; Többens, D. M.; Zander, S.; Pillai, R. S.; Maurin, G.; Coudert, F.-X., et al. *Nature* **2016**, *532*, 348–352.
- (2) Krause, S.; Evans, J. D.; Bon, V.; Senkovska, I.; Coudert, F.-X.; Többens, D. M.; Wallacher, D.; Grimm, N.; Kaskel, S. *Faraday discussions* **2021**, *225*, 168–183.
- (3) Krause, S.; Evans, J. D.; Bon, V.; Senkovska, I.; Iacomi, P.; Kolbe, F.; Ehrling, S.; Troschke, E.; Getzschmann, J.; Többens, D. M., et al. *Nature communications* **2019**, *10*, 1–12.
- (4) Stoeck, U.; Krause, S.; Bon, V.; Senkovska, I.; Kaskel, S. *Chemical Communications* **2012**, *48*, 10841–10843.
- (5) Thangavel, K.; Walenszus, F.; Mendt, M.; Bon, V.; Kaskel, S.; Pöppel, A. *The Journal of Physical Chemistry C* **2023**, DOI: 10.1021/acs.jpcc.2c08905.
- (6) Thangavel, K.; Mendt, M.; Garai, B.; Folli, A.; Bon, V.; Murphy, D. M.; Kaskel, S.; Pöppel, A. *AIP Advances* **2023**, *13*, 015019.
- (7) Bitzer, J.; Otterbach, S.; Thangavel, K.; Kultaeva, A.; Schmid, R.; Pöppel, A.; Kleist, W. *Chem. Eur. J.* **2020**, *26*, 5667–5675.
- (8) Goyal, P.; Paruthi, A.; Menon, D.; Behara, R.; Jaiswal, A.; Keerthy, V.; Kumar, A.; Krishnan, V.; Misra, S. K. *Chemical Engineering Journal* **2022**, *430*, 133088.
- (9) Peedikakkal, A. M. P.; Aljundi, I. H. *ACS omega* **2020**, *5*, 28493–28499.
- (10) Sava Gallis, D. F.; Parkes, M. V.; Greathouse, J. A.; Zhang, X.; Nenoff, T. M. *Chemistry of Materials* **2015**, *27*, 2018–2025.
- (11) Aiyappa, H. B.; Saha, S.; Garai, B.; Thote, J.; Kurungot, S.; Banerjee, R. *Crystal growth & design* **2014**, *14*, 3434–3437.
- (12) Böhlmann, W.; Pöppel, A.; Sabo, M.; Kaskel, S. *The Journal of Physical Chemistry B* **2006**, *110*, 20177–20181.
- (13) Schlichte, K.; Kratzke, T.; Kaskel, S. *Microporous and Mesoporous Materials* **2004**, *73*, 81–88.
- (14) Puerto-Rodríguez, M.; López-Cartes, C.; Ayala, R. *Journal of Solid State Chemistry* **2022**, *312*, 123260.

- 
- (15) Venu, B.; Shirisha, V.; Vishali, B.; Naresh, G.; Kishore, R.; Sreedhar, I.; Venugopal, A. *New Journal of Chemistry* **2020**, *44*, 5972–5979.
- (16) Denysenko, D.; Jelic, J.; Reuter, K.; Volkmer, D. *Chemistry—A European Journal* **2015**, *21*, 8188–8199.
- (17) Denysenko, D.; Volkmer, D. *Faraday Discussions* **2017**, *201*, 101–112.
- (18) Fischer, J.; Sippel, P.; Denysenko, D.; Lunkenheimer, P.; Volkmer, D.; Loidl, A. *The Journal of Chemical Physics* **2015**, *143*, 154505.
- (19) Teufel, J.; Oh, H.; Hirscher, M.; Wahiduzzaman, M.; Zhechkov, L.; Kuc, A.; Heine, T.; Denysenko, D.; Volkmer, D. *Advanced Materials* **2013**, *25*, 635–639.
- (20) Dubey, R. J.-C.; Comito, R. J.; Wu, Z.; Zhang, G.; Rieth, A. J.; Hendon, C. H.; Miller, J. T.; Dinc, M. *Journal of the American Chemical Society* **2017**, *139*, 12664–12669.
- (21) Denysenko, D.; Werner, T.; Grzywa, M.; Puls, A.; Hagen, V.; Eickerling, G.; Jelic, J.; Reuter, K.; Volkmer, D. *Chemical Communications* **2012**, *48*, 1236–1238.
- (22) Denysenko, D.; Grzywa, M.; Tonigold, M.; Streppel, B.; Krkljus, I.; Hirscher, M.; Mugnaioli, E.; Kolb, U.; Hanss, J.; Volkmer, D. *Chemistry—A European Journal* **2011**, *17*, 1837–1848.
- (23) Zhong, G.; Liu, D.; Zhang, J. *Cryst. Growth Des.* **2018**, *18*, 7730–7744.
- (24) Van de Voorde, B.; Bueken, B.; Denayer, J.; De Vos, D. *Chem. Soc. Rev.* **2014**, *43*, 5766–5788.
- (25) D'Amore, M.; Civalleri, B.; Bush, I. J.; Albanese, E.; Ferrabone, M. *J. Phys. Chem. C* **2019**, *123*, 28677–28687.
- (26) Rivera-Torrente, M.; Mandemaker, L. D.; Filez, M.; Delen, G.; Seoane, B.; Meirer, F.; Weckhuysen, B. M. *Chemical Society Reviews* **2020**, *49*, 6694–6732.
- (27) Xuan, W.; Zhu, C.; Liu, Y.; Cui, Y. *Chemical Society Reviews* **2012**, *41*, 1677–1695.
- (28) Steenhaut, T.; Filinchuk, Y.; Hermans, S. *Journal of Materials Chemistry A* **2021**, *9*, 21483–21509.
- (29) Celeste, A.; Paolone, A.; Itié, J.-P.; Borondics, F.; Joseph, B.; Grad, O.; Blanita, G.; Zlotea, C.; Capitani, F. *Journal of the American Chemical Society* **2020**, *142*, 15012–15019.
- (30) Rivera-Torrente, M.; Pletcher, P. D.; Jongkind, M. K.; Nikolopoulos, N.; Weckhuysen, B. M. *ACS Catalysis* **2019**, *9*, 3059–3069.
- (31) Mali, G.; Mazaj, M.; Aron, I.; Hanel, D.; Aron, D.; Jaglii, Z. k. *J. Phys. Chem. Lett.* **2019**, *10*, 1464–1470.

- (32) Giménez-Marqués, M.; Santiago-Portillo, A.; Navalón, S.; Álvaro, M.; Briois, V.; Nouar, F.; Garcia, H.; Serre, C. *Journal of Materials Chemistry A* **2019**, *7*, 20285–20292.
- (33) Liang, H.; Liu, R.; An, X.; Hu, C.; Zhang, X.; Liu, H. *Chemical Engineering Journal* **2021**, *414*, 128669.
- (34) Mandal, S.; Natarajan, S.; Mani, P.; Pankajakshan, A. *Advanced Functional Materials* **2021**, *31*, 2006291.
- (35) Garai, B.; Bon, V.; Krause, S.; Schwotzer, F.; Gerlach, M.; Senkovska, I.; Kaskel, S. *Chemistry of Materials* **2020**, *32*, 889–896.
- (36) Koeberl, M.; Cokoja, M.; Herrmann, W. A.; Kuehn, F. E. *Dalton Transactions* **2011**, *40*, 6834–6859.
- (37) Maniam, P.; Stock, N. *Inorganic chemistry* **2011**, *50*, 5085–5097.
- (38) Pilbrow, J. *Transition ion electron paramagnetic resonance* (Oxford Science Publications), 1990.
- (39) Weil, J. A.; Bolton, J. R., *Electron paramagnetic resonance: elementary theory and practical applications*; John Wiley & Sons: 2007.
- (40) Brustolon, M.; Giamello, E., *Electron Paramagnetic Resonance: A Practitioners Toolkit*; John Wiley & Sons: 2009.
- (41) Schweiger, A.; Jeschke, G., *Principles of pulse electron paramagnetic resonance*; Oxford University Press on Demand: 2001.
- (42) Abragam, A.; Pryce, M. H. L. *Proceedings of the Royal Society of London. Series A. Mathematical and Physical Sciences* **1951**, *205*, 135–153.
- (43) Neese, F., *Origin and Interpretation of Spin Hamiltonian Parameters*, <https://obelix.physik.uni-bielefeld.de/schnack/molmag/material/Muehlheim-Neese-OriginAndInterpretationOfSpinHamiltonianParameters>
- (44) E. Duin, *Electron Paramagnetic Resonance theory*; [http://webhome.auburn.edu/duinedu/epr/1\\_theory.pdf](http://webhome.auburn.edu/duinedu/epr/1_theory.pdf) 2022.
- (45) Ribas, J.; Albela, B.; Stoeckli-Evans, H.; Christou, G. *Inorganic chemistry* **1997**, *36*, 2352–2360.
- (46) Vincent, J. B.; Chang, H. R.; Folting, K.; Huffman, J. C.; Christou, G.; Hendrickson, D. N. *Journal of the American Chemical Society* **1987**, *109*, 5703–5711.
- (47) Bencini, A.; Gatteschi, D., *EPR of exchange coupled systems*; Dover Publications: 2012.
- (48) Lalena, J. N.; Cleary, D. A.; Duparc, O. B. H., *Principles of inorganic materials design*; John Wiley & Sons: 2020.



- (49) Glaser, T., *Basic magnetism*; URL: <https://obelix.physik.uni-bielefeld.de/schnack/molmag/material/Muehlheim-Glaser-Magnetism.pdf>: 2023.
- (50) O'Connor, C. J. *Progress in inorganic chemistry* **1982**, 203–283.
- (51) Pöppl, A.; Kunz, S.; Himsl, D.; Hartmann, M. *The Journal of Physical Chemistry C* **2008**, *112*, 2678–2684.
- (52) Polyukhov, D. M.; Krause, S.; Bon, V.; Poryvaev, A. S.; Kaskel, S.; Fedin, M. V. *J. Phys. Chem. Lett.* **2020**, *11*, 5856–5862.
- (53) Joshi, J. P.; Bhat, S. *Journal of Magnetic Resonance* **2004**, *168*, 284–287.
- (54) Dyson, F. J. *Physical Review* **1955**, *98*, 349.
- (55) Cousins, J.; Dupree, R.; Havill, R. *British Journal of Applied Physics* **1965**, *16*, 1687.
- (56) Welzmler, S.; Heinke, F.; Huth, P.; Bothmann, G.; Scheidt, E.-W.; Wagner, G.; Scherer, W.; Poepl, A.; Oeckler, O. *Journal of Alloys and Compounds* **2015**, *652*, 74–82.
- (57) Augustyniak-Jabokow, M. A.; Yablokov, Y. V.; Andrzejewski, B.; Kempiski, W.; o, S.; Tadyszak, K.; Yablokov, M. Y.; Zhikharev, V. A. *Physics and Chemistry of Minerals* **2010**, *37*, 237–247.
- (58) Thangavel, K.; Morozkin, A.; Murthy, V.; Rayaprol, S.; Pöppl, A.; Nirmala, R. *IEEE Transactions on Magnetics* **2021**, *58*, 1–6.
- (59) Van Doorslaer, S.; Goldfarb, D.; Stoll, S. *EPR Spectroscopy: Fundamentals and Methods*, Wiley **2018**, 377–400.
- (60) Hirscher, N. A.; Arnett, C. H.; Oyala, P. H.; Agapie, T. *Organometallics* **2020**, *39*, 4420–4429.
- (61) Feher, G. *Physica* **1958**, *24*, S80–S87.
- (62) Feher, G. *Physical Review* **1959**, *114*, 1219.
- (63) Davies, E. *Physics Letters A* **1974**, *47*, 1–2.
- (64) Mims, W. *Proceedings of the Royal Society of London. Series A. Mathematical and Physical Sciences* **1965**, *283*, 452–457.
- (65) Kulik, L.; Lubitz, W. *Photosynthesis research* **2009**, *102*, 391–401.
- (66) Bracci, M.; Bruzzese, P. C.; Famulari, A.; Fioco, D.; Guidetti, A.; Liao, Y.-K.; Podvorica, L.; Rezayi, S. F.; Serra, I.; Thangavel, K.; Murphy, D. M. *Electron Paramag. Reson.* **2021**, *27*, 1–46.
- (67) Simenas, M.; Kobalz, M.; Mendt, M.; Eckold, P.; Krautscheid, H.; Banys, J.; Pöppl, A. *The Journal of Physical Chemistry C* **2015**, *119*, 4898–4907.
- (68) imnas, M.; Ciupa, A.; Maczka, M.; Pöppl, A.; Banys, J. *The Journal of Physical Chemistry C* **2015**, *119*, 24522–24528.

- (69) Mendt, M.; Jee, B.; Himsl, D.; Moschkowitz, L.; Ahnfeldt, T.; Stock, N.; Hartmann, M.; Pöppl, A. *Applied Magnetic Resonance* **2014**, *45*, 269–285.
- (70) Mendt, M.; Barth, B.; Hartmann, M.; Pöppl, A. *J. Chem. Phys.* **2017**, *147*, 224701.
- (71) Friedländer, S.; Petkov, P. S.; Bolling, F.; Kultaeva, A.; Böhlmann, W.; Ovchar, O.; Belous, A. G.; Heine, T.; Pöppl, A. *The Journal of Physical Chemistry C* **2016**, *120*, 27399–27411.
- (72) imnas, M.; Jee, B.; Hartmann, M.; Banys, J.; Pöppl, A. *The Journal of Physical Chemistry C* **2015**, *119*, 28530–28535.
- (73) Jee, B.; Hartmann, M.; Pöppl, A. *Molecular Physics* **2013**, *111*, 2950–2966.
- (74) Jee, B.; St. Petkov, P.; Vayssilov, G. N.; Heine, T.; Hartmann, M.; Pöppl, A. *The Journal of Physical Chemistry C* **2013**, *117*, 8231–8240.
- (75) Sheveleva, A.; Anikeenko, A.; Poryvaev, A.; Kuzmina, D.; Shundrina, I.; Kolokolov, D.; Stepanov, A.; Fedin, M. *The Journal of Physical Chemistry C* **2017**, *121*, 19880–19886.
- (76) Nasalevich, M. A.; Hendon, C. H.; Santaclara, J. G.; Svane, K.; Van Der Linden, B.; Veber, S. L.; Fedin, M. V.; Houtepen, A. J.; Van Der Veen, M. A.; Kapteijn, F., et al. *Scientific reports* **2016**, *6*, 1–9.
- (77) Horiuchi, Y.; Toyao, T.; Saito, M.; Mochizuki, K.; Iwata, M.; Higashimura, H.; Anpo, M.; Matsuoka, M. *The Journal of Physical Chemistry C* **2012**, *116*, 20848–20853.
- (78) Chen, D.; Xing, H.; Wang, C.; Su, Z. *Journal of Materials Chemistry A* **2016**, *4*, 2657–2662.
- (79) Zhao, X.; Pattengale, B.; Fan, D.; Zou, Z.; Zhao, Y.; Du, J.; Huang, J.; Xu, C. Mixed-node metal-organic frameworks as efficient electrocatalysts for oxygen evolution reaction. *ACS Energy Lett* **3**: 2520–2526, 2018.
- (80) Cornelio, J.; Lee, S. J.; Zhou, T.-Y.; Alka, A.; Thangavel, K.; Pöppl, A.; Telfer, S. G. *Chemistry of Materials* **2022**, *34*, 8437–8445.
- (81) Buchner, M.; Höfler, K.; Henne, B.; Ney, V.; Ney, A. *Journal of Applied Physics* **2018**, *124*, 161101.
- (82) Dumas, R. K.; Hogan, T. *Magnetic Measurement Techniques for Materials Characterization* **2021**, 39–62.

## Chapter 3

# Adsorption-Induced Breathing Transitions in DUT-49(Cu) MOF

### 3.1 Introduction

Recently, the mesoporous flexible framework DUT-49 with the composition  $[\text{Cu}_2(\text{C}_{40}\text{H}_{20}\text{N}_2\text{O}_8)]$  was discovered by Prof. Dr. Stefan Kaskel's group, Dresden University of Technology and intensively studied (Figure 3.1) using several techniques for several aspects[1–8]. This framework and some related isotopological frameworks show long-lived overloaded metastable states, leading to the previously unknown phenomenon of Negative Gas Adsorption (NGA) (Figure 3.1)[5, 9]. In addition to thermodynamic calculations[10–12], the origin of this phenomenon was studied by various experimental techniques: *In situ* powder X-ray diffraction (PXRD), measured in parallel to physisorption, provided insights into the switching mechanism[7], *in situ*  $^{129}\text{Xe}$  nuclear magnetic resonance (NMR) shed light on the state of guest molecules in the pores of the open (*op*) and closed (*cp*) phases (Figure 3.1b,c)[13], pulsed field gradient (PFG) NMR highlighted the role of self-diffusion in the metastable states[14], mercury intrusion estimated experimental transition pressures[15], adsorptions of various fluids at various temperatures helped to evaluate the empirical rules for reaching NGA[3]. DUT-49(Cu) was successfully explored in the pressure amplification experiments far above the atmospheric pressure using carbon dioxide as working fluid[8].

Despite the large amount of knowledge that has been gained about DUT-49(Cu) so far, further questions remain unresolved. In particular, the detailed framework structure of DUT-49(Cu) during xenon physisorption is not known yet. *In situ* high-pressure  $^{129}\text{Xe}$  NMR studies of DUT-49(Cu) during xenon physisorption discovered many details of the structural *op*  $\leftrightarrow$  *cp* transition, like evidence for NGA or a collective and stepwise kind of phase transition with the coexistence of the *op* and *cp* phase in the respective pressure range[16]. However, corresponding *in situ* PXRD measurements are not feasible for the xenon-loaded MOF due to the high absorption coefficient of

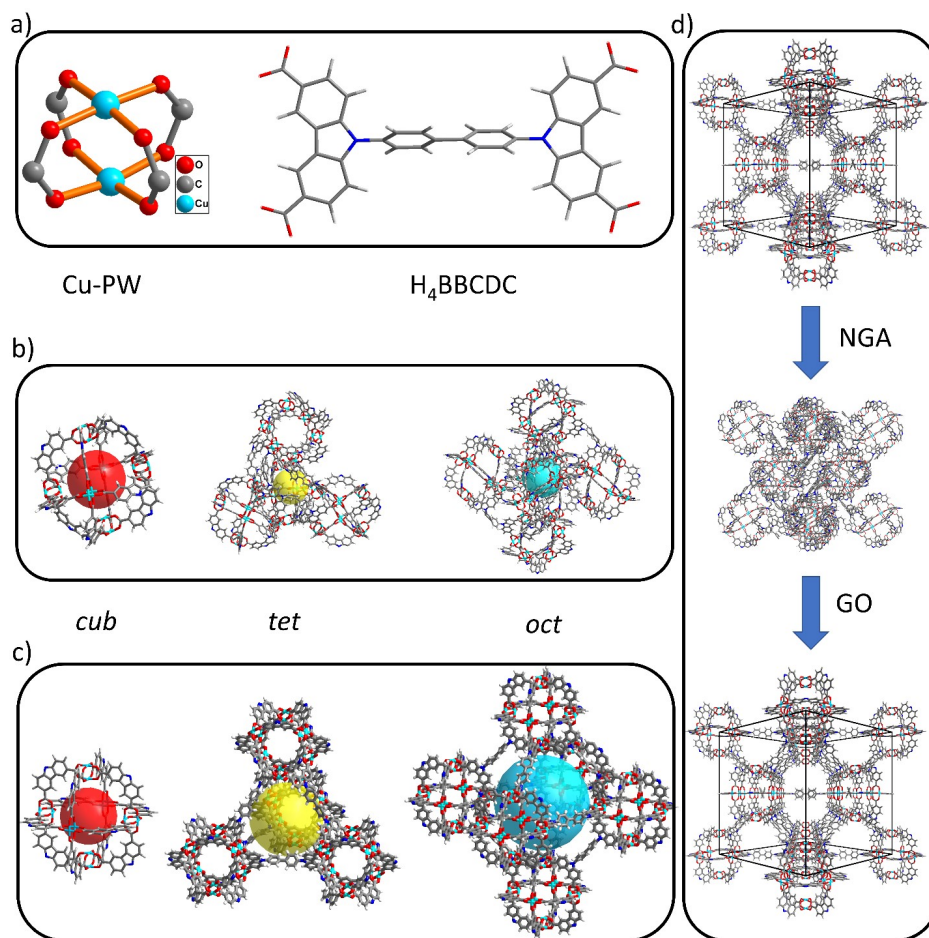


FIGURE 3.1: Crystal structures of DUT-49(Cu) and guest-induced framework dynamics: a) building blocks used in the construction of DUT-49(Cu); b) Pore size of contracted pore (*cp*) phase of DUT-49(Cu); c) Pore system of open pore (*op*) phase of DUT-49(Cu); d) Guest-induced breathing in DUT-49(Cu) including NGA and Gate Opening (GO).[2]

the xenon in the available X-ray energy range[16]. In a previous study, we endeavoured to monitor the physisorption of xenon by PXRD at the synchrotron; however, we could not obtain direct proof because of the strong X-ray absorption of Xe-loaded DUT-49 within the available X-ray energy range[16]. Only indirect evidence of the phase transition could be obtained after removing xenon atoms from the pores of DUT-49 by applying a dynamic vacuum for more than 20 minutes. Nevertheless, detailed insights into structural changes of DUT-49(Cu) upon xenon adsorption are desired since one might expect London (VdW forces) dispersion interactions and hydrogen bonds between the xenon molecules and the MOF [16–21], which might cause a unique response of the MOF framework upon gas loading. Recently, Aquilanti *et al.*[17] reported a hydrogen bonding between noble gases (including xenon and krypton) and water. In specific, they reported that only 50 % Kr is accounted for the VdW forces through the ab initio calculations in which the proton is extended as a binding bridge towards the noble gases. Therefore we may expect a potential hydrogen bond formation between the hydrogen atoms of the organic linker in the MOF framework

and the adsorbed Xe molecules. By looking for alternatives to unravel the structural details of the xenon-loaded DUT-49(Cu), it is noticeable that the metal complexes in DUT-49(Cu) consist of two AFM coupled Cu(II) ions in the so-called PW unit leading to an excited electron spin state with total spin  $S = 1$ [22, 23]. The characteristic magnetic signature of such PWs in the framework can be measured by electron paramagnetic resonance (EPR) spectroscopy[1, 6, 22, 24], and it can be used as a probe to interrogate the local structural changes of the PW units upon gas adsorption[1, 25]. Specialized *in situ* EPR experiments during gas adsorption have been conducted only by a few groups so far[1, 23, 26–28]. In a recent study, the magnetic signature of the copper PW was used to monitor with *in situ* EPR the structural transitions in DUT-49(Cu) induced by n-butane and diethyl ether at  $T = 298$  K[23]. In the present work, we used likewise *in situ* EPR spectroscopy to explore the xenon adsorption and desorption in this MOF from the local view of the PWs at  $T \approx 156$  K [1]. It turns out that the experimentally derived ZFS of the PWs behaves differently during xenon adsorption at  $T \approx 156$  K than it was observed for n-butane and diethyl ether adsorption at  $T = 298$  K[23]. Therefore, we sought for more evidence for our results[1]. Since PXRD experiments are not possible for the xenon-loaded DUT-49, as explained above, we decided to perform additional *in situ* EPR experiments on DUT-49(Cu) during the adsorption of ethylene having a saturated vapor pressure of 78 kPa at 165 K, similar to xenon (b.p. 165 K at 101 kPa)[1]. Furthermore, ethylene belongs to one of the most important industrial chemicals, and it is well-known in organometallic and coordination chemistry to form various  $\pi$ -complexes with 3d-metals[29]. Moreover, the adsorption of ethylene at 199 K shows one of the highest NGA values in DUT-49(Cu), reaching  $\Delta n_{NGA} = 9$  mmol/g[3].

In the following, we monitor the adsorption and desorption of xenon ( $T = 156$  K) and ethylene ( $T = 165$  K) on DUT-49(Cu) by *in situ* EPR spectroscopy and show their different structural response from the local view of the PW units. Adsorption of ethylene on DUT-49(Cu) has not been studied by synchrotron *in situ* PXRD so far[1]. Thus, ethylene adsorption and desorption are monitored by *in situ* PXRD showing a specific interaction of the ethylene molecule with the copper PWs. *In situ* EPR reveals further evidence for distinct interactions of xenon and ethylene with the copper PWs and different behavior of DUT-49(Cu) concerning its *op*  $\leftrightarrow$  *cp* transition in the presence of the two gases[1].

### 3.2 EPR of the virgin state of DUT-49(Cu)

EPR characteristics of DUT-49(Cu): Figure 3.2c shows the EPR spectra of the activated sample DUT-49(Cu) measured at temperatures  $T = 290$  K and  $T = 7$  K, respectively. At  $T = 7$  K, only

a powder signal of an electron spin  $S = 1/2$  species M with anisotropic  $g$ -tensor and a resolved anisotropic HF interaction due to a nuclear spin  $I = 3/2$  could be detected. We assign species M to a monomeric Cu(II) ion. The magnetic energy levels of this Cu(II) species M can be described by the spin Hamiltonian

$$\hat{H}_{monomer} = \mu_B \vec{B} \hat{g} \hat{S} + \hat{S} \hat{A} \hat{I} \quad (3.1)$$

Here,  $\hat{S}$  is a matrix-valued vector operator describing the  $S = 1/2$  electron spin of the Cu(II) ion,  $\mu_B$  is the electron Bohr magneton,  $\vec{B}$  is the applied external magnetic field vector,  $\hat{I}$  is a matrix-valued vector operator describing the nuclear spin  $I = 3/2$  of the copper isotope  $^{63}\text{Cu}$ (69.17%) and  $^{65}\text{Cu}$ (30.83%),  $g$  is the  $g$ -tensor with principal values  $g_x$ ,  $g_y$  and  $g_z$ , describing the electron Zeeman interaction and  $A$  is a tensor with principal values  $A_x$ ,  $A_y$  and  $A_z$  representing the HF interaction between the electron spin and the copper nuclear spin. Corresponding experimentally derived spin Hamiltonian parameters and the respective simulated signals are summarized in the Sec. 3.8 (SI) in Table 3.2 and Figure 3.14. Here HF data refer to the isotope  $^{63}\text{Cu}$ . The low field part of the EPR signal of species M resolves the contribution of two nuclear isotopes, perfectly matching the relative natural abundance of the nuclear copper isotopes  $^{63}\text{Cu}$  and  $^{65}\text{Cu}$  as verified by spectral simulations.

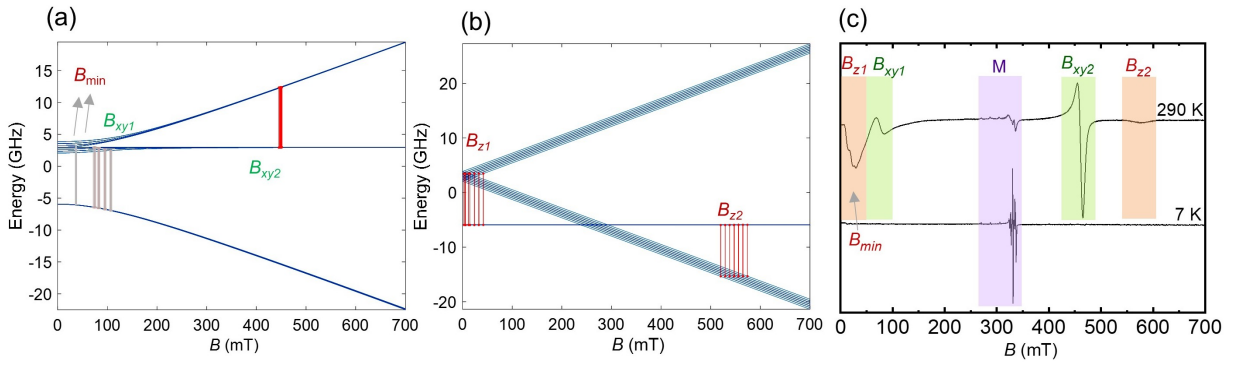


FIGURE 3.2: Energy level plots of  $S = 1$  Cu(II) - Cu(II) dimer in its antiferromagnetically coupled excited triplet state as a function of the applied magnetic field. (a)  $B \parallel xy$ , (b)  $B \parallel z$ . Here  $D = 8985$  MHz and (c) experimental EPR spectra of activated DUT-49(Cu) at  $T = 290$  K (top) and  $T = 7$  K (bottom) show the labelling of the different transitions of the  $S = 1$  signal of species  $A_{cp}$  according to Wassermann *et al.*[30] ( $B_{xy}$  and  $B_z$ ) and the labelling of the Cu(II) monomer species M (purple).  $B_{min}$  is a forbidden transition superpositioned with the  $B_{z1}$  transition.

At  $T = 290$  K, the signal of species M is observed again. In addition, lines which are visible in the field regions  $0 \text{ mT} < B < 200 \text{ mT}$  and  $400 \text{ mT} < B < 600 \text{ mT}$  can be assigned to an  $S = 1$  electron spin species  $A_{op}$ . The corresponding label indicates that this species occurs in the activated sample, which stays in the *op* phase[16, 23]. The  $S = 1$  signal of  $A_{op}$  shows the typical transitions in case the axially symmetric ZFS is of the same order as the microwave frequency[23]. Labels

TABLE 3.1: Experimentally derived spin Hamiltonian parameters of different  $S = 1$  species assigned to copper PW units in DUT-49 (Cu) under different conditions. ( $T$  temperature,  $p/p_0$  relative pressure)

S= 1 species ( $T, p/p_0$ )	$g_{x,y}$	$g_z$	$A_{x,y}$ (MHz)	$A_z$ (MHz)	$D$ (MHz)	$E/D$
$A_{op}$ (290 K, 0.00)	2.039(5)	2.285(5)	< 50	250(20)	8985(15)	< 0.008
$A_{op}$ (156 K, 0.00)	2.034(4)	2.290(3)	< 45	270(8)	8985(15)	< 0.006
$X_{op}$ (156 K, 1.00)	2.036(2)	2.296(2)	< 60	262(3)	9240(15)	< 0.008
$X_{cp}$ (156 K, 0.00)	2.039(2)	2.295(10) <sup>a</sup>	< 60	280(30) <sup>a</sup>	8805(25)	< 0.008
$A_{op}$ (165 K, 0.00)	2.037(2)	2.291(2)	< 45	265(10)	8990(10)	< 0.006
$E_{op}$ (165 K, 1.00)	2.056(3)	2.347(7)	< 58	240(10)	9750(250)	< 0.008
$E_{cp}$ (165 K, 0.00)	2.040(2)	2.306(6)	< 58	235(10)	9115(20)	< 0.006
$A_{cp}$ (165 K, 0.00)	2.038(2)	2.290(6)	< 61	255(10)	8810(20)	< 0.006

<sup>a</sup>larger error due to a small signal-to-noise ratio and/ or significant  $D$ -strain effects

for the different transitions are defined in Figure 3.2, adopting again the notation introduced in a paper by Wasserman, Snyder and Yager[30]. Similar  $S = 1$  spectrum was observed at lower temperatures at different xenon and ethylene pressures, as discussed below. Some show a splitting of the  $B_{z1}$  and  $B_{z2}$  transitions into several lines (Figure 3.20(a, b, e, f) and Figure 3.23(a, b, e, f), Sec. 3.8 in SI). Those lines are indicative of the HF interaction with two copper nuclei. We, therefore, assign all  $S = 1$  signals observed in this study to the thermally populated excited  $S = 1$  state of a corresponding Cu(II) - Cu(II) dimer in the PW units of DUT-49(Cu). Since it has a diamagnetic  $S = 0$  ground state due to the AFM coupled Cu(II) ions in the PW units[22] at  $T < 80$  K, it is EPR silent at  $T = 7$  K (Figure 3.2 and Figure 3.14a in SI)[22, 31]. The energy difference between the  $S = 0$  ground and the  $S = 1$  excited state of the Cu(II) - Cu(II) dimer is ( $2J = -322(6) \text{ cm}^{-1}$  as the isotropic exchange coupling constant) deduced from temperature-dependent EPR signal intensities of the  $S = 1$  signal (see Figure 3.14a, SI). The  $S = 1$  state can be described by the spin Hamiltonian

$$\hat{H}_{dimer} = \mu_B \vec{B} \mathbf{g} \hat{S} + D \left[ \hat{S}_z^2 - \frac{1}{3} S(S+1) \right] + E (\hat{S}_x^2 - \hat{S}_y^2) + \hat{S} A \hat{I}_i \quad (3.2)$$

$\hat{S}$  is a matrix-valued vector operator with components  $S_x$ ,  $S_y$  and  $S_z$ , describing the  $S = 1$  spin of the Cu(II) dimer,  $D$  and  $E$  are the axial and orthorhombic ZFS parameters and  $\hat{I}_i$  ( $i = 1, 2$ ) are the matrix-valued vector operators describing both nuclear spins  $I = 3/2$  of the copper atoms in the PW unit. We assume that the Cu(II) - Cu(II) dimer has such a symmetry that the HF interactions of the electron spin with each nucleus are described by identical tensors, and both copper HF interaction tensors are coaxial. Experimentally derived spin Hamiltonian parameters of species  $A_{op}$  are summarized in Table 3.1. Similar signals were reported for other MOFs containing Cu(II)

- Cu(II) PWs [22, 23, 25, 32], which supports our assignment of this  $S = 1$  signal, as well as of all other  $S = 1$  signals, which we report in this work, to Cu(II) - Cu(II) dimers in the PW units of the MOF. Moreover, the ratio of Cu(II) monomer ( 11%) and Cu(II)-Cu(II) dimer ( 89%) species were found to be 0.12(2) from the EPR simulation of a single spectrum at room temperature.

### 3.3 *In situ* EPR gas adsorption studies

#### 3.3.1 *In situ* EPR in parallel to xenon sorption

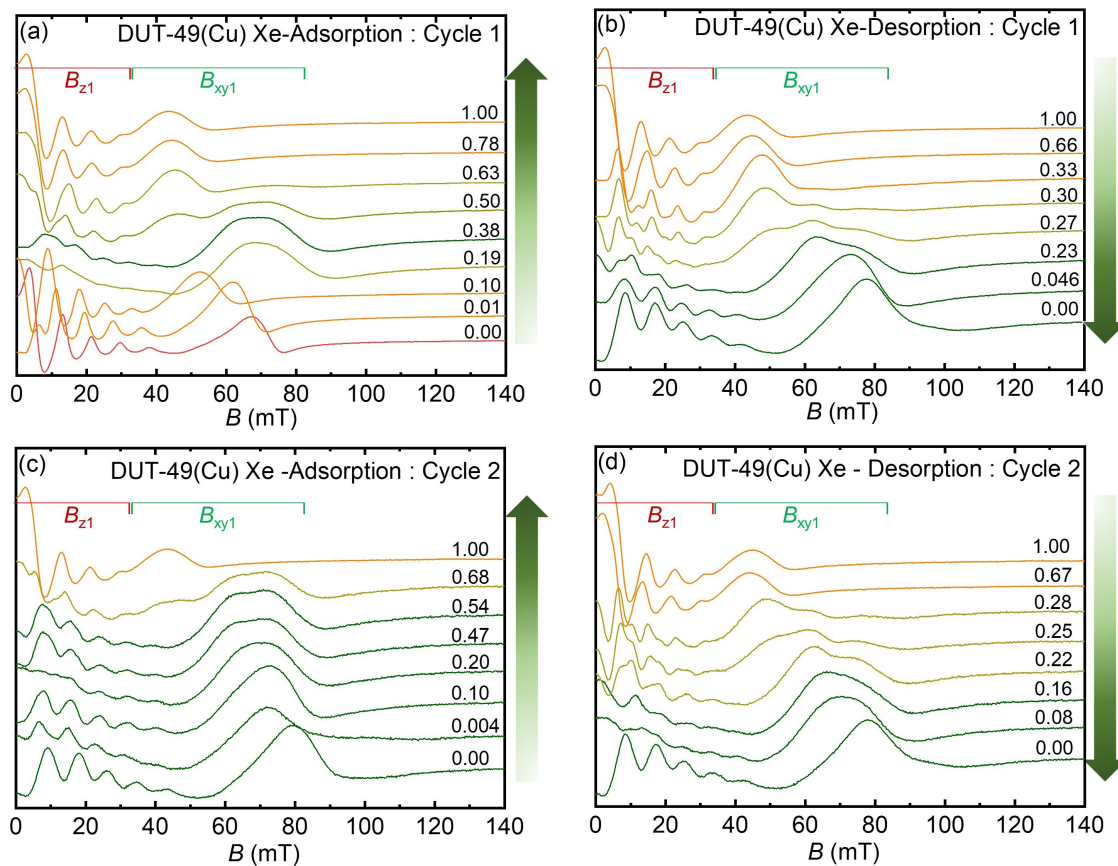


FIGURE 3.3: The low field part of the *in situ* EPR spectra of the  $S = 1$  state of the Cu(II) - Cu(II) dimers in DUT-49(Cu) during (a) xenon adsorption and (b) xenon desorption at 156 K temperature in a first cycle starting with an activated sample. Furthermore, spectra are shown, which were measured in a second cycle at 158 K during (c) adsorption and (d) desorption starting with a sample which went through a full initial xenon ad/desorption cycle after activation. The EPR spectra are labelled with the relative xenon pressures  $p/p_0$  ( $p_0 = 51$  kPa in (a) and (b) and  $p_0 = 55$  kPa in (c) and (d)) at which they were measured. Orange spectra indicate the dominant presence of the *op* phase, green spectra that of the *cp* phase, olive spectra indicate the coexistence of both phases, and the red spectrum corresponds to *op* phase of the gas-free activated sample. The assignment of the various phases is based on correlating the *in situ* EPR spectra with sorption isotherms measured by Krause *et al.*[3]

To monitor the structural changes of the DUT-49(Cu) MOF induced by xenon sorption, EPR



experiments were performed at  $T = 157(2)$  K *in situ* on this material during two xenon ad/desorption cycles. Since DUT-49(Cu) is known to adopt the *op* phase after supercritical activation with  $\text{CO}_2$  but can end up in the *cp* phase after a full ad/desorption cycle[2, 3], we divided our experiments into two ad/desorption cycles.

For the first cycle, we focussed on the Xe adsorption behavior of a gas-free sample prepared only by activation. After that, we reexamined the ad/desorption behavior on the same sample after an initial complete xenon ad/desorption cycle, as explained in the method section. Figure 3.3 shows selected EPR spectra measured *in situ* at  $T = 157(2)$  K during the first and second xenon ad/desorption cycle. Only the low field part of the EPR spectra is presented to enlarge the region where the  $B_{xy1}$  transition occurs. The complete set of spectra can be found in Figure 3.17, SI. The resonance field position of the  $B_{xy1}$  transition is very sensitive to small changes in the ZFS parameter  $D$ , which, in turn, is highly sensitive to small structural changes in the local environment of the PW units[23]. As Figure 3.3 shows, the field position of the  $B_{xy1}$  transition changes significantly with xenon pressure, and the corresponding EPR line splits at certain pressures into two or even three local maxima, indicating the coexistence of two or even three different PW species at the same time[16]. All EPR spectra were analyzed in detail based on spectral simulations according to a protocol explained in the method section. Simulated signals for selected spectra are shown in Figure 3.18, SI. In that way, signals of one PW species  $X_{op}$ , tentatively assigned to the *op* phase, were identified. EPR signals of three more PW species  $X_{cp}$ ,  $X_{cp1}$  and  $X_{cp2}$ , were observed and tentatively assigned to the *cp* phase. Here, X stands for xenon sorption.

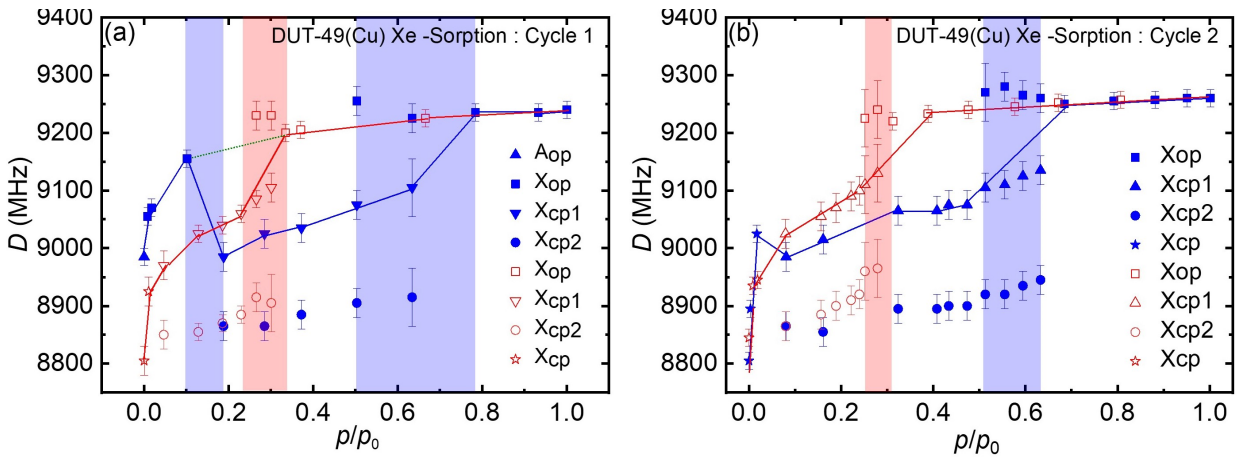


FIGURE 3.4: ZFS parameter  $D$  of the  $S = 1$  state determined for five different Cu PW species  $A_{op}$  (up-pointing triangle)  $X_{op}$  (squares),  $X_{cp1}$  (down-pointing triangles),  $X_{cp2}$  (circles) and  $X_{cp}$  (stars) during xenon adsorption (blue), and subsequent desorption (red) at a) the first ad/desorption cycle at  $T = 156$  K and b) the second ad/desorption cycle at  $T = 158$  K. Regions where the occurrence of structural phase transitions are indicated by the *in situ* EPR data are highlighted in blue during adsorption and in red during desorption. Lines are added as guides for the eyes. (closed symbols adsorption, opened symbols desorption)

The ZFS ( $D$ ) parameters of those four PW species were determined in dependence on the relative pressure, as shown in Figure 3.4, for the first and second cycles. In the following, the final result, shown in Figure 3.4, will be presented as a hypothesis. Then, arguments for this hypothesis will be summarized, including more detailed reasoning for interpreting the data by four different PW species and their tentative assignment to the  $op$  and  $cp$  phase of DUT-49(Cu).

The first EPR spectrum of the activated sample measured under dynamic vacuum conditions ( $p/p_0 = 0.00$ ) in the adsorption branch of the first cycle shows a single  $S = 1$  signal which we assign to the PW species  $A_{op}$  of the  $op$  phase since the activated material is known to adopt the  $op$  phase (Figure 3.3a)[16, 23]. The successive three EPR spectra measured in the pressure range  $0.00 < p/p_0 \leq 0.10$  (Figure 3.3a) show the  $S = 1$  signal of only one PW species  $X_{op}$  (Figure 3.18a, SI), which we assign to PW species in the  $op$  phase again. In this pressure range, the  $D$  parameter of  $X_{op}$  increases with pressure, which is reflected by a distinct continuous shift of the  $B_{xy1}$  transition to lower magnetic fields (Figure 3.3a). Between  $0.10 < p/p_0 \leq 0.19$  the DUT-49(Cu) MOF transforms from the  $op$  to the  $cp$  phase and the EPR spectrum measured at  $p/p_0 = 0.19$  shows now a superposition of two  $S = 1$  signals, which we assign to two PW species  $X_{cp1}$  and  $X_{cp2}$  of the  $cp$  phase with  $D$  parameters significantly smaller in magnitude than that of species  $X_{op}$  at  $p/p_0 = 0.10$ . In the pressure range  $0.19 \leq p/p_0 < 0.50$  the DUT-49(Cu) material remains in the  $cp$  phase, and all EPR spectra measured in this range show a superposition of the two  $S = 1$  signals assigned to the PW species  $X_{cp1}$  and  $X_{cp2}$ . The  $D$  parameters of both species increase slightly with growing pressure in this pressure range (Figure 3.3a). In the pressure range  $0.50 \leq p/p_0 < 0.78$ , the MOF transforms from the  $cp$  phase to the  $op$  phase, which is reflected by the observation of three different  $S = 1$  signals in the EPR spectra measured at  $p/p_0 = 0.50$  and  $p/p_0 = 0.63$  assigned to the PW species  $X_{op}$ ,  $X_{cp1}$  and  $X_{cp2}$ . This indicates the coexistence of the  $op$  and  $cp$  phases at these pressures, as it is typical for a first-order structural phase transition[16] or the presence of crystallite size distribution[33–35]. At pressures  $p/p_0 \geq 0.78$ , the MOF stays in the  $op$  phase, and the EPR spectra show only one signal assigned to the PW species  $X_{op}$ . A schematic phase diagram for DUT-49(Cu) during Xe adsorption, as derived from the observation of the various species in the EPR spectra, is depicted in the lower part of Figure 3.5a.

Subsequently, *in situ* EPR spectra were measured during the desorption. For pressures  $p/p_0 \geq 0.33$  stays in the  $op$  phase since the spectra show only one  $S = 1$  signal assigned to the PW species  $X_{op}$ . In the pressure range  $0.33 > p/p_0 > 0.23$ , the MOF transforms to the  $cp$  phase, accompanied by the superposition of the three EPR signals of  $X_{op}$ ,  $X_{cp1}$  and  $X_{cp2}$  at  $p/p_0 = 0.30$  and  $p/p_0 = 0.27$ . The signal  $X_{op}$  from the  $op$  phase disappears at  $p/p_0 = 0.23$ . Subsequently, the MOF remains in the  $cp$  phase all the way along the desorption branch to the application of dynamic vacuum.

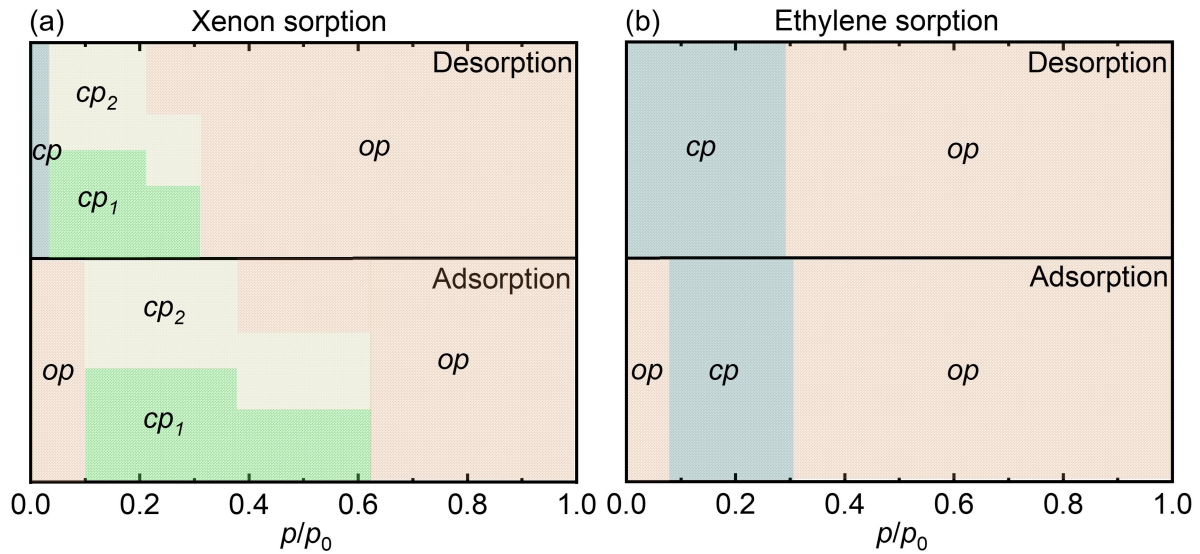


FIGURE 3.5: Schematic phase diagram for DUT-49(Cu) during the first adsorption and desorption cycle of (a) xenon and (b) ethylene, as derived from EPR experiments.

The EPR signals of  $X_{cp1}$  and  $X_{cp2}$  are observed down to  $p/p_0 = 0.046$ . At lower pressures  $p/p_0 = 0.011$ , and under dynamic vacuum, the EPR spectra reveal only one  $S = 1$  signal assigned to a single PW species  $X_{cp}$  of the  $cp$  phase. Again a schematic phase diagram for DUT-49(Cu) during Xe desorption can be developed on the basis of these EPR data and is presented in the upper part of Figure 3.5a.

During the second cycle,  $S = 1$  signals were detected again and assigned to the PW species  $X_{op}$ ,  $X_{cp}$ ,  $X_{cp1}$  and  $X_{cp2}$ . The pressure dependence of their  $D$  parameters is shown in Figure 3.4b. Before the adsorption, under a dynamic vacuum, the MOF is in the  $cp$  phase as prepared by an initial ad/desorption cycle. The  $S = 1$  signal of only one species  $X_{cp}$ , assigned to PWs in the  $cp$  phase, is observed. With increasing pressure, the MOF remains in the  $cp$  phase up to  $p/p_0 = 0.47$ . Here, at pressures  $p/p_0 \leq 0.017$  the EPR spectra show only one  $S = 1$  signal assigned to the PW species  $X_{cp}$ . At greater pressures in the range of  $0.08 \leq p/p_0 \leq 0.47$ , a superposition of two  $S = 1$  signals is observed, which are assigned to two PW species  $X_{cp1}$  and  $X_{cp2}$ , of the  $cp$  phase. The MOF transforms from the  $cp$  to the  $op$  phase in the pressure range  $0.47 < p/p_0 < 0.68$  accompanied by a superposition of the three  $S = 1$  signals assigned to the PW species  $X_{op}$ ,  $X_{cp1}$  and  $X_{cp2}$ . At pressures  $p/p_0 \geq 0.68$ , only a single  $S = 1$  signal of the PW species  $X_{op}$  of the  $op$  phase is observed.

During desorption, the MOF stays in the  $op$  phase at pressures  $p/p_0 \geq 0.31$ , and only one EPR signal assigned to the PW species  $X_{cp}$  is observed in this range. In the range  $0.31 > p/p_0 > 0.24$ , the DUT-49(Cu) transforms to the  $cp$  phase. Correspondingly, three  $S = 1$  signals assigned to the PW species  $X_{op}$ ,  $X_{cp1}$  and  $X_{cp2}$  superimpose in the EPR spectra measured at relative pressures  $p/p_0 = 0.28$  and  $p/p_0 = 0.25$ . Upon further decrease of the xenon pressure, the signal  $X_{op}$  disappears, and

the MOF remains in the  $cp$  phase in the full range  $p/p_0 \leq 0.24$  and two  $S = 1$  signals assigned to the PW species  $X_{cp1}$  and  $X_{cp2}$  are detected by EPR at pressures  $0.24 \geq p/p_0 \geq 0.08$ . At pressures  $p/p_0 < 0.08$  only one  $S = 1$  signal is observed again and assigned to species  $X_{cp}$ . If present, in both ad/desorption cycles, species  $X_{cp1}$  and  $X_{cp2}$  occur with relative abundance 1.5(1.0):1 as derived by spectral simulations. At pressures  $p/p_0 < 0.08$ , only one  $S = 1$  signal is observed again and assigned to species  $X_{cp}$  Figure 3.16b (SI) summarizes the observed phase transitions for the second Xe adsorption/desorption cycle. Figure 3.16b (SI) summarizes the observed phase transitions for the second Xe adsorption/desorption cycle.

Now, the arguments leading to this presented interpretation of the data are going to be discussed. First, the identification of up to three  $S = 1$  signals in one EPR spectrum will be reasoned. There are several spectral indications for a superposition of different  $S = 1$  signals in the EPR spectra. The first obvious reason is a splitting of the  $B_{xy1}$  transition in two or three local maxima, which was observed in Figure 3.3. Obviously, for flexible frameworks such as in the case of DUT-49, even small structural variations at the copper paddle wheels may lead to a distribution of the ZFS parameters ( $D$  and  $E$  strain). However, spectral simulations (Figure 3.19a, SI) reveal that an increasing  $D$  strain just broadens the  $B_{xy1}$  transition but does not cause the splitting of this signal of the  $S = 1$  species. However, a superposition of two or even three species may lead to a distinct splitting of the  $B_{xy1}$  transition, as supported by our spectral simulations presented in Figure 3.18 (SI). The complete simulation parameters are summarized in Table 3.3 (SI). If the differences in the  $D$  values of coexisting species are small ( $D < 20$  MHz) the species cannot be distinguished anymore, and they are represented in a small  $D$  strain. But we need to emphasize that in cases where the line shape of the  $B_{xy1}$  transition shows some kind of splitting or broadening characteristic for two  $S = 1$  species, one has to consider also the possibility that this splitting originates from an orthorhombic ZFS interaction with ZFS parameter  $E > 0$  due to a lowering of the symmetry of the respective PW. However, spectral simulations reveal that an orthorhombic distortion which is larger than the experimental error ( $E/D = 0.008$ ) would lead to a splitting of both transitions  $B_{xy1}$  at 50–80 mT and  $B_{xy2}$  at 460 mT of similar size (Figure 3.19b, SI). Such a splitting has not been observed for the  $B_{xy2}$  transition (Figure 3.18, SI). Otherwise, a small change in the axial ZFS parameter  $D$  for an axial symmetric species leads to a substantial larger shift of the  $B_{xy1}$  transition in comparison with the  $B_{xy2}$  transition. In addition, an orthorhombic distortion of the ZFS tensor would not split the HF lines of the  $B_{z1}$  transition and those of the  $B_{z2}$  transition as verified by spectral simulations (Figure 3.18 and Table 3.3, SI). The same arguments hold for  $E$  strain effects. The important point is that in all cases where the line shape of the  $B_{xy1}$  transitions indicates a superposition of two or three  $S = 1$  signals, we observe a splitting or blurring of the HF lines of the  $B_{z1}$

and  $B_{z2}$  transitions, as illustrated in Figure 3.20 a, b, e, and f (SI) which can only be explained by a superposition of more than one  $S = 1$  signal. In cases where the  $B_{xy1}$  transition shows the typical line shape of one single  $S = 1$  signal, we observe almost always well-resolved and comparable strong HF lines of the  $B_{z1}$  and  $B_{z2}$  transitions of one single  $S = 1$  species (Figure 3.20 a, b, e, and f, SI), otherwise not. This consistent correlation between the splitting or broadening of the  $B_{xy1}$  transition and the splitting or blurring of the HF lines of the  $B_{z1}$  and  $B_{z2}$  transitions throughout all EPR spectra measured during the first and second cycle justifies our identification of the number of  $S = 1$  species contributing to each EPR spectrum.

Next, the reasons for the assignment of the different  $S = 1$  signals will be explained. During the two sorption cycles, several significant spectral changes during small pressure changes were observed by EPR. After activation and cooling down to  $T = 156$  (virgin state), the DUT-49(Cu) is known to stay in the *op* phase[2, 16]. The spectra measured at  $p/p_0 \leq 0.10$  show resolved HF lines at the  $B_{z1}$  and  $B_{z2}$  transitions indicating the presence of only one  $S = 1$  species at the beginning of the adsorption. We therefore assign the  $S = 1$  signal observed in this pressure range to PW species  $A_{op}$  (gas free - activated sample) and  $X_{op}$  (xenon loaded sample) of the *op* phase. After increasing the pressure from  $p/p_0 = 0.10$  to  $p/p_0 = 0.19$  during adsorption in the first cycle, the  $B_{xy1}$  transition suddenly jumps to a higher magnetic field (Figure 3.3a, 3.17 SI) which is related to a discrete decrease of the  $D$  parameter. Furthermore, at  $p/p_0 = 0.10$  the HF lines of the  $B_{z1}$  and  $B_{z2}$  transitions are resolved and become blurred at  $p/p_0 = 0.19$  (Figure 3.17a, SI) indicating the sudden appearance of more than one  $S = 1$  species. Already contributions of two  $S = 1$  species can explain the observed splitting or blurring of the respective HF lines as indicated by spectral simulations (Figure 3.18 Table 3.3, SI). Simulations of the  $B_{xy1}$  line indicate that two  $S = 1$  species are present at  $p/p_0 = 0.19$ . At a similar relative pressure, a sudden flattening of the sorption isotherm at  $T = 165$  K[3] indicates a phase transition from the *op* to the *cp* phase. Thus, we tentatively assign the mentioned spectral changes to a structural phase transition from the *op* to the *cp* phase and assign the  $S = 1$  signals at  $p/p_0 = 0.19$  to two PW species  $X_{cp1}$  and  $X_{cp2}$ , of the *cp* phase. However, we cannot entirely exclude their assignment to two distinct structural phases different to the *op* phase, which coexist in the respective pressure range. This point is further explained in the discussion section. The spectra measured at  $p/p_0 = 0.28$  and  $p/p_0 = 0.38$  (Figure 3.20, SI) show  $S = 1$  signals similar to the signals at  $p/p_0 = 0.19$  with  $B_{xy1}$  transitions shifted only slightly to lower fields and  $B_{z1}$  and  $B_{z2}$  transitions with blurred or split HF lines. Thus, we assign these signals to species  $X_{cp1}$  and  $X_{cp2}$ , which is consistent to the observation that the sorption isotherm at  $T = 165$  K indicates the presence of the *cp* phase at those relative pressures[3]. At  $p/p_0 = 0.50$  and  $p/p_0 = 0.63$  a third  $S = 1$  signal with larger  $D$  parameter superimposes with the signals assigned to species  $X_{cp1}$  and  $X_{cp2}$ .

Its  $D$  parameter is somewhat larger than those of species  $X_{op}$  continuing the increase of  $D$  with growing xenon pressure as observed for species  $X_{op}$  at pressures  $p/p_0 \leq 0.10$ . We therefore assign that third  $S = 1$  signal likewise to species  $X_{op}$ . The sorption isotherm at  $T = 165$  K indicates a  $cp$  to  $op$  phase transition at similar relative pressures[3], which supports our EPR-derived observation of a coexistence of the  $cp$  and  $op$  phase at  $p/p_0 = 0.50$  and  $p/p_0 = 0.63$ . Consistently, at  $p/p_0 \geq 0.78$  only one  $S = 1$  signal is observed with same  $D$  parameter like  $X_{op}$  at  $p/p_0 = 0.63$  has. And whereas at  $p/p_0 = 0.50$  the HF lines of the  $B_{z1}$  and  $B_{z2}$  transitions are split and blurred, at pressures  $p/p_0 \geq 0.63$  those lines resolve clearly the dominant contribution of a single  $S = 1$  species, namely  $X_{op}$ . This justifies the only presence of the  $op$  phase with a single PW species  $X_{op}$  at the high pressure end of the adsorption branch.

For the same reasons as discussed for the adsorption branch, we assign the  $S = 1$  signals observed during desorption at pressures  $p/p_0 \geq 0.33$  to the single PW species  $X_{op}$ . In particular, the  $B_{z1}$  and  $B_{z2}$  lines resolve the dominant contribution of only one PW species (Figure 3.20b and d, SI). At  $p/p_0 = 0.30$  and  $p/p_0 = 0.27$ , the  $B_{xy1}$  transitions indicate the presence of three species again, and consistently, the  $B_{z1}$  and  $B_{z2}$  transitions show split and blurred HF lines. The two additional species have similar  $D$  parameters, like  $X_{cp1}$  and  $X_{cp2}$ . Since the sorption isotherm at  $T = 165$  K indicates the  $op$  to  $cp$  transition at similar relative pressures[3], we interpret the  $S = 1$  signals at those pressure as a superposition of signals of the species  $X_{op}$ ,  $X_{cp1}$  and  $X_{cp2}$ . Consistently at lower pressures, the signal of species  $X_{op}$  has vanished, indicating the presence of the  $cp$  phase only. At lowest pressures  $p/p_0 \leq 0.01$ , the  $B_{xy1}$  transition shows the typical shape of a single  $S = 1$  species and the  $B_{z1}$  transition indicates contribution of only one species. We therefore tentatively assign the  $S = 1$  signals at those pressures to a single PW species  $X_{cp}$  of the  $cp$  phase. Experiences with other gases show that the MOF stays in the  $cp$  phase at the end of the full ad/desorption cycle and the xenon sorption isotherm shows no indication for another desorption triggered phase transition after the MOF has transformed from the  $op$  to the  $cp$  phase[2, 3]. We like to add that the HF lines at the  $B_{z2}$  transition at 570 mT are only poorly resolved at  $p/p_0 \leq 0.01$  (Figure 3.20f, SI) indicating some  $D$ -strain effects for the final  $cp$  phase.

Similar reasons explain our interpretation of the second ad/desorption cycle starting with the  $cp$  phase instead of the  $op$  phase of a virgin sample as described above. No- $op$  to  $cp$  transition is expected during adsorption up to  $p/p_0 < 0.51$ [16, 23], and consequently, the *in situ* EPR spectra do not indicate any adsorption-triggered structural transition within this pressure range but only the presence of the species  $X_{cp1}$  and  $X_{cp2}$  (Figure 3.4b). However, the  $cp$  to  $op$  transition occurs here at almost the same pressures  $p/p_0 = 0.51$ , in comparison with the first cycle. In addition, the *in situ* EPR spectra reveal a very similar behavior during the remaining second ad/desorption cycle as

observed for the virgin state sample (Figures 3.17 in SI).

Polyukhov *et al.*[23] reported *in situ* EPR investigations of DUT-49(Cu) similar to the xenon sorption study in the present work but with other gases, namely n-butane and diethyl ether at 298 K. They reported that the ZFS parameter  $D$  of PWs in the *op* phase of DUT-49(Cu) is smaller than for PWs in the *cp* phase during n-butane and diethyl ether sorption. This result contrasts with our interpretation of the xenon data, where  $D$  is larger for PWs in the *op* phase than for PWs in the *cp* phase. Therefore, we sought further experimental evidence to support the above explanation for the xenon *in situ* EPR data. Unfortunately, direct monitoring of phase transitions by *in situ* PXRD studies on xenon-loaded DUT-49(Cu) is not possible because of the large absorption coefficient of xenon at available X-ray energies. This leads to strong attenuation of the X-ray beams preventing the measurement of meaningful diffraction patterns. The contraction of DUT-49(Cu) to the *cp* phase could be proved by *in situ* PXRD after desorption of the majority of xenon molecules from the pores[16]. Thus, we were searching for a gas for which both *in situ* EPR and *in situ* PXRD measurements are possible and which, contrarily to n-butane and diethyl ether, has a similar vapor pressure like xenon at temperatures  $T \approx 160$  K[36]. We identified ethylene as an appropriate gas and conducted additional *in situ* EPR and *in situ* PXRD measurements during ethylene ad/desorption on DUT-49(Cu). The corresponding results are going to be reported in the next section.

The *in situ* EPR spectra of the monomeric Cu(II) species M having  $S = 1/2$  have been likewise analyzed (Figure 3.28, SI). Their spectral simulations do not show significant changes of the cupric ion spin Hamiltonian parameters during xenon sorption (Table 3.5, SI).

### 3.3.2 *In situ* EPR in parallel to ethylene sorption

EPR spectra of DUT-49(Cu) were measured *in situ* while exposing the MOF to ethylene at distinct gas pressures. First, the ethylene adsorption was studied by increasing the ethylene pressure stepwise at  $T = 165(1)$  K. Subsequently, the ethylene desorption was studied by *in situ* EPR, decreasing the ethylene pressure back to the application of dynamic vacuum at the same temperature. Selected EPR spectra measured during this ad/desorption cycle are shown in Figure 3.6. In contrast to the xenon data, almost all experimental EPR spectra can be understood by a contribution of a single  $S = 1$  signal. The  $B_{z1}$  and  $B_{z2}$  transitions show resolved HF lines at almost all pressures indicating the only contribution of one single  $S = 1$  species (Figure 3.23, SI). Exceptions occur during the *op* to *cp* transition during desorption and at pressures  $p/p_0 < 0.07$  (Figure 3.6b) in the desorption branch, the corresponding HF lines become broadened and blurred. We interpret this again as a coexistence of the *op* and *cp* phases for  $p/p_0 = 0.20$  and the occurrence of some  $D$ -strain for

$p/p_0 < 0.07$ , but not as the presence of more than one species within one structural phase of DUT-49(Cu). As shown in Figure 3.23, The EPR signature of the  $B_{xy1}$  transition varies with changing ethylene pressure.

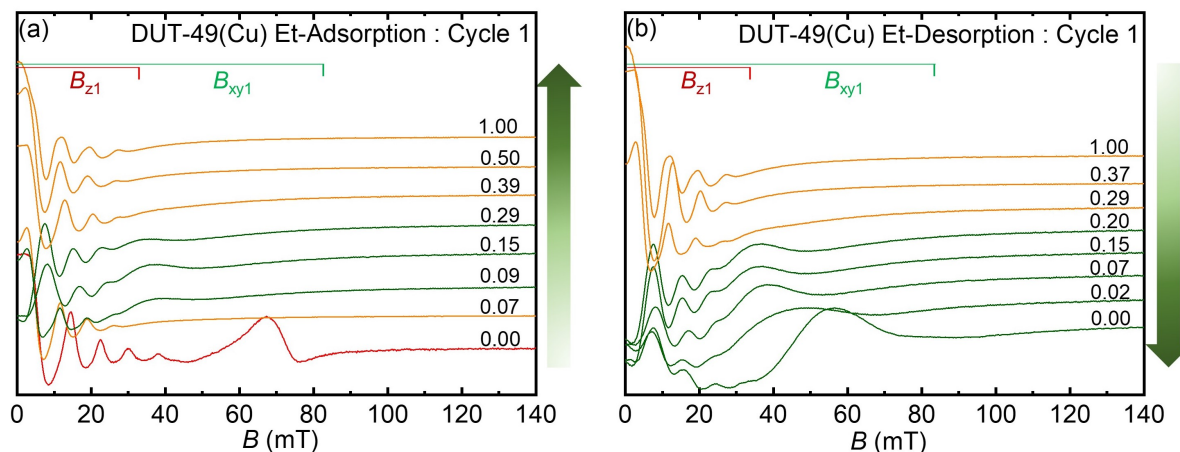


FIGURE 3.6: The low field part of the *in situ* EPR spectra of the  $S = 1$  state of the Cu(II) - Cu(II) dimers in DUT-49(Cu) during (a) ethylene adsorption and (b) ethylene desorption at 165 K temperature in a first cycle starting with an activated sample (red). The EPR spectra are labelled with the relative ethylene pressures  $p/p_0$  ( $p = 82$  kPa). Orange spectra indicate the dominant presence of the *op* phase, green spectra that of the *cp* phase, and the red spectrum corresponds to the *op* phase of the gas-free activated sample.

In some pressure regions, the  $B_{xy1}$  transition is visible, allowing the determination of the  $D$  parameter from its field position as described in the previous sections. However, in some pressure regions, the  $B_{xy1}$  transition is not visible anymore, indicating correspondingly high  $D$  parameters ( $D > 9400$  MHz). Nevertheless, the magnitude of  $D$  in these cases can still be determined from the field position of the  $B_{z1}$  transition within some experimental error. The experimentally derived pressure dependency of  $D$  over the entire ad/desorption cycle is shown in Figure 3.7. As in the previous case of Xe sorption, the identification of various copper PW species with distinct  $D$  parameters in the *in situ* EPR spectra during ethylene adsorption and desorption allows us to draw a conclusion about the phase composition of the MOF at a certain gas pressure (Figure 3.5b). The adsorption/desorption cycle starts with the activated DUT-49(Cu) under a dynamic vacuum. Here the material is expected to be in its *op* phase.

The corresponding EPR spectrum shows a single  $S = 1$  signal which we assign again to a species  $A_{op}$  of PWs in the activated *op* phase. Its EPR signal shows the  $B_{xy1}$  transition since it has a ZFS parameter  $D = 8965(10)$  MHz. After a slight increase in the ethylene pressure to  $p/p_0 = 0.0022$ , the EPR spectrum had changed significantly and showed a single  $S = 1$  signal in which the  $B_{xy1}$  transition has vanished due to an increase of the  $D$  parameter (Figure 3.23, SI). However, according to the *in situ* PXRD results and the sorption isotherm explained below, we assign this signal to the PW species  $E_{op}$  of the ethylene-loaded *op* phase. We propose to interpret this huge



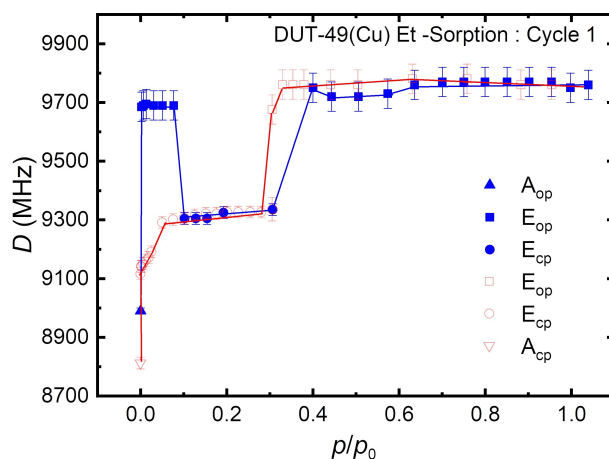


FIGURE 3.7: ZFS parameter  $D$  of the  $S = 1$  state of the PW species  $A_{op}$  and  $A_{cp}$  (triangles), as well as  $E_{op}$  (squares) and  $E_{cp}$  (circles), determined at different relative pressures  $p/p_0$  ( $p_0=82$ ) by *in situ* EPR on DUT-49(Cu) during ethylene adsorption (blue) and subsequent desorption (red) at the temperature  $T = 165$  K. Lines are added as a guide for the eyes. (closed symbols adsorption, opened symbols desorption)

change of  $D$  at such small ethylene pressures as the first evidence for immediate chemisorption of ethylene at the open coordination sites of the Cu(II) ions in the PW units. According to the sorption isotherm discussed below (Figures 3.10b and d), at  $p/p_0 = 0.0025$  the amount of adsorbed ethylene in DUT-49(Cu) is 3.4  $C_2H_4$  molecules per Cu-PW, which is sufficient for an occupation of each coordinative unsaturated metal site (CUS) with a single ethylene molecule. The changes in the  $g_z$  parameter further support this interpretation, as explained below. Increasing the pressure further in the adsorption branch up to  $p/p_0 = 0.07$ , no significant spectral changes are observed (Figure 3.23, SI). Only the  $S = 1$  species  $E_{op}$  contributes to the spectra in this pressure range. At the next pressure  $p/p_0 = 0.09$ , the EPR spectrum has changed significantly. It shows the signal of a single  $S = 1$  species  $E_{cp}$  but with a significantly decreased  $D$  value. In accordance with the sorption isotherm (Figure 3.10b) and the results of the *in situ* PXRD measurements explained below, we interpret this spectral change as the occurrence of the *op* to *cp* phase transition at pressures  $0.07 < p/p_0 < 0.09$  and assign species  $E_{cp}$  to PWs in the ethylene-loaded *cp* phase. In the pressure range  $0.09 \leq p/p_0 \leq 0.31$  the MOF remains in the *cp* phase since, with increasing pressure, the EPR spectra show only small spectral changes of the single  $S = 1$  species  $E_{cp}$ . We explain the sudden change in the EPR spectrum at  $p/p_0 = 0.39$ , indicating an increase of the parameter  $D$  again, with the occurrence of the *cp* to *op* transition in the range  $0.31 < p/p_0 < 0.40$  and assign the single  $S = 1$  species observed at  $p/p_0 = 0.40$  to  $E_{op}$ . Only the signal of this species  $E_{op}$  is observed in the EPR spectrum up to the highest pressure close to condensation without significant spectral changes, showing that DUT-49(Cu) remains in the *op* phase, which is further supported by the sorption isotherm and the *in situ* PXRD results presented below.

During the subsequent decrease of the ethylene pressure, the EPR spectra show only the signal of species  $E_{op}$  up to  $p/p_0 = 0.33$ . In particular, no line of the  $B_{xy1}$  transition is observed at those pressures due to the large  $D$  parameter of species  $E_{op}$  (Figure 3.7). At  $p/p_0 = 0.31$ , a less intense line of the  $B_{xy1}$  transition occurs (Figure 3.23b, SI). The size of its  $D$  parameter suggests its assignment to species  $E_{cp}$ , indicating the onset of the structural  $op$  to  $cp$  transition in accordance with the sorption isotherm and *in situ* PXRD experiments, as explained below. However, the shape of the  $B_{z1}$  transition (Figure 3.23b, SI) still indicates the presence of species  $E_{op}$  indicating the coexistence of the  $op$  and  $cp$  phase at  $p/p_0 = 0.30$ . The EPR spectra measured at pressures  $p/p_0 < 0.30$  show only one  $S = 1$  signal. According to its  $D$  parameter, we assign it to species  $E_{cp}$ , which indicates that the MOF stays in the  $cp$  phase at low pressures. But, under dynamic vacuum conditions, the EPR signal of species  $E_{cp}$  does not coincide with that of species  $X_{cp}$  measured under the same conditions after the first and second xenon ad/desorption cycles (Figure 3.3). This indicates a stronger binding of the ethylene molecules to the MOF surface. To verify this hypothesis, the valve to the pump was closed, and the temperature was increased to  $T = 215$  K after the full ethylene ad/desorption cycle. Indeed, a significant increase in pressure was observed at that temperature, indicating the desorption of remaining ethylene from the MOF. Next, the valve to the pump was opened, and the material was activated under those conditions for a few minutes. Then, the sample was cooled back to  $T = 165$  K, and a second *in situ* EPR spectrum was measured under dynamic vacuum conditions. Now, it shows the EPR signal of a single  $S = 1$  species  $A_{cp}$ , which coincides with that of species  $X_{cp}$  under dynamic vacuum conditions (Figure 3.3b). This indicates that both species can be assigned to PWs in the activated  $cp$  phase of DUT-49(Cu).

As explained above, during ethylene adsorption, a more significant increase in the  $D$  parameter was observed at small pressures ( $p/p_0 = 0.0022$ ) compared to the xenon adsorption experiments. Furthermore, after the full ethylene ad/desorption cycle, the sample had to be activated at a higher temperature to remove the remaining ethylene from the MOF, preparing species  $A_{cp}$  of the  $cp$  phase. However, no further activation was necessary to obtain an EPR spectrum identical to that of species  $A_{cp}$  after the xenon ad/desorption cycle. These results indicate a considerably stronger interaction of the MOF framework with the ethylene than with the xenon molecules. The question is if the EPR results can reveal the interaction site of the ethylene molecules with the DUT-49 framework. The immediate jump of the ZFS parameter  $D$  at low pressures during the ethylene adsorption (Figure 3.7) might indicate direct adsorption of ethylene at the CUS site of the cupric ions in the PW units. However, the  $D$  parameter increased at small pressures also during the xenon adsorption, although not as much and as abruptly. The ZFS parameter  $D$  depends on the dipolar and exchange interaction between both Cu(II) ions of the PW[23], preventing a simple

correlation of its magnitude with the geometry of the PW units and the coordination environment of their Cu(II) ions. This is different for the principal values of the Cu(II)  $g$ - and HF tensors. It is known for Cu(II) ions that the size of the  $g_z$  and  $A_z$  parameters roughly correlate with the symmetry of the Cu(II) coordination environment[37, 38].

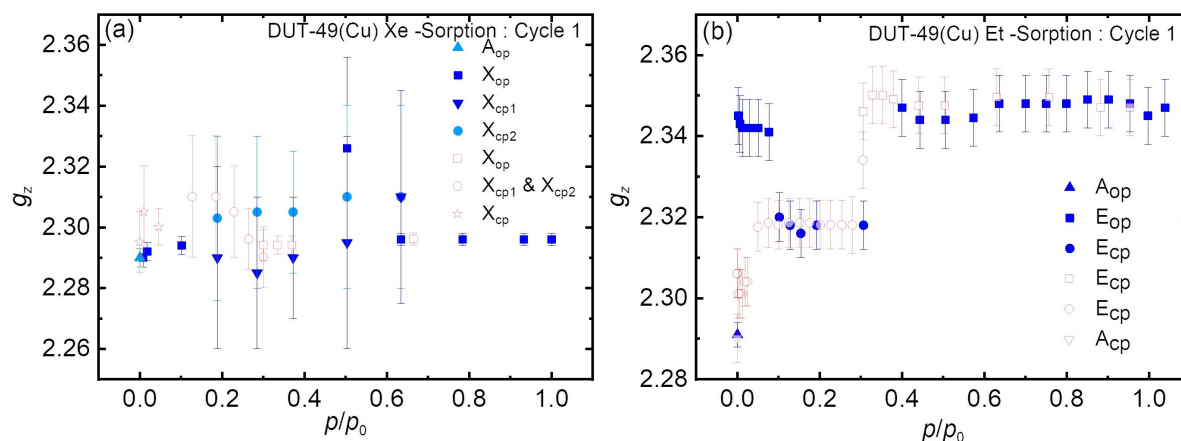


FIGURE 3.8: Parameter  $g_z$  of the  $S = 1$  state of different PW species (labels defined in the legends) as determined by *in situ* EPR for a) the first xenon ad/desorption cycle and b) the ethylene ad/desorption cycle. Note that in a) during adsorption, the values for  $X_{cp1}$  and  $X_{cp2}$  have large errors due to the huge systematic error which arises from an interpretation of the single line of the  $B_{z2}$  transition by a superposition of  $X_{cp1}$ ,  $X_{cp2}$ , and for some pressures, even  $X_{op}$ . During desorption in a), the  $B_{z2}$  line was simulated by a single  $S = 1$  species with the  $D$  parameter of species  $X_{cp1}$  and the  $g_z$  parameter was determined in that way. (closed symbols adsorption, opened symbols desorption)

If one assumes that both  $g$ - and HF-tensors of the monomeric Cu(II) ions are coaxial with identical principal values, the  $g$ -tensor of the  $S = 1$  state formed by both Cu(II) ions in a PW is equal to each of the monomeric  $g$ -tensors, whereas the HF tensor of the  $S = 1$  state is exactly half the size of the each monomeric HF tensor in case of strong isotropic exchange[39]. The dependence of the  $g_z$  parameter of the  $S = 1$  state of the Cu(II) - Cu(II) dimers in the PW units on the pressure during ethylene ad/desorption is shown in Figure 3.8 and compared with the  $g_z$  dependence on the pressure in the first xenon ad/desorption cycle. Corresponding figures for  $g_{x,y}$  and for  $A_z$  can be found in the SI (Figures 3.24 and 3.25). Species  $A_{op}$ , as well as species  $A_{cp}$ , have parameters  $g_z \approx 2.28$  and  $A_z \approx 260$  MHz, which is typical for square planar coordination of the monomeric Cu(II) ions[30, 31, 37, 40]. This is in line with the expected coordination geometry of the Cu(II) ions in the activated material, where no molecules bind axially to the Cu(II) ions. During the full xenon ad/desorption cycle, the corresponding  $g_z$  and  $A_z$  parameters do not change significantly, indicating any significant interaction of the xenon molecules with the CUS of the Cu(II) ions. In contrast to that, the corresponding values adopt  $2.35 > g_z > 2.30$  and  $210 \text{ MHz} < A_z < 250 \text{ MHz}$  for PW species in the ethylene loaded DUT-49(Cu) (Figures 3.21b and 3.25b, SI). Those values are typical for a square pyramidal symmetry of the Cu(II) coordination environment[30, 31, 37, 40, 41]

and give direct evidence for the coordination of the adsorbed ethylene molecules at the Cu(II) via their axial CUS as already reported for CuZn PW units in HKUST-1[42, 43].

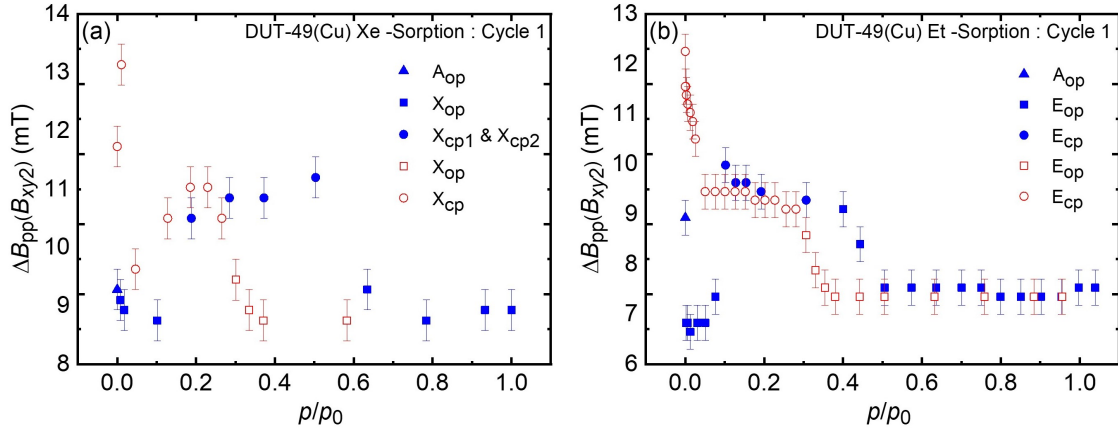


FIGURE 3.9: Peak-to-peak line width  $\Delta B_{pp}(B_{xy2})$  of the  $S = 1$  state of the Cu(II) - Cu(II) dimers as determined during a) the first xenon ad/desorption cycle and b) the ethylene ad/desorption cycle from the *in situ* EPR spectra. (closed symbols adsorption, opened symbols desorption)

We further want to comment on the peak-to-peak line width  $\Delta B_{pp}(B_{xy2})$  of the  $B_{xy2}$  transition, whose size might reflect the degree of structural disorder. Figure 3.9 compares again  $\Delta B_{pp}(B_{xy2})$  measured during ethylene sorption with the corresponding line widths measured in the xenon sorption *in situ* EPR experiments. We define this line width as the difference of the magnetic field positions, where the amplitude of the signal of the  $B_{xy2}$  transition adopts its minimum and maximum in a respective experimental EPR spectrum. We have chosen this line width parameter as a measure for the disorder since, among all line width parameters, it is best defined and can be easily extracted from the experimental EPR spectra with reasonable accuracy. Within the same ad/desorption cycle  $\Delta B_{pp}(B_{xy2})$  is smaller in the  $op$  phases than in the  $cp$  phase, indicating a higher degree of order in the  $op$  phase. Furthermore,  $\Delta B_{pp}(B_{xy2})$  is systematically smaller in the ethylene samples than in the xenon-loaded samples, indicating that xenon adsorption leads likewise to a higher degree of disorder than ethylene adsorption.  $\Delta B_{pp}(B_{xy2})$  is the smallest for the ethylene-loaded  $op$  phase. Even the activated  $op$  phase has a larger  $\Delta B_{pp}(B_{xy2})$ . This indicates that the adsorption of ethylene increases the order of the local environment of the PW units in the  $op$  phase.  $\Delta B_{pp}(B_{xy2})$  is highest during the desorption of xenon or ethylene in the  $cp$  phase, indicating that a small amount of xenon or ethylene in the  $cp$  phase leads to a higher degree of disorder in the framework.

Finally, *in situ* EPR spectra of the  $S = 1/2$  Cu(II) monomer species M were likewise investigated for the ethylene sorption cycles (Figure 3.27, SI). As in the xenon sorption experiments, spectral simulations (Figure 3.28b, SI) do not indicate any changes in its spin Hamiltonian parameters

during ethylene adsorption and desorption.

### 3.4 *In situ* PXRD in parallel to ethylene sorption at 165 K

In order to confirm the findings observed in *in situ* EPR experiments, adsorption and desorption of ethylene at 165 K were followed by PXRD (Figure 3.10)[1].

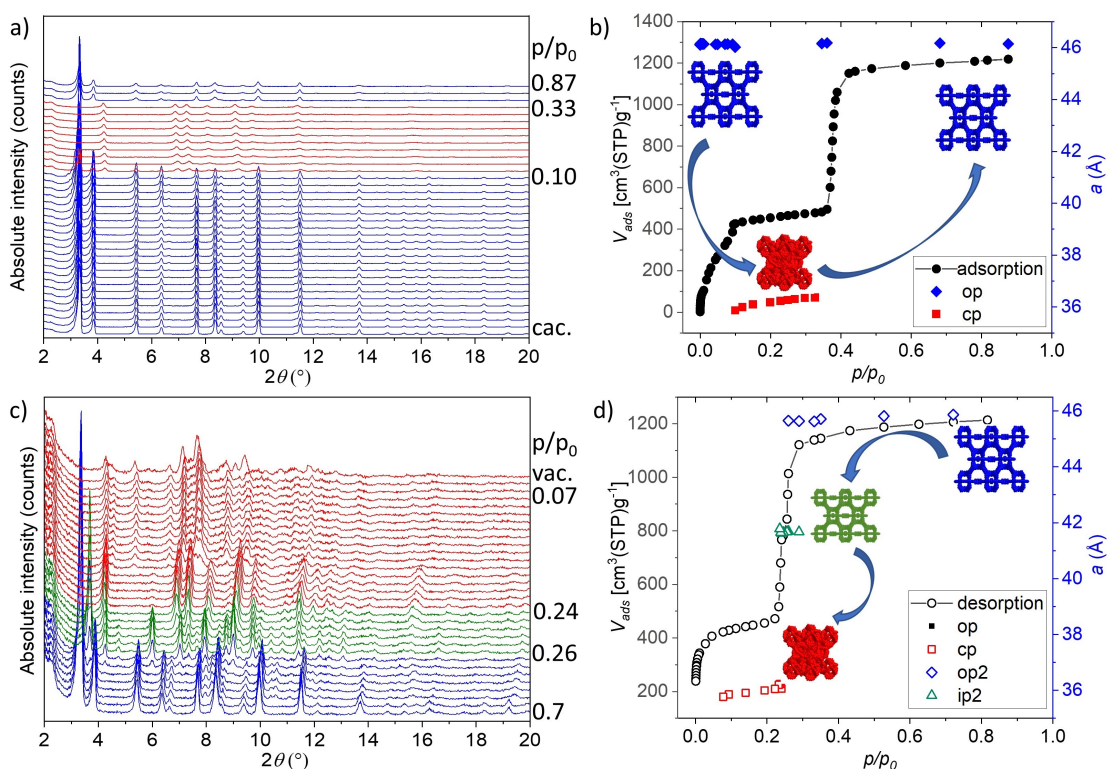


FIGURE 3.10: (a,c) PXRD patterns were measured in parallel to (b) adsorption and (d) desorption of ethylene on DUT-49(Cu). The right axis shows the evolution of unit cell parameter  $a$ , and the inset visualizes the structural transformations in the system.

The analysis of the low-pressure range  $p/p_0 < 0.095$  of the adsorption branch indicates no structural transitions showing the characteristic PXRD patterns of the *op* phase in all cases (Figure 3.10a, PXRDs 1-23). PXRDs measured in the pressure range  $p/p_0 = 0.095 - 0.36$  and, as expected, indicating the presence of the *cp* phase. PXRD patterns at higher pressures suggest the reopening of the structure. No NGA could be observed in the adsorption experiment, which is consistent with empirical correlations, predicting for ethylene the lowest NGA temperature of  $T = 177$  K[3]. The desorption of the ethylene shows the reverse transition to the *cp* phase (Figure 3.10(c,d)). However, surprisingly, a detailed analysis of PXRD patterns (between  $p/p_0 = 0.6 - 0.3$  during desorption) indicates the presence of an unknown phase, which was not observed in earlier studies. Indexing these PXRDs results in the cubic space group with an axis length of 41.66 - 41.78 Å, which

### 3.4. *In situ* PXRD in parallel to ethylene sorption at 165 K

indicates an intermediate phase (*ip*). All earlier observed intermediate phases show a cubic unit cell with a minimal axis length of 43.0 Å.

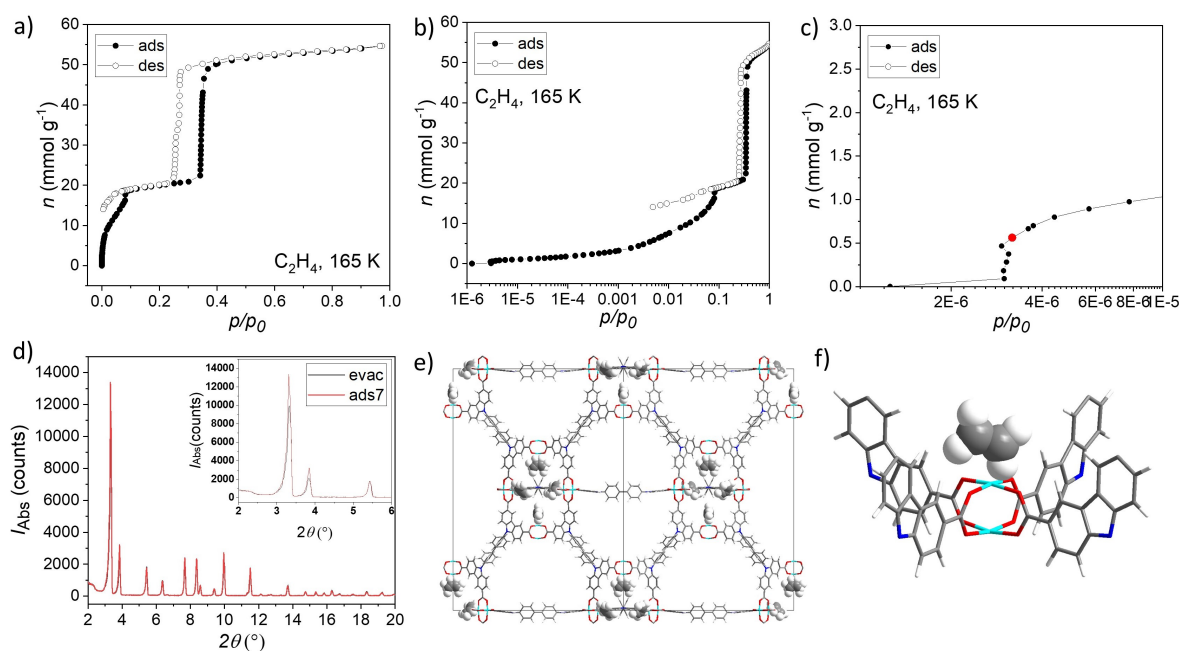


FIGURE 3.11: Adsorption and desorption isotherms of ethylene on DUT-49(Cu) at  $T = 165$  K, shown at a (a) linear and (b) logarithmic pressure scale. Zoomed low-pressure range of the (c) adsorption isotherm and the (d) PXRD patterns measured on DUT-49(Cu) sample in vacuum (black) and adsorption point 7 (red). PW unit (e) and projection of unit cell along (110) direction (f) showing the adsorption sites of ethylene molecules.

This fact indicates that ethylene guest molecules show a stronger interaction with the framework and induce an extra local minimum in the free energy profile of the system. The *ip* phase could not be captured by *in situ* EPR experiments either because of a very similar local environment of Cu-PW or because of the narrow pressure range in which *ip* phase can be captured. PXRD patterns below  $p/p_0 = 0.24$  during desorption indicate the presence of the *cp* phase and are in line with *in situ* EPR observations. Apart from the *ip* phase, the behavior of DUT-49(Cu) upon ethylene physisorption in terms of phase transitions is comparable with the physisorption of other fluids close to the standard boiling point[2].

In order to prove the observation obtained by *in situ* EPR and point out the chemisorption of ethylene at low loadings, the low-pressure region of the ethylene isotherm and corresponding PXRD patterns were analyzed in detail (Figure 3.11). Detailed analysis of the low-pressure range of the adsorption isotherm of ethylene at  $T = 165$  K (Figure 3.11c) indicates the pronounced steep step at  $p/p_0 = 3 \times 10^{-6}$ . Since no phase transition was observed in the PXRD patterns measured in this range, the step could be associated with the chemisorption of ethylene on Cu-PW, as suggested by the *in situ* EPR results. In order to prove this hypothesis, the PXRD pattern, measured

at  $p/p_0 = 3.2 \times 10^{-6}$  and a loading of  $0.56 \text{ mmol g}^{-1}$  ( $0.5 \text{ C}_2\text{H}_4$  per Cu-PW), was analyzed in detail (Figure 3.11d). The visual comparison of PXRD patterns, measured in a dynamic vacuum and point 7 of the isotherm, indicates significant differences in intensities. Rietveld refinement of PXRD allowed to locate one of the ethylene molecules inside the pores, resulting in the preferable adsorption site, close to the copper atom, located on the inner side of the metal-organic polyhedra (Figure 3.11(d e)). The distance of  $2.38 \text{ \AA}$ , measured between the copper atom and the dummy point between the carbon atoms in ethylene, confirms the chemisorption of the fluid proposed by *in situ* EPR.

### 3.5 Discussions

The presented results clearly show the occurrence of characteristic  $op \leftrightarrow cp$  transitions of DUT-49(Cu) during xenon (157(2) K) and ethylene (165 K) sorption. This is an expected result since equivalent transitions of this material were observed in earlier studies upon the adsorption of other gases, including xenon[3, 7]. Starting in the  $op$  phase after activation, the MOF contracts to the  $cp$  phase upon initial adsorption of xenon or ethylene and reopens back to the  $op$  phase at the threshold pressure. During successive desorption of xenon, only one phase transition from the  $op$  phase to the  $cp$  phase is observed, and the MOF stays in the  $cp$  phase under dynamic vacuum conditions. In the case of ethylene, an intermediate pore phase with quite a small unit cell volume of  $72300 \text{ \AA}^3$  was observed for the first time in PXRD patterns, measured in the desorption branch of ethylene isotherm. For comparison, methane desorption at 111 K leads to the formation of the intermediate phase with a unit cell volume of  $84400 \text{ \AA}^3$ [2]. Furthermore, for both gases, we did not observe any indications of NGA during adsorption at the above-mentioned temperatures, which is in line with earlier studies[2].<sup>26</sup> However, the present study reveals some additional new insights, which are discussed in the following in more detail.

The  $op \leftrightarrow cp$  transitions of DUT-49(Cu) during xenon sorption were already observed earlier by sorption isotherms at  $T = 165 \text{ K}$ [3]. However, up to now, the structural details of the respective xenon loaded phases have not been fully characterized due to the strong absorption of X-rays by the xenon molecules preventing the determination of the corresponding crystal structures by *in situ* X-ray diffraction experiments[16]. The present *in situ* EPR study cannot reveal all structural details of the xenon-loaded phases, but it can probe the local coordination environment of the copper PWs via their magnetic signature. For a complete structural characterization of the xenon-loaded DUT-49(Cu), we suggest corresponding neutron diffraction experiments. However, the present EPR study discovered already an unexpected occurrence of two PW species  $X_{cp1}$  and  $X_{cp2}$ ,

during xenon sorption at pressures where the MOF is expected to stay in the *cp* phase. We suggest two interpretations for this observation. Either two different structural xenon-loaded phases of DUT-49(Cu) *cp* with slightly different distortion of the PW unit coexist in the respective pressure ranges, or alternatively, DUT-49(Cu) adopts one single xenon loaded *cp* phase, but with a larger unit cell which contains two chemically different PW species  $X_{cp1}$  and  $X_{cp2}$ . Although we cannot judge without any doubt, which interpretation is correct, we suggest that the second of both is more likely for the following reasons: As verified by spectral simulations of the corresponding EPR spectra, the relative ratio of the amount of both PW species  $X_{cp1}$  and  $X_{cp2}$  is roughly one to one (1.5(10):1) as one would expect when two different kind of PW species are contained in the unit cell of one single *cp* phase. In case two different phases exist in the pressure ranges where the *cp* phase is presumed, one might expect that their relative ratio varies significantly with varying xenon pressure. But there is no indication of such behavior since the EPR signals show at all corresponding pressures roughly the same constant ratio of  $X_{cp1}$  and  $X_{cp2}$ . Furthermore, at the lowest xenon pressure, only one *cp* PW species ( $p/p_0 = 0.011$ , see Table S2 and Figure 3.20b, ESI)  $X_{cp}$  occurs suddenly upon a small pressure drop, without any preliminary decrease of the intensity of the EPR signal of one of both species  $X_{cp1}$  and  $X_{cp2}$ , which one might expect if one of two phases vanishes upon xenon desorption as it is likewise observed during the *op*  $\leftrightarrow$  *cp* transitions. But this transition from two to one PW species at the lowest pressures can be easily understood if the full xenon-loaded *cp* phase has two chemically non-equivalent PW species in its unit cell. In this case, at some pressure, the structure must change to a state with one PW in its unit cell upon xenon desorption since it is known from XRD characterization that the guest-free *cp* phase of DUT-49(Cu) has only one PW species in its unit cell[2]. A structure of the *cp* phase with two different PW species in its unit cell has never been observed for DUT-49(Cu) to the best of our knowledge. The fact that it occurs after xenon loading might be related to a large number of electrons of the xenon molecule, which might lead to significant dispersion interactions between xenon and the MOF surface, uniquely altering its structure[17]. Also, hydrogen bonds between xenon and protons of the MOF framework might play a role in this context[17]. The fact that xenon alters the structure of the MOF significantly is already indicated by the distinct increase of the ZFS parameter  $D$  of the *op* phase during xenon adsorption at the first and small pressure step  $p/p_0 = 0.01$  during adsorption. But we must admit that possibly the EPR detected ZFS parameter  $D$  is highly sensitive to structural details due to the contributing anisotropic exchange and dipolar interaction ( $D_{dip} \propto 1/R^3$ , where  $R$  is the distance between Cu(II)-Cu(II) ions[23, 44]), which cannot be resolved by X-ray diffraction methods. It might be possible that two PW species in the unit cell of the *cp* phase do also occur after the adsorption of other gases, which has not been discovered



yet since the corresponding structural differences are too small to be resolved by X-ray diffraction. Still, even within the sensitivity of EPR, the *cp* phase of the ethylene-loaded DUT-49(Cu) has only one PW species in the unit cell in accordance with the PXRD results, as reported in the present study. And also, Polyukhov *et al*[23]. observed by *in situ* EPR only one PW species for the *cp* phase upon the adsorption of diethyl ether and n-butane adsorption at room temperature, indicating that the interaction of xenon with the surface of DUT-49(Cu) at 157(2) K is unique, indeed, compared to the interaction of other adsorbed gases with the MOF surface.

The observed opposite changes of the *D* parameter during the *op*  $\leftrightarrow$  *cp* phase transformation observed in the presence of diethyl ether and n-butane in ref[23]. versus xenon and ethylene adsorption experiments (this work) might be related to the different natures of the gases and their unique interaction with the MOF framework. But this might also be associated with the different temperature regimes. A detailed understanding of this issue is complicated by the fact that anisotropic magnetic exchange interaction between both Cu(II) ions in the PW units contributes significantly to the ZFS parameter *D* in addition to their dipolar interaction[23]. Whereas the dipolar interaction can be directly related to the distance between both Cu(II) ions[23], a correlation of the anisotropic exchange interaction with structural details is considerably more complicated since this interaction is determined by the overlap of various orbitals involved in the chemical bonds bridging both Cu(II) ions[44]. A corresponding detailed analysis, which certainly has to include first principle quantum chemical calculations, goes beyond the scope of the present experimentally focused study. We like to note that quantum chemical calculations of the ZFS parameters of copper PWs or related structural motifs with cupric ion pairs are very rare so far[45, 46]. Maurice *et al.*[46] demonstrated for a single Cu PW system that advanced quantum chemical approaches such as complete active space self-consistent field (CASSCF) and post CASSCF methods can provide ZFS parameters with only 5 % deviation from the experimental data that is already in the range of the changes of the *D* parameter observed in our sorption experiments. However, more systematic studies comparing experimental and computed ZFS parameters for various structures containing Cu PWs are desirable in order to derive reliable structural parameters from the measured *D* parameters.

We believe that this difference between our study and that of Polyukhov *et al.*[23] cannot be simply explained by the strength of the interaction of the respective gas with the CUS of the copper PW units. Polyukhov *et al.*[23] observed the same relative size of the *D* parameters of the *op* and *cp* phase for both n-butane and diethyl ether adsorption, although they report strong chemisorption for diethyl ether and weak physisorption for n-butane. The same qualitative behavior is reported in the present study. As we have shown in the result section, ethylene strongly binds to the CUS

of the PW units, whereas xenon does not strongly interact with these sites. However, as in the study of Polyukhov *et al.*[23], the order of magnitude of the  $D$  parameters of PWs in the *op* and *cp* phases is for both gases the same. We, therefore, suppose that the reported differences of the  $D$  parameters between our study and the study of Polyukhov *et al.*[23] is most likely related to the different temperature regimes, which modulate the response of the MOF framework to the gas adsorption in distinct and different ways. We suggest further *in situ* EPR experiments with other gases at different temperatures to explore this question in more detail.

As reported in the result section, ethylene binds strongly to the CUS as verified by large changes of the  $D$  and  $g_z$  parameters after the first and small pressure step during adsorption, by the strong gas uptake at the smallest ethylene pressures observed in the sorption isotherm and by the observation that ethylene remains adsorbed in the MOF at  $T = 165$  K after a full ad/desorption cycle. Chemisorption of the ethylene to the open CUS was proved by *in situ* PXRD, indicating the binding distance of 2.38 Å and showing a steep step in the isotherm at very low pressure. Xenon does not interact strongly with the CUS since the  $g_z$  parameters of all PW species of the xenon-loaded phases stay almost constant at values similar to the activated material typical for a square planar coordination environment of the respective Cu(II) ions[41]. Such weak interaction with the CUS is further confirmed by the observation that no additional activation at higher temperature is necessary to obtain the guest-free *cp* phase after a full ad/desorption cycle like it was necessary after the ethylene ad/desorption cycle.

We further observed distinctly different  $g_z$  parameters of the PWs in the ethylene-loaded *cp* and *op* phases. These differences must be related to some changes in the local coordination environment of the respective Cu(II) ions. We argue that these differences are mainly related to differences in the coordination of the ethylene molecules to the Cu(II) ions in the *op* and *cp* phases. Otherwise, if these changes in the  $g_z$  parameters were related to slight variations in the carboxyl group coordination environment of the cupric ions, which in turn mediate alterations of the linker arrangement, we would have expected correspondingly different values for the Cu(II)  $g_z$  values of PWs in the xenon loaded *op* and *cp* phases which we did not observe (Figure 3.8).

As described in the result section, the peak-to-peak line width  $\Delta B_{pp}(B_{xy2})$  of the  $B_{xy2}$  transition indicates a systematically smaller structural disorder in the ethylene-loaded MOF in comparison with the xenon-loaded one (Figure 3.9). This seems reasonable since we expect, upon ethylene loading, a more homogeneous and more defined distribution of adsorption sites of ethylene molecules due to their strong binding at the CUS. In contrast, xenon will exhibit only weak London dispersion (VdW force[18]) interactions[17, 18] with the DUT-49(Cu) framework, and presumably also some hydrogen bonding formation with the organic linker cannot be excluded a priori.[17]

Therefore, we may expect a more inhomogeneous and less defined distribution of adsorption sites for the xenon molecules in DUT-49(Cu) in comparison with the ethylene molecules, which in turn might result in higher structural disorder and consequently explain the larger peak-to-peak line widths of the  $B_{xy2}$  transition of the xenon loaded MOF compared to the ethylene loaded material. The largest line widths of these transitions were observed at the lowest pressures during desorption (Figure 3.9b) which perfectly fits the suggested correlation with the homogeneity of adsorption sites. At full gas loading, the adsorption sites should be occupied with the highest homogeneity because most possible sites are occupied by a gas molecule. But, during desorption at low pressures, some adsorption sites are occupied, some not in an inhomogeneous manner, leading to larger structural disorders. This situation might explain that the largest broadening of the  $B_{xy2}$  transition occurs during desorption at low pressures. The observation that the  $cp$  phase always shows larger values of  $\Delta B_{pp}(B_{xy2})$  than the  $op$  phase (Figure 3.9) might be likewise explained by larger strains in the  $cp$  phase causing larger inhomogeneous distortions of the PW units. A higher disorder of the  $cp$  phase compared to the  $op$  phase was also revealed by PXRD[2].

Besides the typical Cu(II) - Cu(II) PW species, an additional paramagnetic Cu(II) monomer species M with  $S = 1/2$  can be observed in DUT-49(Cu). The  $g_z$  and  $A_z$  parameters for the  $op$  phase of the parent ( $g_z = 2.266(2)$ ,  $A_z = 569(3)$  MHz) and xenon adsorbed ( $g_z = 2.273(2)$ ,  $A_z = 560(3)$  MHz) material differ only slightly and are comparable to those that have been observed for Cu(II) - Zn(II) PW species in activated zinc doped HKUST-1[42, 45]. Therefore we may assign the Cu(II) monomer species M to some defective PW units where for instance, one of the two cupric ions is missing or substituted by a diamagnetic metal ion such as Cu(I). Likewise, the ethylene-filled DUT-49(Cu) leads to values  $g_z = 2.295(3)$ ,  $A_z = 500(8)$  MHz that were also found for ethylene coordinating to the cupric ions of these Cu(II) - Zn(II) PW in HKUST-1[42], indicating once again the coordination of ethylene to Cu(II) in the PW species of DUT-49(Cu). However, the Cu(II) spin Hamiltonian parameters of this defective PW species M are not sensitive to the  $op \leftrightarrow cp$  phase transformations in this MOF induced by either xenon or ethylene. Either the defective PW units are located in a fraction of the MOF material that does not undergo the  $op \leftrightarrow cp$  phase transformations, or the related structural changes in the Cu(II) coordination environment of such defects are just too small in order to change the spin Hamiltonian parameters of the metal ion significantly.

## 3.6 Conclusion

*In situ* EPR spectroscopy can be successfully employed to explore the phase transformations in DUT-49 (Cu) induced by xenon and ethylene adsorption and desorption. EPR, as a local method, detects structural changes of the Cu(II) - Cu(II) PW units of this MOF that are related to its *op*  $\leftrightarrow$  *cp* phase transformation. As previously already discussed by Polyukhov *et al*[23], the major information here is provided by the ZFS of the  $S = 1$  state of the copper dimer in the PW unit. However, its ZFS can be changed either by small structural changes of the PW unit that are caused by the phase transformations of the framework or by coordinating an additional molecule to the cupric ions at their CUS sites, for instance, observed in the case of ethylene adsorption. The same holds for the  $g_z$  principal value of its  $g$ -tensors in cases where the structural changes are sufficiently large, which was again observed for ethylene sorption. Therefore, a reliable interpretation of the local *in situ* EPR data of such copper PW units requires support from additional complementary bulk techniques such as adsorption isotherm measurements and/or *in situ* PXRD. On the other hand, *in situ* EPR proved to be very helpful in cases where PXRD measurements are not feasible and may reveal structural details that are not accessible by adsorption isotherm measurements, as in the case of xenon adsorption/desorption over DUT-49(Cu). Here, the EPR data indicate an enlargement of the unit cell in the *cp* phase with now two chemically different PW species, which occurs in the adsorption as well as desorption branch. The ZFS data reveal different degrees of structural disorder of the framework in dependence on the pore filling of the specific framework phase. A higher degree of structural disorder was observed in the xenon-loaded DUT-49(Cu) in comparison with the ethylene adsorption case, and in general, the *op* phase exhibits a higher degree of order, the latter is supported by *in situ* PXRD experiments during the ethylene sorption process.

Finally, we emphasize that the AFM-coupled copper dimers with the ZFS of their excited  $S = 1$  spin state represent very sensitive magnetic probes for detecting even small structural changes at the PW units of the MOF framework. Therefore, they are suitable probes to explore phase transformations in MOF frameworks having such Cu(II) - Cu(II) PW units on a local scale by EPR spectroscopy as a complementary technique to more conventional methods in this research area, such as diffraction methods and adsorption isotherm measurements. However, the determination of the corresponding specific structural parameters of the PW units, such as bond lengths and angles and their changes which are encoded in the two ZFS parameters  $D$  and  $E$  is a demanding task as the ZFS is determined by a delicate interplay of the dipolar and anisotropic exchange interaction between the two cupric ions. Such a profound analysis of the ZFS data requires advanced

quantum chemical computations and should be the subject of future studies but is beyond this work.

## 3.7 Experimental section

### Synthesis and structural characterization

DUT-49(Cu) was synthesized using an established procedure[4]. The sample was desolvated using a supercritical CO<sub>2</sub> drying protocol using acetone-filled MOF as a starting material. The phase purity of the sample was proven by PXRD (Figure 3.12a, Sec. 3.8). Nitrogen physisorption at 77 K confirmed the desired porosity and flexibility of the sample (Figure 3.12b, Sec. 3.8). SEM images confirmed the average crystallite size of 25  $\mu\text{m}$  (Figure 3.12c, Sec. 3.8).

### Physical methods

Powder X-ray diffraction (PXRD) patterns were collected in transmission geometry on an STOE STADI P diffractometer, equipped with a line focus Cu X-ray tube, operated at 40 kV / 30 mA, and focusing Ge (111) monochromator ( $\lambda = 0.15405$  nm) and MYTHEN (DECTRIS) detector. A scan speed of 120 s/step and a detector step size of  $2\theta = 6$  was used in the measurements.

SEM images of DUT-49 were taken with secondary electrons in a HITACHI SU8020 microscope using 1.0 kV acceleration voltage and 15.2–16.4 mm working distance. The powdered samples were prepared on a sticky carbon sample holder. To avoid degradation upon exposure to air, an inert gas sample holder was used, and the powder was prepared under an argon atmosphere. For crystal size determination, a series of 15 images were recorded.

Volumetric adsorption experiments were carried out on a BELSORP-max instrument (MICROTRAC MRB) using gases of high purity (nitrogen: 99.99%, xenon: 99.95 %, ethylene: 99.9 %). Equilibration conditions for each point were set to 1 % pressure change within 350 s. The dead volume was routinely determined using helium. Liquid nitrogen was used as a coolant for measurements at 77 K.

#### ***In situ* PXRD in parallel to ethylene physisorption at 165 K**

*In situ* PXRD experiments on DUT-49(Cu) in parallel to adsorption and desorption of ethylene at 165 K were conducted using a customized setup based on laboratory powder X-ray diffractometer Empyrean-2 (PANALYTICAL GmbH), equipped with a closed-cycle helium cryostat (ARS DE-102) and home-built X-ray transparent adsorption cell, connected to volumetric adsorption instrument BELSORP-max (Microtrac MRB). The TTL trigger was used to establish the communication between BELSORP-max and Empyrean software and ensure the measurement of the adsorption isotherm and PXRD pattern data collection in a fully automated mode in the pre-defined points of the isotherm. The parallel linear Cu-K $\alpha$ 1 beam, obtained by using a hybrid 2xGe(220) monochromator, 4 mm mask, and primary divergence and secondary anti-scatter slits with 1/4° opening, were used for data collection. A Pixcel-3D detector in 1D scanning mode (255 active channels) was used. The diffraction experiments were performed using  $\omega$ 2 $\theta$  scans in transmission geometry in the range of  $2\theta = 3$ -70°.

#### ***In situ* EPR in parallel to xenon and ethylene physisorption**

All EPR measurements on DUT-49(Cu) were performed using a continuous-wave (CW) BRUKER EMXmicro X-band (9.4 GHz) spectrometer with Oxford instruments ESR900 cryostat. For the preparation of the EPR samples, the activated MOF was transferred under an argon atmosphere in a glove box into an EPR quartz glass tube. The tube was connected to a home-built KF 16 aluminum adapter. After the sample loading, the adapter was closed with a KF 16 blind flange in the glove box, keeping the sample under inert conditions for transport. Via the aluminum adapter, the EPR samples were connected to a home-built gas loading line for *in situ* EPR experiments[28]. At this line, they were activated at 120 °C under dynamic vacuum conditions to remove all adsorbed molecules. The gas pressure for the phase transformation depends on the temperature and the chosen gas. For our EPR experiments, we chose temperatures for *in situ* EPR adsorption experiments at which previous volumetric adsorption experiments exhibit phase transformations and a complete hysteresis for comparison. In addition, our setup for *in situ* EPR experiments is limited to gas pressures  $p \leq 100$  kPa[28]. Based on these limitations and the published volumetric adsorption for Xe and ethylene adsorption over DUT-49(Cu)[3], the following measurement temperatures were selected. The *in situ* EPR sorption measurements were performed for xenon at  $T = 156$  K for cycle 1 and  $T = 158$  K for cycle 2, and for ethylene sorption at  $T = 165(1)$  K (only one cycle). The temperatures were precisely determined by identifying the vapor pressure  $p_0$  during the *in situ* EPR experiments through a pronounced decrease of the pressure due to freezing (xenon) or

condensation (ethylene) of the gas after  $p_0$  was reached[36]. In the case of xenon sorption at  $T = 156$  K (cycle 1) and at  $T = 158$  K (cycle 2), the pressures  $p_0$  were 51.0 kPa and 55.0 kPa, respectively, whereas for ethylene sorption at  $T = 165$  K  $p_0 = 82.0$  kPa holds. In the *in situ* EPR experiments, the xenon or ethylene pressure was increased stepwise for successive adsorption and decreased stepwise for subsequent desorption. The error of the given relative pressures is of the order of 10 % due to the experimental error of  $p_0$ . Before a second xenon ad/desorption cycle, the MOF was initialized in the *cp* phase by exposing the activated sample at  $T = 158$  K to xenon in a first sorption cycle to pressures up to  $p_0 = 55.0$  kPa, followed by the desorption of the xenon gas up to the application of dynamic vacuum conditions.

The EPR spectra were simulated with MATLAB R2021a, using the Easy Spin EPR simulation package version 5.2.35[47], which is based on the numerical diagonalization of the spin Hamiltonian. The errors are estimated from the simulation process by manual iterations where no change in the spectral feature was observed within the error region for the changing spin Hamiltonian parameters. The spin Hamiltonian parameters of the various  $S = 1$  signals in this work were determined by spectral simulations using a protocol explained next. The respective labels of the transitions and the Hamiltonian parameters are defined in the Results section. The principle values of the  $g$ - and hyperfine (HF) interaction tensors do not change the resonance field of the  $B_{xy1}$  transition significantly at least within their expected ranges[30]. Thus, we estimated in the first step the  $g$ - and HF interaction principle values based on values reported in the literature[23]. Assuming these values, we determined the ZFS parameter  $D$  by simulating the  $B_{xy1}$  transition. Spectral simulations justified that variations of the  $g$ - and HF interaction tensors within their expected ranges[48] are hidden in the corresponding experimental error of  $D$ , derived from the field position of the  $B_{xy1}$  transition, so far. After that, the principle values of the  $g$ - and HF interaction tensors were determined by simulating the  $B_{xy2}$  transition, from which one deduces  $g_{x,y}$  and  $A_{x,y}$ , and, most importantly, by simulating the  $B_{z2}$  transition from which one obtained the  $g_z$  and  $A_z$  parameters.

## 3.8 Supplementary material for chapter 3

### S1. Characterization of DUT-49(Cu)

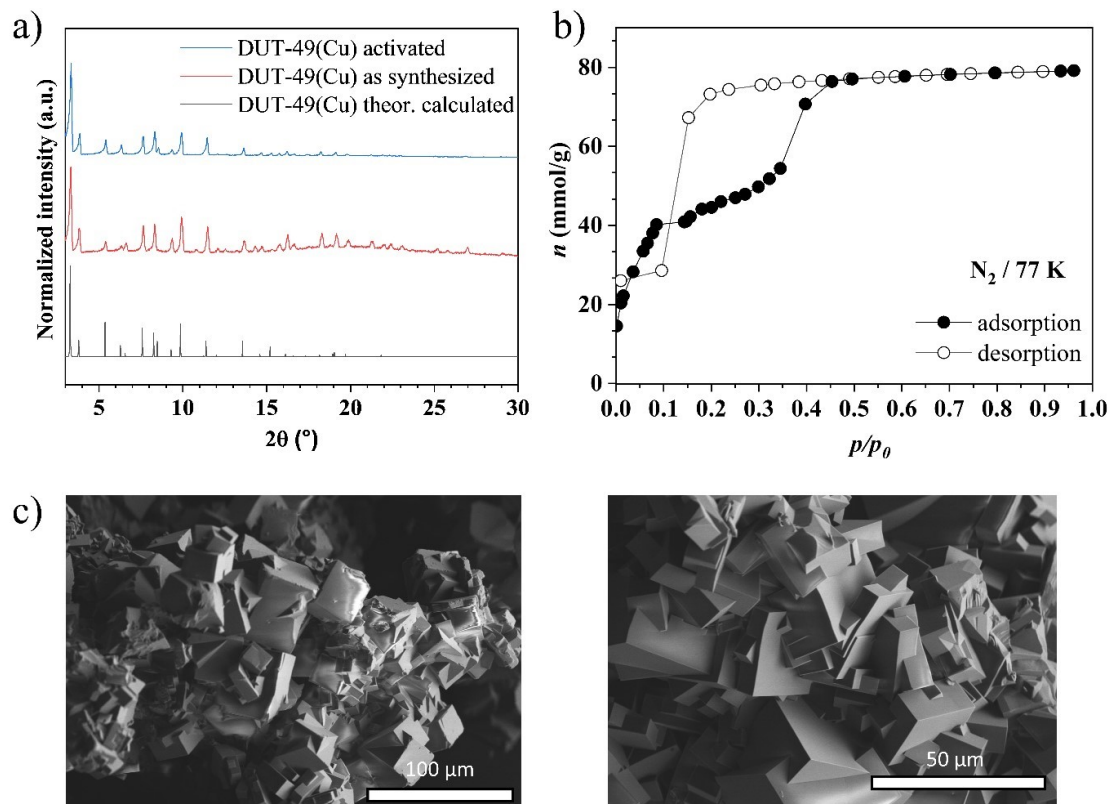


FIGURE 3.12: Characterization of DUT-49(Cu) sample: (a) PXRD patterns, (b) nitrogen physisorption at 77 K, and (c) SEM images.

### S2. Conventional xenon gas isotherm of DUT-49(Cu) at 165 K

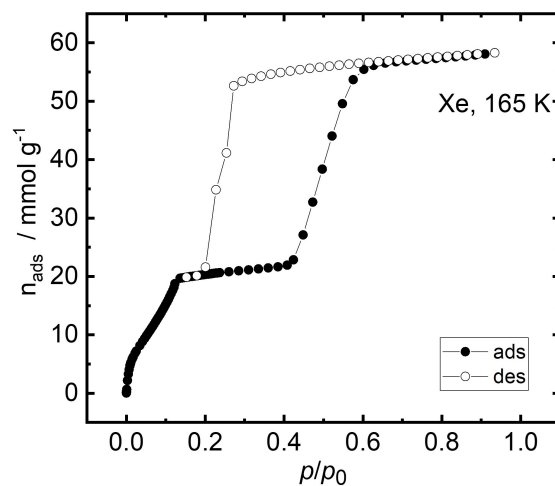


FIGURE 3.13: Adsorption and desorption isotherms of xenon on DUT-49(Cu) at  $T = 165$  K



### S3. Temperature-dependent EPR data

The EPR spectra were recorded at different temperatures (mostly  $\Delta T = 20$  K) in order to distinguish the spin states of Cu(II) dimers in the paddle wheel (PW) unit. The isotropic exchange interaction couples the two  $S = 1/2$  spins of the Cu(II) ions and gives rise to an  $S = 1$  triplet state and singlet  $S = 0$  state, and further, the degeneracy of the  $S = 1$  state is lifted by the zero-field splitting (ZFS). From Figure 3.14, it can be seen that the Cu(II) dimers in the PW unit behave like an  $S = 1$  species above 60 K temperature due to the excited state antiferromagnetic interaction between Cu(II) ions.

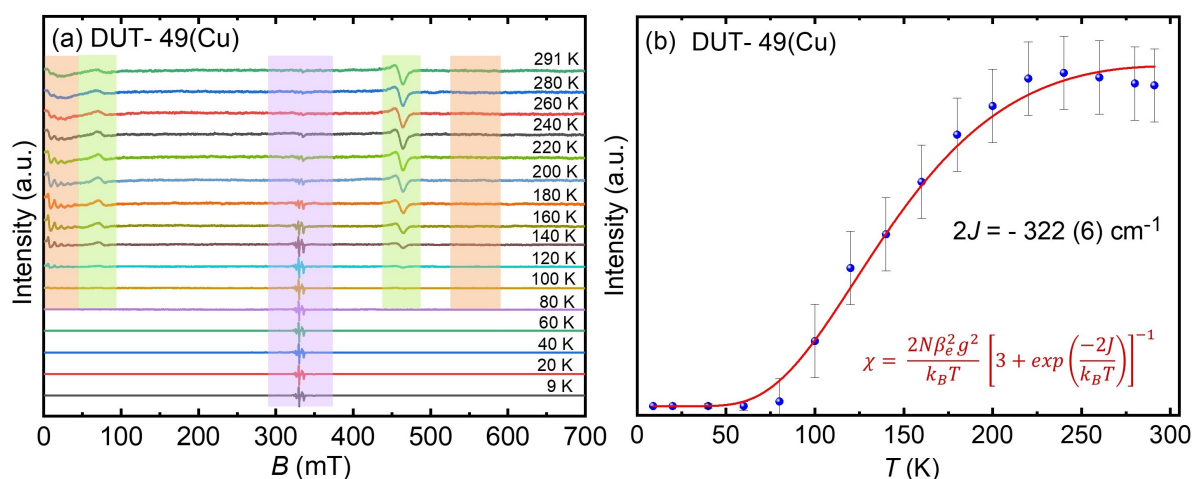


FIGURE 3.14: (a) Temperature-dependent EPR data of DUT-49(Cu), and (b) Bleaney Bowers fit on the EPR intensity of the  $S = 1$  state of the Cu(II) - Cu(II) dimers extracted from temperature-dependent EPR data.

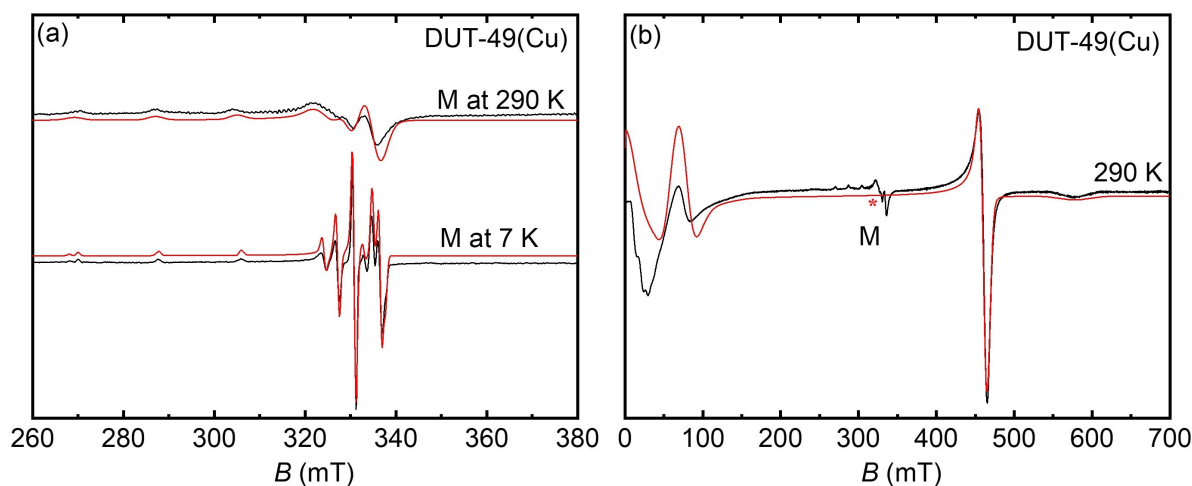


FIGURE 3.15: EPR spectra of activated DUT-49(Cu) showing (a) the  $S = 1/2$  Cu(II) monomer species (M) at 7 K & 290 K, and (b) the thermally populated  $S = 1$  Cu(II) pair species ( $A_{op}$ ) in the PW units at 290 K (\* corresponds to M). Redline simulated spectrum.

The intensity extracted from the temperature-dependent EPR data was fitted using the Bleaney-Bowers equation[22] for the magnetic susceptibility of an exchange-coupled homonuclear species,

### 3.8. Supplementary material for chapter 3

TABLE 3.2: Experimentally derived spin Hamiltonian parameters of  $S = 1/2$  species M assigned to Cu(II) monomer measured at 7 K and 290 K and  $S = 1$  assigned to Cu(II)-Cu(II) dimer at 290 K. (Quadrupole coupling of Cu(II) monomer,  $Q_{xx,yy} = -5(2)$  MHz,  $Q_{zz} = 10(2)$  MHz)

Species ( $T, S$ )	$g_{x,y}$	$g_z$	$A_{x,y}$ (MHz)	$A_z$ (MHz)	$D$ (MHz)	$E/D$
M (7 K, $S = 1/2$ )	2.038(2)	2.266(2)	95(3)	569(3)	-	-
$A_{op}$ (290 K, $S = 1/2$ )	2.040(3)	2.272(2)	95(3)	559(5)	-	-
$A_{op}$ (290 K, $S = 1$ )	2.039(5)	2.285(5)	<50	250(20)	8985(15)	<0.008

and the isotropic exchange interaction ( $2J$ ) is found to be  $2J = -322(6) \text{ cm}^{-1}$  (eqn. 2.31).

The sign of the  $2J$  value indicates an antiferromagnetic exchange interaction between Cu(II) dimers in the paddlewheel through the OCO units from the ligand being involved in a superexchange mechanism[49]. In general superexchange occurs between partly occupied orbitals of two magnetic ions because of the Pauli principle (If between partly occupied and unoccupied, it could be a weakly ferromagnetic interaction owing to Hund's rule)[49]. In this case, the singlet is the ground state with the thermally populated triplet lying  $322(6) \text{ cm}^{-1}$  above. As the Cu(II) dimer is in its  $S = 0$  ground state at temperatures below 80 K, the signals observed from the low-temperature EPR measurements ( $T < 80$  K) indicate the presence of Cu(II) monomers attributed to the broken paddle wheel or extraframework Cu(II) species.

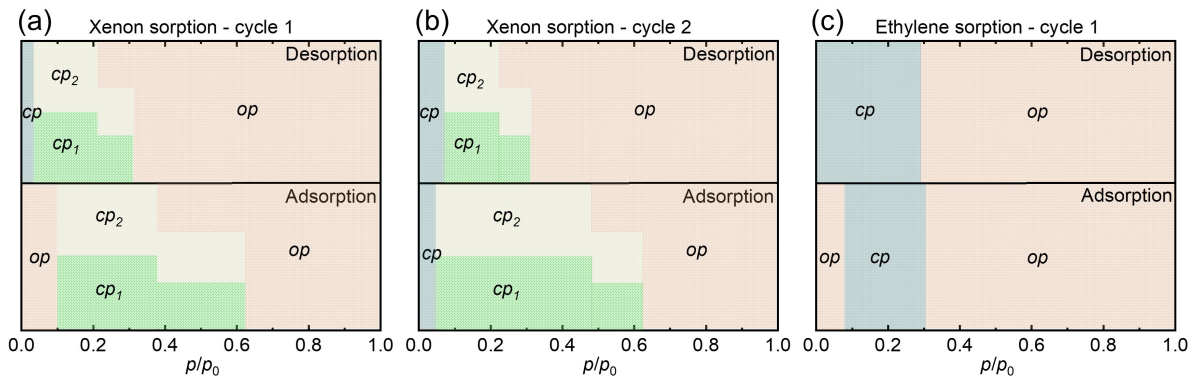


FIGURE 3.16: Schematic phase diagram for DUT-49(Cu) during the adsorption and desorption cycle of (a) xenon cycle 1, (b) xenon cycle 2 and (c) ethylene cycle 1 as derived from EPR experiments.

## S4. EPR data and simulations

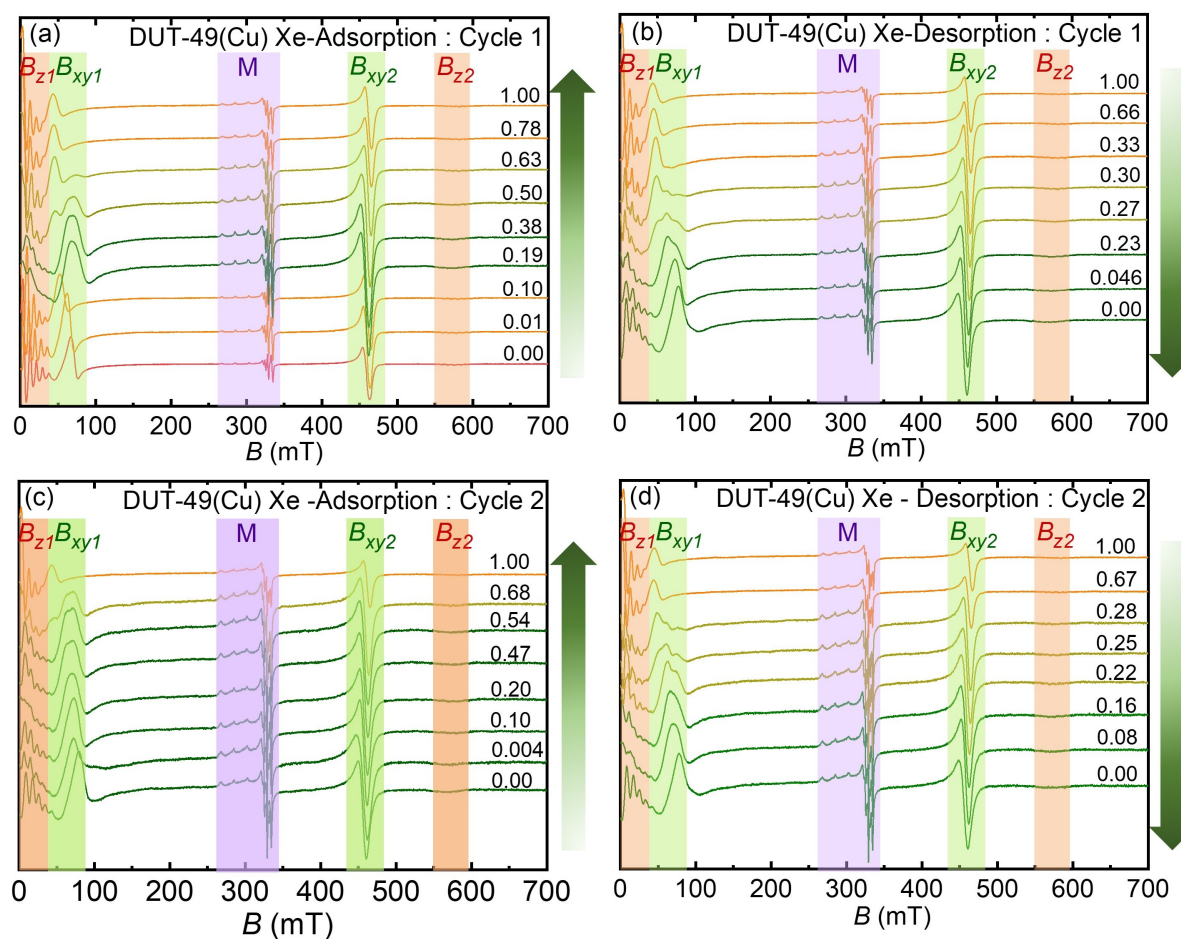


FIGURE 3.17: *In situ* EPR spectra of DUT-49(Cu) during (a) xenon adsorption and (b) xenon desorption at 156 K temperature in a first cycle starting with an activated sample. Furthermore, spectra are shown, which were measured in a second cycle at 158 K during (c) adsorption and (d) desorption starting with a sample which went through a full initial xenon ad/desorption cycle after activation. The EPR spectra are labelled with the relative xenon pressures  $p/p_0$  ( $p_0 = 51$  kPa in (a) and (b) and  $p_0 = 55$  kPa in (c) and (d)) at which they were measured. Orange spectra indicate the dominant presence of the *op* phase, green spectra that of the *cp* phase, olive spectra indicate the coexistence of both phases, and the red spectrum corresponds to *op* phase of the gas-free activated sample. The assignment of the various phases are based by correlating the *in situ* EPR spectra with sorption isotherm measured by Krause *et al*[3].

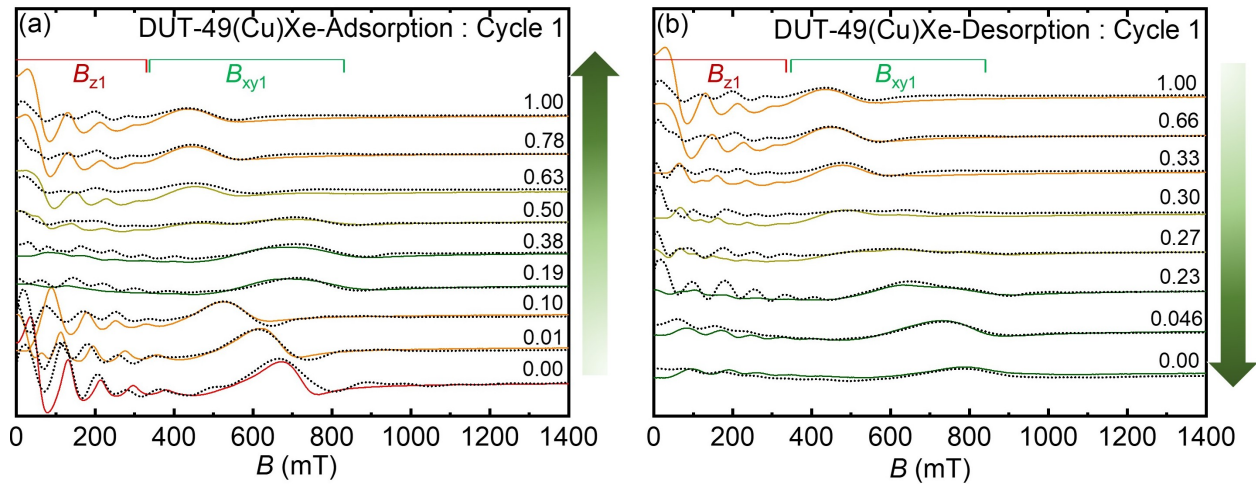


FIGURE 3.18: Selected experimental (solid lines) and simulated (dotted lines) EPR spectra of (a) xenon adsorption and (b) xenon desorption over DUT-49(Cu) at 156 K temperature in a first cycle starting with an activated sample. Furthermore, spectra are shown, which were measured in a second cycle at 158 K during (c) adsorption and (d) desorption starting with a sample which went through a full initial xenon ad/desorption cycle after activation. Special focus in the simulations were given in reproducing the line shape of the  $B_{xy1}$  transition as this very sensitive to variations in the parameter  $D$  whereas the  $B_{z1}$  transition at  $B < 50$  mT with its multiple HF splitting is difficult to simulate correctly. The EPR spectra are labelled with the relative xenon pressures  $p/p_0$  ( $p_0 = 51$  kPa) in (a) and (b) at which they were measured. Orange spectra indicate the dominant presence of the  $op$  phase, green spectra that of the  $cp$  phase, olive spectra indicate the coexistence of both phases, and the red spectrum corresponds to  $op$  phase of the gas-free activated sample as we derive in this work by *in situ* EPR correlated to a sorption isotherm measured by Krause *et al*[3]

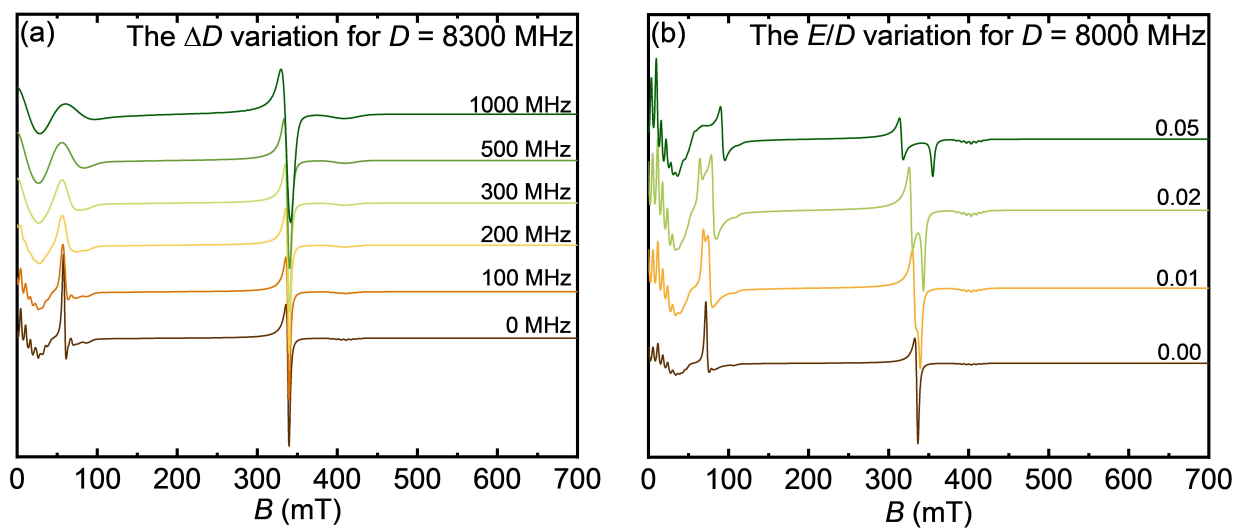


FIGURE 3.19: Simulation of (a)  $\Delta D$  variation and (b)  $E/D$  ratio variation for fixed  $D$  values.

TABLE 3.3: Experimentally derived spin Hamiltonian parameters of different  $S = 1$  species assigned to PW units in DUT-49 (Cu) during xenon sorption recorded at 156 K in the first cycle. ( $A_{x,y} < 60$  MHz and  $E/D < 0.008$ ,  $p_0 = 51$  kPa)

Phase	P ( $p/p_0$ )	$g_{xx,yy}$	$g_{zz}$	$A_{zz}$ (MHz)	$D$ (MHz)
Adsorption					
$A_{op}$	0.00	2.034(4)	2.290(3)	270(8)	8985(15)
$X_{op}$	0.01	2.034(8)	2.290(3)	270(8)	9055(15)
$X_{op}$	0.02	2.034(4)	2.292(3)	270(8)	9070(15)
$X_{op}$	0.10	2.035(8)	2.294(3)	270(8)	9155(15)
$X_{cp2}$	0.19	2.038(8)	2.293(27)	300(60)	8865(25)
$X_{cp1}$		2.038(5)	2.290(30)	290(70)	8985(25)
$X_{cp2}$	0.28	2.037(6)	2.305(25)	270(70)	8865(25)
$X_{cp1}$		2.037(6)	2.285(25)	265(65)	9025(25)
$X_{cp2}$	0.38	2.037(5)	2.305(20)	290(50)	8885(25)
$X_{cp1}$		2.037(5)	2.290(20)	270(70)	9035(25)
$X_{op}$	0.50	2.037(11)	2.326(30)	270(150)	9255(25)
$X_{cp2}$		2.037(11)	2.310(30)	250(150)	8905(25)
$X_{cp1}$		2.037(11)	2.295(25)	250(150)	9075(25)
$X_{op}$	0.63	2.029(11)	2.296(2)	262(3)	9225(25)
$X_{cp2}$		2.029(11)	2.310(30)	250(150)	8915(25)
$X_{cp1}$		2.029(11)	2.310(35)	250(150)	9105(25)
$X_{op}$	0.78	2.036(5)	2.296(2)	262(3)	9235(15)
$X_{op}$	0.93	2.036(1)	2.296(2)	262(3)	9235(15)
$X_{op}$	1.00	2.036(2)	2.296(2)	262(3)	9240(15)
Desorption					
$X_{op}$	0.66	2.036(1)	2.296(2)	262(2)	9225(15)
$X_{op}$	0.37	2.037(1)	2.294(3)	266(2)	9205(15)
$X_{op}$	0.33	2.037(1)	2.294(3)	266(3)	9200(15)
$X_{op}$	0.30	2.033(11)	2.294(3)	266(6)	9230(25)
$X_{cp2}$		2.033(11)	2.290(10)	280(40)	8915(50)
$X_{cp1}$		2.033(11)	2.290(10)	280(40)	9105(25)
$X_{op}$	0.27	2.039(100)	2.296(10)	290(40)	9230(25)
$X_{cp2}$		2.039(10)	2.296(10)	290(40)	8915(25)
$X_{cp1}$		2.039(10)	2.296(10)	290(40)	9085(15)
$X_{cp2}$	0.23	2.039(6)	2.305(15)	290(40)	8885(15)
$X_{cp1}$		2.039(6)	2.305(15)	290(40)	9060(15)
$X_{cp2}$	0.18	2.040(5)	2.310(20)	290(40)	8870(15)
$X_{cp1}$		2.040(5)	2.310(20)	290(40)	9040(15)
$X_{cp2}$	0.13	2.039(5)	2.310(20)	300(40)	8855(15)
$X_{cp1}$		2.039(5)	2.310(20)	300(40)	9015(15)
$X_{cp2}$	0.046	2.039(5)	2.300(6)	270(20)	8855(25)
$X_{cp1}$		2.039(5)	2.300(6)	270(20)	8970(25)
$X_{op}$	0.011	2.040(1)	2.305(15)	270(20)	8925(25)
$X_{op}$	0.00	2.039(1)	2.295(10)	280(30)	8805(25)

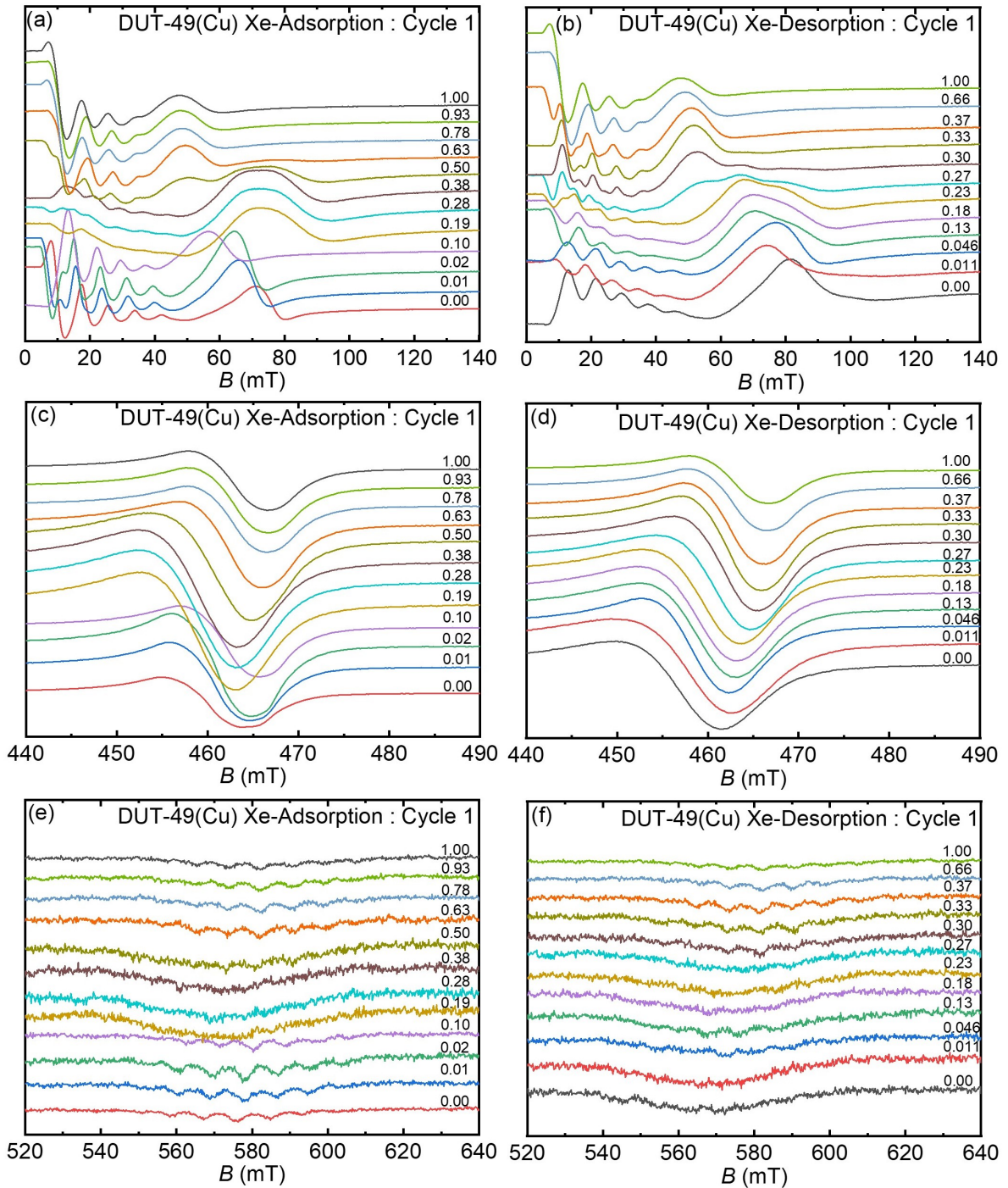


FIGURE 3.20: Enlarged X-band *in situ* EPR spectra of (a & b)  $B_z$  and  $B_{xy1}$  transition, (c & d)  $B_{xy2}$  and, (e & f)  $B_{z2}$  transitions measured during the first cycle of xenon adsorption and desorption respectively, recorded at 156 K.

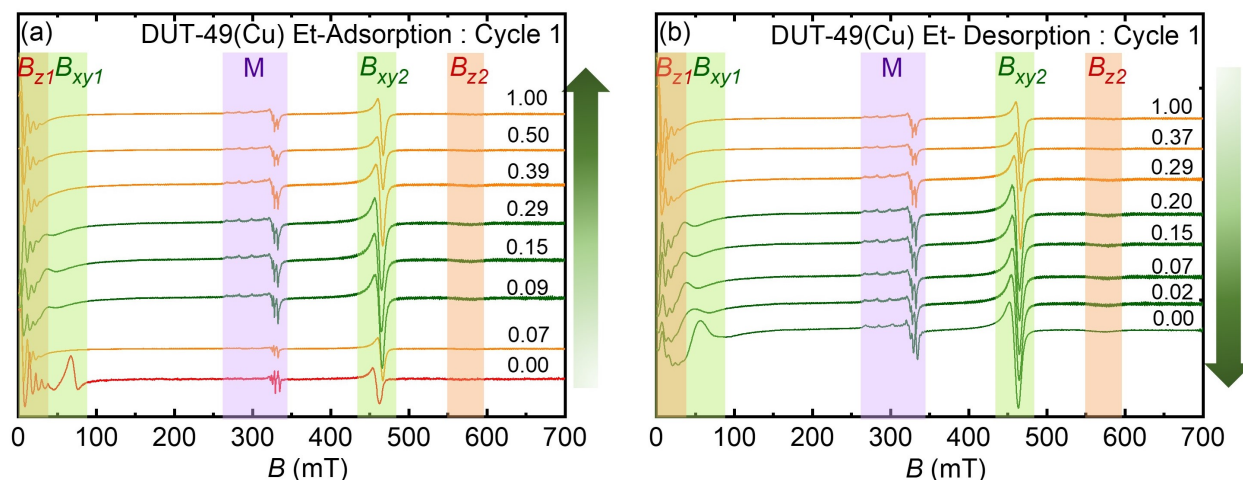


FIGURE 3.21: *In situ* EPR spectra of DUT-49(Cu) during (a) ethylene adsorption and (b) ethylene desorption at 165 K temperature in a first cycle starting with an activated sample (red). The EPR spectra are labelled with the relative ethylene pressures  $p/p_0$  ( $p_0 = 82$  kPa), orange spectra indicate the dominant presence of the  $op$  phase, green spectra that of the  $cp$  phase, olive spectra indicate the coexistence of both phases, and the red spectrum corresponds to the  $op$  phase of the gas-free activated sample.

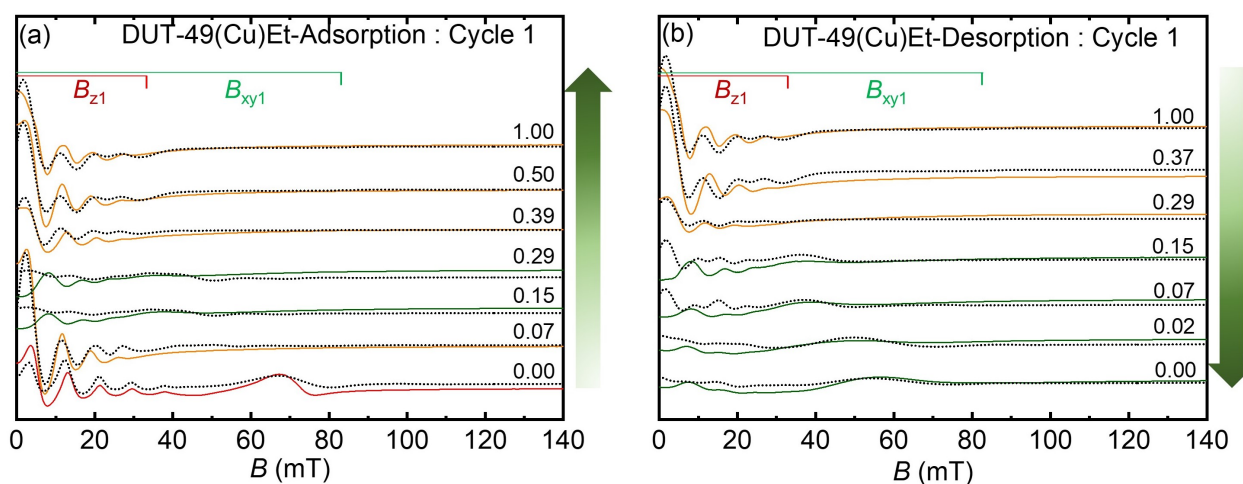


FIGURE 3.22: Selected EPR simulations of (a) Ethylene adsorption and (b) ethylene desorption at 165 K temperature in a first cycle starting with an activated sample (red). The EPR spectra are labelled with the relative ethylene pressures  $p/p_0$  ( $p_0 = 82$  kPa) Orange spectra indicate the dominant presence of the  $op$  phase, green spectra that of the  $cp$  phase, olive spectra indicate the coexistence of both phases, and the red spectrum corresponds to the  $op$  phase of the gas-free activated sample.

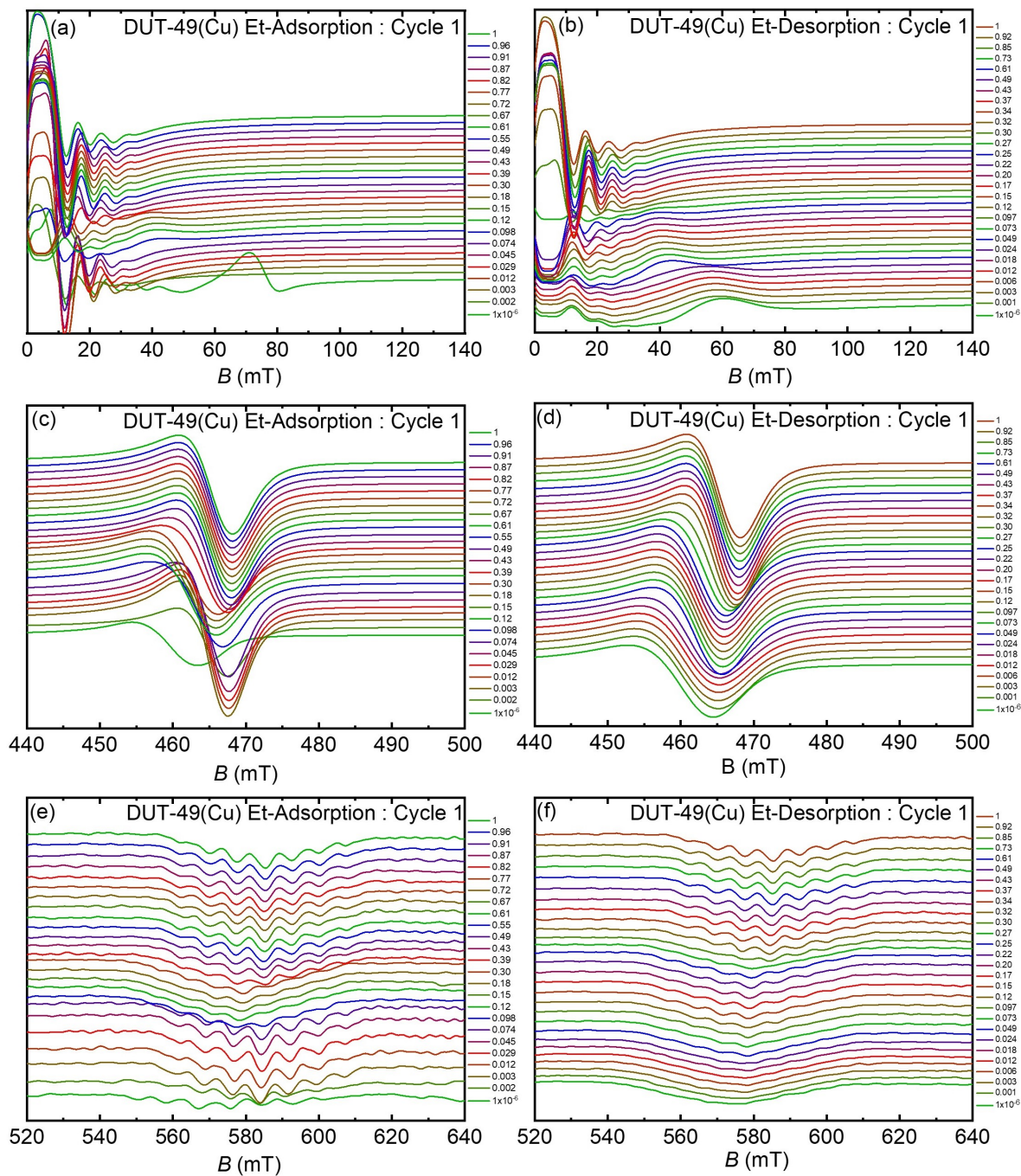


FIGURE 3.23: Enlarged X-band *in situ* EPR spectra of (a & b)  $B_{z1}$  and  $B_{xy1}$  transition, (c & d)  $B_{xy2}$  and (e & f)  $B_{z2}$  transition measured during cycle1 ethylene adsorption and desorption, respectively, recorded at 165(1) K.



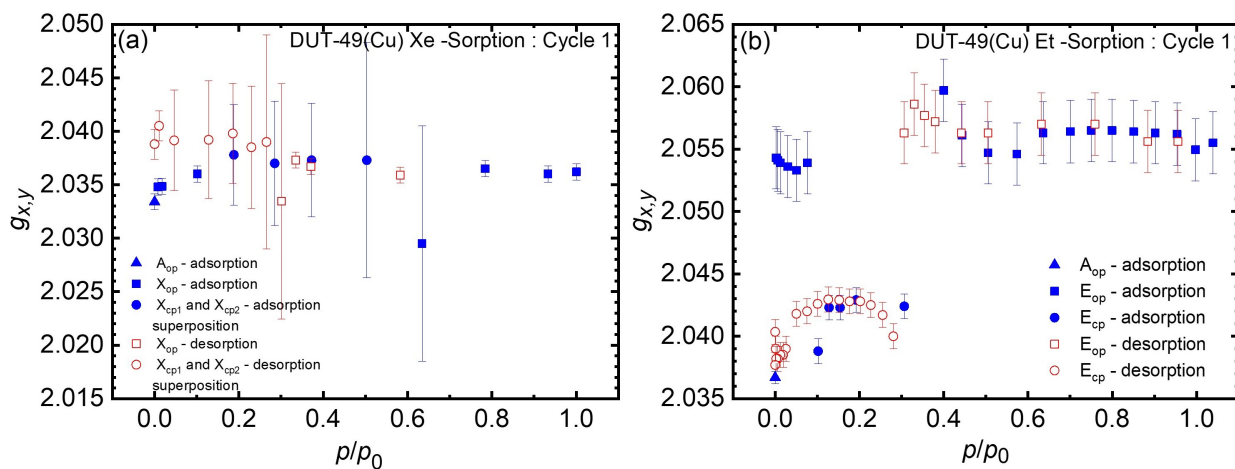


FIGURE 3.24: Parameters  $g_{x,y}$  of the  $S = 1$  state of different PW species (labels defined in the legends) as determined by *in situ* EPR for a) the first xenon ad/desorption cycle and b) the ethylene ad/desorption cycle.

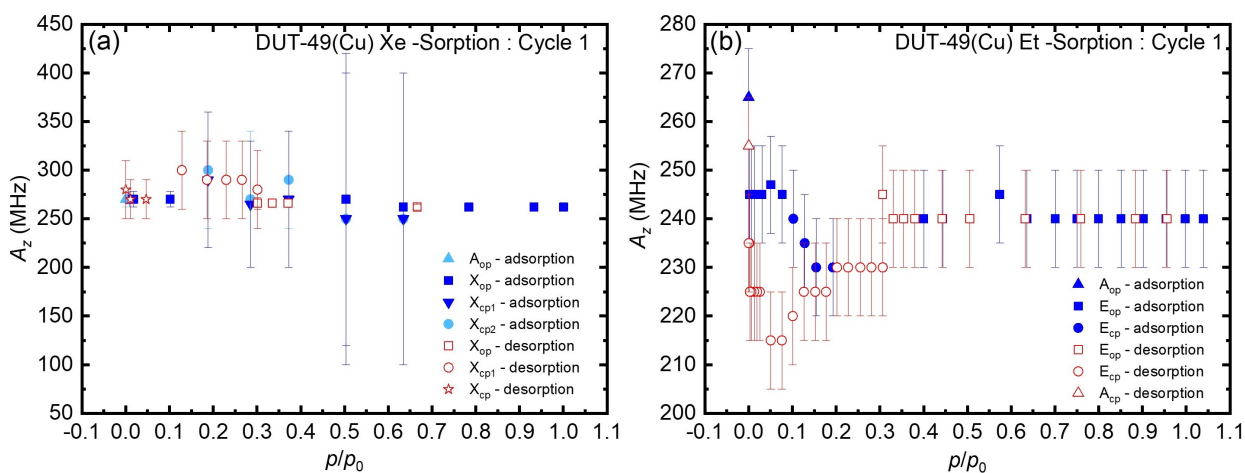


FIGURE 3.25:  $A_z$  parameters of the  $S = 1$  state of different PW species (labels defined in the legends) as determined by *in situ* EPR for a) the first xenon ad/desorption cycle and b) the ethylene ad/desorption cycle.

### 3.8. Supplementary material for chapter 3

TABLE 3.4: Experimentally derived spin Hamiltonian parameters of different  $S = 1$  species assigned to PW units in DUT-49 (Cu) during ethylene sorption recorded at 165 K. ( $A_{x,y} < 58$  MHz and  $E/D < 0.006$ )

Phase	P ( $p/p_0$ )	$g_{xx,yy}$	$g_{zz}$	$A_{zz}$ (MHz)	D (MHz)
Adsorption					
$A_{op}$	0.00	2.037(2)	2.291(0)	265(10)	8990(10)
$E_{op}$	0.0022	2.054(3)	2.345(7)	245(10)	9685(250)
$E_{op}$	0.006	2.054(3)	2.343(7)	245(10)	9690(250)
$E_{op}$	0.013	2.054(3)	2.342(7)	245(10)	9695(250)
$E_{op}$	0.03	2.054(3)	2.342(7)	245(10)	9690(250)
$E_{op}$	0.05	2.053(3)	2.342(7)	247(10)	9690(250)
$E_{op}$	0.07	2.054(3)	2.341(7)	245(10)	9690(250)
$E_{cp}$	0.09	2.039(1)	2.320(6)	240(10)	9305(20)
$E_{cp}$	0.12	2.042(1)	2.318(6)	235(10)	9305(20)
$E_{cp}$	0.19	2.0438(1)	2.318(6)	230(10)	9305(20)
$E_{cp}$	0.29	2.042(1)	2.318(6)	230(10)	9325(20)
$E_{op}$	0.39	2.059(3)	2.347(7)	240(10)	9750(250)
$E_{op}$	0.44	2.056(3)	2.344(7)	240(10)	9750(250)
$E_{op}$	0.50	2.055(3)	2.344(7)	240(10)	9750(250)
$E_{op}$	0.57	2.055(3)	2.345(7)	245(10)	9750(250)
$E_{op}$	0.63	2.056(3)	2.345(7)	240(10)	9750(250)
$E_{op}$	0.70	2.056(3)	2.348(7)	240(10)	9750(250)
$E_{op}$	0.79	2.056(3)	2.348(7)	240(10)	9750(250)
$E_{op}$	0.85	2.056(3)	2.349(7)	240(10)	9750(250)
$E_{op}$	0.90	2.056(3)	2.349(7)	240(10)	9750(250)
$E_{op}$	0.95	2.056(3)	2.348(7)	240(10)	9750(250)
$E_{op}$	1.00	2.056(3)	2.347(7)	240(10)	9750(250)
Desorption					
$E_{op}$	0.95	2.056(3)	2.347(7)	240(10)	9760(250)
$E_{op}$	0.88	2.056(3)	2.343(7)	240(10)	9760(250)
$E_{op}$	0.75	2.057(3)	2.349(7)	240(10)	9780(250)
$E_{op}$	0.60	2.057(3)	2.349(7)	240(10)	9780(250)
$E_{op}$	0.50	2.056(3)	2.348(7)	240(10)	9780(250)
$E_{op}$	0.44	2.056(3)	2.348(7)	240(10)	9760(250)
$E_{op}$	0.37	2.057(3)	2.349(7)	240(10)	9760(250)
$E_{op}$	0.33	2.059(3)	2.350(7)	240(10)	9760(250)
$E_{op}$	0.30	2.0056(3)	2.346(7)	245(10)	9760(250)
$E_{cp}$	0.29	2.040(1)	2.318(7)	230(10)	9325(20)
$E_{cp}$	0.25	2.042(3)	2.318(6)	230(10)	9325(20)
$E_{cp}$	0.22	2.043(1)	2.318(6)	230(10)	9325(20)
$E_{cp}$	0.20	2.043(1)	2.318(6)	230(10)	9325(20)
$E_{cp}$	0.17	2.043(1)	2.319(6)	225(10)	9320(20)
$E_{cp}$	0.15	2.043(1)	2.319(6)	225(10)	9320(20)
$E_{cp}$	0.07	2.042(1)	2.318(6)	215(10)	9300(20)
$E_{cp}$	0.01	2.039(1)	2.304(6)	225(10)	9160(20)
$E_{cp}$	0.003	2.038(1)	2.301(6)	225(10)	9140(20)
$E_{cp}$	0.00	2.038(1)	2.290(6)	255(10)	9115(20)

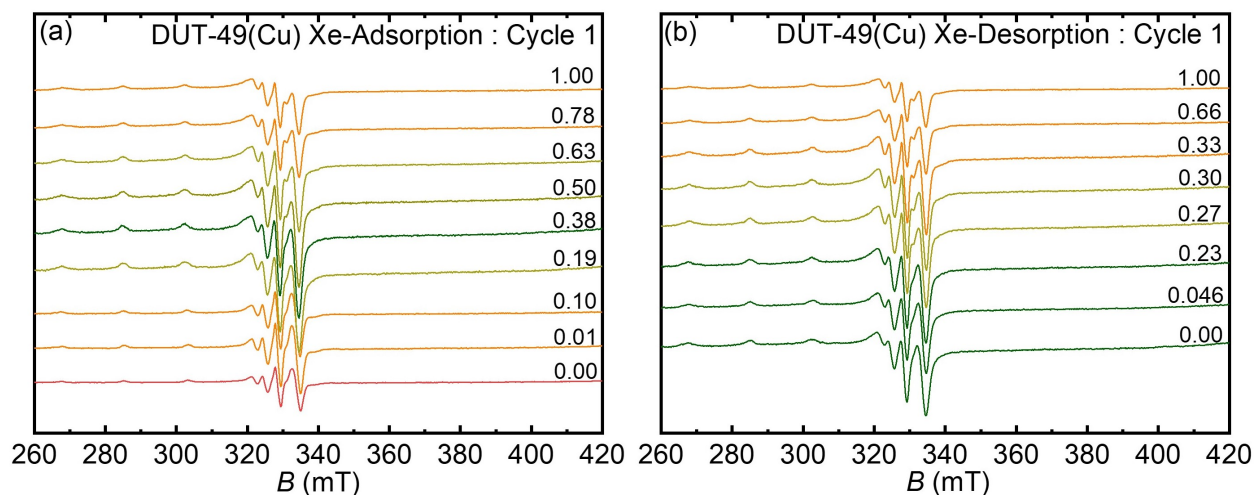


FIGURE 3.26: Cu(II) monomer species during a) xenon adsorption and (b) xenon desorption at 156 K temperature in the first cycle, starting with an activated sample. The EPR spectra are labelled with the relative xenon pressures  $p/p_0$  ( $p_0 = 51$  kPa) at which they were measured. Orange spectra indicate the dominant presence of the  $op$  phase, green spectra that of the  $cp$  phase, olive spectra indicate the coexistence of both phases, and the red spectrum corresponds to  $op$  phase of the activated sample.

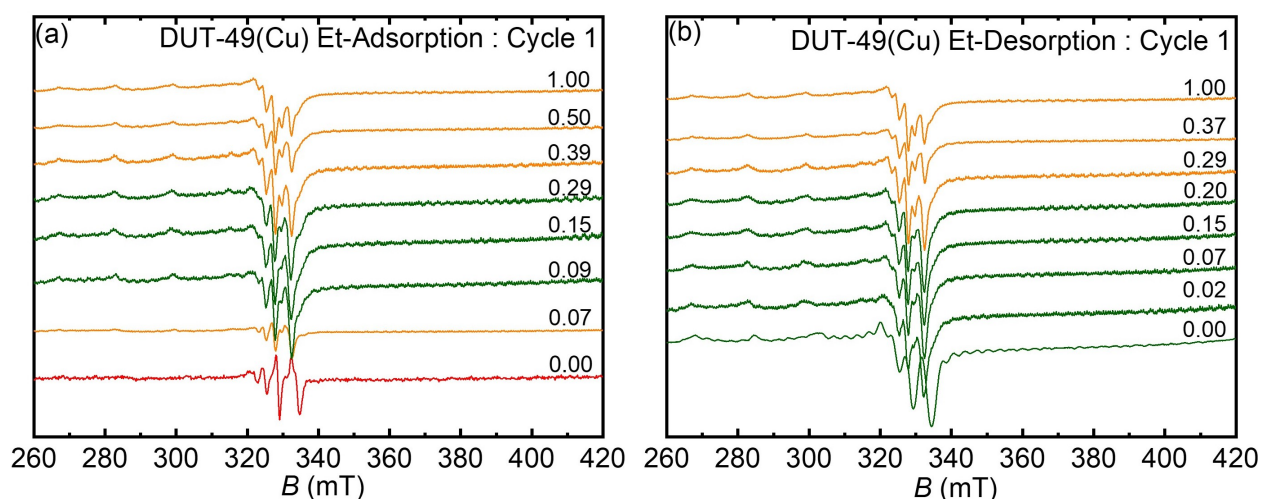


FIGURE 3.27: *In situ* EPR spectra the  $S = 1/2$  Cu(II) monomer species M during (a) ethylene adsorption and (b) ethylene desorption at 165 K temperature of an activated sample. The EPR spectra are labelled with the relative ethylene pressures  $p/p_0$  at which they were measured. (yellow spectra indicate the dominant presence of the  $op$  phase, green spectra that of the  $cp$  phase, and red spectra indicate the gas-free  $op$  phase.)

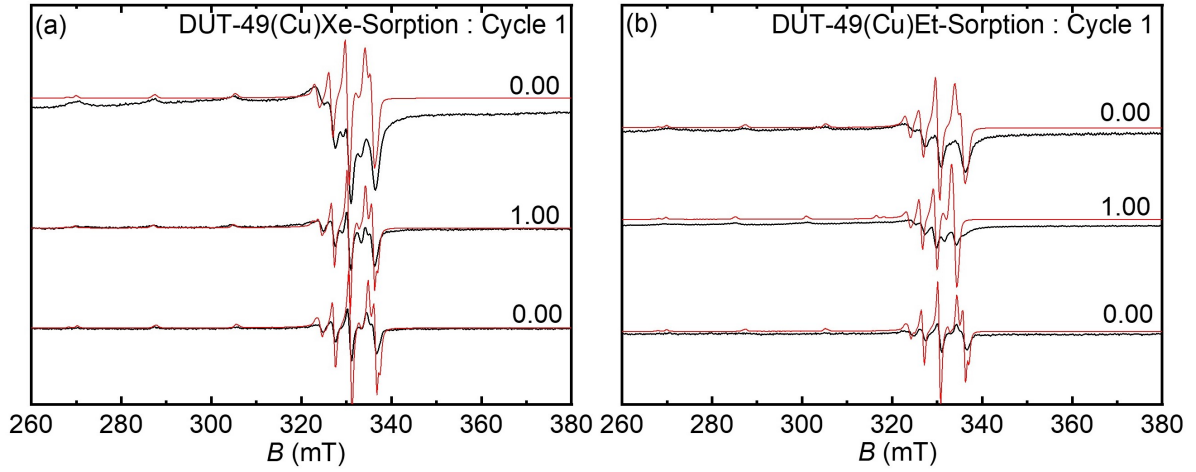


FIGURE 3.28: *In situ* EPR spectra the  $S = 1/2$  Cu(II) monomer species M for cycle 1 (a) xenon at 156 K and (b) ethylene at 165 K during sorption process (red line corresponding simulation). The EPR spectra are labelled with the relative ethylene pressures  $p/p_0$ .

TABLE 3.5: Spin Hamiltonian parameters  $g$ ,  $A$ ,  $Q$  of  $S = 1/2$  Cu(II) monomer for the xenon (156 K) and ethylene (165K) during the sorption process for the selected conditions. ( $Q_{xx,yy} = 5(2)$  MHz,  $Q_{zz} = 10(2)$  MHz)

Phase	P ( $p/p_0$ )	$g_{xx,yy}$	$g_{zz}$	$A_{xx,yy}$ (MHz)	$A_{zz}$ (MHz)
xenon					
$A_{op}$	0.00	2.056(2)	2.299(3)	95(3)	560(3)
$X_{op}$	1.00	2.054(2)	2.301(2)	90(4)	560(3)
$X_{cp}$	0.00	2.056(2)	2.298(2)	95(3)	560(3)
Ethylene					
$A_{op}$	0.00	2.044(3)	2.280(3)	95(3)	560(3)
$E_{op}$	1.00	2.049(2)	2.303(3)	85(4)	500(8)
$E_{cp}$	0.00	2.046(2)	2.278(2)	95(3)	560(3)

# Bibliography

- (1) Thangavel, K.; Walenszus, F.; Mendt, M.; Bon, V.; Kaskel, S.; Pöppel, A. *The Journal of Physical Chemistry C* **2023**, DOI: 10.1021/acs.jpcc.2c08905.
- (2) Krause, S.; Bon, V.; Senkovska, I.; Stoeck, U.; Wallacher, D.; Többens, D. M.; Zander, S.; Pillai, R. S.; Maurin, G.; Coudert, F.-X., et al. *Nature* **2016**, 532, 348–352.
- (3) Krause, S.; Evans, J. D.; Bon, V.; Senkovska, I.; Coudert, F.-X.; Többens, D. M.; Wallacher, D.; Grimm, N.; Kaskel, S. *Faraday discussions* **2021**, 225, 168–183.
- (4) Krause, S.; Bon, V.; Senkovska, I.; Többens, D. M.; Wallacher, D.; Pillai, R. S.; Maurin, G.; Kaskel, S. *Nature communications* **2018**, 9, 1–8.
- (5) Krause, S.; Evans, J. D.; Bon, V.; Senkovska, I.; Iacomi, P.; Kolbe, F.; Ehrling, S.; Troschke, E.; Getzschmann, J.; Többens, D. M., et al. *Nature communications* **2019**, 10, 1–12.
- (6) Thangavel, K.; Mendt, M.; Garai, B.; Folli, A.; Bon, V.; Murphy, D. M.; Kaskel, S.; Pöppel, A. *AIP Advances* **2023**, 13, 015019.
- (7) Bon, V.; Brunner, E.; Pöppel, A.; Kaskel, S. *Advanced Functional Materials* **2020**, 30, 1907847.
- (8) Bon, V.; Krause, S.; Senkovska, I.; Grimm, N.; Wallacher, D.; Többens, D. M.; Kaskel, S. *Angewandte Chemie* **2021**, 133, 11841–11845.
- (9) Krause, S.; Evans, J. D.; Bon, V.; Senkovska, I.; Ehrling, S.; Iacomi, P.; Többens, D. M.; Wallacher, D.; Weiss, M. S.; Zheng, B., et al. *Chemical science* **2020**, 11, 9468–9479.
- (10) Evans, J. D.; Bocquet, L.; Coudert, F.-X. *Chem* **2016**, 1, 873–886.
- (11) Evans, J. D.; Krause, S.; Kaskel, S.; Sweatman, M. B.; Sarkisov, L. *Chemical science* **2019**, 10, 5011–5017.
- (12) Goeminne, R.; Krause, S.; Kaskel, S.; Verstraelen, T.; Evans, J. D. *Journal of the American Chemical Society* **2021**, 143, 4143–4147.
- (13) Kolbe, F.; Krause, S.; Bon, V.; Senkovska, I.; Kaskel, S.; Brunner, E. *Chemistry of Materials* **2019**, 31, 6193–6201.
- (14) Walenszus, F.; Bon, V.; Evans, J. D.; Kaskel, S.; Dvoyashkin, M. *The Journal of Physical Chemistry Letters* **2020**, 11, 9696–9701.

- (15) Krause, S.; Evans, J. D.; Bon, V.; Senkovska, I.; Ehrling, S.; Stoeck, U.; Yot, P. G.; Iacomì, P.; Llewellyn, P.; Maurin, G., et al. *The Journal of Physical Chemistry C* **2018**, *122*, 19171–19179.
- (16) Schaber, J.; Krause, S.; Paasch, S.; Senkovska, I.; Bon, V.; Töbrens, D. M.; Wallacher, D.; Kaskel, S.; Brunner, E. *The Journal of Physical Chemistry C* **2017**, *121*, 5195–5200.
- (17) Aquilanti, V.; Cornicchi, E.; Moix Teixidor, M.; Saendig, N.; Pirani, F.; Cappelletti, D. *Angewandte Chemie International Edition* **2005**, *44*, 2356–2360.
- (18) Banerjee, D.; Simon, C. M.; Elsaidi, S. K.; Haranczyk, M.; Thallapally, P. K. *Chem* **2018**, *4*, 466–494.
- (19) Perry IV, J. J.; Teich-McGoldrick, S. L.; Meek, S. T.; Greathouse, J. A.; Haranczyk, M.; Allendorf, M. D. *The Journal of Physical Chemistry C* **2014**, *118*, 11685–11698.
- (20) Demir, H.; Greathouse, J. A.; Staiger, C. L.; Perry IV, J. J.; Allendorf, M. D.; Sholl, D. S. *Journal of Materials Chemistry A* **2015**, *3*, 23539–23548.
- (21) Ryan, P.; Farha, O. K.; Broadbelt, L. J.; Snurr, R. Q. *AIChE Journal* **2011**, *57*, 1759–1766.
- (22) Pöppl, A.; Kunz, S.; Himsl, D.; Hartmann, M. *The Journal of Physical Chemistry C* **2008**, *112*, 2678–2684.
- (23) Polyukhov, D. M.; Krause, S.; Bon, V.; Poryvaev, A. S.; Kaskel, S.; Fedin, M. V. *J. Phys. Chem. Lett.* **2020**, *11*, 5856–5862.
- (24) Friedländer, S.; Simenas, M.; Kobalz, M.; Eckold, P.; Ovchar, O.; Belous, A. G.; Banys, J.; Krautscheid, H.; Pöppl, A. *The Journal of Physical Chemistry C* **2015**, *119*, 19171–19179.
- (25) Simenas, M.; Kobalz, M.; Mendt, M.; Eckold, P.; Krautscheid, H.; Banys, J.; Pöppl, A. *The Journal of Physical Chemistry C* **2015**, *119*, 4898–4907.
- (26) Mendt, M.; Maliuta, M.; Ehrling, S.; Schwotzer, F.; Senkovska, I.; Kaskel, S.; Pöppl, A. *The Journal of Physical Chemistry C* **2022**, *126*, 625–633.
- (27) Nevjestic, I.; Depauw, H.; Leus, K.; Rampelberg, G.; Murray, C. A.; Detavernier, C.; Van Der Voort, P.; Callens, F.; Vrielinck, H. *The Journal of Physical Chemistry C* **2016**, *120*, 17400–17407.
- (28) Mendt, M.; Vervoorts, P.; Schneemann, A.; Fischer, R. A.; Pöppl, A. *J. Phys. Chem. C* **2019**, *123*, 2940–2952.
- (29) Mehara, J.; Watson, B. T.; Noonikara-Poyil, A.; Zacharias, A. O.; Roithová, J.; Rasika Dias, H. *Chemistry—A European Journal* **2022**, *28*, e202103984.
- (30) Wasserman, E.; Snyder, L.; Yager, W. *The Journal of Chemical Physics* **1964**, *41*, 1763–1772.

- (31) Bleaney, B.; Bowers, K. *Proceedings of the Royal Society of London. Series A. Mathematical and Physical Sciences* **1952**, 214, 451–465.
- (32) Bitzer, J.; Otterbach, S.; Thangavel, K.; Kultaeva, A.; Schmid, R.; Pöppl, A.; Kleist, W. *Chem. Eur. J.* **2020**, 26, 5667–5675.
- (33) Krause, S.; Hosono, N.; Kitagawa, S. *Angewandte Chemie International Edition* **2020**, 59, 15325–15341.
- (34) Ehrling, S.; Miura, H.; Senkovska, I.; Kaskel, S. *Trends in Chemistry* **2021**, 3, 291–304.
- (35) Kavooosi, N.; Bon, V.; Senkovska, I.; Krause, S.; Atzori, C.; Bonino, F.; Pallmann, J.; Paasch, S.; Brunner, E.; Kaskel, S. *Dalton Transactions* **2017**, 46, 4685–4695.
- (36) Air Liquide Gas Encyclopedia <https://encyclopedia.airliquide.com/>.
- (37) Hoffmann, S. K.; Goslar, J.; Lijewski, S.; Zalewska, A. *Journal of Magnetic Resonance* **2013**, 236, 7–14.
- (38) Peisach, J.; Blumberg, W. *Archives of biochemistry and biophysics* **1974**, 165, 691–708.
- (39) Buluggiu, E. *Journal of Physics and Chemistry of Solids* **1980**, 41, 1175–1180.
- (40) Sakaguchi, U.; Addison, A. W. *Journal of the Chemical Society, Dalton Transactions* **1979**, 600–608.
- (41) Hathaway, B.; Billing, D. *Coordination Chemistry Reviews* **1970**, 5, 143–207.
- (42) Kultaeva, A.; Böhlmann, W.; Hartmann, M.; Biktagirov, T.; Pöppl, A. *The Journal of Physical Chemistry C* **2019**, 123, 26877–26887.
- (43) Kultaeva, A.; Böhlmann, W.; Hartmann, M.; Biktagirov, T.; Pöppl, A. *The journal of physical chemistry letters* **2019**, 10, 7657–7664.
- (44) Bencini, A.; Gatteschi, D., *EPR of exchange coupled systems*; Dover Publications: 2012.
- (45) Jee, B.; St. Petkov, P.; Vayssilov, G. N.; Heine, T.; Hartmann, M.; Pöppl, A. *The Journal of Physical Chemistry C* **2013**, 117, 8231–8240.
- (46) Maurice, R.; Sivalingam, K.; Ganyushin, D.; Guihery, N.; de Graaf, C.; Neese, F. *Inorganic Chemistry* **2011**, 50, 6229–6236.
- (47) Stoll, S.; Schweiger, A. *Journal of magnetic resonance* **2006**, 178, 42–55.
- (48) Misra, S. K., *Multifrequency electron paramagnetic resonance: theory and applications*; John Wiley & Sons: 2011.
- (49) Lalena, J. N.; Cleary, D. A.; Duparc, O. B. H., *Principles of inorganic materials design*; John Wiley & Sons: 2020.

## Chapter 4

# Post-Synthetically Modified Paddle Wheel-Based Bimetallic MOFs

### 4.1 Introduction

Another outstanding aspect of MOF materials is post-synthetic modification (PSM) which means that even after the complete synthesis, the structure can be altered, the SBU can be substituted by desired paramagnetic ions partly or completely, and the linker can be modified. PSM of MOF materials was carried out in a number of ways, such as modification of linker(ligand) and/or metal ion and adsorption/exchange of guest species to improve many of their properties. PSM is a promising and widely used strategy for generating novel scaffolds exhibiting improved physical and chemical properties compared to the parent frameworks[1–3]. In many instances, the existing feature of a parent framework gets better in the resultant MOF after the modification. Though PSM-resulting materials have some difficulties in verifying successful incorporation/metal exchange and the magnetic properties of resulting mixed metal clusters at times, EPR is a unique and powerful complimentary tool to elucidate such properties of PSM MOFs[3, 4] when paramagnetic ions are involved. In this aspect, EPR spectroscopy has been successfully used to investigate PW-type Fe and Zn incorporated HKUST-1 and DUT-49(M,M) MOFs.

### 4.2 Magnetic coupling of divalent metal centers in bimetallic DUT-49 MOFs

As a notable and representative candidate of flexible MOFs, DUT-49(Cu) (Figure 2.1) has gained attention due to the unique phenomenon of NGA, originating from an unprecedented structural contraction during gas adsorption. Among several bivalent TMIs, Cu(II) has been known to form PW motif easily, due to the favorable dd interaction[5]. At the same time, there are reports that



describe the M(II)M(II) PW involving other metal ions such as Zn, Fe, Co, Ni, etc. [6–9]. However, according to Garai *et al.*[10], direct synthesis of the DUT-49 framework with other bivalent metal nodes remained inefficient and sometimes not possible. Meanwhile, they found that DUT-49(Co) could be easily synthesized via solvothermal reaction and the other TMIs can be post-synthetically modified with 100% incorporation efficiency. Further, Garai *et al.*[10] demonstrated PSM DUT-49 frameworks with a wide variety of metal cations, e.g., Mn(II), Fe(II), Ni(II), Zn(II), Cu(II), and Cd(II) and studied the effect on the framework property by varying different bivalent metal ions as the structural node for DUT-49 framework. In this regard, we verified the post-exchange modification of DUT-49(Co) MOF with bimetallic Zn(II), Cu(II), Mn(II) TMIs[4]. The ratio of the bimetallic ions are varied by means of EDAX analysis and named accordingly as DUT-49(Cu<sub>0.7</sub>Zn<sub>0.3</sub>) and DUT-49(Cu<sub>0.5</sub>Mn<sub>0.5</sub>) for mixed MOFs, and DUT-49(Cu) and DUT-49(Mn) for monometallic MOFs.

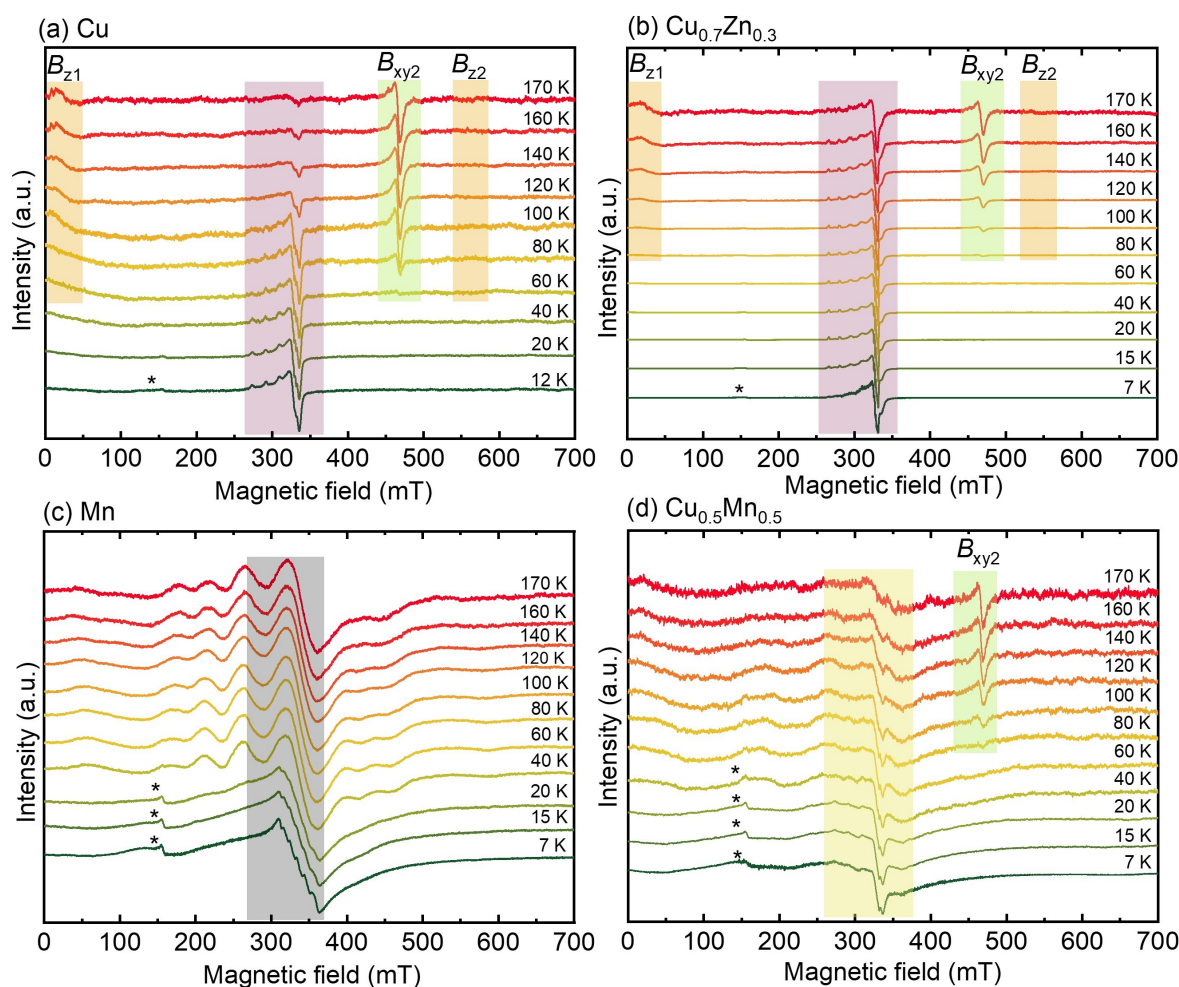


FIGURE 4.1: Temperature-dependent X-band EPR experiments from  $T = 7$  K to  $T = 170$  K for (a) DUT-49(Cu), (b) DUT-49(Cu<sub>0.7</sub>Zn<sub>0.3</sub>), (c) DUT-49(Mn), (d) DUT-49(Cu<sub>0.5</sub>Mn<sub>0.5</sub>) (a weak signal at  $\sim 150$  mT indicates the minor Co impurity species, a violet bar in (a) & (b)  $S = 1/2$  Cu(II) monomer, gray bar in (c) a mixture of  $S = 1/2$  Cu(II) &  $S = 5/2$  Mn(II) monomers, and yellow bar in (d)  $S = 5/2$  Mn(II) monomer).

Temperature-dependent CW-X band EPR measurements were performed in the range  $7 \text{ K} < T < 170 \text{ K}$  for four MOFs, illustrated in Figure 4.1(a-d). No dominant EPR signals of Co(II) could be detected after the post-synthetic metal ion exchange procedure in the four studied samples. The violet bar ( $\sim 260 \text{ mT} < B < \sim 360 \text{ mT}$ ) in Figures 4.1(a) and (b) indicates the Cu(II) monomer having a  $3d^9$  ground state with an electron spin  $S = 1/2$  interacting with the nuclear spin  $I^{Cu} = 3/2$  of the two copper isotopes  $^{63,65}\text{Cu}$ . The spin Hamiltonian for the Cu(II) monomer species has been evaluated using the Spin Hamiltonian eqn.3.1. The simulated spin Hamiltonian parameters of Cu(II) monomer (Figure 4.2a) for the monometallic DUT-49(Cu) are  $g_{xx} = 2.052(3)$ ,  $g_{yy} = 2.060(2)$ ,  $g_{zz} = 2.335(4)$ ,  $A_{xx,yy} = 30(5) \text{ MHz}$ ,  $A_{zz} = 545(8) \text{ MHz}$  which could be assigned to the defective Cu-Cu paddlewheel units or extra framework cupric ions[3, 11].

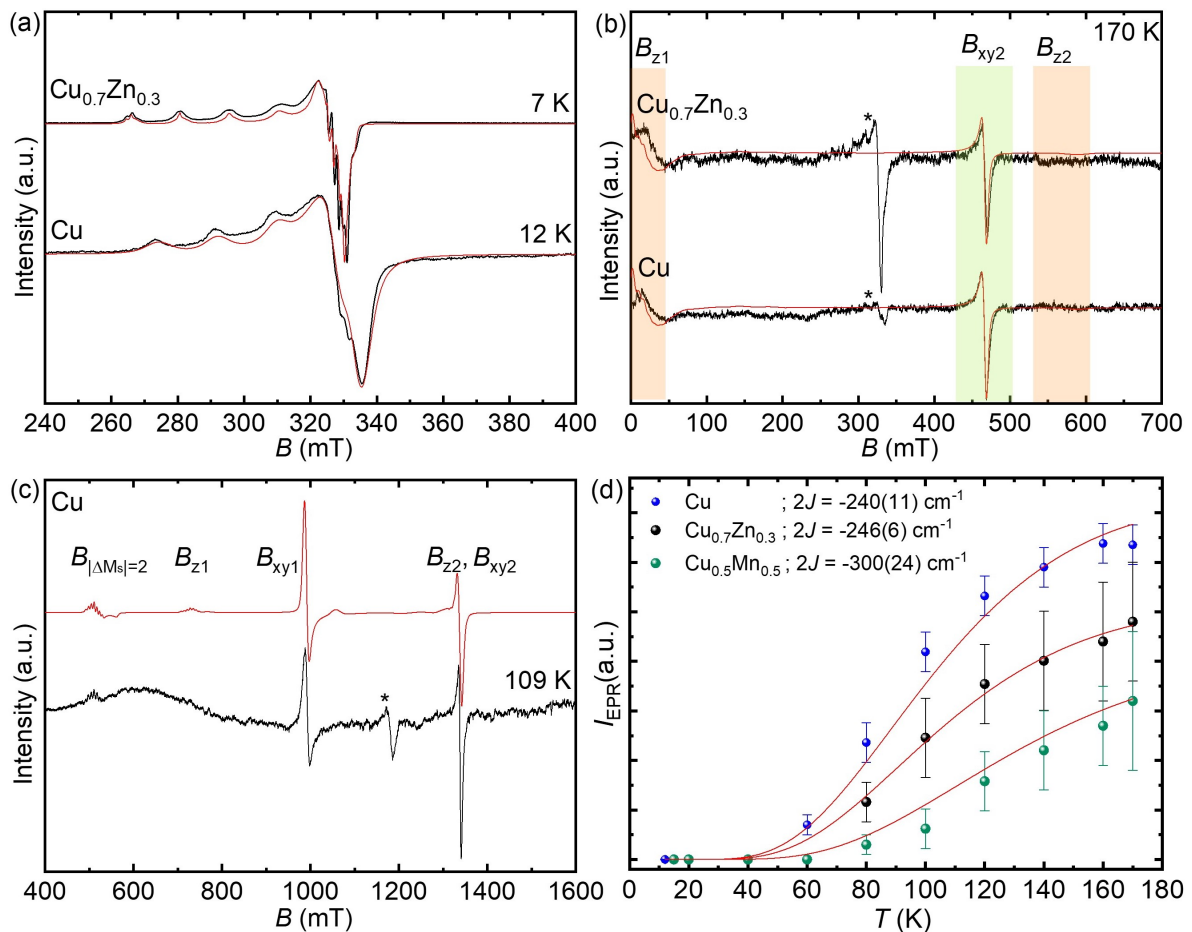


FIGURE 4.2: Experimental (black) and simulated (red) spectra of (a) the  $S = 1/2$  spin state of the Cu(II) monomer, (b) the  $S = 1$  spin state of the Cu(II) - Cu(II) dimer of DUT-49(Cu) and DUT-49( $\text{Cu}_{0.7}\text{Zn}_{0.3}$ ) at X-band frequency, (c) the  $S = 1$  spin state of the Cu(II) - Cu(II) dimer of DUT-49(Cu) at Q-band frequency (for the spin Hamiltonian parameters, see the text, \* signals in (b) & (c) indicate  $S = 1/2$  Cu(II) monomer) and (d) The intensity extracted from the temperature-dependent X-band EPR data of DUT-49(M, M) fitted using Bleaney Bowers susceptibility equations for the coupled  $S = 1/2$  dimer species. (Blue points - DUT-49(Cu), black points - DUT-49( $\text{Cu}_{0.7}\text{Zn}_{0.3}$ ), green points - DUT-49( $\text{Cu}_{0.5}\text{Mn}_{0.5}$ ), and red line Bleaney Bowers susceptibility fit)

The spectral features illustrated in Figure 4.1b for bimetallic DUT-49(Cu<sub>0.7</sub>Zn<sub>0.3</sub>) are similar to the monometallic DUT-49(Cu) MOF (Figure 4.1a). However, in bimetallic DUT-49(Cu<sub>0.7</sub>Zn<sub>0.3</sub>), 30% Zn(II) incorporation on the Cu(II) sites yields more Cu(II) monomer species in comparison with DUT-49(Cu) and shows the intense signal of Cu(II) monomer species till 170 K at  $\sim 260$  mT  $< B < \sim 360$  mT magnetic field range. This confirms the presence of Cu(II) - Zn(II) PW combination within the framework. The simulated spin Hamiltonian parameters of Cu(II) monomer (Figure 4.2a) for the bimetallic DUT-49(Cu<sub>0.7</sub>Zn<sub>0.3</sub>) are  $g_{xx} = 2.048(5)$ ,  $g_{yy} = 2.073(4)$ ,  $g_{zz} = 2.333(4)$ ,  $A_{xx} = 26(3)$  MHz,  $A_{yy} = 40(5)$  MHz,  $A_{zz} = 470(8)$  and the values are consistent with the PW based Cu<sup>II</sup> monomer species for the bimetallic Zn<sub>0.03</sub>Cu<sub>2.97</sub>(BTC)<sub>2</sub> MOF[12] with secondary species B (17%) where  $g_{xx} = 2.0284(4)$ ,  $g_{yy} = 2.0602(5)$ ,  $g_{zz} = 2.3350(4)$ ,  $A_{xx,yy} = 25(3)$  MHz and  $A_{zz} = 479(7)$  MHz.

Moreover, the experimental results of DUT-49(Cu) clearly show the formation of Cu(II) - Cu(II) dimer above 60 K, where the two cupric ions with their  $S = 1/2$  spin states couple to a total  $S = 1$  state in the PW unit. Likewise, DUT-49(Cu<sub>0.7</sub>Zn<sub>0.3</sub>) and DUT-49(Cu<sub>0.5</sub>Mn<sub>0.5</sub>) indicate the Cu(II) - Cu(II) dimer formation above 80 K. The Spin Hamiltonian parameters of the  $S = 1$  spin state of the Cu(II) - Cu(II) dimer were evaluated using the spin Hamiltonian eqn.3.2. For the DUT-49(Cu) and DUT-49(Cu<sub>0.7</sub>Zn<sub>0.3</sub>) MOFs, parameters  $D = 9990(45)$  MHz with a strain of  $= 450$  MHz,  $E = 0$ ,  $g_{xx,yy} = 2.065(8)$ ,  $g_{zz} = 2.355(6)$ ,  $A_{xx,yy} = 10(6)$  MHz and  $A_{zz} = 220(9)$  MHz were obtained from spectral simulations (Figures 4.2b and 4.2c). The ZFS spectral features are labelled according to Wassermann *et al.*[13], where  $B_{z1}$  and  $B_{z2}$  represent the parallel, and  $B_{xy1}$  (out of the X-band magnetic field range due to large ZFS) and  $B_{xy2}$  represent the perpendicular ZFS transitions of the Cu(II) - Cu(II) dimer. However, all spectral transitions of the  $S = 1$  species belonging to the Cu(II) - Cu(II) dimer can be seen in the Q-band spectrum(Figure 4.2c). Weak signals () at 150 mT in Figure 4.1 are tentatively assigned to high spin Co(II) impurities ( $g = \sim 5.2$  4.2) from the parent sample or defects[14]. The total spin states of Cu(II) -Cu(II), Cu(II) -Zn(II), Cu(II) -Mn(II), and Mn(II) -Mn(II) metal dimers in the PW units at a temperature of 7 K (LS low spin) and 160 K (HS high spin) are summarized in Table 4.1.

The Cu(II) - Cu(II) dimers in the PW units are well separated by the long linker (H<sub>4</sub>BBCDC) in DUT-49, which prevents the inter dimer exchange interactions. Moreover, an EPR signal intensity of the  $S = 1$  spin state of these magnetically coupled Cu(II) - Cu(II) dimers in the PW units, which is proportional to the magnetic susceptibility, was extracted from temperature-dependent X-band EPR data for all MOFs (Figure 4.2d). The isotropic exchange coupling constant of the Cu(II) - Cu(II) dimer can be estimated using the Bleaney-Bowers susceptibility equation[11] of exchange coupled identical dimer species with  $S_1 = 1/2$  and  $S_2 = 1/2$  (eqn. 2.31).

The EPR intensity extracted from the double integration of  $B_{xy2}$  and  $B_{z22}$  parts of the  $S = 1$

## 4.2. Magnetic coupling of divalent metal centers in bimetallic DUT-49 MOFs

signal and the  $2J$  - value is found to be  $-240(11) \text{ cm}^{-1}$ ,  $-246(6) \text{ cm}^{-1}$  and  $-300(24) \text{ cm}^{-1}$  for DUT-49(Cu), DUT-49( $\text{Cu}_{0.7}\text{Zn}_{0.3}$ ) and DUT-49( $\text{Cu}_{0.5}\text{Mn}_{0.5}$ ) MOFs, respectively (Figure 4.2d). The sign of the  $2J$  - value indicates the excited state of antiferromagnetically coupled dimers, where the  $S = 1$  triplet state is the thermally populated excited state, and the  $S = 0$  singlet state corresponds to the ground state. Such an antiferromagnetic (AFM) exchange coupling is the characteristic behavior of Cu(II) - Cu(II) PW species[11, 15, 16].

TABLE 4.1: Total spin ( $S$ ) states of metal dimers in the PW units of DUT-49(M,M) MOFs at a temperature of 7 K and 160 K as derived from EPR experiments.

MOF	Spin centers in the PW units	$S$	$S$ at 7 K (LS)	$S$ at 170 K (HS)
DUT-49(Mn)	Mn-Mn	$S_{Mn(5/2)}-S_{Mn(5/2)}$	0	5*
DUT-49( $\text{Cu}_{0.5}\text{Mn}_{0.5}$ )	Cu-Mn	$S_{Cu(1/2)}-S_{Mn(5/2)}$	2	3*
		$S_{Mn(5/2)}-S_{Mn(5/2)}$	0	5*
		$S_{Cu(1/2)}-S_{Cu(1/2)}$	0	1
		$S_{Cu(1/2)}-S_{Zn(0)}$	1/2	1/2
DUT-49( $\text{Cu}_{0.7}\text{Zn}_{0.5}$ )	Cu-Zn	$S_{Cu(1/2)}-S_{Cu(1/2)}$	0	1
		$S_{Cu(1/2)}-S_{Cu(1/2)}$	0	1

Lower spin states  $S = 0, 1, 2, 3, 4$  in the case of Mn-Mn and  $S = 0, 1, 2$  in the case of Cu-Mn dimers are likewise populated at elevated temperatures.

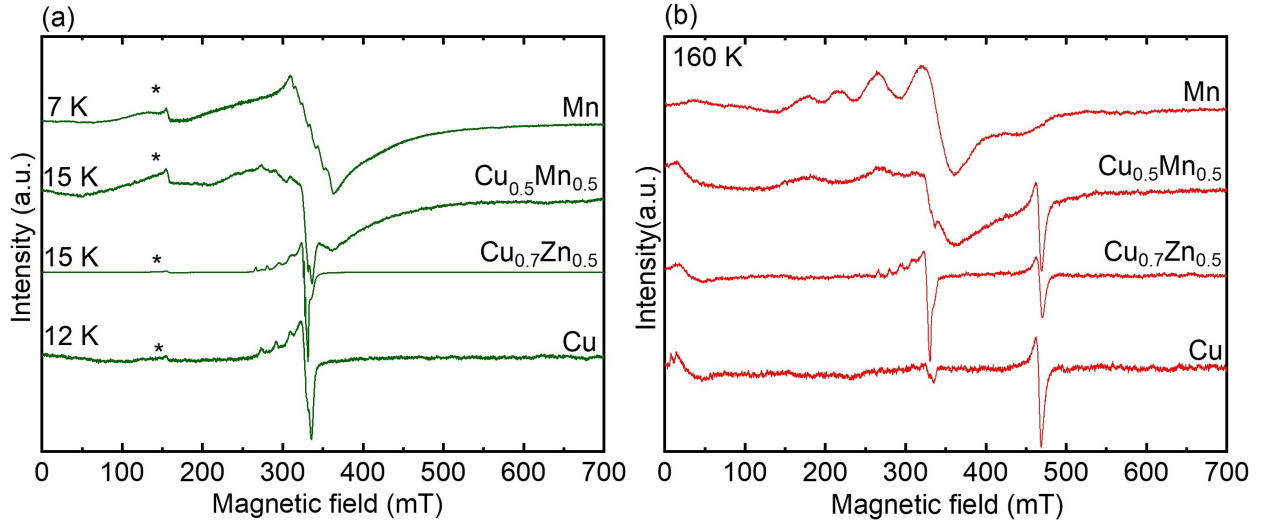


FIGURE 4.3: Comparison of X-band EPR experiments of DUT-49( $\text{M}_x\text{M}_{1-x}$ ) MOFs recorded at (a) low and (b) 160 K temperatures ( a weak signal at  $\sim 150$  mT indicates the minor Co(II) impurity species.

Figure 4.1c shows the temperature-dependent X- band EPR spectra of DUT-49(Mn). The low-temperature spectrum at  $T = 7$  K shows a signal at  $g = 2.007$  with a resolved hfs into six lines (Figure 4.3a). The  $g$ -value and the hfs sextet are characteristics of isolated Mn(II) ion[17] with an  $S = 5/2$  high spin state and a hyperfine interaction (hfi) with the  $^{55}\text{Mn}$  nucleus having  $I^{Mn} = 5/2$

characterised by an isotropic hyperfine coupling constant of  $A_{iso} = 240$  MHz. The spectrum exhibits only the central  $M_s = +1/2 \leftrightarrow -1/2$  spin transitions, whereas the outer  $M_s = \pm 1/2 \leftrightarrow \pm 3/2$  and  $M_s = \pm 3/2 \leftrightarrow \pm 5/2$  transitions are not resolved presumably because of large  $D$  strain effects. For spectra recorded at  $T > 30$  K (Figure 4.1c & 4.3a), a new multiline spectrum emerges, covering a broad field range of  $\sim 150$  mT  $< B < \sim 550$  mT at X-band frequencies. The intensity of this spectrum increase with rising temperatures. A comparable behavior is observed in the temperature-dependent Q-band spectra of DUT-49(Mn) (Figure 4.4a). Based on the multiline characteristic and temperature dependence, we may assign this spectrum to AFM-coupled Mn(II) - Mn(II) dimers. In this case of AFM coupled Mn(II) dimers, we expect total spin states  $S = 0, 1, 2, 3, 4,$  and  $5$  ( $S = 0$  singlet ground state), which is increasingly populated with rising temperatures. However, the poor resolution of the X- and Q- band spectra prevented a determination of the Spin Hamiltonian parameters of the Mn(II) - Mn(II) dimers here by simulation or fitting procedures. CW W- band spectra did not provide a better resolution and suffered from poor signal-to-noise ratios.

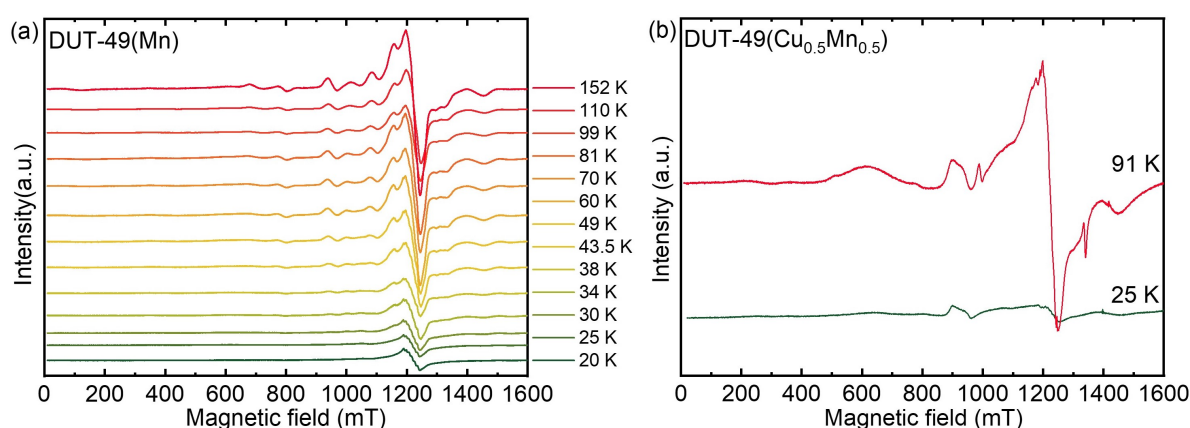


FIGURE 4.4: Temperature-dependent Q-band EPR spectra of (a) DUT-49(Mn) and (b) DUT-49(Cu<sub>0.5</sub>Mn<sub>0.5</sub>) MOFs

Meanwhile, the low-temperature X- band (Figures 4.1d & 4.32b) and Q- band (Figure 4.4b) EPR spectra of DUT-49(Cu<sub>0.5</sub>Mn<sub>0.5</sub>) show the coexistence of Cu(II) and Mn(II) monomer species with the emergence of Cu(II) - Cu(II) dimer as well upon increasing temperature above 80 K. Some characteristic spectral features of the Mn(II) - Mn(II) dimers at about 1450 mT, 1200 mT, and 900 mT are likewise distinguishable at Q- band whereas the X- band spectra suffer here from low signal to noise ratios and poor resolution except for the Cu(II) - Cu(II) dimer spectrum. An additional low field signal at 700 mT in the Q-band spectrum indicates the existence of further magnetic species in DUT-49(Cu<sub>0.5</sub>Mn<sub>0.5</sub>), which we tententially assign to an AFM coupled Cu(II) - Mn(II) dimer with possible total spin states  $S = 2$  and  $S = 3$ .

### 4.3 HKUST-1 MOFs

HKUST-1, also known as CuBTC or  $\text{Cu}_3\text{BTC}_2$  is one of the well-studied Cu-based MOF materials which contains dimeric copper PW units (Figure 2.2), especially for the adsorption of  $\text{CO}_2$ ,  $\text{CH}_4$ , and volatile organic compounds[3, 18, 19](Here onwards,  $\text{Cu}_3\text{BTC}_2$  MOF will be referred to as CuBTC). Usually, the two axial positions of the PWs are occupied by water/other solvent molecules. The removal of these molecules from the axial positions by heat/vacuum treatment leads to the formation of CUS at the Cu(II) atoms[3, 12, 20–22]. These CUS can enable direct metal-guest interaction during the adsorption process, and it is fascinating to investigate several types of metal-guest interactions in the MBTC (M- Cr, Mn, Fe, Co, Ni, Zn, Mo, Ru) frameworks[3]. Moreover, the combination of different bimetals in one framework can lead to outstanding new properties. In HKUST-1 structure, several combinations of PWs, such as Cu-Ru, Cu-Zn, Cu-Ni, Cu-Pd, Cu-Ag, Cu-Mn, Cu-Fe, Cu-Co, have been reported so far[3, 12, 18, 19]. In this regard, we examined Zn and Fe incorporated CuBTC MOFs through their magnetic signature, and these MOFs will be referred to as ZnCuBTC and FeCuBTC, respectively, in the proceeding sections.

#### 4.3.1 Zinc incorporated CuBTC MOF

The challenges encountered by Garai *et al.*[10] in synthesizing bimetallic DUT-49 MOFs via direct synthesis route and the 100 % incorporation efficiency from the PSM technique motivated us to investigate another bimetallic PW-based MOF by the PSM route. Hence, we attempted to synthesize Zn(II) incorporated CuBTC MOF via PSM technique where 5% of Zn(II) ions were incorporated on the Cu(II) sites (Figure 4.5) and evidenced by EDAX analysis( $\text{Zn}_{0.15}\text{Cu}_{2.85}\text{BTC}_2$ ). The phase purity was confirmed by PXRD given in Figure 4.10, and further, we utilized CW and pulse EPR techniques to interrogate the mixed PW formation and hf interaction between framework protons and the metal ions.

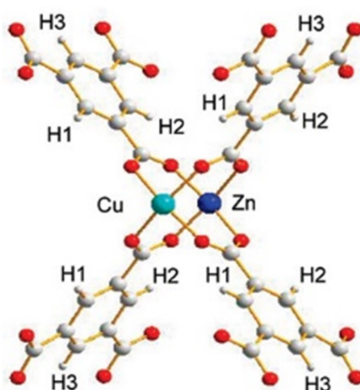


FIGURE 4.5: Bimetallic Zn incorporated CuBTC PW structure

Figure 4.6 shows temperature-dependent X-band EPR measurements of activated ZnCuBTC MOF in the range of  $10 \text{ K} < T < 292 \text{ K}$ . Similar to other PW-based MOFs, at low temperatures ( $< 80 \text{ K}$ ), one can observe the  $S = 1/2$  Cu(II) monomer species at  $\sim 260 \text{ mT} < B < \sim 360 \text{ mT}$  and might be attributed to the Cu(II)-Zn(II) PW units[4, 12]. The spin Hamiltonian parameters of hydrated and activated PSM ZnCuBTC are summarized in Table 4.2, and the simulated values (Figure 4.7) are well consistent with the Cu(II) monomer species of 1% Zn(II) doped CuBTC MOF[12] which is synthesized by solvothermal(SOL) technique ( $\text{Zn}_{0.03}\text{Cu}_{2.97}\text{BTC}_2$ ) where precursors of Zn and Cu ions are added together directly. Since the spin Hamiltonian parameters are slightly different from the Cu(II) monomer of parent CuBTC[12], we assign this particular feature to the  $S = 1/2$  Cu(II) monomer corresponds to the Cu(II)-Zn(II) PW units and not to the typical extra framework cupric ions or defective PW units. Unlike other PW-based Cu(II) monomer species discussed earlier, the activated ZnCuBTC shows an additional feature due to the  $^{63,65}\text{Cu}$  NQI (Table 4.2, Figure 4.7b), whereas it is absent for the water-coordinated hydrated PSM ZnCuBTC MOF.

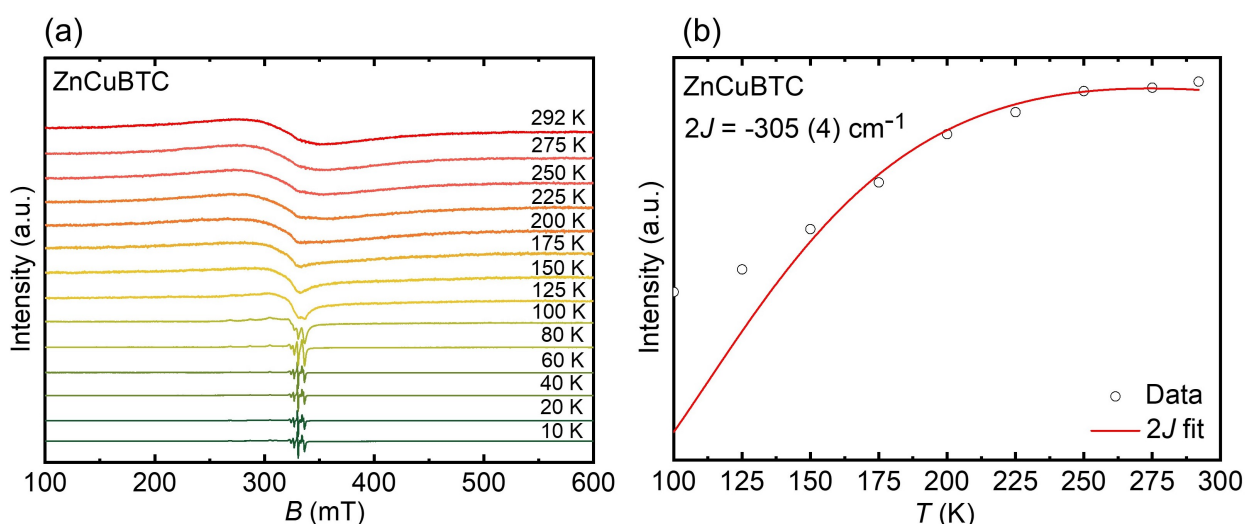


FIGURE 4.6: (a) Temperature-dependent X-band EPR spectra and (b) The intensity extracted from the temperature-dependent X-band EPR data of activated PSM ZnCuBTC fitted using Bleaney Bowers susceptibility equations for the coupled  $S = 1/2$  dimer species

At room temperature, the typical resolved spectrum of excited state of the AFM coupled Cu(II)-Cu(II) dimers with spin  $S = 1$  state (e.g. Figure 4.2b of DUT-49(Cu)) is not observed, instead a single isotropic ( $g_{iso} = \sim 2.11$ ) broadened signal is obtained with  $\Delta B^{pp} = 79 \text{ mT}$  at RT, which is comparable to the  $\Delta B^{pp}$  - value observed for CuBTC MOF[3, 4, 11]. Since PW units are not well separated by BTC linker, it is not magnetically isolated, and the inter-PW couplings cause broadening due to the exchange interactions between the populated  $S = 1$  state of Cu-Cu dimers in the CuBTC-based MOFs[3, 11]. However, the intensity extracted from the whole spectrum range of the temperature-dependent EPR data above  $T > 100 \text{ K}$  was fitted using the Bleaney-Bowers

equation[11] for an exchange-coupled homonuclear species, and the isotropic exchange interaction ( $2J$ ) is found to be  $2J = -305(4) \text{ cm}^{-1}$  (Figure 4.6b). The value of  $2J$  is in accordance with the exchange coupling constants of other antiferromagnetically coupled Cu(II) dimers[4, 11, 23].

TABLE 4.2: Spin Hamiltonian parameter of  $S = 1/2$  Cu(II) monomer species in PSM ZnCuBTC MOF measured at  $T = 7 \text{ K}$

PSM ZnCuBTC MOF	$g_{xx,yy}$	$g_{zz}$	$A_{xx,yy}$	$A_{zz}$	$Q_{xx,yy}$	$Q_{zz}$
Hydrated	2.055(2)	2.330(1)	45(3)	475(5)	-	-
Activated	2.041(1)	2.274(2)	95(3)	565(3)	-5(3)	10(2)

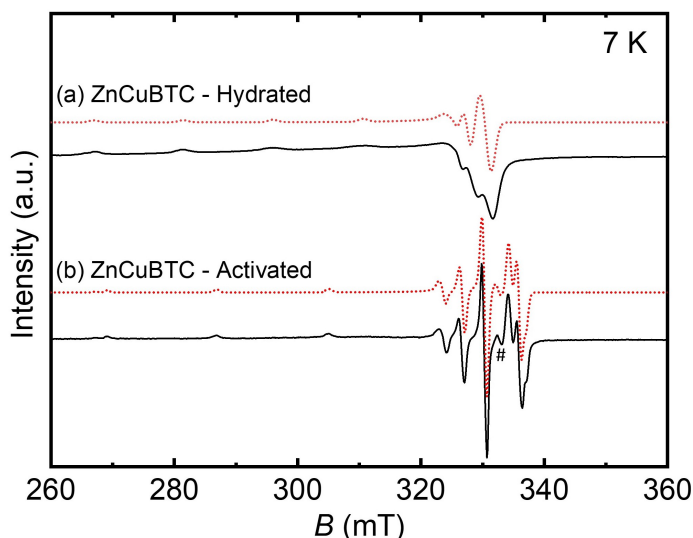


FIGURE 4.7: Experimental (black) and simulated (red) spectra of (a) hydrated and (b) activated PSM ZnCuBTC MOFs (# - additional feature due to NQI)

In addition to the CW EPR experiments, Davies ENDOR results of PSM ZnCuBTC are compared with the SOL ZnCuBTC MOF[12] to resolve weak ligand hf coupling between the Cu(II) ions and the closer  $^1\text{H}$  nuclei from the BTC linker with spin  $I^H = 1/2$  (Figure 4.5) which are hidden within the linewidth of the CW EPR spectrum. Figure 4.8 illustrates the orientation-selective X-band  $^1\text{H}$  ENDOR spectrum at  $B = 340 \text{ mT}$  ( $g_{xx,yy}$  position) of PSM ZnCuBTC and compares it with the solvothermally synthesized SOL ZnCuBTC MOF[12]. Jee *et al.*[12] evidenced the interaction of H1 proton from the linker (Figure 4.5) with the cupric ions in the PW unit and the corresponding H1 proton ENDOR feature is comparable with the PSM ZnCuBTC result (Figure 4.8). Further, this doublet H1 proton feature with  $\sim 1.2 \text{ MHz}$  splitting is a characteristic spectral signature of the nuclear environment of the cupric ions in ZnCuBTC MOF[12]. In this way, the ENDOR result ensures the formation of Zn(II)-Cu(II) pairs, and the  $S = 1/2$  Cu(II) monomer ions involved in hf



interactions are from the bimetallic Zn(II)-Cu(II) PW units. However, the signature of Zn(II) nuclei with spin  $I^{Zn} = 5/2$  could not be detected due to its low natural abundance of 4.11 % [12].

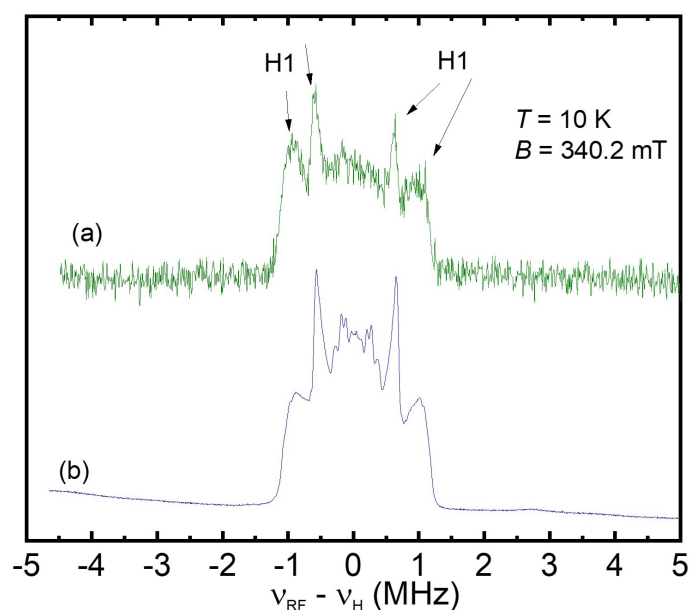


FIGURE 4.8: Experimental orientation selective CW X-band  $^1\text{H}$  ENDOR spectra of (a) PSM Zn-CuBTC (this work) and (b) SOL ZnCuBTC [12] at  $B = 340$  mT.

### 4.3.2 Iron incorporated CuBTC MOF

In a similar fashion, Bitzer *et al.* [3] attempted to synthesize Fe-incorporated CuBTC by several syntheses ways such as solvothermal, microwave-assisted, syntheses at ambient pressure along with PSM technique [24]). From those syntheses techniques, they also got undesired side products such as  $\alpha\text{-Fe}_2\text{O}_3$ , MIL-100(Fe) and denoted those compounds as CuBTC/ $\alpha\text{-Fe}_2\text{O}_3$  and CuBTC/MIL-100(Fe). Through the doping of metal ions in the Cu-Cu PW units via the PSM technique was feasible in DUT-49 and HKUST-1 MOFs, the PSM technique mentioned in ref. [24] was not successful in obtaining FeCuBTC MOF material. Therefore, they found a way to synthesize a phase pure Fe-CuBTC MOF through microwave-assisted method [3] with 30 % Fe incorporation, and the complex bimetallic mixed PW structure inspired us to scrutinize the local structure to confirm the mixed PW formation. In this regard, we interrogated the bimetallic FeCuBTC MOF in comparison with the parent CuBTC MOF and the mixed phase CuBTC/ $\alpha\text{-Fe}_2\text{O}_3$  and CuBTC/MIL-100(Fe) compounds by means of EPR spectroscopy as a complementary study along with the XRD, XANES (X-ray Absorption Near Edge Structure), EXAFS (Extended X-ray Absorption Fine Structure) and IR results [3].

EPR spectra have been recorded for the above-mentioned four materials to corroborate further the results (see Figure 4.9 and Table 4.3). All samples showed comparable EPR spectra at 15 K displaying the signal of monomeric Cu(II) species (A) with partly resolved Cu(II) hyperfine (hf) splitting (parameters of A:  $g_{zz} = 2.340$ ,  $g_{xx,yy} = 2.05$ ,  $A_{zz} = 485$  MHz). These features might be assigned to defective Cu-Cu paddle-wheel units or extra-framework cupric ions. Only for FeCuBTC, an additional broad baseline signal (B) was observed. The  $g_{xx}/yy$  spectral position at 328 mT of signal A was present in the spectra recorded at 100 K for all samples and at RT for CuBTC, CuBTC/MIL-100(Fe), and CuBTC/Fe<sub>2</sub>O<sub>3</sub>. In CuBTC at RT, an additional broad signal (C) with a line width of about 80 mT and an isotropic  $g$ -value of  $g = 2.149$  was observed, which could be assigned to the excited  $S = 1$  state of the antiferromagnetically coupled Cu(II) ions of the Cu-Cu paddle-wheel units.[11] Presumably, the signal observed for CuBTC/MIL-100(Fe) at RT displaying a comparable line width might be likewise assigned to the Cu-Cu paddle-wheel although the  $g$ -value was somewhat lower. In the case of CuBTC/Fe<sub>2</sub>O<sub>3</sub>, the line width of this signal was considerably smaller, and an assignment to the Cu-Cu paddle-wheel was questionable, although its  $g$ -value was close to that of CuBTC MOF.

FeCuBTC exhibited a distinct spectrum at RT. Here, an intense EPR signal (D) with a smaller  $g$ -value ( $g = 2.023$ ) and line width (36 mT) was observed. The total EPR signal intensity at room temperature was higher in comparison to the three other samples (see Table 4.3). Neither signal A of the monomeric Cu(II) species nor signal C of Cu-Cu paddle wheel units were detected for FeCuBTC at RT. Moreover, the resolved fine structure signals of the  $S = 1$  state of the Cu-Cu paddle-wheels[11], which are typically observed at 20 mT and 474 mT at 100 K, were not detected. Based on its  $g$ -value, signal D cannot be assigned to either monomeric Cu(II) species or Cu(II) pairs in the paddle-wheel unit. Therefore, we suggest that it was related to Cu(II)-Fe(III) species in these samples. In addition, a comparison of the RT and 100 K spectra of FeCuBTC revealed that signal D did not disappear with decreasing temperature but exhibited a pronounced line broadening. Consequently, the broad baseline signal (B) recorded at 10 K for this sample might likewise be assigned to Cu(II)-Fe(III) species. Note that high spin Fe(III) species in a highly symmetric octahedral or tetrahedral environment would also provide an isotropic signal at  $g = 2.00$ . However, the disappearance of signal features for FeCuBTC, which would indicate Cu-Cu paddle-wheel units, suggested that signal D was not related to such Fe(III) species but would instead indicate coupled Cu(II)-Fe(III) moieties.

Furthermore, the substantially larger overall EPR signal intensity of FeCuBTC in comparison with CuBTC, CuBTC/MIL-100(Fe) and CuBTC/Fe<sub>2</sub>O<sub>3</sub> supported this interpretation, where a novel EPR active species was formed in FeCuBTC, which was not present in the other three

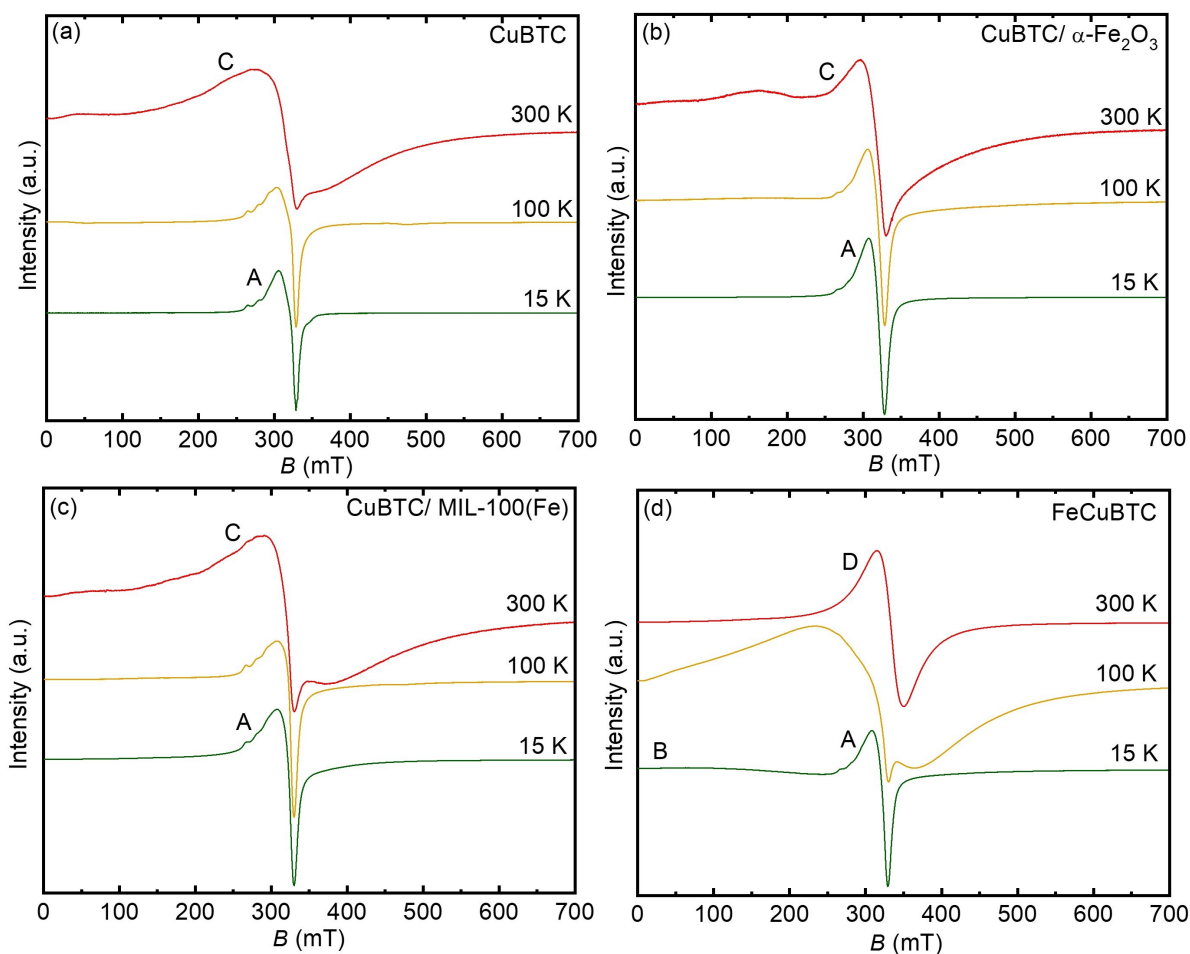


FIGURE 4.9: EPR spectra of (a) CuBTC, (b) CuBTC/ $\alpha$ -Fe<sub>2</sub>O<sub>3</sub>, (c) CuBTC/MIL-100(Fe) and (d) FeCuBTC measured at 15 K, 100 K, and 300 K temperatures.

materials. Although the exact nature of these Cu(II)-Fe(III) species could not be derived from these experiments, its  $g$ -value and temperature dependence revealed some of its characteristics. The assumption of strongly exchanged coupled Cu(II)-Fe(III) pairs and the coupling between the Cu(II) electron spin ( $S_{Cu} = 1/2$ ) the iron electron spin ( $S_{Fe} = 5/2$ ) results in two spin states of the pair,  $S = 2$  and  $S = 3$ . According to Buluggiu *et al*[25], the  $S = 3$  state provides a  $g$ -value of  $g_{pair} = 2.00$ , which was in reasonable agreement with the measured  $g$ -parameters of signal  $D$  if typical isotropic  $g$ -values of 2.15 and 2.00 are assumed for Cu(II) and Fe(III). The isotropic nature of the signal  $D$  was indicative of strong magnetic exchange interactions among the Cu(II)-Fe(III) species. The strong line broadening with decreasing temperature was astonishing and atypical for paramagnetic systems, but such effects are common for magnetic materials[26].

In addition, EPR analysis complements the EXAFS results indicating the presence of both bimetallic Fe-Cu and monometallic Fe-Fe PW units in FeCuBTC MOF[3] but not in other CuBTC/MIL-100(Fe) and CuBTC/Fe<sub>2</sub>O<sub>3</sub> compounds.

#### 4.4. Conclusion

TABLE 4.3: Comparison of intensity/mass, relative total EPR signal intensity, isotropic  $g'$ -value and line width  $\Delta B_{pp}$ (mT) at  $T = 300$  K temperature.

Sample	Intensity/ mass	Relative total EPR signal intensities	Isotropic ' $g_A$ '	Linewidth $\Delta B^{pp}$ (mT)
CuBTC	156	1	2.149	80.0
CuBTC/Fe <sub>2</sub> O <sub>3</sub>	467	3.1	2.130	35.0
CuBTC/MIL-100(Fe)	270	1.7	2.102	83.0
FeCuBTC	1476	9.5	2.023	36.0

#### 4.4 Conclusion

**DUT-49(M,M)**: EPR spectroscopy revealed for both transition metal dimers, Cu(II)- Cu(II) and Mn(II) - Mn(II), in the paddle wheel units of MOFs DUT-49(Cu) and DUT-49(Mn) an antiferromagnetic coupling. Besides these metal dimers in the regular paddle wheel units, monomeric paramagnetic Cu(II) and Mn(II) species are observed, which most likely indicates the presence of defective paddle wheels with a missing metal ion. In the case of the mixed metal ion MOF DUT-49(Cu<sub>0.7</sub>Zn<sub>0.3</sub>), the formation of binuclear paramagnetic Cu(II) - Zn(II) dimers besides the antiferromagnetic coupled Cu(II) - Cu(II) dimers in the paddlewheel units could be confirmed. More complicated spectra have been obtained for MOF DUT-49(Cu<sub>0.5</sub>Mn<sub>0.5</sub>) that allowed for the unambiguous identification of Cu(II) - Cu(II) dimers and further indicated the presence of Mn(II) - Mn(II) dimers and AFM coupled Cu(II) - Mn(II) dimers. Our results confirm the complete PSM ion exchange of Co(II) in the DUT-49 framework by other divalent transition metal ions, such as Cu(II), Zn(II), and Mn(II), through the magnetic coupling of the divalent metal centers.

**ZnCuBTC**: The diamagnetic 5% of Zn(II) ions are incorporated on the Cu(II) sites, and the post-exchange modification of Zn(II) in CuBTC MOF is successfully evidenced by the CW EPR results. In addition, the pulse ENDOR result evidenced the hf coupling between the distinct framework protons with the Cu(II) ions which is pretty much comparable with the reported literature[12] and once again confirmed the Zn(II)-Cu(II) PW formation.

In conclusion, EPR spectroscopy confirms PSM is possible in PW-based MOFs through the magnetic coupling of metal centers.

**FeCuBTC**: It was found that a careful, in-depth characterization of the obtained mixed-metal materials and a comparison to other Fe- and Cu-containing materials was necessary to undoubtedly confirm the formation of a truly phase-pure FeCuBTC material. The recorded EPR spectra supported the hypothesis of bimetallic PWs for FeCuBTC.

## 4.5 Experimental Details

### DUT-49(M,M)

The parent MOF DUT-49(Co) was synthesized from the solvothermal reaction using a metal ion precursor and the organic linker mentioned in B. Garai *et al*[10]. Further, via post-ion exchange modification, Co(II) ion was exchanged [10] by Mn(II), Cu(II) and Zn(II) metal centers and obtained DUT-49(Cu), DUT-49(Mn), DUT-49(Cu<sub>0.5</sub>Mn<sub>0.5</sub>) and DUT-49(Cu<sub>0.7</sub>Zn<sub>0.3</sub>) MOFs[10]. Continuous wave (CW) X-band EPR measurements were performed from  $T = 7$  K to  $T = 170$  K temperature range. As the sample is immersed in polar solvent acetone, it is not possible to record signals above  $T = 170$  K due to dielectric losses unless using the capillary technique. For the X-band experiments, a Bruker EMXmicro spectrometer connected with a Bruker ER4119HS cylindrical cavity using a He cryostat ESR900, Oxford instruments, was used. Experimental parameters microwave power, modulation amplitude and modulation frequency were maintained at 0.2 mW, 10 G, and 100 kHz, respectively, for all the X-band measurements to acquire good-quality spectra. CW Q-band EPR spectra were measured using Bruker EMX 10-40 spectrometer fitted with a cylindrical cavity and an Oxford Instruments CF935 cryostat at  $T = 20$  K and 152 K. At Q-band frequency, microwave power, modulation frequency and modulation amplitude were set to 1.8 - 18 mW based on the signal quality, 100 kHz and 2.7 mT, respectively. W-band experiments (95 GHz) were performed using an Elecsys E600 spectrometer equipped with a Bruker E600 1021H TeraFlex resonator and a superconducting magnet (Bruker 6T SC). At W-band frequency, microwave power was kept at 5  $\mu$ W with modulation frequency and modulation amplitude equal to 100 kHz and 5 G, respectively.

### ZnCuBTC and FeCuBTC

The CuBTC MOF was synthesized according to the procedure described elsewhere[27, 28]. Further, Zn(II) PSM was done similarly to the procedure described elsewhere[24]. The comparison of the PXRD of PSM ZnCuBTC MOF in Figure 4.10 is in good agreement with the diffraction pattern of CuBTC MOF before PSM, which is in cubic structure (space group  $Fm\bar{3}m$ ) [19, 24]. The SEM image in Figure 4.11 shows the morphology of PSM ZnCuBTC MOF is in  $\sim 10$  micron-sized polygon shapes and the similar morphology was reported for other CuBTC MOFs[29, 30]. The EDAX result reveals the fraction of the post-synthetically incorporated Zn(II), and it is found to be Zn - 5% and Cu - 95% ( $Zn_{0.15}Cu_{2.85}(BTC)_2$ ).

The synthesis procedure of the FeCuBTC MOF is mentioned in J. Bitzer *et al*[3].

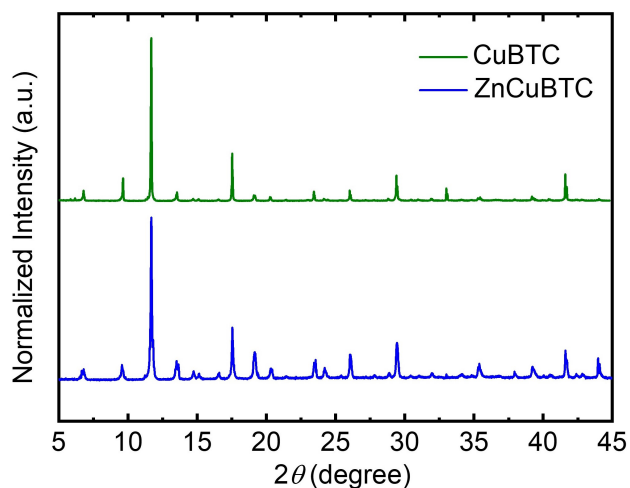


FIGURE 4.10: PXRD of Post synthetically modified ZnCuBTC confirming the formation

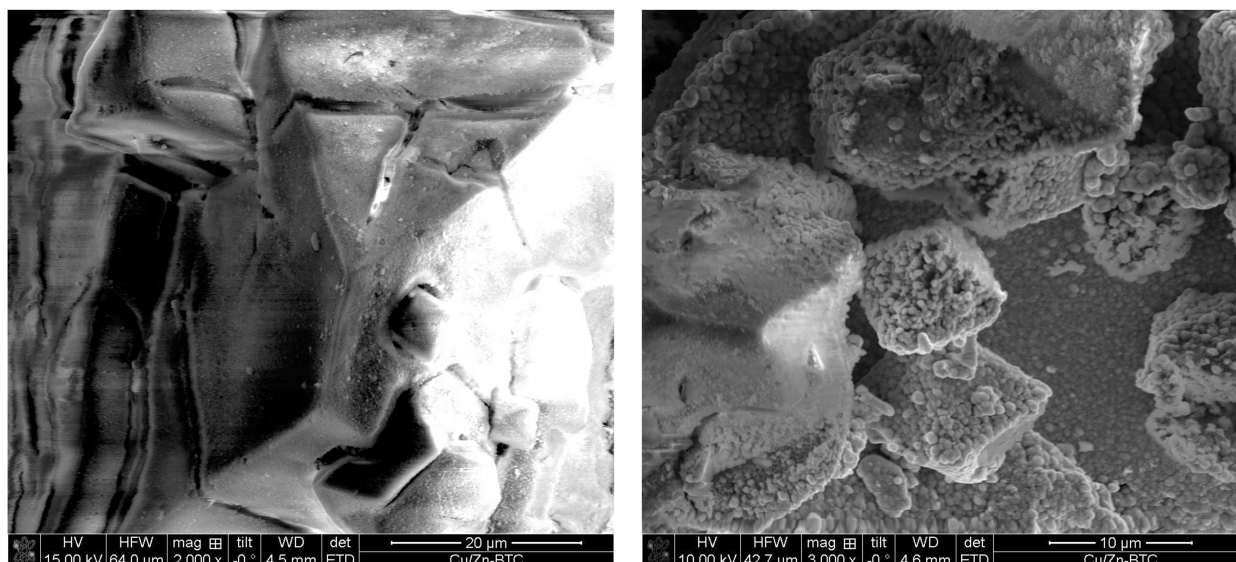


FIGURE 4.11: SEM images of PSM ZnCuBTC MOF in different magnifications

The EPR spectra were measured on a BRUKER EMXmicro X-band spectrometer using an Oxford instruments ESR900 cryostat. As all spectra were found to be broadened, the modulation amplitude has been maintained as 10 G for the EPR measurements. The microwave power has been kept at either 2 mW or 0.2 mW depending on the signal quality. EPR spectra were simulated in MATLAB R2019b, using the EasySpin EPR data simulation package[31] version 6.6.0-dev.47, which is based on numerical diagonalization of the spin Hamiltonian.

# Bibliography

- (1) Mandal, S.; Natarajan, S.; Mani, P.; Pankajakshan, A. *Advanced Functional Materials* **2021**, *31*, 2006291.
- (2) Denysenko, D.; Volkmer, D. *Faraday Discussions* **2017**, *201*, 101–112.
- (3) Bitzer, J.; Otterbach, S.; Thangavel, K.; Kultaeva, A.; Schmid, R.; Pöppl, A.; Kleist, W. *Chem. Eur. J.* **2020**, *26*, 5667–5675.
- (4) Thangavel, K.; Mendt, M.; Garai, B.; Folli, A.; Bon, V.; Murphy, D. M.; Kaskel, S.; Pöppl, A. *AIP Advances* **2023**, *13*, 015019.
- (5) Koeberl, M.; Cokoja, M.; Herrmann, W. A.; Kuehn, F. E. *Dalton Transactions* **2011**, *40*, 6834–6859.
- (6) Aiyappa, H. B.; Saha, S.; Garai, B.; Thote, J.; Kurungot, S.; Banerjee, R. *Crystal growth & design* **2014**, *14*, 3434–3437.
- (7) Ehrling, S.; Senkovska, I.; Bon, V.; Evans, J. D.; Petkov, P.; Krupskaya, Y.; Kataev, V.; Wulf, T.; Krylov, A.; Vtyurin, A., et al. *Journal of Materials Chemistry A* **2019**, *7*, 21459–21475.
- (8) Maniam, P.; Stock, N. *Inorganic chemistry* **2011**, *50*, 5085–5097.
- (9) Bhunia, M. K.; Hughes, J. T.; Fettinger, J. C.; Navrotsky, A. *Langmuir* **2013**, *29*, 8140–8145.
- (10) Garai, B.; Bon, V.; Krause, S.; Schwotzer, F.; Gerlach, M.; Senkovska, I.; Kaskel, S. *Chemistry of Materials* **2020**, *32*, 889–896.
- (11) Pöppl, A.; Kunz, S.; Himsl, D.; Hartmann, M. *The Journal of Physical Chemistry C* **2008**, *112*, 2678–2684.
- (12) Jee, B.; Eisinger, K.; Gul-E-Noor, F.; Bertmer, M.; Hartmann, M.; Himsl, D.; Pöppl, A. *The Journal of Physical Chemistry C* **2010**, *114*, 16630–16639.
- (13) Wasserman, E.; Snyder, L.; Yager, W. *The Journal of Chemical Physics* **1964**, *41*, 1763–1772.
- (14) Ehrling, S.; Mendt, M.; Senkovska, I.; Evans, J. D.; Bon, V.; Petkov, P.; Ehrling, C.; Walenszus, F.; Pöppl, A.; Kaskel, S. *Chemistry of Materials* **2020**, *32*, 5670–5681.
- (15) Polyukhov, D. M.; Krause, S.; Bon, V.; Poryvaev, A. S.; Kaskel, S.; Fedin, M. V. *J. Phys. Chem. Lett.* **2020**, *11*, 5856–5862.

- (16) Bencini, A.; Gatteschi, D., *EPR of exchange coupled systems*; Dover Publications: 2012.
- (17) Schreurs, J. *The Journal of Chemical Physics* **1978**, *69*, 2151–2156.
- (18) Goyal, P.; Paruthi, A.; Menon, D.; Behara, R.; Jaiswal, A.; Keerthy, V.; Kumar, A.; Krishnan, V.; Misra, S. K. *Chemical Engineering Journal* **2022**, *430*, 133088.
- (19) Peedikakkal, A. M. P.; Aljundi, I. H. *ACS omega* **2020**, *5*, 28493–28499.
- (20) Prestipino, C.; Regli, L.; Vitillo, J. G.; Bonino, F.; Damin, A.; Lamberti, C.; Zecchina, A.; Solari, P.; Kongshaug, K.; Bordiga, S. *Chemistry of materials* **2006**, *18*, 1337–1346.
- (21) Jee, B.; St. Petkov, P.; Vayssilov, G. N.; Heine, T.; Hartmann, M.; Pöppl, A. *The Journal of Physical Chemistry C* **2013**, *117*, 8231–8240.
- (22) Jee, B.; Koch, K.; Moschkowitz, L.; Himsl, D.; Hartman, M.; Pöppl, A. *The Journal of Physical Chemistry Letters* **2011**, *2*, 357–361.
- (23) Thangavel, K.; Walenszus, F.; Mendt, M.; Bon, V.; Kaskel, S.; Pöppl, A. *The Journal of Physical Chemistry C* **2023**, DOI: 10.1021/acs.jpcc.2c08905.
- (24) Sava Gallis, D. F.; Parkes, M. V.; Greathouse, J. A.; Zhang, X.; Nenoff, T. M. *Chemistry of Materials* **2015**, *27*, 2018–2025.
- (25) Buluggiu, E. *Journal of Physics and Chemistry of Solids* **1982**, *43*, 997–1001.
- (26) Goede, O.; Backs, D.; Heimbrod, W.; Kanis, M. *physica status solidi (b)* **1989**, *151*, 311–318.
- (27) Böhlmann, W.; Pöppl, A.; Sabo, M.; Kaskel, S. *The Journal of Physical Chemistry B* **2006**, *110*, 20177–20181.
- (28) Schlichte, K.; Kratzke, T.; Kaskel, S. *Microporous and Mesoporous Materials* **2004**, *73*, 81–88.
- (29) Kim, D.; Kim, I. J.; Kwon, H. T.; Paeng, K.; Lee, H. *ACS omega* **2023**.
- (30) Maleki, A.; Hayati, B.; Naghizadeh, M.; Joo, S. W. *Journal of Industrial and Engineering Chemistry* **2015**, *28*, 211–216.
- (31) Stoll, S.; Schweiger, A. *Journal of magnetic resonance* **2006**, *178*, 42–55.



## Chapter 5

# Atomistic and electronic structure of Ni(II)-NO adduct in a MFU-4l(Ni):NO<sub>2</sub> MOF

### 5.1 Introduction

The interaction of nitric oxide with transition metal ions (TMIs) supported on microporous systems has been abundantly studied with a view of finding the relationship among bonding, stability, and reactivity of the metal-nitrosyl group[1–6]. Moreover, NO adsorption studies may reveal valuable information about the accessibility, number, chemical reactivity and electron pair acceptor strength [1, 4, 7–12] of the TMIs sites as well as provide fundamental insights into the mechanism of essential processes, e.g. abatement of NO<sub>x</sub> emissions [3, 4, 13, 14].

Infrared (IR) spectroscopy has been successfully employed to probe metal-NO adducts encapsulated in microporous materials[2, 3, 15]. This technique has been proven to be exceedingly powerful for revealing NO-adducts even in operando conditions[16, 17]. However, IR spectroscopy cannot provide direct insight into the intimate features of metal-nitrosyl chemical bonding, which is particularly nontrivial to unravel. This ambiguity arises from the close relative energy of the NO-\* orbitals compared to the d orbitals of first-row TMIs, which makes the accurate description of the oxidation and/or spin state of such species difficult[18–20].

Due to the paramagnetic nature of metal-NO adducts, electron paramagnetic resonance (EPR) spectroscopy is ideally suitable for obtaining exquisite details on the cryptic bonding of NO to transition metal centers[1, 10, 11, 14, 21, 22]. The application of sophisticated pulse EPR techniques allows assessing the degree of covalency and spin delocalization between the metal-NO bond as well as the one with all the other ligands magnetically active, offering additional complementary insight into the electronic structure of the NO-metal ion bonding with respect of IR

spectroscopies [23, 24]. The subsequent reproduction of the EPR spectroscopic findings with electronic structure methods translates the experimental findings into microscopic structures enabling structure-function correlation of metal-NO species[25–28].

While EPR investigations of NO adsorption over metal oxide surfaces and zeolites are abundant[4–6, 10, 23–26, 29], only a few magnetic resonance studies of such species have been reported for the metal-organic framework (MOF) compounds[30–33], a class of microporous materials which has attracted substantial research interest within the last decades. In these systems, the coordination of NO with coordinatively unsaturated (CUS) metal ions has been probed by EPR methodologies. On the one hand, weak physisorption of nitric oxide at closed-shell Al(III) sites was detected in MIL-100 by observing the interaction of the unpaired electron of NO with the nuclear spin of  $^{27}\text{Al}$  nucleus[31]. Analysis employing density functional theory (DFT) indicated that about 95%–97% of the spin density is located at the NO molecule and only 2%–4% on the aluminium ion, underlying the weak interaction of the probe molecule with the framework metal ion.

On the other hand, thermally stable paramagnetic EPR active Ni(II)NO adducts occurred upon adsorption of NO at defective open-shell Ni(II) paddle-wheel species in DUT-8(Ni). Based on their  $g$ -tensor, two distinct Ni(II)NO moieties have been identified and interpreted in terms of an axially and equatorially binding nitroxide molecule[32] and comparison with previously published investigations of Ni(II)NO complexes formed at the surface of Ni-doped MgO powders[34, 35]. However, direct proof of this coordination motive and a deeper understanding of the corresponding electronic structure has not been presented yet.

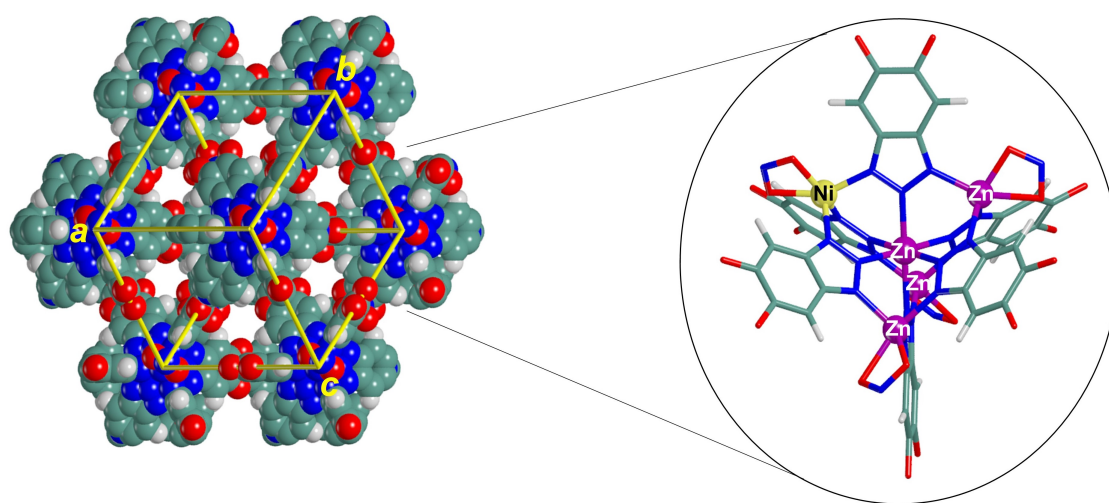


FIGURE 5.1: View along the  $(-1 -1 -1)$  face of Ni-MFU-4l-NO<sub>2</sub> space-filling periodic model. An inset of the main subunit of the material is shown on the right. C, N, O, Ni, Zn and H are green, blue, red, yellow, violet, and white colour, respectively.

In this work[1], a Ni(II)-substituted variant of the rigid MFU-4l(arge) framework family[36] comprising Ni-NO<sub>2</sub> coordination units[37] is adopted as a model case for the formation of Ni(II)NO species in a metal-organic framework. Through post-synthetic metal and ligand exchange, the Ni(II) ions substitute the peripheral Zn(II) sites in the pentanuclear Kuratowski-type SBU, displaying five-fold coordination with three nitrogen atoms (N<sub>f</sub>) from the SBU and two oxygen atoms from coordinating nitrite ion (see Figure 5.1)[38]. This leaves a potential sixth CUS site for the binding of an adsorbed nitric oxide molecule to form a stable six-fold octahedral-type coordination of the nickel ion.

First, high-field W-band CW EPR spectroscopy is employed to verify the  $S = 1$  electron spin state of the Ni(II) ions in MFU-4l-NO<sub>2</sub> prior to NO adsorption. Subsequently, conventional X-band CW-EPR experiments are employed to reveal the formation of Ni(II)NO complexes upon the exposure of Ni(II)-containing MFU-4l-NO<sub>2</sub> to gaseous nitric oxide. Pulse EPR experiments reveal the <sup>14</sup>N hyperfine (hf) interactions with the nitrogen nuclei N<sub>f</sub> belonging to the first and second coordination sphere of nickel ion and with the NO allowing to assess the nature of the chemical bonding between the nickel and the different nitrogen ligands. Cutting-edge quantum chemical computations of the magnetic parameters of the five-coordinated Ni(II) ion in the parent Ni-MFU-4l-NO<sub>2</sub> compound and of the Ni(II)NO species formed after NO adsorption translate the spectroscopic findings into atomistic structure unravelling the unique electronic structure of nickel-nitrosyl moieties supported on a MOF platform[1].

## 5.2 EPR investigations of Ni-MFU-4l-NO<sub>2</sub>

### 5.2.1 CW-EPR spectroscopy and coordination geometry of Ni(II) in Ni-MFU-4l-NO<sub>2</sub>

In general, non-Kramer (integer spin) systems like the Ni(II) ion having a d<sup>8</sup> electronic configuration with spin  $S = 1$  are challenging to detect in EPR experiments at conventional X- and Q-band mw frequencies because of their large ZFS[39–41]. As a consequence, the allowed EPR transitions ( $\Delta M_s = \pm 1$ ) cannot be excited by mw quanta being too small. Only a very few Ni(II)-containing materials were characterized employing X- and Q- band EPR spectroscopy for Ni(II) species having smaller or comparable ZFS to the MW frequency[40–42]. In order to overcome these complications, CW high-frequency EPR (HF-EPR) spectroscopy techniques[43–45], ( $\sim 90$  GHz to  $\sim 611$  GHz and magnetic fields up to  $\sim 22$  T) and even time-domain terahertz EPR measurements[46] were utilized to acquire the complete triplet spectrum of the  $S = 1$  Ni(II) species. Furthermore, temperature- and field-dependent magnetic susceptibility measurements also provided spin Hamiltonian parameters for such high-spin Ni(II) systems[39, 43].

In our case, Ni-MFU-4l-NO<sub>2</sub> was first measured at Q-band frequency (see SI, Figure 5.10b), and a part of the triplet spectrum was observed at 300 mT. The indication of ZFS is ambiguous to conclude the value of the ZFS of Ni(II) species as the energy of ZFS is expected to be larger than the MW quanta energy at Q-band. In order to obtain the ZFS along with other spin Hamiltonian parameters, a W-band CW-EPR spectrum was recorded at 20 K (see Figure 5.2). Interestingly, ZFS energy of Ni(II) ion is not so large, and an intense forbidden transition ( $\Delta M_s = \pm 2$ ) arose at 1450 mT in the W-band spectrum, whereas some poorly resolved allowed transitions ( $\Delta M_s = \pm 1$ ) were observed at high fields 20004000 mT. The following spin Hamiltonian was used for the Ni(II) species with spin  $S = 1$  to interpret the Q- and W-band EPR data.

$$\hat{H} = \mu_B \vec{B} \mathbf{g} \hat{S} + D [\hat{S}_z^2 - \frac{1}{3} S(S+1)] + E (\hat{S}_x^2 + \hat{S}_y^2) \quad (5.1)$$

where the first term is the electron Zeeman interaction between  $S = 1$  electron spins of the Ni(II) ions and the applied external magnetic field with the Bohr magneton  $\mu_B$ , the electron spin operator  $\hat{S}$ , the electron  $g$ -tensor  $\mathbf{g}$ , and the applied external magnetic field  $\vec{B}$ . The second term indicates the zero-field splitting (ZFS), and  $D$  and  $E$  are the axial and rhombic ZFS parameters, respectively.

The spin Hamiltonian parameters of the Ni(II) species  $g_{xx} = 2.050$ ,  $g_{yy} = 2.050$ ,  $g_{zz} = 2.060$ ,  $D = 35.5$  GHz ( $1.18 \text{ cm}^{-1}$ ), and  $E = 0.5$  GHz ( $0.17 \text{ cm}^{-1}$ ) are obtained by spectral simulation and suggests that the symmetry around Ni(II) ion is slightly rhombic. Figure 5.11 (see SI) shows the angular dependencies of the Ni(II) EPR signals computed with the derived spin Hamiltonian parameters at W- and Q-band frequencies, confirming the assignment of the signals observed at about 1450 mT (W-band, SI Figure 5.11a) and 300 mT (Q-band, SI Figure 5.11b) to the  $\Delta M_s = \pm 2$  transition and the consistency of both experiments.

It is well-known that zero-field splitting is intrinsically connected with the geometric structure of Ni(II) complexes and originated from the spin-spin interactions mediated by the ligand field and from the spin-orbit coupling[44–46]. While relatively small ZFS values were reported for octahedral Ni(II) complexes[47–50], larger ZFS parameters occur for tetrahedral coordination[44, 51]. Hence, the estimated values of  $D$  and  $E$  for Ni(II) ions in Ni-MFU-4l-NO<sub>2</sub> may be used to retrieve peculiar details on the five coordination-based atomistic structures of the Ni(II) paramagnetic center, as discussed below.

To transpose the spectroscopic results extracted from the analysis of W-band experiment into a microscopic structure, *ab initio* calculations of the  $g$ -tensor and ZFS were performed on the

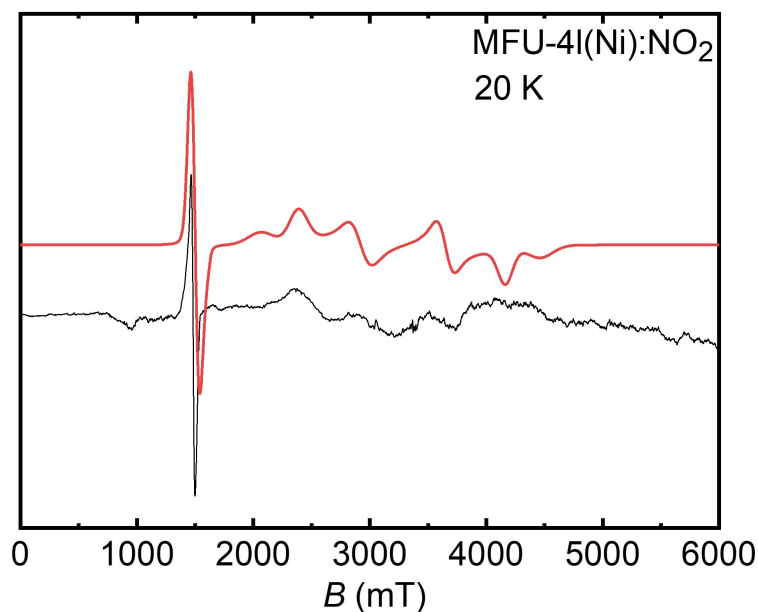


FIGURE 5.2: Experimental (black line) and simulated (red line) CW EPR W-band spectrum of Ni(II) ions having  $S = 1$  in Ni-MFU-4l-NO<sub>2</sub> obtained at 20 K.

optimized structure of Ni(II)-MFU-4l reported in Figure 5.3. The Ni(II) ion occupies a single peripheral site of the Kuratowski-type SBU displaying a five-fold coordination with three lattice nitrogen atoms and two oxygen atoms from the NO<sub>2</sub> - ligand. The Ni-O bond lengths are slightly longer ( $\approx 0.27$  nm) as compared to the Ni-N bond lengths ( $\approx 0.20$  nm). A quantitative analysis from EDAX results indicates that the amount of Ni in the material is 22.5 % in atomic weight (and 21 % in molar weight) in comparison with Zn(II) centers, justifying the assumption of considering only one Ni(II) site per one SBU in the model.

Although DFT calculations of the ZFS often fail to arrive at the correct sign and magnitude of  $D$  and/or  $E$  parameters[52, 53], the computed  $D$  and  $E$  parameters obtained at B2PLYP/def2-QZVP level of theory are in good agreement with the experimental ones (see Table 5.1). The superiority of double-hybrid functionals with respect to more common hybrid functionals lies in a better description of the excited states of different multiplicities, which contribute significantly to the ZFS parameters[54]. The prevalent source of computed ZFS arises from the spin-orbit coupling effect, in agreement with other open-shell transition metal ions[55]. The calculated spin-spin contribution accounts only for 0.3 % for  $D$  and 9 % for  $E$  parameters. For comparison, a tetrahedral Ni(II) ion in the Ni-MFU-4l model with a Cl<sup>-</sup> ligand (see SI Figure 5.12b and Table 5.1) instead of NO<sub>2</sub><sup>-</sup> provides an axially symmetric  $g$  - and ZFS tensor with  $D$  parameter that is further overestimated with respect to the experimental value validating the five-coordinated structure presented in Figure 5.3. Otherwise, a slightly rhombic  $g$  -tensor is predicted from the calculations for Ni-MFU-4l-NO<sub>2</sub> model (Table 5.1) consistent with the experimental values.

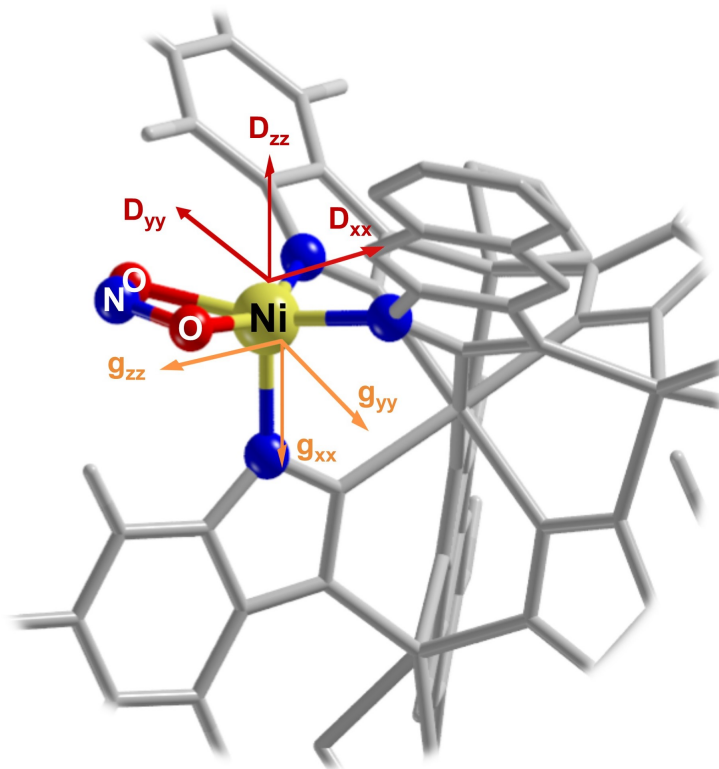


FIGURE 5.3: Geometry optimized periodic structures at B3LYP-D3/pob-TZVP-2 of Ni-MFU-4l-NO<sub>2</sub>. The computed  $g$ - and  $D$ -tensor frames are also reported.

TABLE 5.1: Experimental and computed spin Hamiltonian parameters for spin  $S = 1$  Ni(II) incorporated in different Ni-MFU-4l-X framework variants. Uncertainty values for the  $g_{ij}$ ,  $D$ , and  $E/D$  parameters of 0.006, 0.01 cm<sup>-1</sup> and 0.01 were estimated for the experimental values, respectively.

	Geometry (ligand X)	$g_{xx}$	$g_{yy}$	$g_{zz}$	$D$ (cm) <sup>-1</sup>	$E/D$
Computed	Four-coordinated(Cl)	2.186	2.186	2.194	1.62	0.01
	Five-coordinated(NO <sub>2</sub> )	2.133	2.175	2.191	1.53	0.09
Experimental		2.000	2.025	2.060	1.18	0.14

To summarize, the analysis of the W-band spectrum evidences the presence of Ni(II) species incorporated within the Ni-MFU-4l-NO<sub>2</sub> framework via post-synthetic ion exchange modification. The microscopic structure of such Ni(II) centers is retrieved by comparing the experimental spin Hamiltonian parameters, in particular the ZFS, with the computed ones, and it may be ascribed as five-coordinated Ni(II) ion located on one of the peripheral sites of the SBUs of the Ni-MFU-4l-NO<sub>2</sub>. Additionally, in complement with the EPR analyses, IR spectra for the Ni-MFU-4l-NO<sub>2</sub> and Ni-MFU-4l-Cl complexes are consistent with the spectra extracted from the DFT calculations (see SI, Figure 5.18).

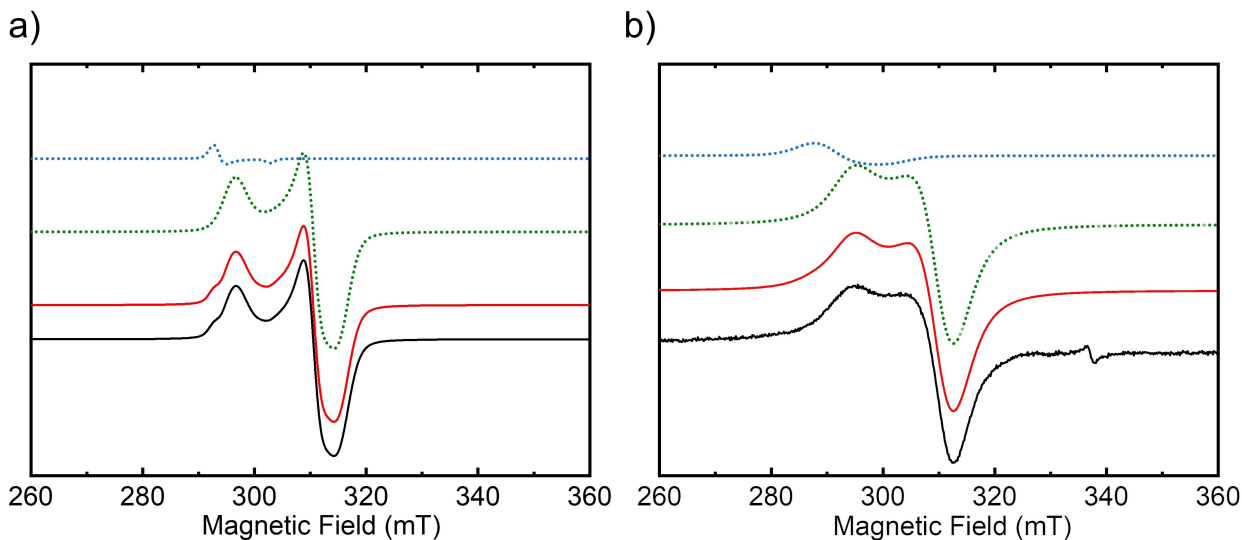


FIGURE 5.4: Experimental (black lines) and simulated (red lines) X-band CW EPR spectra of the Ni(II)-NO adduct in Ni-MFU-4l-NO<sub>2</sub> formed upon NO adsorption and recorded at (a) 10 K and (b) 288 K. The simulation is composed of the sum of two different species A (dotted green line) and B (dotted blue line). The small signal around  $\sim 340$  mT corresponds to the radical.

### 5.2.2 CW and pulsed EPR investigations of the Ni(II)NO adduct in Ni-MFU-4l-NO<sub>2</sub>

Interaction of the thermally activated Ni-MFU-4l-NO<sub>2</sub> with adsorbed NO was initially monitored by CW-EPR. The recorded X-band EPR spectra at 10 K and 288 K are shown in Figure 5.4 and display the appearance of an intense EPR signal upon adsorption of nitric oxide over Ni-MFU-4l-NO<sub>2</sub>. The complete set of temperature-dependent ( $\Delta T = \sim 25$  K) EPR data ranging from 10 K up to 288 K is given in SI Figure 5.13a and Table 5.4. The signal intensity and linewidth increase with higher NO loading (see SI, Figure 5.20). For the NO adsorption on the parent MOF, the spin Hamiltonian for the resulting Ni(II)-NO species with spin  $S = 1/2$  can be written as

$$\hat{H} = \mu_B \vec{B} \mathbf{g} \hat{S} + \sum_i (\hat{S} A_i^N \hat{I}_i^N + \mu_n \vec{B} g_n \hat{I}_i^N + \vec{I}_i^N Q_i^N \hat{I}_i^N) \quad (5.2)$$

Here  $g$  is the electronic  $g$ -tensor of the Ni(II)-NO moiety,  $\mu_n$  is the Bohr magneton of the nucleus,  $g_n$  is the <sup>14</sup>N nuclear  $g$ -factor,  $\hat{I}_i^N$  the <sup>14</sup>N nuclear spin operator, and  $A_i^N$  and  $Q_i^N$  are the <sup>14</sup>N HF and NQ interactions tensors of the nitrogen of the adsorbed NO molecule and of the nitrogen atoms in the first ( $N_{f1-f3}$ ) and second ( $N_s$ ) coordination spheres of the triazole linkers coordinating to the Ni(II) ion in the Kuratowski-type SBU (Figure 5.7).

Spectral simulations reveal that the spectra in Figure 5.4 are composed of a superposition of a major species A (93 % signal contribution) with principal values of its  $g$ -tensor given in Table 5.2 and a minor species B (7 % signal contributions) with principal values  $g_{xx,yy} = 2.296$ ,  $g_{zz} < 2.224$ . The EPR signal intensity follows the expected  $1/T$  behavior of a paramagnetic system

according to Curies law (see SI, Figure 5.13b). Both,  $g$ -values and linewidths, exhibit a weak temperature dependence, which is presented and discussed in Supplementary Figures 5.14 and 5.15. The obtained  $g$ -values for species A and B,  $g_{ii} > g_e$ , where  $g_e = 2.0023$  is the  $g$ -value of the free electron, indicate that the unpaired electron resides in a  $3d^9$  orbital of the Ni(II) ion[34, 35] of the Kuratowski-type SBU and is not localized in the antibonding  $\pi_z^*$  orbital of the adsorbed NO molecule. The latter case has been typically observed for nitric oxide physisorbed on metal oxide surfaces, in zeolites, and MOFs with CUS sites at closed-shell metal ions, where  $g_e \geq g_{ii}$  holds[21]. Moreover, the EPR spectra of these NO adsorption complexes are usually not detectable at room temperature because of the small adsorption energies of the nitric oxide molecules[8, 9, 11–14, 19, 20, 22]. Here, only a weak temperature dependence of  $g_{ii}$  and linewidths has been observed (see SI, Figure 5.14).

The observed paramagnetic  $3d^9$  ground state of the Ni(II)NO adsorption complex has been interpreted in terms of a Ni(I)NO<sup>+</sup> species[34, 35] or by an AFM coupled Ni(II)NO adduct[34, 35], where the later assignment has been strongly supported by recent quantum chemical computations[34, 35]. In the following, we will restrict our discussion to the major species A and assign the minor species B to a Ni(II)NO adsorption complex, which is formed at nickel ion associated with a structural defect of the MOF framework or at a residual four-coordinated tetrahedral Ni(II) ion with a Cl<sup>−</sup> ligand being left from the initially synthesized Ni-MFU-4l material. However, as this minor species B accounts for only 7 % of the total Ni(II) it cannot be identified in the W band spectra of Ni-MFU-4l-NO<sub>2</sub> (Figure 5.2), and unambiguous assignment is not possible.

According to second-order perturbation theory, a ( $d_{x^2-y^2}$ ) ground state leads to principal values of the  $g$ -tensor[56–58]

$$g_{xx,yy} \approx g_e + \frac{2\lambda}{\Delta_{1,2}}; g_{zz} \approx g_e + \frac{8\lambda}{\Delta_3} \quad (5.3)$$

reflecting the symmetry of the experimentally obtained  $g$ -tensor  $g_{zz} > g_{xx,yy} > g_e$  of the Ni(II)-NO species A. Here,  $\lambda$  is the spinorbital coupling constant of the Ni(II) ion ( $315 \text{ cm}^{-1}$ ),  $\Delta_1$  and  $\Delta_2$  are the energy splitting between the ( $3d_{x^2-y^2}$ ) ionic ground state accommodating the unpaired electron and the ( $3d_{yz}$ ) and ( $3d_{xz}$ ) excited states, whereas  $\Delta_3$  corresponds to the energy difference between the ground state and the ( $3d_{xy}$ ) excited state. Therefore, having an unpaired electron in the ( $3d_{x^2-y^2}$ ) nickel atomic orbital (AO), an AFM coupling between the adsorbed NO molecule and the Ni(II) ion can be established by the interaction of the unpaired electrons in the antibonding  $\pi_z^*$  molecular orbital of the NO and the  $3d_{z^2}$  AO of the nickel ion in leading to a ( $d_{yz}$ )<sup>2</sup>( $d_{xz}$ )<sup>2</sup>( $d_{xy}$ )<sup>2</sup>( $d_{x^2-y^2}$ )<sup>↑</sup>( $d_{z^2}$ )<sup>↑</sup>( $\pi_z^*$ )<sup>↓</sup> ground state configuration of the Ni(II)-NO moiety[34, 35].



The lack of <sup>14</sup>N hyperfine structure in the CW-EPR spectra indicates that the spin density is predominantly based on the nickel ion. As a result of this, the hyperfine interactions from the N nuclei of the organic linker and NO are small, and the information is hidden in the inhomogeneously broadened line of the CW-EPR spectrum. To recover the missing couplings arising from <sup>14</sup>N ( $I = 1$ ), and obtain details on the local coordination environment of the Ni(II)NO species, pulse EPR measurements (HYSCORE and ENDOR) were carried out at X-band.

Orientation-selective <sup>14</sup>N Davies ENDOR spectra of Ni(II)NO in MFU-4l-NO<sub>2</sub> are reported in Figure 5.5. An ENDOR signal represents an NMR absorption which is observed as a change in the echo signal intensity at a fixed resonant magnetic field,  $B_0$ . The ENDOR pattern for the  $\Delta m_I = \pm 1$  transitions for <sup>14</sup>N ( $I = 1$ ), are expected to obey the following equation for the nuclear transition frequencies of the electron spin manifolds with  $\alpha$  and  $\beta$  corresponding to  $M_s = \pm 1/2$

$$\nu_{\alpha,\beta}(m_I \leftrightarrow m_I + 1) = | (A/2 \pm \nu_I + 3Q(m_I - 1/2)) | \quad (5.4)$$

where  $A$  and  $Q$  are the orientation-dependent hyperfine and quadrupole interaction constants, depending on the tensors  $A_i^N$  and  $Q_i^N$ , and the orientation of the external magnetic field, respectively, and  $\nu_I = 1.00$  MHz is the nuclear Larmor frequency of <sup>14</sup>N at X-band[59]. In a strong coupling regime ( $|A| > 2|\nu_I|$ ), as occurs in this case, the equation describes a pattern consisting of two groups of  $2I$  lines each, centered at  $A/2$  and separated by  $2\nu_I$ . Within each group, the resonances are separated by  $3Q$ .

The low field <sup>14</sup>N ENDOR spectrum of Ni(II)NO in MFU-4l-NO<sub>2</sub> (Figure 5.5) corresponds to a single crystal-like orientation and is characterized by an unresolved set of  $2I = 2$  quadrupole lines separated by  $2\nu_I$  and centered at a frequency corresponding to  $A/2$ . The quadrupole splitting is partially resolved at higher fields generating complex ENDOR spectra. Spectral features at 320 mT and 325 mT suggest the existence of two sets of <sup>14</sup>N nuclei, one with a larger hyperfine coupling (contributing especially to the high-frequency part of the spectra, hereafter named <sup>14</sup>N(1), the other with a smaller coupling responsible for the splitting structure in the low-frequency region hereafter referred to as <sup>14</sup>N(2)). This assignment was confirmed by a simulation analysis, which proved impossible to convincingly fit simultaneously the spectra recorded at three field positions with a single nitrogen species. The involvement of two interacting <sup>14</sup>N species dramatically complicates the simulation procedure by increasing the number of unknown parameters. For this reason, the relative orientations of the quadrupole coupling and hyperfine coupling tensors with respect to the  $g$ -tensor principal axes frame were fixed from DFT calculations(vide infra). Careful scrutiny of the ENDOR spectra evinced that the <sup>14</sup>N(2) signal is given by multiple nitrogen nuclei

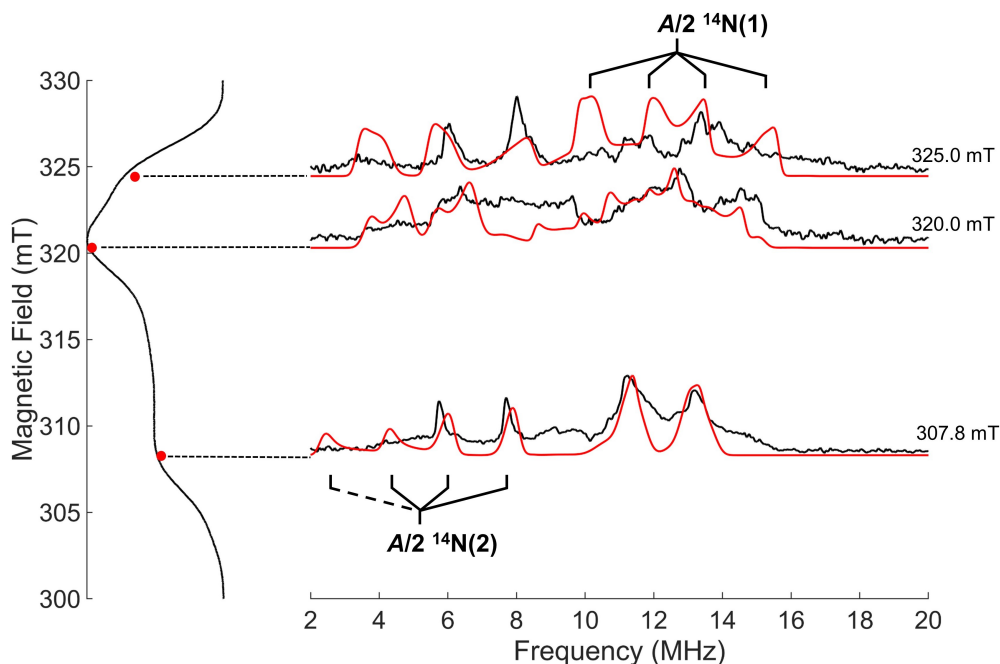


FIGURE 5.5: Experimental (black) and simulated (red) X-band <sup>14</sup>N ENDOR spectra of Ni(II)NO adduct in Ni-MFU-4l-NO<sub>2</sub> recorded at different magnetic field settings. The simulation of the <sup>14</sup>N(2) signal was obtained by using one of the DFT-computed sets of Euler angles for the triazole <sup>14</sup>N. The ESE spectrum with the corresponding field positions at which the ENDOR spectra were taken is plotted on the left-hand side. All spectra were recorded at 10 K.

possessing comparable magnitude of hyperfine and quadrupole couplings but slightly different orientations of the corresponding  $A_{1,2}^N$  and  $Q_{1,2}^N$  tensors with respect to the  $g$ -tensor. Nevertheless, the spectral resolution does not allow the complete disentangling of nitrogen nuclei magnetically equivalent but with different orientations of the hyperfine and quadrupole tensors. Simulations of the field-dependent ENDOR spectra allowed to extract of the principal values of the <sup>14</sup>N tensors  $A_{1,2}^N$  and  $Q_{1,2}^N$ . The <sup>14</sup>N hf interaction tensors are found to be axially symmetric within the accuracy of the simulation procedure, and the corresponding isotropic Fermi contact ( $a_{iso}$ ) and dipolar ( $T$ ) hf coupling parameters[59] are given in Table 5.2 (for further details, see SI, Table 5.5). The sign of the principal values of tensors  $A_{1,2}^N$  was assigned according to the *ab initio* calculations. The estimated nq interaction tensors are rhombic and presented in terms of the NQ coupling parameter  $e^2qQ/h$  and the rhombic distortion parameter  $\eta$ [59]. The contribution from the different species was properly weighted in the simulation in order to fit better the experimental plot (<sup>14</sup>N(1) and <sup>14</sup>N(2) species were considered in 1:1 ratio).

The decomposition of the <sup>14</sup>N hfi tensors  $a_{iso}$  and  $T$  components allows the extraction of exquisite information on the nature of Ni-N chemical bonding. The dominant  $a_{iso}$  contribution in the <sup>14</sup>N(2) hf coupling tensor implies a large  $s$ -character of the Ni-<sup>14</sup>N(2) bonds diagnostic for a prevalent

$\sigma$ -type bonding. On the other hand, the <sup>14</sup>N(1) hf interaction is dominated by the dipolar  $T$  contribution pinpointing to a main p-character of the Ni-<sup>14</sup>N(1) bond. The degree of spin delocalization in the 2s ( $\rho_s$ ) and 2p ( $\rho_p$ ) orbitals of the two different nitrogen species may be derived from the extracted hf couplings. By using the atomic parameters for nitrogen ( $a_0 = 1540.33$  MHz and  $b_0 = 127.22$  MHz)[60] and considering a unitary spin density in the 2s and 2p orbitals,  $\rho_s = 0.003$  and  $\rho_s = 0.10$  for N(1) while  $\rho_s = 0.007$  and  $\rho_p = 0.012$  for N(2). These values clearly reflect the substantial p-character of the Ni-N(1) bond with respect to the Ni-N(2) bond.

TABLE 5.2: Computed and experimental spin Hamiltonian parameters for the prevalent Ni(II)NO species in Ni-MFU-4l-NO<sub>2</sub>. The labels of the nuclei refer to the ones reported in Figure 5.7. Hyperfine and quadrupole couplings are given in MHz. Uncertainty values for the  $g$  -,  $A$ -tensors,  $e^2qQ/h$  and  $\eta$  of 0.005, 0.5 MHz, 1.5 MHz and 0.4 were estimated for the experimental values, respectively. For the simulation of the spectra, the computed  $g$ -frame and Euler angles for  $A$ - and quadrupole tensors were adopted.

	g - tensor			A - tensor		Q - tensor		
	$g_{xx}$	$g_{yy}$	$g_{zz}$	$a_{iso}$	$ T $	$ e^2qQ/h $	$\eta$	
Experimental	2.136	2.167	2.270	<sup>14</sup> N(1)	-3.0	13.0	2.7	0.8
				<sup>14</sup> N(2)	11.0	1.5	3.2	0.6
				N <sub>s</sub>	1.0	0.4	3.2	0.8
Computed	2.226	2.255	2.276	N <sub>NO</sub>	-3.9	11.0	5.0	0.3
				N <sub>f1</sub>	9.9	1.3	4.7	0.5
				N <sub>f2</sub>	9.6	1.3	4.6	0.4
				N <sub>f3</sub>	8.0	1.1	4.3	0.4
				N <sub>s</sub>	0.6	0.3	5.8	0.5

The X-band HYSCORE spectra of NO adsorbed Ni(II)-MFU-4l-NO<sub>2</sub> recorded at three field positions are reported in Figure 5.6. In <sup>14</sup>N HYSCORE spectra, the correlation peaks ( $\nu_\alpha, \nu_\beta$ ) and ( $\nu_\beta, \nu_\alpha$ ) are further split into multiplets due to the nq interaction. In this case, the <sup>14</sup>N hyperfine interaction detected by HYSCORE experiments is approximately twice the nitrogen Larmor frequency at X-band frequency, leading to the so-called cancellation regime[61]. Therefore, the transitions detected are assigned to <sup>14</sup>N nuclei weakly coupled to the Ni(II)NO adduct, likely located on the second coordination sphere. Cross peaks at ( $\pm 1.6, \pm 4.2$ ) and ( $\pm 4.2, \pm 1.6$ ) MHz are assigned to ( $\nu_-, \nu_{DQ}$ ) frequencies, the signals at (+3.2, +4.2) and (+4.2, +3.2) MHz correspond to ( $\nu_+, \nu_{DQ}$ ) and ( $\nu_{DQ}, \nu_+$ ) frequencies while the low-frequency ridges at ( $\pm 0.6, +1.6$ ) and ( $\pm 1.6, +0.6$ ) may be assigned to ( $\nu_0, \nu_-$ ) frequencies. An additional feature appearing at about 4 MHz in the spectra is due to the nuclear double-quantum transition frequency ( $\nu_{DQ}$ ) of the other electron spin manifold. The full set of spin Hamiltonian parameters for such weakly coupled nitrogen nuclei (N<sub>(s)</sub>) was recovered by fitting the HYSCORE spectra simultaneously at three magnetic fields and are likewise summarized in Table 5.2.

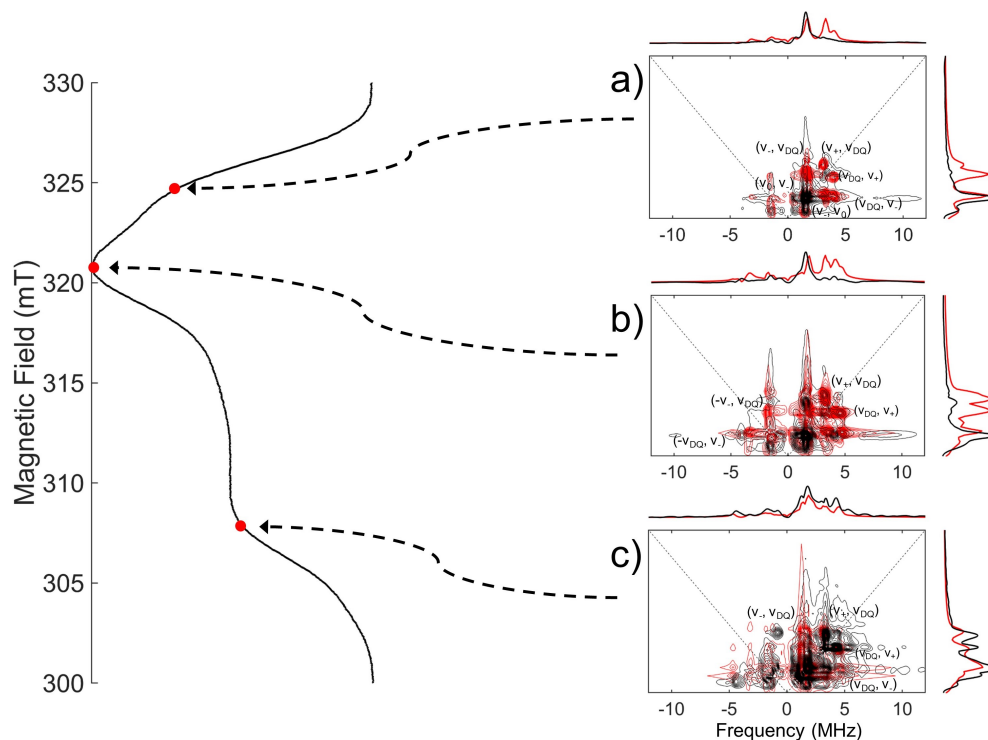


FIGURE 5.6: Simulation (in red) of the X-band <sup>14</sup>N HYSCORE spectrum (in black) of Ni(II)-NO adduct in Ni-MFU-4l-NO<sub>2</sub> recorded at a) 325.0 mT, b) 320.8 mT, and c) 309.0 mT. The ESE detected EPR signal of Ni(II)NO is reported on the left side. Spectra were recorded at 10 K.

Summarizing, the combination of CW-EPR and hyperfine techniques provide evidence that, upon NO adsorption on Ni(II)-MFU-4l-NO<sub>2</sub> material, a Ni(II)NO adduct is formed in which the spin density is prevalently located at the nickel center. The absence of resolved <sup>14</sup>N hyperfine splitting in the CW-EPR spectra points out that only minute spin density is retained on the NO moiety and N ligands from the Ni-MFU-4l-NO<sub>2</sub> framework. Therefore the NO binding mode to the Ni(II) ion occurs via the following spin pairing mechanism  $\text{NO}\uparrow + \text{Ni(II)}\uparrow\uparrow \rightarrow [\uparrow\text{Ni(II)}(\uparrow\uparrow)\text{NO}]$ , as it was previously proposed on other systems containing metal-nitrosyl bonding[6, 14, 62–64]. Most importantly, hyperfine techniques allowed us to detect the hidden <sup>14</sup>N hf interaction from coordinating nitrogen ligands. In a complementary fashion, HYSCORE experiments indicate the presence of remote nitrogen atoms belonging to the second coordination sphere of the Ni(II)NO species. In contrast, ENDOR measurements indicate the presence of two magnetically inequivalent nitrogen species directly linked to the Ni ion, each of them displaying a different degree of covalency of the Ni-N chemical bond.

### 5.3 Geometric and electronic structure of Ni(II)NO in MFU-4l-NO<sub>2</sub>

It is widely established that NO binds transition metal centers through the nitrogen atom[18]. In metal-nitrosyl complexes, the NO character may range from that of a nitrosyl cation (NO<sup>+</sup>), which binds to the metal with a metal-NO angle of about 180°, to that of a nitrosyl anion (NO<sup>-</sup>), for which a bond angle of about 120° might be predicted. The occurrence of the former case instead of the latter depends on the amount of electron density donated from the antibonding orbital of NO to the metal 3d orbital and vice versa ( $\sigma$ -donation/ $\pi$ -back donation). A generalized description of the metal-NO bonding mechanism is provided by the {MNO}<sup>n</sup> formulation proposed by Feltham and Enemark[65, 66], where M is the metal center and n is the sum of the metal *d*-electrons and the nitrosyl  $\pi^0$  electrons. For instance, for a six-coordinated complex with n = 9, like our case, the metal-N-O angle is predicted to be bent[65–67].

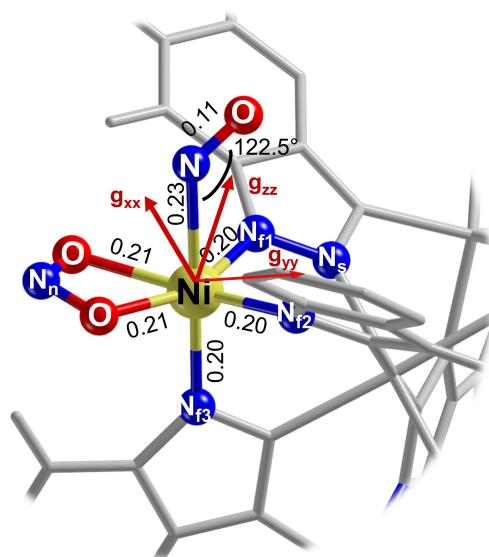


FIGURE 5.7: Atomistic structure of Ni(II)NO species in Ni-MFU-4l-NO<sub>2</sub> as obtained after the geometry optimization of the periodic model. The labels of the significant nuclei are reported. The relevant bond lengths are given in nm. The computed *g*-tensor orientations are shown in red.

The adsorption of NO on the peripheral Ni(II) site of Ni-MFU-4l-NO<sub>2</sub> was modelled by exploiting periodic boundary conditions, and the optimized geometry is shown in Figure 5.7. The computed absolute adsorption energy of NO to Ni(II) site ( $\Delta E_{ads} = 31.0$  kJ/mol) is higher in absolute value than that of NO on the peripheral Zn(II) ions ( $\Delta E_{ads} = 12.0$  kJ/mol, see also SI, Figure 5.16), validating the appearance of nickel species in the X-band EPR spectra upon NO adsorption. The computed adsorption energy  $\Delta E_{ads} = 31.0$  kJ/mol is in the range of the activation energy  $E_{A2} = 23(1)$  kJ/mol determined from the temperature dependence of the homogeneous line width of the CW EPR signal of the Ni(II)NO adduct at higher temperatures (SI, Figure 5.15). Thus, we may speculatively relate the homogeneous line broadening of the EPR signal at elevated temperatures

to the onset of the desorption progress of the nitric oxide molecules from the Ni(II) ions, as already observed for other NO adsorption complexes[34, 35]. The formation of Ni(II)NO adduct leads to a pseudo-octahedral geometry in which the Ni-N-O bond angle is slightly bent (122.5°), as predicted by Walsh-type diagrams[65, 66]. The parent Ni-N<sub>f</sub> and Ni-O bonds are utterly preserved, and their length underwent a small increase with respect to the values for the five-coordinated nickel ion, especially the Ni-N<sub>f3</sub> distance (Figure 5.7). The major elongation of the Ni-N<sub>f3</sub> bond is consistent with the weakening of the metal-ligand bond trans to the nitrosyl predicted by the {MNO}<sup>n</sup> model for a six-coordinated complex[68]. Similar structural changes were reported for porphyrin systems[69, 70]. The N-O bond length (0.11 nm) of the nitric oxide ligand is slightly shorter than the one relative to the gas-phase value. The reduction of the N-O bond length is a clear reflection of the depopulation of the antibonding  $\pi^*$  orbital, which contains the unpaired electron in the NO molecule.

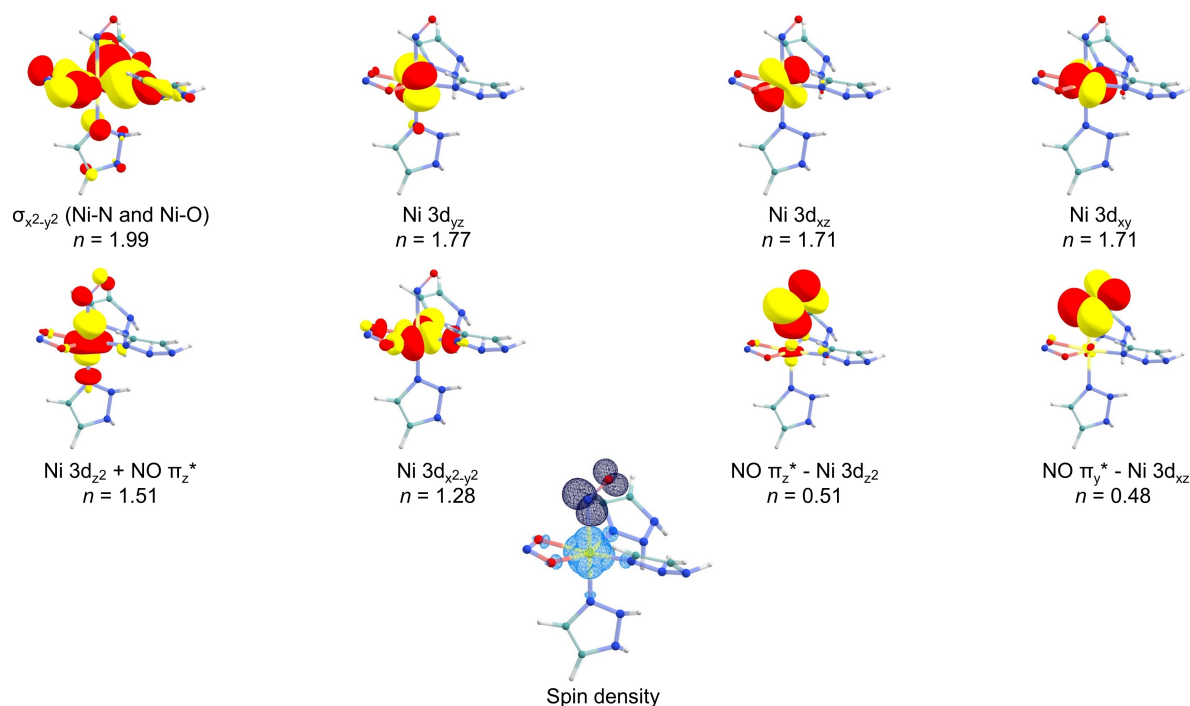


FIGURE 5.8: Contour plots of the most important natural orbitals (with predominant Ni 3d and NO  $\pi^*$  character) optimized with the CASSCF(11e,11o) calculation and spin density map. Indicated qualitative nature and fractional occupation number ( $n$ ) are reported. Contour values:  $\leq 0.03$  a.u. for the orbitals and  $\pm 0.003$  electrons/ $a_0$  for the spin density (the positive sign is shown in cyan, the negative sign in dark blue). N, O, Ni, C and H atoms are reported in blue, red, yellow, green and white, respectively

Nevertheless, a detailed depiction of the electronic structure of nickel-nitrosyl complexes may not be accurately described by means of widely used approximate DFT methods. Indeed, the open-shell  $3d^8$  configuration of Ni(II), along with the non-innocent NO ligand, generates a multi-configurational character in the Ni(II)NO electronic structure, extensively observed in the case of

the nitrosyl ligands[14, 64, 71–75]. Therefore, CASSCF calculations have been employed adopting an active space composed of 11 electrons and 11 orbitals (11e,11o), which involves all the 3d Ni orbitals, the NO  $\pi^*$  orbitals, the  $\sigma$ -bonding orbitals describing the covalent bonding with the framework of the Ni-MFU-4l-NO<sub>2</sub> and the nitrite ligand and three 4d Ni orbitals.

A graphical representation of some of the CAS-optimized natural orbitals is given in Figure 5.8 (see SI, Figure 5.19 for the visualization of the complete set of orbitals). The bonding between Ni and NO is based on a  $\sigma$ -type bond composed of the bonding ( $d\pi^2 + \pi_z^*$ ) and the antibonding ( $d\pi^2 - \pi_z^*$ ) molecular orbitals (the cluster model was oriented in order to have the z-axis passing through the Ni(II)NO bond). The  $\sigma$ -bonding orbital is mainly represented by the Ni  $3d_z^2$  ( $\approx 86\%$ ) orbital, while the  $\sigma$ -antibonding orbital is composed of the NO  $\pi_z^*$  ( $\approx 58\%$ ),  $\pi_y^*$  ( $\approx 23\%$ ) and Ni  $3d_z^2$  ( $\approx 5\%$ ) orbitals. The different contributions of the Ni- and NO-based fragment orbitals into the bonding and antibonding natural orbitals indicate the presence of non-negligible ionic components in the NiNO  $\sigma$ -bond.

CASSCF calculations correctly predicted a doublet ( $S = 1/2$ ) ground state, in line with the experimental evidence. The most representative contribution to the Ni(II)NO electronic structure is provided by the Ni(II)( $S=1$ )NO<sup>0</sup>( $S = 1/2$ ) resonance structure (85.1 %) with the following electronic configuration:  $(d_{yz})^2(d_{xz})^2(d_{xy})^2(d_{x^2-y^2})^\uparrow(d_{z^2})^\uparrow(\pi_z^*)^\downarrow$ . Such configuration describes the antiferromagnetic coupling between the unpaired electrons on the Ni(II)  $3d_{z^2}$  orbital and the NO  $\pi_z^*$  orbital. Thereby, its dominant role entirely agrees with the proposed spin pairing mechanism of the NO binding. The remaining contributions to the Ni(II)NO ground state are given by Ni(I)( $S = 1/2$ ) NO<sup>+</sup>( $S = 0$ ) with an electronic configuration of  $(d_{yz})^2(d_{xz})^2(d_{xy})^2(d_{z^2})^2(d_{x^2-y^2})^\uparrow$  and Ni(III)( $S = 1/2$ ) NO<sup>-</sup>( $S = 0$ ) with an electronic configuration of  $(d_{yz})^2(d_{xz})^2(d_{z^2})^2(d_{x^2-y^2})^\uparrow(d_{xy})^\uparrow(\pi_z^*)^\downarrow$ , which account for 8.9 % and 1.3 %, respectively. The larger contribution of the cationic resonance structure with respect to the anionic one agrees well with the NO <sup>$\delta^+$</sup>  formulation of the nitrosyl moiety, already reported in other precedented studies[14].

The SOMO of the doublet spin state is mainly a Ni  $3d_{x^2-y^2}$  orbital with a slight overlap with the hybrid  $sp$  orbitals of the N<sub>f</sub> and O atoms of the NO<sub>2</sub> ligand. The calculated spin density exhibits a positive region predominantly localized on the nickel center, with minute portions on the N<sub>f</sub> and O atoms of the NO<sub>2</sub> ligand. On the other hand, a negative spin density is predicted on the nitrosyl ligand (Figure 5.8, at the bottom) due to the effective polarization induced by the unpaired electron spin density in the  $3d_{x^2-y^2}$  orbital perpendicular to the Ni-NO bond. Given the positive gyromagnetic ratio  $\gamma$  of the <sup>14</sup>N nuclear spin, a negative contribution of the spin distribution in the nitrogen 2s orbital corresponds to a negative hf interaction. This is indeed the case of the N atom of NO. On the contrary, a positive hf interaction is calculated for N<sub>f</sub> atoms because of a direct spin

density transfer via the overlap of the hybrid  $sp$  orbitals of N<sub>f</sub> atoms with the Ni  $3d_{x^2-y^2}$  orbital.

The rhombic  $g$ -tensor is correctly reproduced, and the trend  $g_{zz} > g_{yy} > g_{xx}$ , is detected experimentally for the main Ni(II)NO species validating the microscopic structure proposed in Figure 5.7. The computed orientation of the  $z$  principal axis of the  $g$ -tensor is approximately perpendicular with respect to the plane defined by the  $d_{x^2-y^2}$  orbital, as it typically happens when the unpaired electron is in the  $d_{x^2-y^2}$  orbital. Overall, the computed quadrupole interaction for the different nitrogen nuclei is in reasonable agreement with the experimental findings.

The computed <sup>14</sup>N hf couplings from nitrogen ligands directly bound to Ni may be grouped into two families of nitrogen nuclei, in agreement with ENDOR experiments. N<sub>f1</sub>, N<sub>f2</sub> and N<sub>f3</sub> possess almost identical hyperfine and quadrupole couplings, which nicely fit with the experimental values found for <sup>14</sup>N(2). Moreover, they are characterized by Euler angles different from each other (SI Table 5.5). A spectral simulation of the ENDOR spectra obtained by using the calculated Euler angles for N<sub>f1</sub>, N<sub>f2</sub> and N<sub>f3</sub> is reported in Figure 5.17 (SI) confirming that, by considering nitrogen nuclei with similar spin Hamiltonian parameters but different orientation of the hyperfine and quadrupole tensors (as predicted by quantum chemical calculations), a satisfying explanation of the features of the low-frequency spectra may be obtained. This permits to assign <sup>14</sup>N(2) species to nitrogen atoms from the SBU, forming a  $\sigma$ -bond with the nickel center. On the other hand, <sup>14</sup>N(1) signal is consistent with the computed <sup>14</sup>N hyperfine couplings from the NO ligand, which correctly reproduces the large dipolar contribution. The weak <sup>14</sup>N hf interaction detected by HYSORE experiments is instead consistent with the ones calculated for nitrogen atoms of the benzobistriazolate immediately close to the nitrogen linked to the nickel (N<sub>s</sub> in Figure 5.7).

TABLE 5.3: Calculated bond length ( $d$  in nm), computed spin populations (%) at Ni ( $\rho_{Ni}$ ) and NO ligand ( $\rho_{NO}$ ) and experimental maximum <sup>14</sup>N hyperfine couplings ( $A_{max} = |a_{iso} + 2T|$ , in MHz) of Ni(II)NO moieties detected in this work and in Ni-doped ZSM-5 system. The data relative to ZSM-5 are taken from Pietrzyk *et al.*[14]

	System	Geometry	$d_{Ni-NO}$	$d_{N-O}$	$\rho_{Ni}$	$\rho_{NO}$	${}^N A_{max}$	Reference
Ni(II)-NO in MFU-4l	MOF	Pseudo-octahedral	0.230	0.114	+1.55	-0.35	329.0	This work
Ni(II)-NO in ZSM-5	Zeolite	Square pyramidal	0.190	0.117	+1.22	-0.27	14.0	[14]

Although the binding mechanism of NO to Ni(II) ion occurs in the same way (e.g. spin pairing mechanism) regardless the nature of the embedding considered, there are substantial structural and magnetic differences between the Ni(II)NO adduct described here and the ones reported for other microporous systems. Table 5.3 summarizes the main structural, electronic and magnetic differences between the nickel-nitrosyl complex in this work and the one recently characterized



by Pietrzyk *et al.*[14] in zeolite-type material. Apart from the different coordination geometry (pseudo-octahedral instead of square pyramidal), the Ni-NO bond distance is longer while the N-O bond length is slightly shorter compared to what is reported for Ni-ZSM-5 material[14]. This is consistent with a weaker NO associative mechanism agreeing with the lower NO adsorption energy reported here compared to zeolite case. Such tiny structural details affect the electronic structure and, thus, the EPR parameters. Because of the shorter N-O bond, the NO ligand acquires a partial positive charge. The cationic resonance structure (Ni(I)( $S = 1/2$ )NO<sup>+</sup>) has a higher contribution (8.9 %) compared to the case in ZSM-5 (6.3 %) in the description of the ground state. Consequently, the positive spin population on the Ni ion as well as the negative spin population on the NO ligand induced by spin polarization are larger than the ones reported by Pietrzyk[14] (see Table 5.3). The experimental <sup>14</sup>N hyperfine couplings of the nitrosyl ligand clearly reflect the changes in spin distribution whereby larger hf interactions are detected in MFU-4l-NO<sub>2</sub> compared to ZSM-5 case.

## 5.4 Conclusion

EPR spectroscopy and quantum chemical calculations were carried out to assess the geometric and electronic structure of Ni(II)NO moieties in Ni(II)-MFU-4l-NO<sub>2</sub> material. W-band CW-EPR detected five-coordinated Ni(II) species assigned to the peripheral sites of the parent Ni-MFU-4l-NO<sub>2</sub>, MOF in agreement with DFT calculations. Such divalent nickel centers are capable of chemoselective capture of gaseous NO-forming mononitrosyl complexes with electron spin  $S = 1/2$ , which can be easily identified by CW X-band EPR measurements. The nature of the Ni(II)NO bond and of the NiN<sub>f</sub> bonds was ascertained by ENDOR studies and thoroughly accounted for by DFT/CASSCF calculations. While the bonding of Ni with N<sub>f</sub> ligands from the SBU is characterized by a direct spin density transfer via overlap of the nitrogen *sp* orbitals with the nickel  $3d_{x^2-y^2}$  orbital, the NO bonding is due to spin pairing mechanism  $\text{NO}\uparrow + \text{Ni(II)}\uparrow\uparrow \rightarrow [\uparrow\text{Ni(II)}(\uparrow\downarrow)\text{NO}]$  whereby the transfer of spin density arises via spin polarization of the NO  $\pi$  orbital perpendicular to the Ni  $3d_{x^2-y^2}$  orbital. The results presented here highlight the capabilities of sophisticated EPR techniques in combination with quantum chemical calculations in providing fundamental insights into the non-obvious electronic structure of open-shell species docked in metal-organic frameworks.

## 5.5 Experimental techniques and methods

### Ni-MFU-4l-NO<sub>2</sub> sample preparation and structural characterization

The parent Ni-MFU-4l preparation and the side-ligand post-synthetic exchange modification were done similarly to a previously published procedure[38]: First, Ni-MFU-4l was synthesized by a post-synthetic exchange of 150 mg MFU-4l with a solution of 12 mmol NiCl<sub>2</sub>.6H<sub>2</sub>O in 30 mL DMF at 60 °C for 20 h. The light greenish MOF was filtrated and washed with 2.5 mL DMF and MeOH. The success of the nickel exchange was proved by energy dispersive X-ray analysis (EDAX) measurement(chemical formula: [Zn<sub>4</sub>NiCl<sub>4</sub>(BTDD)<sub>3</sub>], where H<sub>2</sub>-BTDD is bis(1H-1,2,3-triazolo[4,5-b],[4,5-i]dibenzo[1,4]dioxin[76]). Then, a 1 M solution of LiNO<sub>2</sub> in methanol (0.4 mL, 0.4 mmol) was added to the Ni-MFU-4l suspension (150 mg, approx. 0.12 mmol) in acetonitrile (30 mL). The mixture was stirred for 30 min at room temperature (RT), and the precipitate was filtered off and washed with methanol and CH<sub>2</sub>Cl<sub>2</sub>. Finally, the washed sample dried at 80 °C under vacuum, yielding 140 mg of Ni-MFU-4l-NO<sub>2</sub> as a greenish-yellow product with an analytically determined chemical composition [Zn<sub>4</sub>Ni(NO<sub>2</sub>)<sub>3</sub>Cl<sub>1</sub>(BTDD)<sub>3</sub>].

Powder X-ray diffraction (PXRD) pattern was recorded using Seifert XRD 3003 TT diffractometer equipped with a Meteor 1D detector at room temperature. The microstructure and stoichiometry were analysed using the scanning electron microscope (SEM - model Philips XL 30 FEG) and EDAX model EDAX SiLi detector fitted with SEM), respectively. Fourier transform Infrared (FTIR) spectroscopy has been performed in the range 1600 400 cm<sup>-1</sup> on a Bruker Equinox 55 FT-IR spectrometer.

### EPR sample preparation

The CW Q- and W- band experiments on Ni-MFU-4l-NO<sub>2</sub> were acquired in the hydrated state. Further, The CW X-band and pulse experiments were performed on the NO-adsorbed sample in the below-mentioned condition. 4.7 mg of parent MOF was transferred into a conventional quartz glass X-band tube, and the sample was activated at 120 °C for overnight to remove the extra framework solvent/water molecules before the NO gas adsorption. After the thermal activation, the colour of the sample changed from pale green to dark yellowish green colour. Then the sample was loaded with nitric oxide (0.2 mbar) using a vacuum line at 294 K, and the NO gas was condensed into the EPR tubes by applying a liquid nitrogen cold trap to ensure that the entire amount of loaded NO was trapped within the EPR tube. After NO gas loading, the sample was immediately sealed, keeping the NO adsorbed at the parent Ni-MFU-4l-NO<sub>2</sub> sample in the EPR tube. Ultimately, the NO adsorbed sample was in a lite whitish-green colour.

## EPR spectroscopy

CW X-band (9.5 GHz) EPR spectra were measured at a temperature ranging from 10 K to 288 K employing a Bruker EMXmicro spectrometer fitted with a Bruker ER4119HS cylindrical cavity using a He cryostat ESR900, Oxford instruments. The CW Q-band (34 GHz) EPR spectrum was recorded using Bruker EMX 10-40 spectrometer fitted with a cylindrical cavity and an Oxford Instruments CF935 cryostat at  $T = 300$  K. The high magnetic field of W-band (95 GHz) EPR requires a superconducting magnet, Bruker 6T SC and the W-band spectra were measured at  $T = 20$  K using an Elexsys E600 spectrometer equipped with a Bruker E600-1021H TeraFlex resonator. The EPR intensities of the X-band signals ranging from  $T = 10$  K to  $T = 288$  K (Figure. 5.13b) were extracted by taking double integration of the full-range EPR spectrum.

The EPR data were simulated by MATLAB R2019b using the EasySpin toolbox (version 6.0.0-dev36), which is based on numerical diagonalization of the spin Hamiltonian[77]. In the simulations of the CW EPR spectra, the <sup>14</sup>N hf and nq coupling has been neglected as no nitrogen hf splitting was resolved here.

The X-band ESE detected EPR spectra were recorded with the pulse sequence  $\pi/2 - \tau - \pi - \tau - echo$ . The lengths of microwave (mw) pulsed  $t_{\pi/2} = 16$  ns and  $t_{\pi} = 32$  ns, a  $\tau$  value of 120 ns and a shot repetition rate of 3.55 kHz were adopted.

X-band HYSORE[78] experiments were performed with the pulse sequence  $\pi/2 - \tau - \pi/2 - t_1 - \pi - t_2 - \pi/2 - \tau - echo$ , applying an eight-step phase cycle for deleting unwanted echoes. Pulse lengths of  $t_{\pi/2} = 16$  ns and  $t_{\pi} = 32$  ns and a shot repetition rate of 1.77 kHz were used. The increment of the time intervals  $t_1$  and  $t_2$  was 16 ns giving a data matrix of 200 × 200 points; the pulse delay  $\tau$  value was set to 146 ns. The time traces of HYSORE spectra were baseline corrected with a third-order polynomial, apodized with a hamming window and zero-filled to 2048 points. After the 2D Fourier transformation, the absolute-value frequency spectra were obtained.

X-band ENDOR spectra were recorded using the Davies ENDOR pulse sequence  $\pi - \pi_{RF} - \pi/2 - \tau - \pi - \tau - echo$ [79]. Mw pulse lengths  $t_{\pi/2} = 100$  ns and  $t_{\pi} = 200$  ns, and a radiofrequency pulse length  $t_{\pi_{RF}} = 10$   $\mu$ s, together with the mw pulse delay  $\tau = 820$  ns were employed.

## Models and Computational Details

### Periodic and Cluster Models

Geometry optimization and the following frequency calculations of Ni-MFU-4l-NO<sub>2</sub> structure were performed by adopting periodic boundary conditions that better describe the crystalline environment of the metal-organic framework. Starting from the purely zincous structure (space

group  $Fm\bar{3}m$ ) invented by Volkmer *et al.*[80], one Zn(II)-Cl coordination unit among the four peripheral coordination sites of each Kuratowski-type SBU was substituted by one Ni(II)-Cl coordination unit. In this way, one Ni(II) site was introduced per SBU, removing the cubic space group symmetry in the model (space group  $P1$ ). Subsequently, the  $\text{Cl}^-$  anions were replaced by  $\text{NO}_2^-$  ligands in order to reproduce the experimental composition of the material. Adsorption of the nitric oxide molecule was simulated by positioning a NO molecule close to the peripheral Ni(II) or Zn(II) sites of the previously optimized structures and reoptimizing the whole adduct.

Periodic calculations have been complemented with molecular cluster calculations to compute the  $g$ -tensor, the ZFS parameters  $D$  and  $E$ ,  $^{14}\text{N}$  hf and nq coupling tensors  $A_i^N$ ,  $Q_i^N$  including the orientation of their principal axes frame with respect to the  $g$ -tensor principal axes frame. Cluster models were cut out from the corresponding optimized periodic structures. The dangling bonds were saturated with hydrogen atoms oriented along the broken bonds to keep the local environment as in the optimized periodic models. Thus, no further geometry optimization of the cluster models was performed: the EPR parameters were computed, maintaining the same atomic coordinates as the ones in the relaxed periodic structures. The resulting net charge on the cluster models was always set to 0.

### Computational Details

Periodic geometry optimizations and frequencies calculations were carried out by using the massive parallel version of CRYSTAL17 code (MPPCRYSTAL)[81, 82] in the frame of Density Functional Theory (DFT) adopting the hybrid B3LYP method, Beckes three parameters exchange functional and the correlation functional from Lee, Yang and Parr[83, 84]. The semi-empirical dispersion corrections for the van der Waals (vdW) interactions were employed by using the Grimme approach in the so-called DFTD3 method in conjunction with a three-body correction[85, 86]. The pop-TZVP-rev2 basis set[87] was used for all the elements of the MOF framework while the atoms of the NO molecule were treated with Ahlrichs VTZP basis set[88].

A pruned grid consisting of 75 radial points and a maximum number of 974 angular points in regions relevant to chemical bonding has been adopted. The accuracy of the calculation of the two-electron integrals in the Coulomb and exchange series was controlled by setting truncation criteria at the values of  $10^{-7}$  except for the pseudo-overlap of the Hartree-Fock (HF) exchange series, which was fixed to  $10^{-25}$ . Due to the large unit cell in the direct space, a shrink factor equal to 1 was used to diagonalize the Hamiltonian matrix in 1 k-point of the first Brillouin zone. The default value of mixing (30%) of the Kohn-Sham (KS) matrix at a cycle with the previous one was adopted. The threshold in energy variation of SCF cycles was set equal to  $10^{-7}$  Hartree

for geometry optimization and equal to  $10^{-10}$  Hartree for frequency calculations. The number of unpaired electrons in the unit cell was locked to two for the case of Ni(II) and to one for Ni(II)-NO in order to guide the SCF procedure to converge to a triplet and doublet spin state of the system wavefunction, respectively.

Harmonic vibrational frequencies were computed at the center of the first Brillouin zone in the reciprocal space ( $\Gamma$  point) from the diagonalization of the mass-weighted Hessian matrix of the second energy derivatives with respect to atomic displacement[89–91]. One displacement for each atom along each Cartesian direction was considered to numerically compute the second energy derivatives.

Molecular cluster calculations were carried out with ORCA (v5.0.3) code[92]. The spin-orbit coupling (SOC) contribution (not negligible for Ni species)[93] was explicitly treated by using a complete mean-field spin-orbit operator (SOMF)[94]. The potential was constructed to include one-electron terms, compute the Coulomb term in a semi-numeric way, incorporate exchange via one-centre exact integrals, including the spin-other orbit interaction and include local DFT correlation (SOCFlags 1,2,3,1 in ORCA). Concerning the Ni-MFU-4l-NO<sub>2</sub> cluster model with NiII, ZFS and *g*-tensor were computed at the double-hybrid DFT level of theory by employing the B2PLYP functional[95]. The def2-QZVP basis set was employed for the Ni nucleus, while the def2-TZVPP basis sets were employed for all the other atoms[96]. Increased integration grids were employed (DefGrid3 keyword), and tight energy convergence settings were applied throughout (TightSCF keyword). The resolution of identity (RI)[97] (in conjunction with the corresponding auxiliary basis sets was adopted[98]. In case no auxiliary basis set was available, the AutoAux keyword was employed to automatically build the auxiliary basis set[99]. The relaxed Møller-Plesset (MP2) density was used to compute the EPR parameters, and all the electrons were kept active (NoFrozenCore keyword). Both the spin-orbit and spin-spin contributions were taken into account for the computation of the ZFS interaction.

The *ab initio* prediction of the electronic structure for the Ni(II)-NO adduct was based on single-point complete active space self-consistent field (CASSCF) calculations on the cluster model extracted from the optimized periodic structure. The def2-QZVP basis set was employed for Ni, EPR-III[100] for the coordinating N nuclei, def2-TZVP[96] for the coordinating O nuclei and def2-SVP[96] for all the other atoms. The adopted active space (CAS) contains 11 electrons and 11 orbitals composed of five Ni 3d orbitals, two orbitals with predominant NO  $\pi^*$  character (namely  $\pi_z^*$  and  $\pi_y^*$ , where the *z*-axis coincides with the Ni-NO bond), one  $\sigma$ -type orbital that describes covalent bonding between Ni and the nitrogen atoms from the linkers and three double-shell orbitals of Ni (to describe radial correlation effects). State-averaged (SA) CASSCF calculations, including

15 doublet and 10 quartet states, were adopted to optimize the active orbitals and compute the  $g$ -tensor.

$^{14}\text{N}$  hyperfine and quadrupole couplings from the coordinating nitrogen nuclei of the first and second coordination spheres were obtained by performing a ground-state complete active space configuration interaction (CASCI) calculation of the previously optimized SA-CASSCF wavefunction. The Euler angles relative to the orientations of the  $^{14}\text{N}$  hyperfine and quadrupole tensors were instead obtained at PBE0[97] /EPR-III level of theory.

## 5.6 Supplementary material for Chapter 5

### Structural characterizations

PXRD obtained at 300 K ( Figure 5.9a) confirms that post-synthetic ion exchanged Ni-MFU-4l-NO<sub>2</sub> is in a single phase and crystallizes within space group  $Fm\bar{3}m$  (no. 225, cubic crystal system). SEM result ascertains the agglomerated particles ranging from 1 to 3  $\mu\text{m}$  range (inset Figure 5.9a). The EDAX result reveals the fraction of the post-synthetically incorporated Ni(II), and the ratio of Ni (20 %) and Zn (80 %) is found to be 1:4. The IR spectra result recorded between 1600 400  $\text{cm}^{-1}$  confirms the successful formation of Ni-MFU-4l-NO<sub>2</sub> (Figure 5.9b).

IR bands of Ni-MFU-4l:NO<sub>2</sub> ( $\text{cm}^{-1}$ ): 1625 (w), 1575 (w), 1461 (vs), 1351 (vs), 1210 (sh), 1183 (vs), 1025 (w), 922 (s), 867 (m), 817 (m), 535 (m), 430 (w) matches with the reported values[76], where, w, s, m ,vs, sh indicates weak, strong, medium, very strong and shoulder, respectively.

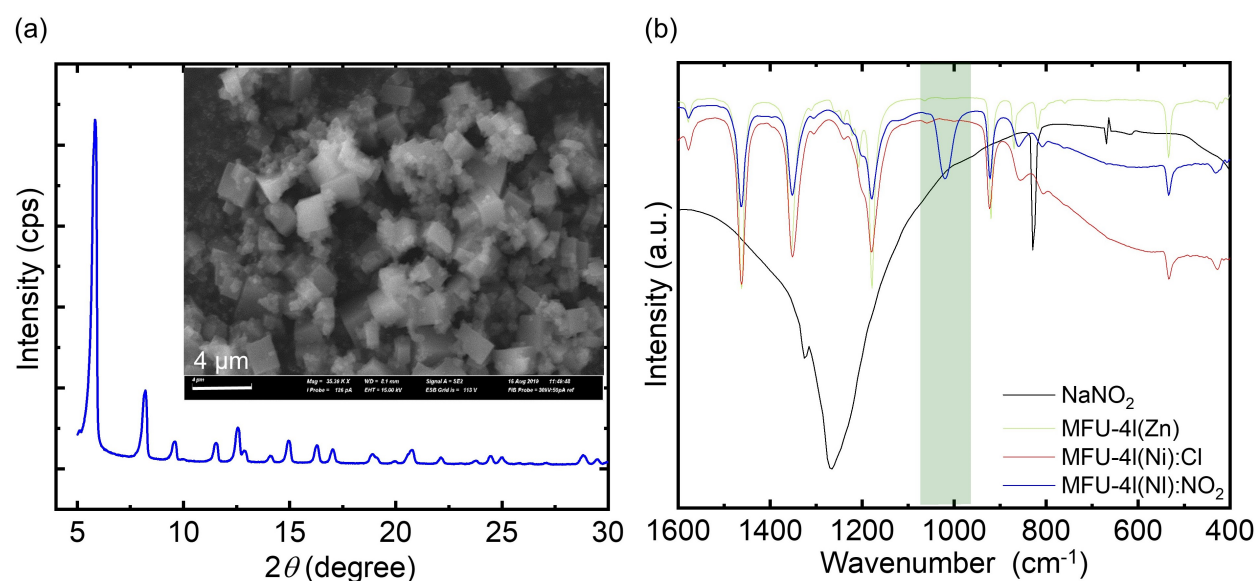


FIGURE 5.9: (a) PXRD and SEM image (inset: scale bar - 4  $\mu\text{m}$  ) of Ni-MFU-4l:NO<sub>2</sub> and (b) IR spectra comparison of various MFU-4l materials

Simulation of Q- and W- band EPR spectra of Ni(II) in Ni-MFU-4l:NO<sub>2</sub>

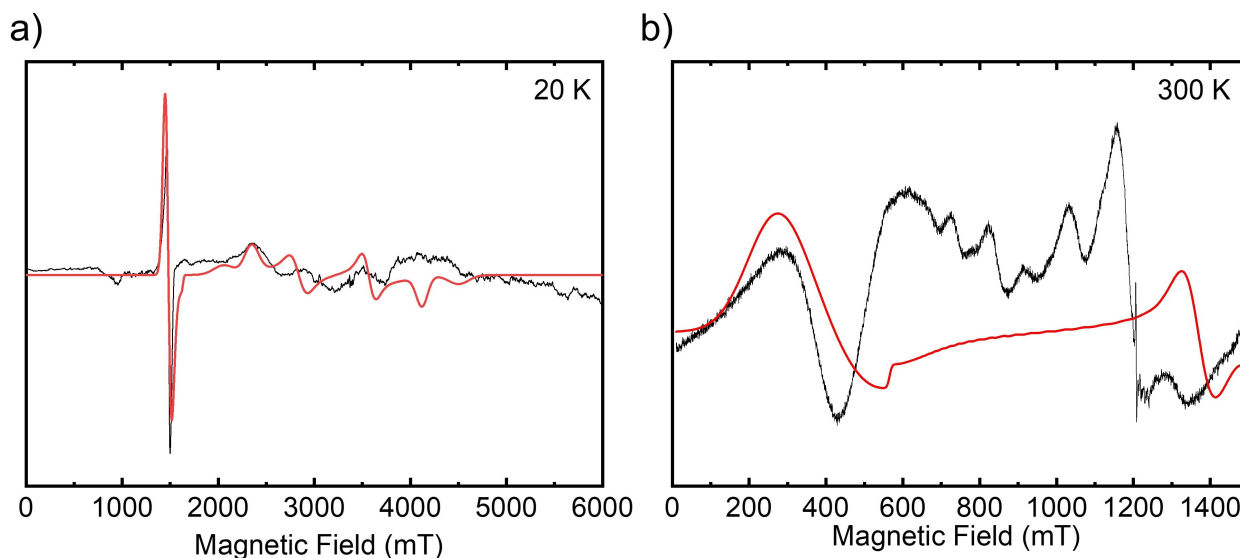


FIGURE 5.10: (a) W-band and (b) Q-band EPR spectra (black) and simulation (red) of the spin  $S = 1$  of Ni(II) in Ni-MFU-4l:NO<sub>2</sub> with the spin Hamiltonian parameters  $g_{xx} = 2.050(5)$ ,  $g_{yy} = 2.055(6)$ ,  $g_{zz} = 2.060(5)$ ,  $D = 35.5(5)$  GHz and  $E = 0.5$  GHz. (the extra signals of Q-band data are from the EPR cavity and the radical from the MOF sample.)

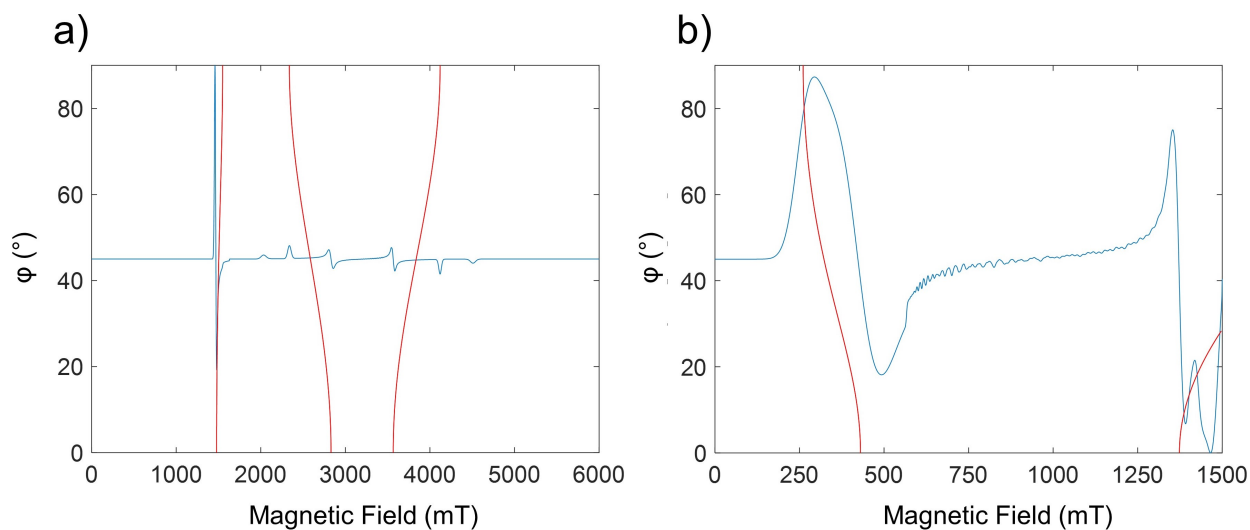


FIGURE 5.11: Angular dependent road map for the  $S = 1$  Ni(II) species at (a) W-band and (b) Q-band frequency (Blue - simulated EPR spectra with spin Hamiltonian parameters  $g_{iso} = 2.05$ ,  $D = 35500$  MHz and  $E = 5000$  MHz; Red A road map of the expected spectral position).

### Geometry optimization of Ni-MFU-41:NO<sub>2</sub> and Ni-MFU-41:Cl

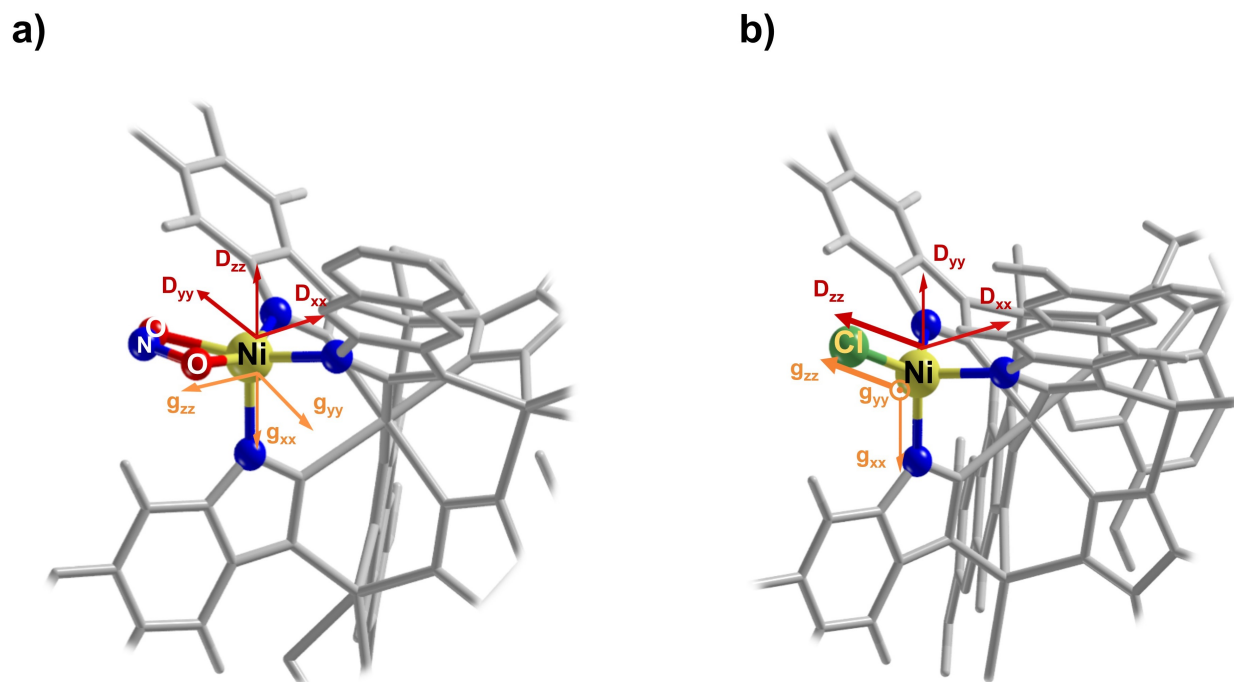


FIGURE 5.12: Geometry optimized periodic structures at B3LYP-D3/pob-TZVP-rev2 of (a) Ni-MFU-41:NO<sub>2</sub> and (b) Ni-MFU-41:Cl. The computed  $g$ - and  $D$ -frames are also reported. Nitrogen and oxygen atoms are shown in blue and red, respectively. The other atoms are labelled in the figures.



Temperature-dependent CW X-band data of NO adsorbed Ni-MFU-4l:NO<sub>2</sub>TABLE 5.4: Experimental spin Hamiltonian parameters for the Ni(II)-NO adduct in Ni-MFU-4l:NO<sub>2</sub> of species A recorded at several temperatures. (Gaussian ( $\Delta B_G^{pp}$ ) and Lorentzian ( $\Delta B_L^{pp}$ ) broadening)

$T$ (K)	$g_{xx}$	$g_{yy}$	$g_{zz}$	$\Delta B_G^{pp}$ (mT)	$\Delta B_L^{pp}$ (mT)
10	2.1358(5)	2.1672(5)	2.2705(5)	2.1(1)	0.8(1)
20	2.1358(5)	2.1672(5)	2.2705(5)	2.1(1)	0.8(1)
50	2.1358(5)	2.1672(5)	2.2705(5)	2.1(1)	0.8(1)
75	2.1358(4)	2.1672(5)	2.2720(5)	2.1(1)	1.1(1)
100	2.1376(6)	2.1672(6)	2.2727(6)	2.1(1)	1.1(1)
125	2.1385(5)	2.1685(7)	2.2745(4)	2.1(1)	1.20(7)
150	2.1392(8)	2.1690(7)	2.2757(6)	2.1(1)	1.35(6)
175	2.1410(6)	2.1692(9)	2.2766(5)	2.1(1)	1.35(10)
200	2.1446(6)	2.1710(7)	2.2780(8)	2.1(1)	1.40(7)
225	2.1498(8)	2.1725(10)	2.2788(8)	2.2(2)	1.45(10)
250	2.1518(9)	2.1740(8)	2.2800(9)	2.3(3)	2.0(1)
280	2.1545(4)	2.1745(6)	2.2820(9)	2.3(4)	3.3(2)
200	2.1545(7)	2.1745(5)	2.2850(6)	2.5(5)	4.20(10)

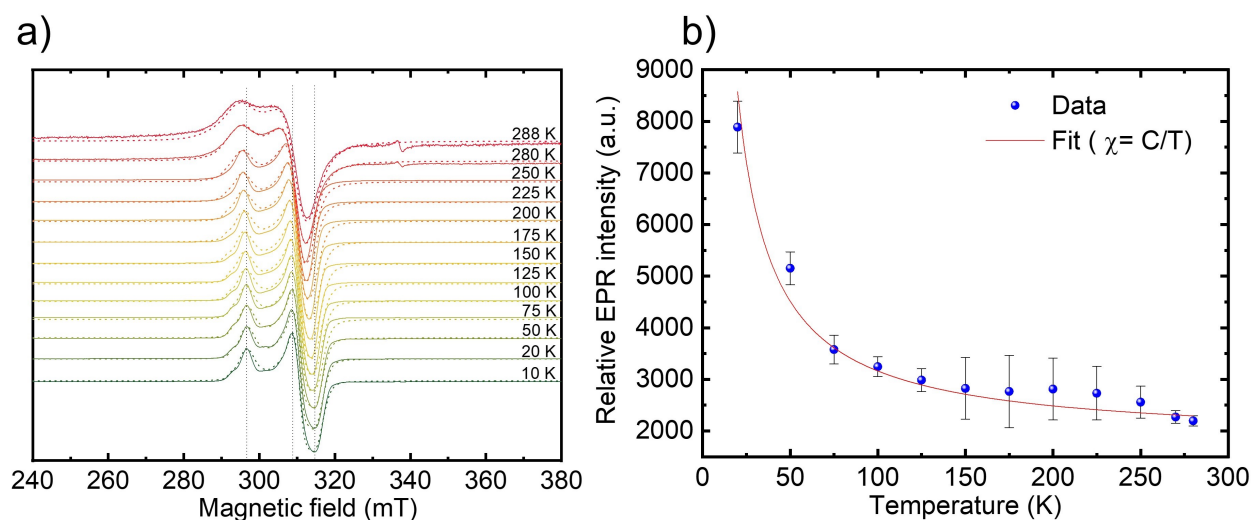


FIGURE 5.13: (a) Temperature-dependent X-band EPR spectra of NO adsorbed over Ni-MFU-4l:NO<sub>2</sub> ranging from temperature 10 K to 288 K (solid line experimental data and dotted line simulation of the sum of two different species A and B) and (b) Intensity corresponds to magnetic susceptibility as a function of temperature, extracted from double integration of full range temperature dependent EPR data (fit red: paramagnetic susceptibility fit). The small signal around 340 mT corresponds to the radical.

All three principal values  $g_{ii}$  of the  $g$ -tensor of the Ni(II)-NO species A in Ni-MFU-4l:NO<sub>2</sub>:NO as determined by spectral simulations (Table 5.4) increase with rising temperature (Fig. 5.14a-c). Such temperature-dependent  $g$ -tensor but also hfi tensor parameters of paramagnetic transition

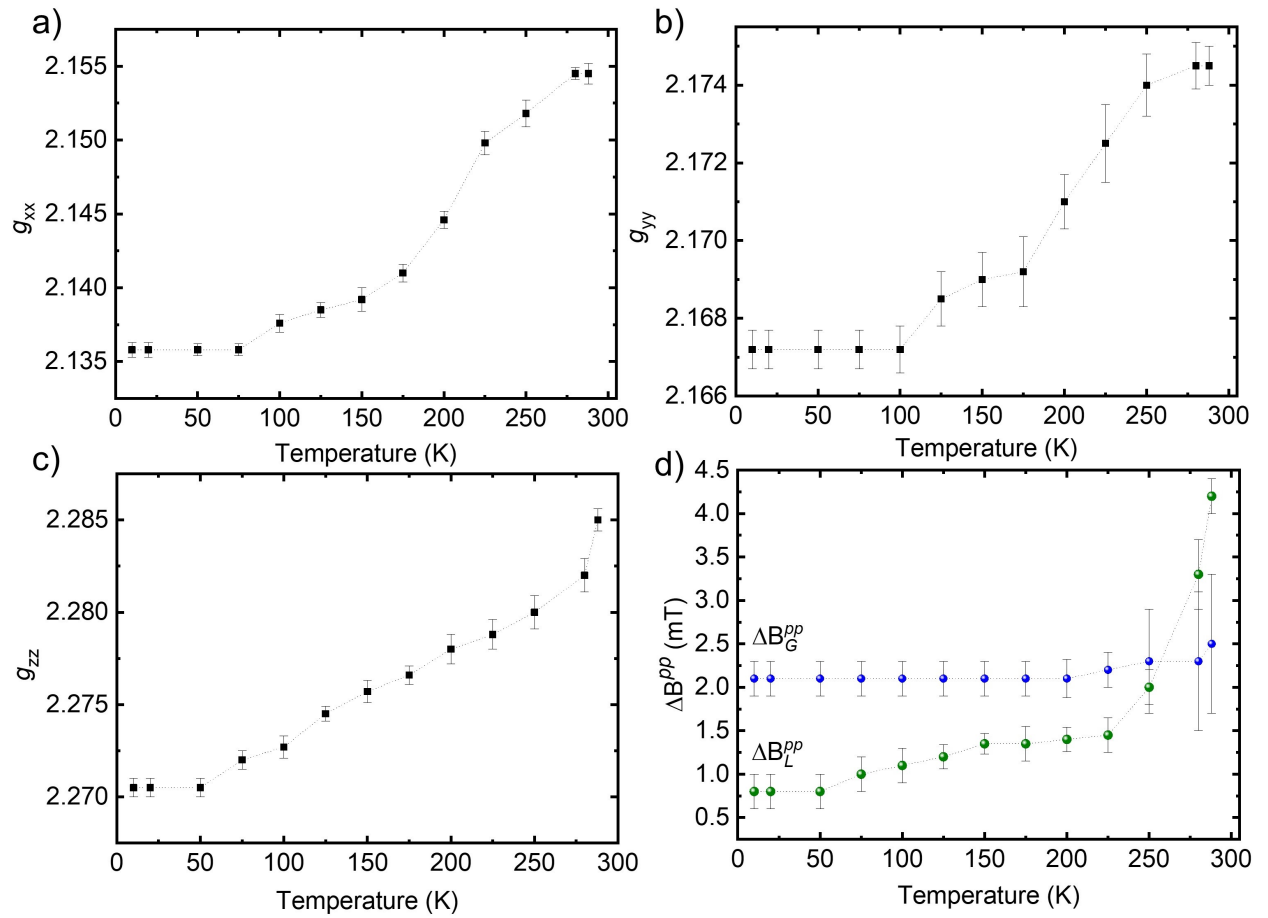


FIGURE 5.14: The temperature-dependent trend of  $g$ -tensor parameters (a)  $g_{xx}$ , (b)  $g_{yy}$ , (c)  $g_{zz}$  and (d) Gaussian (blue) and Lorentzian (black) linewidth for NO adsorbed MFU-4l(Ni):NO<sub>2</sub> system (species A).

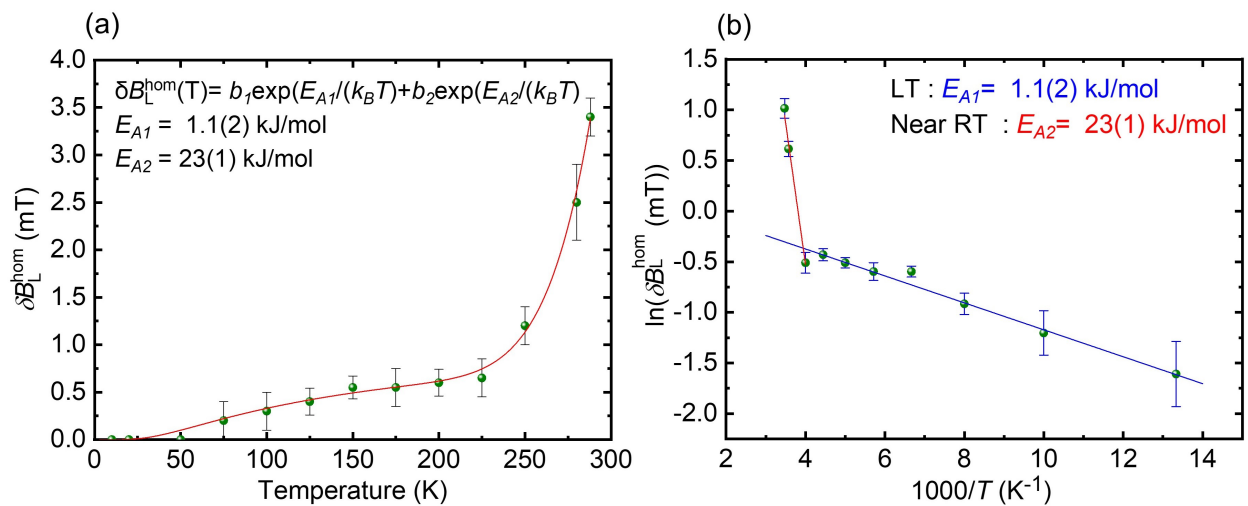


FIGURE 5.15: Arrhenius plot of the homogeneous (a) EPR linewidths,  $\delta B_L^{hom}$  and (b)  $\ln(\delta B_L^{hom})$  of Ni(II)-NO adduct in Ni-MFU-4l:NO<sub>2</sub>. The activation energies were found to be  $E_{A1} = 1.1(2)$  kJ/mol for the lower temperature range (75 K–250 K) and  $E_{A2} = 23(1)$  kJ/mol for the higher temperature range (250 K–288 K).  $\delta B_L^{hom}(T) = \delta^{total} B_i(T) - \delta^{total} B_i(50 \text{ K})$

metal ions or adsorption complexes in solids can be caused by motional effects of these species either related to lattice vibrations or internal motional processes. However, these motional processes result in a partial averaging of the principal values.<sup>2,3</sup> In the case of Ni-MFU-4l:NO<sub>2</sub>:NO, all three parameters  $g_{ii}$  of the Ni(II)-NO adsorption complex increase with temperature, and no averaging of the principal values is observed. Therefore, we rather suggest that temperature-dependent enhancements of the mean values of the nitrogenmetal ion bond length in the nickel coordination might lead to the observed temperature dependence of the  $g_{ii}$  parameters. These would result in smaller energy splitting  $\Delta_j$  between the ( $3d_{x^2-y^2}$ ) ground state and the excited states giving rise to an increase of all three parameters  $g_{ii}$  (eq. 5.3).

The spectral simulations also revealed that the total linewidth of the EPR signal of the Ni(II)-NO species A in Ni-MFU-4l:NO<sub>2</sub>:NO is composed of a Gaussian  $\Delta B_G^{pp}$  and a Lorentzian  $\Delta B_L^{pp}$  linewidth contribution (Table 5.4) (Figure 5.14d). Whereas the Gaussian linewidth  $\Delta B_G^{pp}$ , usually associated with an inhomogeneous line broadening, appears to be temperature independent within the error margin of the simulations, the Lorentzian linewidth contribution indicating homogeneous broadening increases at a temperature above  $T > 50$  K. For the later, we calculated the temperature-dependent contribution  $\Delta B_L^{hom}(T)$  to the total Lorentzian line broadening according to

$$\delta B_L^{hom}(T) = \Delta B_L^{pp}(T) - \Delta B_L^{pp}(T = 50K) \quad (5.5)$$

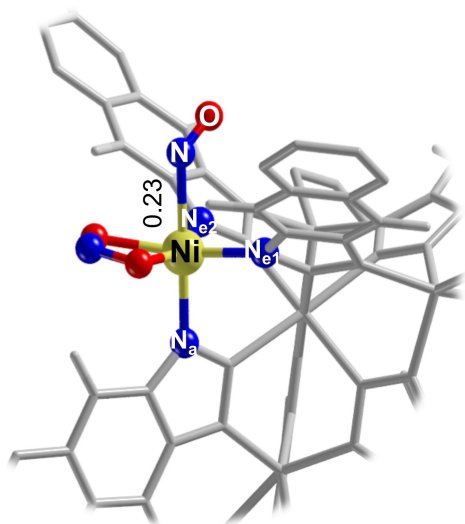
presented in Figure 5.15.  $\Delta B_L^{pp}(T)$  seems to be determined by two temperature-dependent processes, both following approximately an Arrhenius-type behavior

$$\delta B_L^{hom}(T) = b_1 \exp\left(-\frac{E_{A1}}{k_B T}\right) + b_2 \exp\left(-\frac{E_{A2}}{k_B T}\right) \quad (5.6)$$

with the absolute values of  $E_{A1} = 1.1(2)$  kJ/mol (11(2) meV),  $E_{A2} = 23(1)$  kJ/mol (240(35) meV),  $b_1 = 1$  mT,  $b_2 = 42974$  mT, and the Boltzmann constant  $k_B$ . Elucidation of the exact nature of the two motional processes is beyond the scope of this work, but we may assume that they might be related to spin-lattice relaxation ( $E_{A1}$ ) and starting desorption processes of NO at elevated temperatures ( $E_{A2}$ ).

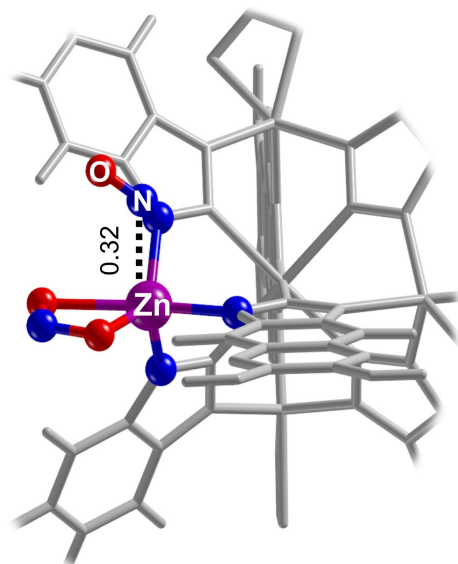
Optimized structure of Ni(II)-NO versus Zn(II)-NO adsorption complexes in Ni-MFU-4l:NO<sub>2</sub>

a)



$\Delta E = 0.0$  kJ/mol

b)



$\Delta E = 26.3$  kJ/mol

FIGURE 5.16: Atomistic structure of Ni-MFU-4l:NO<sub>2</sub>-NO adduct. (a) Ni(II)-NO and (b) Zn(II)-NO binding sites. The metal-nitrosyl bond distances are reported in nm together with the computed relative electronic energy for the two configurations.

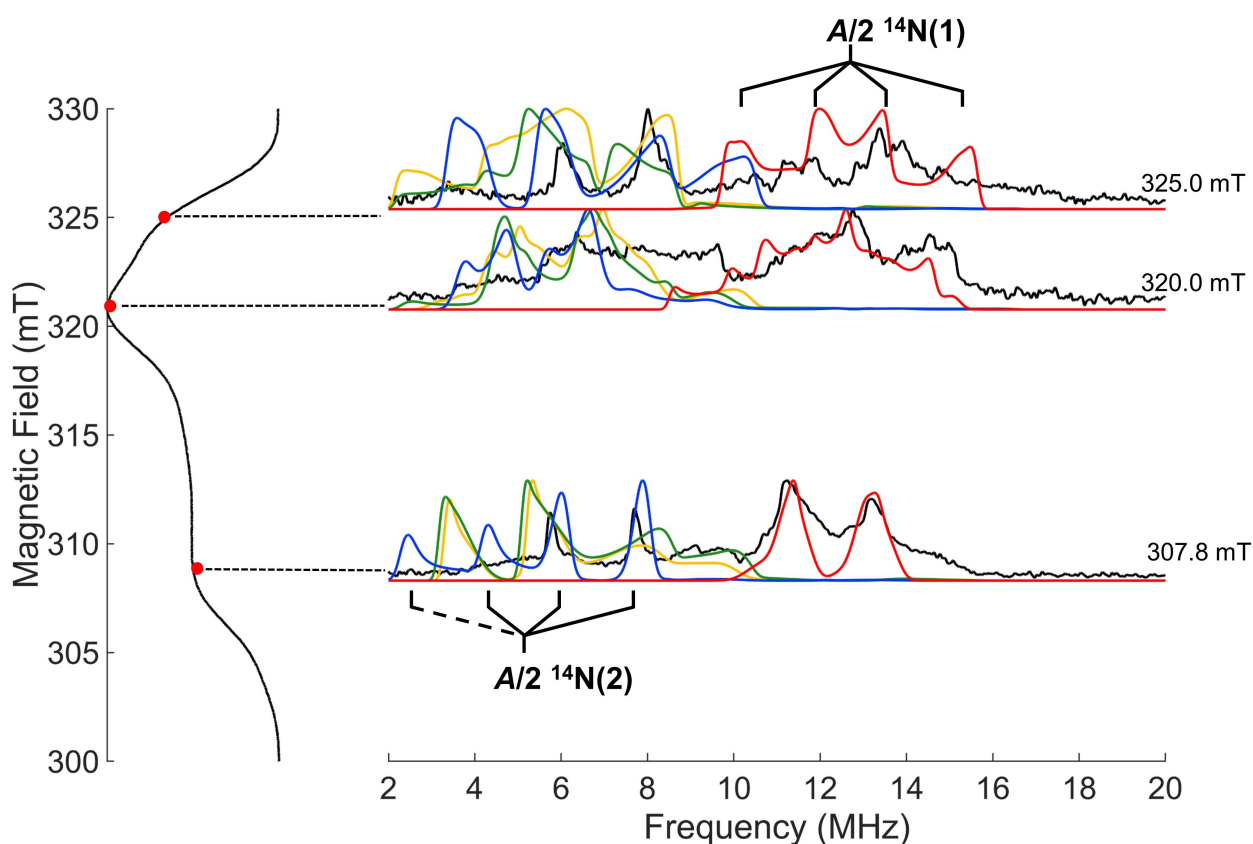
Experimental and simulated <sup>14</sup>N ENDOR spectra of the Ni(II)-NO adsorption complex in Ni-MFU-4l:NO<sub>2</sub>

FIGURE 5.17: X-band <sup>14</sup>N ENDOR spectra simulation of the Ni(II)-NO species in Ni-MFU-4l:NO<sub>2</sub> highlighting the contribution of each <sup>14</sup>N species. The black lines are the experimental spectra. The ESE spectrum with the corresponding field position sampled is plotted on the left. The blue, green and yellow lines represent the simulation obtained with the spin Hamiltonian of <sup>14</sup>N(2) by using the orientation computed from  $N_{f1}$ ,  $N_{f2}$  and  $N_{f3}$ , respectively. The red line is obtained by using the spin Hamiltonian parameters of <sup>14</sup>N(1).

TABLE 5.5: Computed Euler rotation of hyperfine ( $\alpha, \beta, \gamma$ ) and quadrupolar tensors ( $\alpha', \beta', \gamma'$ ) to the  $g$ -tensor. First rotation by  $\alpha$  around  $z$ ; second rotation by  $\beta$  around  $y'$ ; third rotation by  $\gamma$  around  $z''$ . A positive sign corresponds to a clockwise rotation, a negative sign to a counterclockwise rotation. The tensor values (calculated at CASSCF level of theory) are in MHz, while angles (calculated at DFT level of theory) are in degrees.  $g$ -tensor = [2.226 2.255 2.276]

	$^{14}\text{N}$ A -tensor					
	$A_x$	$A_y$	$A_z$	$\alpha$	$\beta$	$\gamma$
$N_{NO}$	-14.8	-14.3	-24.9	79.0	11.7	-106.3
$N_{f1}$	8.4	8.6	12.7	-136.7	50.4	114.7
$N_{f2}$	8.1	8.3	12.4	42.7	30.8	-56.4
$N_{f3}$	6.8	6.9	10.4	-120.7	13.2	138.6
$N_s$	0.4	-0.3	1.2	-48.4	14.6	53.1
	$^{14}\text{N}$ Q -tensor					
	$ e^2qQ/h $	$\eta$	$\alpha'$	$\beta'$	$\gamma'$	
$N_{NO}$	5.0	0.3	140.0	12.9	-98.9	
$N_{f1}$	4.7	0.5	-140.0	49.2	132.3	
$N_{f2}$	4.6	0.4	21.1	18.7	-41.5	
$N_{f3}$	4.3	0.4	-146.7	19.6	154.4	
$N_s$	5.8	0.5	84.2	39.3	-80.2	

### Computed and experimental IR spectra for Ni-MFU-4l:NO<sub>2</sub> and Ni-MFU-4l:Cl

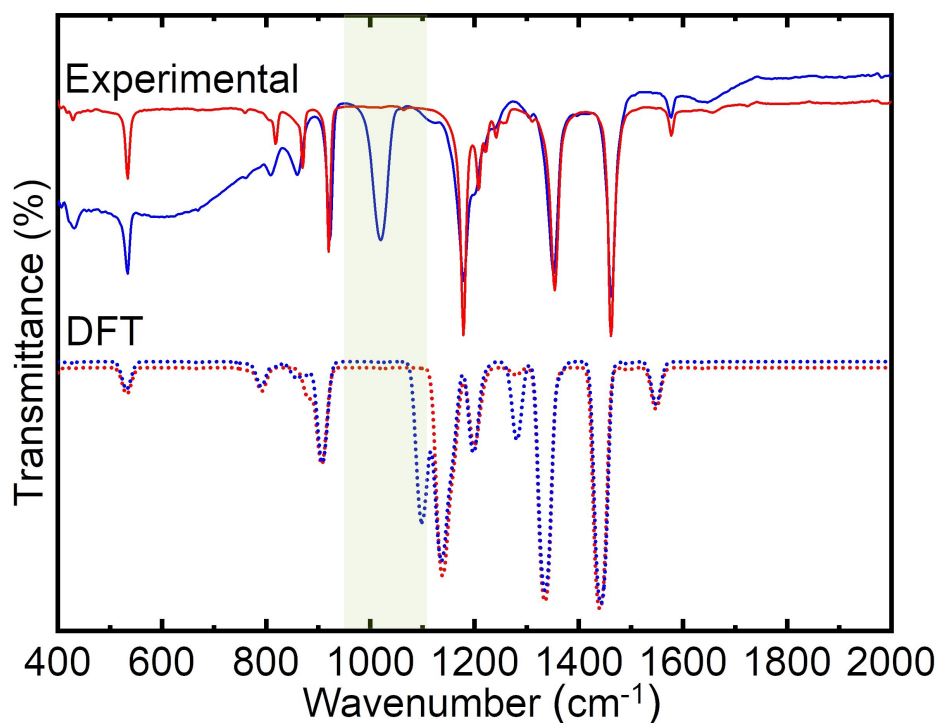


FIGURE 5.18: Calculated (at B3LYP-D3(ABC)/pob-TZVP-rev2 level of theory) and experimental comparison of IR spectra for the Ni-MFU-4l:NO<sub>2</sub> (blue spectra) and Ni-MFU-4l:Cl (red spectra) samples.

### Contour plots of natural CASSCF(11e,11o) orbitals of the Ni(II)-NO adsorption complex

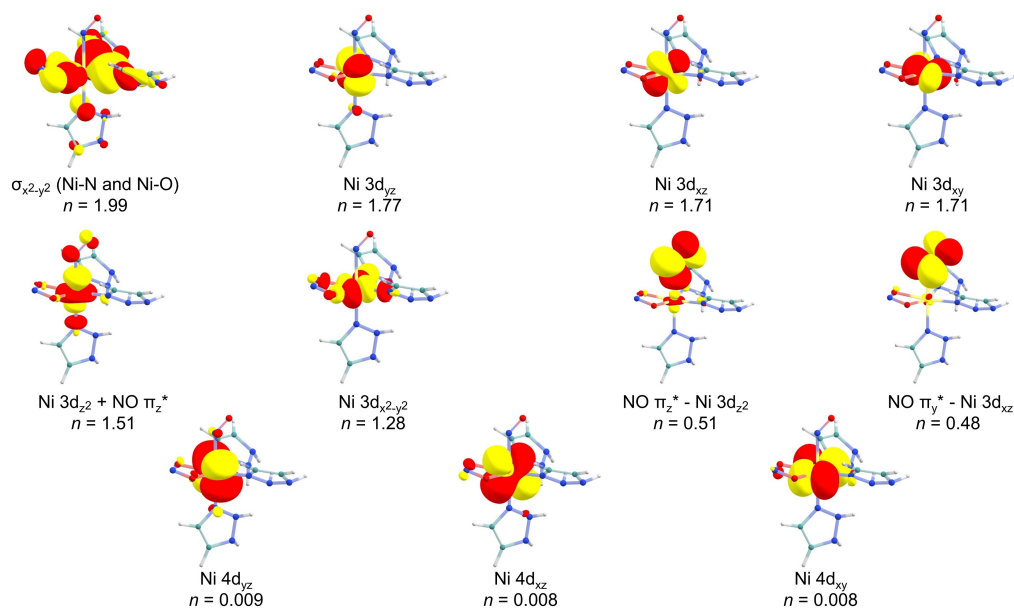


FIGURE 5.19: Contour plots ( $\pm 0.03$  a.u.) of natural CASSCF(11e,11o) orbitals with indicated qualitative character and fractional occupation number ( $n$ ). N, O, Ni, C, Zn and H atoms are reported in blue, red, yellow, green, violet and white, respectively.

### Comparison of EPR spectra with different amounts of NO loading over Ni-MFU-4l:NO<sub>2</sub>

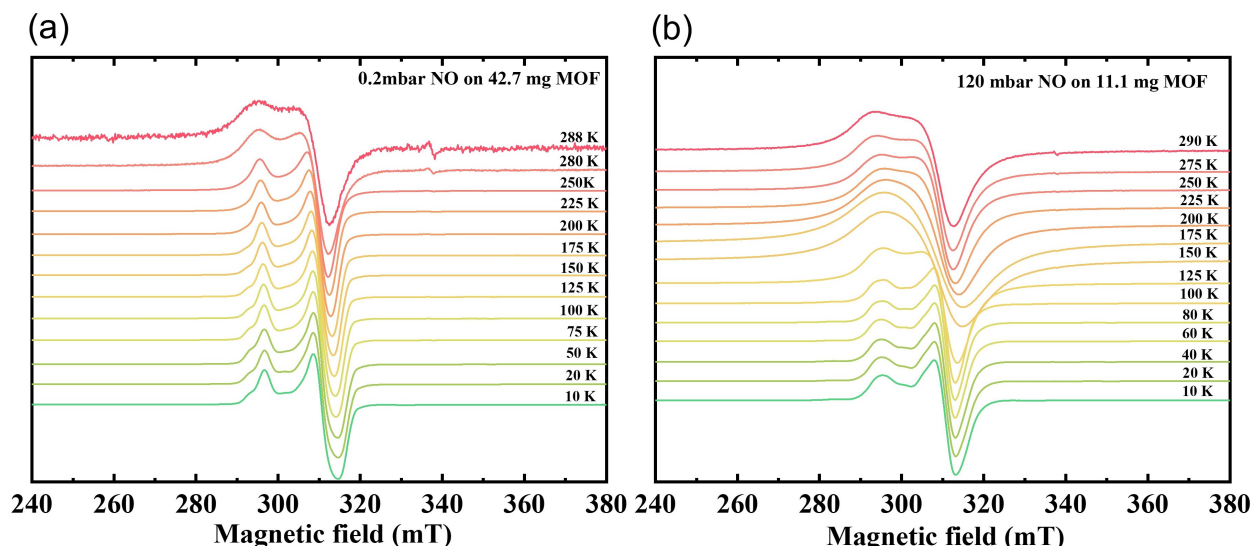


FIGURE 5.20: Temperature-dependent X-band EPR spectra of NO adsorbed over Ni-MFU-4l:NO<sub>2</sub> (a) with 0.2 and (b) 120 mbar

# Bibliography

- (1) Thangavel, K.; Bruzzese, P. C.; Mendt, M.; Folli, A.; Knippen, K.; Volkmer, D.; Murphy, D. M.; Pöppl, A. *Physical Chemistry Chemical Physics* **2023**, DOI: 10.1039/D3CP01449E.
- (2) Andrews, L.; Citra, A. *Chemical reviews* **2002**, *102*, 885–912.
- (3) Hadjiivanov, K. I. *Catalysis Reviews* **2000**, *42*, 71–144.
- (4) Sojka, Z.; Che, M.; Giamello, E. *The Journal of Physical Chemistry B* **1997**, *101*, 4831–4838.
- (5) Spoto, G.; Zecchina, A.; Bordiga, S.; Ricchiardi, G.; Martra, G.; Leofanti, G.; Petrini, G. *Applied Catalysis B: Environmental* **1994**, *3*, 151–172.
- (6) Giamello, E.; Murphy, D.; Magnacca, G.; Morterra, C.; Shioya, Y.; Nomura, T.; Anpo, M. *Journal of Catalysis* **1992**, *136*, 510–520.
- (7) Witzel, F.; Karge, H. G.; Gutsze, A.; Härtel, U. *Chemie Ingenieur Technik* **1991**, *63*, 744–746.
- (8) Rudolf, T.; Böhlmann, W.; Pöppl, A. *Journal of Magnetic Resonance* **2002**, *155*, 45–56.
- (9) Nechita, M.-T.; Berlier, G.; Ricchiardi, G.; Bordiga, S.; Zecchina, A. *Catalysis letters* **2005**, *103*, 33–41.
- (10) Poepl, A.; Rudolf, T.; Manikandan, P.; Goldfarb, D. *Journal of the American Chemical Society* **2000**, *122*, 10194–10200.
- (11) Poppl, A.; Rudolf, T.; Michel, D. *Journal of the American Chemical Society* **1998**, *120*, 4879–4880.
- (12) Umamaheswari, V.; Hartmann, M.; Pöppl, A. *Magnetic Resonance in Chemistry* **2005**, *43*, S205–S214.
- (13) Fisicaro, P.; Giamello, E.; Berlier, G.; Lamberti, C. *Research on chemical intermediates* **2003**, *29*, 805–816.
- (14) Pietrzyk, P.; Góra-Marek, K.; Mazur, T.; Mozgawa, B.; Rado, M.; Chiesa, M.; Zhao, Z.; Sojka, Z. *Journal of Catalysis* **2021**, *394*, 206–219.
- (15) Jensen, S.; Tan, K.; Feng, L.; Li, J.; Zhou, H.-C.; Thonhauser, T. *Journal of the American Chemical Society* **2020**, *142*, 16562–16568.
- (16) Ahrens, M.; Marie, O.; Bazin, P.; Daturi, M. *Journal of Catalysis* **2010**, *271*, 1–11.



- 
- (17) SchieSSer, W.; Vinek, H.; Jentys, A. *Applied Catalysis B: Environmental* **2001**, *33*, 263–274.
- (18) Ford, P. C.; Lorkovic, I. M. *Chemical reviews* **2002**, *102*, 993–1018.
- (19) McCleverty, J. *Chemical reviews* **2004**, *104*, 403–418.
- (20) Wyllie, G. R.; Scheidt, W. R. *Chemical reviews* **2002**, *102*, 1067–1090.
- (21) Chiesa, M.; Giamello, E.; Che, M. *Chemical reviews* **2010**, *110*, 1320–1347.
- (22) Umamaheswari, V.; Hartmann, M.; Pöppl, A. *The Journal of Physical Chemistry B* **2005**, *109*, 19723–19731.
- (23) Yahiro, H.; Lund, A.; Shiotani, M. *Spectrochimica Acta Part A: Molecular and Biomolecular Spectroscopy* **2004**, *60*, 1267–1278.
- (24) Chiesa, M.; Giamello, E. *Catalysis Letters* **2021**, 1–20.
- (25) Sojka, Z.; Pietrzyk, P. *Spectrochimica Acta Part A: Molecular and Biomolecular Spectroscopy* **2004**, *60*, 1257–1265.
- (26) Pietrzyk, P.; Sojka, Z. *The Journal of Physical Chemistry A* **2005**, *109*, 10571–10581.
- (27) Podolska-Serafin, K.; Pietrzyk, P. *Journal of Molecular Structure* **2019**, *1180*, 754–763.
- (28) ejka, J.; ilková, N.; Nachtigall, P., *Molecular Sieves: From Basic Research to Industrial Applications: Proceedings of the 3rd International Zeolite Symposium (3rd FEZA), Prague, Czech Republic, August 23-26, 2005*; Elsevier.
- (29) Gutjahr, M.; Böttcher, R.; Pöppl, A. *The Journal of Physical Chemistry B* **2002**, *106*, 1345–1349.
- (30) Barth, B.; Mendt, M.; Pöppl, A.; Hartmann, M. *Microporous and Mesoporous Materials* **2015**, *216*, 97–110.
- (31) Mendt, M.; Barth, B.; Hartmann, M.; Pöppl, A. *J. Chem. Phys.* **2017**, *147*, 224701.
- (32) Mendt, M.; Gutt, F.; Kavoosi, N.; Bon, V.; Senkovska, I.; Kaskel, S.; Pöppl, A. *The Journal of Physical Chemistry C* **2016**, *120*, 14246–14259.
- (33) Jee, B.; Koch, K.; Moschkowitz, L.; Himsl, D.; Hartman, M.; Pöppl, A. *The Journal of Physical Chemistry Letters* **2011**, *2*, 357–361.
- (34) Giamello, E.; Garrone, E.; Guglielminotti, E.; Zecchina, A. *Journal of molecular catalysis* **1984**, *24*, 59–69.
- (35) Chiesa, M.; Paganini, M. C.; Giamello, E.; Di Valentin, C.; Pacchioni, G. *Journal of Molecular Catalysis A: Chemical* **2003**, *204*, 779–786.
- (36) Denysenko, D.; Grzywa, M.; Tonigold, M.; Streppel, B.; Krkljus, I.; Hirscher, M.; Mugnaioli, E.; Kolb, U.; Hanss, J.; Volkmer, D. *Chemistry—A European Journal* **2011**, *17*, 1837–1848.

- (37) Biswas, S.; Grzywa, M.; Nayek, H. P.; Dehnen, S.; Senkowska, I.; Kaskel, S.; Volkmer, D. *Dalton transactions* **2009**, 6487–6495.
- (38) Denysenko, D.; Jelic, J.; Reuter, K.; Volkmer, D. *Chemistry—A European Journal* **2015**, *21*, 8188–8199.
- (39) Walsh, J. P.; Sproules, S.; Chilton, N. F.; Barra, A.-L.; Timco, G. A.; Collison, D.; McInnes, E. J.; Winpenny, R. E. *Inorganic Chemistry* **2014**, *53*, 8464–8472.
- (40) Amrutha, K.; Kathirvelu, V. *Journal of Physics and Chemistry of Solids* **2021**, *157*, 110224.
- (41) Wilson, C. R.; Riley, M. J.; Wang, D.; Hanson, G. R. *Chemical physics* **1997**, *217*, 63–70.
- (42) Amrutha, K.; Kathirvelu, V. *Magnetic Resonance in Chemistry* **2022**, *60*, 414–421.
- (43) Krzystek, J.; Park, J.-H.; Meisel, M. W.; Hitchman, M. A.; Stratemeier, H.; Brunel, L.-C.; Telser, J. *Inorganic chemistry* **2002**, *41*, 4478–4487.
- (44) Krzystek, J.; Ozarowski, A.; Telser, J. *Coordination chemistry reviews* **2006**, *250*, 2308–2324.
- (45) Krzystek, J.; Zvyagin, S.; Ozarowski, A.; Trofimenko, S.; Telser, J. *Journal of magnetic resonance* **2006**, *178*, 174–183.
- (46) Lu, J.; Ozel, I. O.; Belvin, C. A.; Li, X.; Skorupskii, G.; Sun, L.; Ofori-Okai, B. K.; Dinc, M.; Gedik, N.; Nelson, K. A. *Chemical science* **2017**, *8*, 7312–7323.
- (47) Collison, D.; Helliwell, M.; Jones, V. M.; Mabbs, F. E.; McInnes, E. J.; Riedi, P. C.; Smith, G. M.; Pritchard, R. G.; Cross, W. I. *Journal of the Chemical Society, Faraday Transactions* **1998**, *94*, 3019–3025.
- (48) Van Dam, P. J.; Klaassen, A. A.; Reijerse, E. J.; Hagen, W. R. Application of high frequency EPR to integer spin systems: Unusual behavior of the double-quantum line, 1998.
- (49) Mroziski, J.; Skorupa, A.; Pochaba, A.; Dromzée, Y.; Verdaguer, M.; Goovaerts, E.; Varcammen, H.; Korybut-Daszkiewicz, B. *Journal of Molecular Structure* **2001**, *559*, 107–118.
- (50) Pardi, L. A.; Hassan, A. K.; Hulsbergen, F. B.; Reedijk, J.; Spek, A. L.; Brunel, L.-C. *Inorganic Chemistry* **2000**, *39*, 159–164.
- (51) Jiang, S.-D.; Maganas, D.; Levesanos, N.; Ferentinos, E.; Haas, S.; Thirunavukkuarasu, K.; Krzystek, J.; Dressel, M.; Bogani, L.; Neese, F., et al. *Journal of the American Chemical Society* **2015**, *137*, 12923–12928.
- (52) Kubica, A.; Kowalewski, J.; Kruk, D.; Odelius, M. *The Journal of Chemical Physics* **2013**, *138*, 064304.
- (53) Neese, F. *Coordination Chemistry Reviews* **2009**, *253*, 526–563.

- (54) Ye, S.; Neese, F. *Inorganic chemistry* **2010**, *49*, 772–774.
- (55) Neese, F. *Journal of the American Chemical Society* **2006**, *128*, 10213–10222.
- (56) Hayes, W.; Wilkens, J. *Proceedings of the Royal Society of London. Series A. Mathematical and Physical Sciences* **1964**, *281*, 340–365.
- (57) Abragam, A.; Bleaney, B., *Electron paramagnetic resonance of transition ions*; Oxford University Press: 2012.
- (58) Atherton, N., *Principles of Electron Spin Resonance*; Ellis Horwood PTR Prentice Hall physical chemistry series; Ellis Horwood: 1993.
- (59) Harmer, J. R., *Hyperfine spectroscopy–ENDOR*; Wiley & Sons: 2018.
- (60) Fitzpatrick, J. A.; Manby, F. R.; Western, C. M. *The Journal of chemical physics* **2005**, *122*, 084312.
- (61) Mims, W.; Peisach, J. *The Journal of Chemical Physics* **1978**, *69*, 4921–4930.
- (62) Praneeth, V.; Neese, F.; Lehnert, N. *Inorganic chemistry* **2005**, *44*, 2570–2572.
- (63) Wäckerlin, C.; Chylarecka, D.; Kleibert, A.; Müller, K.; Iacovita, C.; Nolting, F.; Jung, T. A.; Ballav, N. *Nature communications* **2010**, *1*, 61.
- (64) Daniel, C.; Gourlaouen, C. *Molecules* **2019**, *24*, 3638.
- (65) Enemark, J. H.; Feltham, R. D. *Journal of the American Chemical Society* **1974**, *96*, 5002–5004.
- (66) Geoffroy, G. L., *Topics in inorganic and organometallic stereochemistry*; John Wiley & Sons: 2009.
- (67) Enemark, J.; Feltham, R. *Coordination Chemistry Reviews* **1974**, *13*, 339–406.
- (68) Hoffmann, R.; Chen, M. M.; Elian, M.; Rossi, A. R.; Mingos, D. M. P. *Inorganic Chemistry* **1974**, *13*, 2666–2675.
- (69) Scheidt, W. R.; Hatano, K.; Rupprecht, G.; Piciulo, P. *Inorganic Chemistry* **1979**, *18*, 292–299.
- (70) Dierks, E. A.; Hu, S.; Vogel, K. M.; Yu, A. E.; Spiro, T. G.; Burstyn, J. N. *Journal of the American Chemical Society* **1997**, *119*, 7316–7323.
- (71) Stpniewski, A.; Rado, M.; Góra-Marek, K.; Broclawik, E. *Physical Chemistry Chemical Physics* **2016**, *18*, 3716–3729.
- (72) Radon, M.; Broclawik, E.; Pierloot, K. *The Journal of Physical Chemistry B* **2010**, *114*, 1518–1528.
- (73) Freitag, L.; Knecht, S.; Angeli, C.; Reiher, M. *Journal of chemical theory and computation* **2017**, *13*, 451–459.

- (74) AmpSSler, T.; Monsch, G.; Popp, J.; Riggenmann, T.; Salvador, P.; Schröder, D.; Klüfers, P. *Angewandte Chemie International Edition* **2020**, *59*, 12381–12386.
- (75) Bower, J. K.; Sokolov, A. Y.; Zhang, S. *Angewandte Chemie International Edition* **2019**, *58*, 10225–10229.
- (76) Denysenko, D.; Volkmer, D. *Faraday Discussions* **2017**, *201*, 101–112.
- (77) Stoll, S.; Schweiger, A. *Journal of magnetic resonance* **2006**, *178*, 42–55.
- (78) Höfer, P.; Grupp, A.; Nebenführ, H.; Mehring, M. *Chemical physics letters* **1986**, *132*, 279–282.
- (79) Davies, E. *Physics Letters A* **1974**, *47*, 1–2.
- (80) Denysenko, D.; Grzywa, M.; Jelic, J.; Reuter, K.; Volkmer, D. *Angewandte Chemie International Edition* **2014**, *53*, 5832–5836.
- (81) Dovesi, R.; Erba, A.; Orlando, R.; Zicovich-Wilson, C. M.; Civalleri, B.; Maschio, L.; Rérat, M.; Casassa, S.; Baima, J.; Salustro, S., et al. *Wiley Interdisciplinary Reviews: Computational Molecular Science* **2018**, *8*, e1360.
- (82) Erba, A.; Baima, J.; Bush, I.; Orlando, R.; Dovesi, R. *Journal of chemical theory and computation* **2017**, *13*, 5019–5027.
- (83) Lee, C.; Yang, W.; Parr, R. G. *Physical review B* **1988**, *37*, 785.
- (84) Beeke, A. D. J. *Chem. Phys* **1993**, *98*, 5648–6.
- (85) Grimme, S.; Antony, J.; Ehrlich, S.; Krieg, H. *The Journal of chemical physics* **2010**, *132*, 154104.
- (86) Grimme, S.; Ehrlich, S.; Goerigk, L. *Journal of computational chemistry* **2011**, *32*, 1456–1465.
- (87) Vilela Oliveira, D.; Laun, J.; Peintinger, M. F.; Bredow, T. *Journal of Computational Chemistry* **2019**, *40*, 2364–2376.
- (88) Eichkorn, K.; Weigend, F.; Treutler, O.; Ahlrichs, R. *Theoretical Chemistry Accounts* **1997**, *97*, 119–124.
- (89) Zicovich-Wilson, C. M.; Pascale, F.; Roetti, C.; Saunders, V.; Orlando, R.; Dovesi, R. *Journal of computational chemistry* **2004**, *25*, 1873–1881.
- (90) Pascale, F.; Zicovich-Wilson, C. M.; López Gejo, F.; Civalleri, B.; Orlando, R.; Dovesi, R. *Journal of computational chemistry* **2004**, *25*, 888–897.
- (91) Carteret, C.; De La Pierre, M.; Dossot, M.; Pascale, F.; Erba, A.; Dovesi, R. *The Journal of chemical physics* **2013**, *138*, 014201.
- (92) Neese, F. *Wiley Interdisciplinary Reviews: Computational Molecular Science* **2022**, *12*, e1606.

- 
- (93) Remenyi, C.; Reviakine, R.; Arbuznikov, A. V.; Vaara, J.; Kaupp, M. *The Journal of Physical Chemistry A* **2004**, *108*, 5026–5033.
- (94) HeSS, B. A.; Marian, C. M.; Wahlgren, U.; Gropen, O. *Chemical Physics Letters* **1996**, *251*, 365–371.
- (95) Grimme, S. *The Journal of chemical physics* **2006**, *124*, 034108.
- (96) Weigend, F.; Ahlrichs, R. *Physical Chemistry Chemical Physics* **2005**, *7*, 3297–3305.
- (97) Whitten, J. L. *The Journal of Chemical Physics* **1973**, *58*, 4496–4501.
- (98) Weigend, F. *Physical chemistry chemical physics* **2006**, *8*, 1057–1065.
- (99) Stoychev, G. L.; Auer, A. A.; Neese, F. *Journal of chemical theory and computation* **2017**, *13*, 554–562.
- (100) Barone, V. *The Journal of Physical Chemistry* **1995**, *99*, 11659–11666.

## Chapter 6

# Cr(III) trimer complexes in the MIL-101(Cr) and bimetallic MIL-100(Al/Cr) MOFs

### 6.1 Introduction

In recent years, the magnetic behaviors of MOFs have been getting attention in the field of molecular magnetism since they consist of a paramagnetic SBU along with the organic connecting linker[1]. Among MOFs, MIL (Materials Institute Lavoisier) -101 and MIL-100 MOF families are complex MOFs in crystal structure just with a single linker and SBU. In addition, these MOFs have pores in two different sizes[2] (29 Å and 34 Å for MIL-101; 25 Å and 29 Å for MIL-100) that allow the adsorption of gas and liquid[3, 4]. MIL-101(M) and MIL-100(M) frameworks contain trinuclear metal ions  $M(III)_3$  in the octahedral units, and four trimers, forming a supertetrahedron. In MIL-100, the trimers are connected through benzene tricarboxylate (BTC) linker and in MIL-101, the linker is benzene dicarboxylate (BDC)[3]. MIL-100(Al) and MIL-101(Al) MOFs have been investigated for the sorption and separation of gases, adsorption of liquids[5], upon high-pressure effect[6], ethylene polymerization[7] and encapsulation of chemical species[5]. In addition, Mali *et al.*[8] investigated the magnetism of Al(III) and Fe(III) mixed metals in MIL-100 MOF by means of  $^{27}Al$  NMR and spectroscopy and reported the arrangement of those metal ions (3Fe and/or 2Fe1Al units, 1Fe2Al units) within the framework. Such bimetal-organic MIL-100 and MIL-101 frameworks with coordinatively unsaturated metal sites may serve as Lewis acid sites for highly efficient catalytic processes[9, 10].

Understanding the pairwise magnetic exchange interaction in the metal trimer clusters is complicated, and the term magnetic 'frustration' (Figure 6.1b) often describes this situation[11]. The

influence of anti-symmetric exchange on the electronic properties of trinuclear Cu(II)<sub>3</sub> metal complexes was experimentally observed for the first time by Tsukerlat *et al.*[11, 12]. Likewise, anti-symmetric exchange interaction of Cr(III)<sub>3</sub> trimer cluster was experimentally investigated by M. Honda *et al.*,[13] A. Vlachos *et al.*,[14] A. Figuerola *et al.*,[15] by means of SQUID magnetometry and EPR spectroscopy. Furthermore, the role played by the guest-framework intermolecular interactions, influence of adsorption on the intramolecular interactions and the changes in the internal structure can be elucidated by tracking the paramagnetic species in the SBU[1, 4, 16–19]. In this regard, EPR spectroscopy is one of the inevitable tools to understand the change in the local structure of MOFs due to guest molecular interaction during *ex situ*[17, 20] and *in situ*[16, 18, 21] gas adsorption, liquid adsorption, post synthetically modified ion exchange,[22, 23] and inter molecular magnetic couplings [22, 24, 25] by monitoring the behavior of paramagnetic metal ions in the SBU.

Herein, we studied and discussed the local structure and the intramolecular interaction of EPR active Cr(III) trimer complex of the MIL-101(Cr) and magnetically diluted bimetallic MIL-100(Al<sub>0.8</sub>Cr<sub>0.2</sub>) MOFs with Al(III)<sub>3-x</sub>Cr(III)<sub>x</sub> units for the comparison by means of SQUID magnetometer and multi-frequency EPR spectroscopy techniques[26].

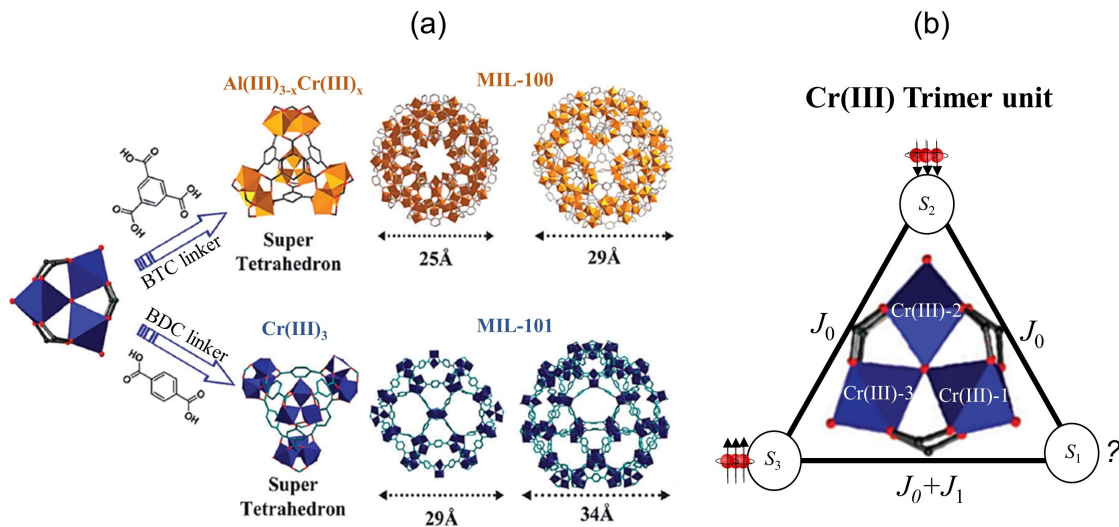


FIGURE 6.1: (a) Cr(III)/Al(III) ions are in the octahedral trimer units and four trimers, forming a supertetrahedra (Modified from rivera *et al.*[27] with permission from the Royal Society of Chemistry.) showing MIL-101(Cr) and MIL-100(Al<sub>0.8</sub>Cr<sub>0.2</sub>) frameworks, and (b) Scheme of the trimer unit contains three  $S = 3/2$  Cr(III) spins shows the situation of spin ‘frustration’ ( $J_0$  and  $J_1$  are the exchange coupling parameters).

In general, the exchange Hamiltonian for the Cr(III) trimers can be written as [13, 28],

$$\hat{H}_{Ex} = -2J_0(\hat{S}_1 \cdot \hat{S}_2 + \hat{S}_2 \cdot \hat{S}_3 + \hat{S}_3 \cdot \hat{S}_1) - 2J_1(\hat{S}_3 \cdot \hat{S}_1), \quad (6.1)$$

where  $\hat{S}_1$ ,  $\hat{S}_2$  and  $\hat{S}_3$  are the Cr(III) spin operators with single  $S_i = 3/2$  spins for each chromium ion.  $J_0$  is the main exchange parameter and  $|J_1/J_0| \ll 1$ . Eqn.6.1 results in five degenerate energy levels corresponding to the total spin states  $S_T = 1/2, 3/2, 5/2, 7/2$  and  $9/2$  of the trimer with the twofold degenerate  $S_T = 1/2$  state being the ground state in the case of antiferromagnetically (AFM) coupled trimers when  $J_1 = 0$ . The degeneracy of the  $S_T = 1/2$  state will be further lifted only when  $J_1 \neq 0$  [13]. However,  $J_1$  is considered to be negligible since Cr(III) ions in the trimer unit is assumed to be in equal distance.

Also, the Hamiltonian of inter-trimer interaction can be defined by [13, 28],

$$\hat{H}_{in} = -2J_{in}(\hat{S}_{iT} \cdot \hat{S}_{jT}), \quad (6.2)$$

where  $S_{iT}$  and  $S_{jT}$  correspond to the total spins of  $i$ -th and  $j$ -th trimers, respectively. In case of EPR experiments, the additional terms

$$\hat{H} = \mu_B \vec{B} \mathbf{g} (\hat{S}_1 + \hat{S}_2 + \hat{S}_3) + \sum_{i=1}^3 (D_{ZFS,i} \{ \hat{S}_{i,z}^2 - S_i[S_i + 1]/3 \} + E_{ZFS,i} \{ \hat{S}_{i,x'}^2 - \hat{S}_{i,y'}^2 \}) + D(\hat{S}_1 \times \hat{S}_2 + \hat{S}_1 \times \hat{S}_3 + \hat{S}_2 \times \hat{S}_3) \quad (6.3)$$

must be considered in the spin-Hamiltonian for the Cr(III) trimers, where the first term represents the Zeeman interaction between  $S = 3/2$  electron spins of the chromium ions and the external magnetic field ( $\mu_B$  is the Bohr magneton,  $\mathbf{g}$  is the  $g$ -tensor,  $B$  is the external magnetic field). The second term corresponds to the zero field splitting (ZFS) with the axial and rhombic ZFS parameters  $D_{ZFS,i}$  and  $E_{ZFS,i}$  and the third term describes the antisymmetric exchange contribution caused by the Dzyaloshinsky-Moriya (D-M) interaction. Here  $D$  is a pseudo-vector directed perpendicular to a plane defined by the Cr(III) ions in the trimers [13].

## 6.2 SQUID magnetometry results

Figure 6.2 shows the temperature variation of zero-field-cooling (ZFC), field cooled cooling (FCC) and field cooled warming (FCW) magnetic susceptibility behavior of MIL-101(Cr) and MIL-100( $\text{Al}_{0.8}\text{Cr}_{0.2}$ ) MOFs obtained in 0.5 T magnetic field. The  $M$ - $T$  (magnetization vs temperature) behavior of both the MOFs suggests a paramagnetic nature. The paramagnetic susceptibility of both the MOFs follows Curie-Weiss (C-W) law (eqn. 6.4) for temperatures  $T > 15$  K (MIL-101(Cr)) and  $T > 120$  K



(MIL-100(Al<sub>0.8</sub>Cr<sub>0.2</sub>)). The fitted parameters (Figure 6.2a & 6.2b insets) yield effective paramagnetic moment ( $\mu_{eff}$ ) and paramagnetic Curie temperature ( $\theta_p$ ) values as -82 K and 5.43  $\mu_B$ /f.u. (f.u.-formula unit), respectively for MIL-101(Cr) MOF. While for MIL-100(Al<sub>0.8</sub>Cr<sub>0.2</sub>), it is -87 K and 3.14  $\mu_B$ /f.u., respectively. The occurrence of a negative sign of  $\theta_p$  of both the MOFs indicates the existence of AFM interactions in the system.

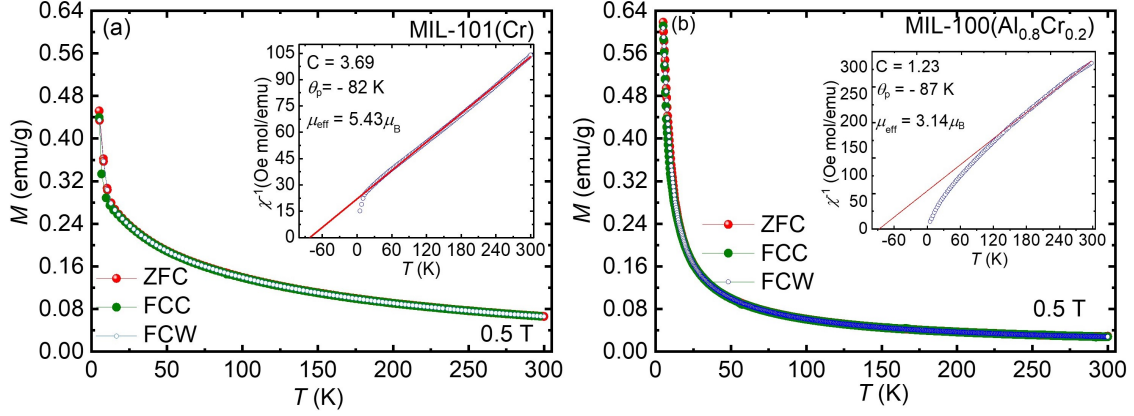


FIGURE 6.2: ZFC, FCC and FCW  $M$ - $T$  curves of (a) MIL-101(Cr), and (b) MIL-100(Al<sub>0.8</sub>Cr<sub>0.2</sub>) with an applied field of 0.5 T. (Insets: The temperature-dependence of the reciprocal of the magnetic susceptibility of its corresponding ZFC curves.)

The magnetic susceptibility can be written as

$$\chi = \frac{C}{T - \theta_p} \quad (6.4)$$

where,  $\chi$  is the magnetic susceptibility,  $C$  is the Curie constant, and  $\theta_p$  is the paramagnetic Curie temperature.

Also,  $\mu_{eff}$  was calculated using the following relation,

$$\mu_{eff} = \sqrt{\frac{3k_B C}{N\mu_B^2}} = \sqrt{8C} \quad (6.5)$$

where,  $\mu_{eff}$  is the effective Bohr magneton,  $k_B$  is the Boltzmann constant,  $C$  is the Curie constant,  $N$  is the Avogadro number and  $\mu_B$  is the electron Bohr magneton. ZFC, FCC, and FCW curves for both materials are identical (Figure 6.2), and No magnetic hysteresis effects at any temperatures were observed, as shown by field-dependent magnetization measurements (Figure 6.3).

For MIL-101(Cr) the overall temperature-dependence of  $\chi^{-1}$  is typical for Cr(III) trimers[13, 14, 17]. Therefore, using [13, 14, 17]

$$\theta_p = 5 \frac{(J_0 + \frac{J_1}{3})}{k_B} \quad (6.6)$$

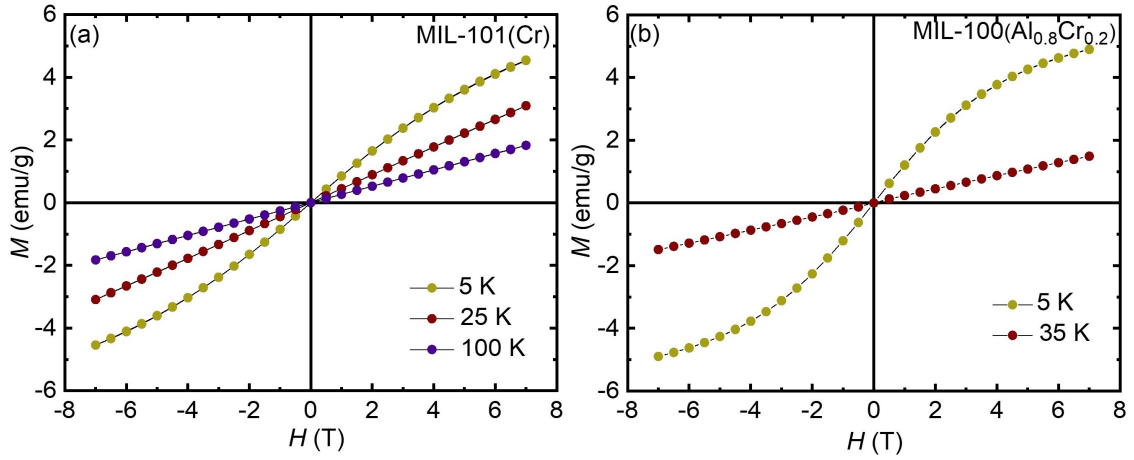


FIGURE 6.3:  $M$ - $H$  curves recorded at 5 K, 25 K and 100 K for (a) MIL-101(Cr) and, 5 K and 35 K for (b) MIL-100( $\text{Al}_{0.8}\text{Cr}_{0.2}$ ).

TABLE 6.1: Paramagnetic Curie temperature ( $\theta_p$ ), effective magnetic moment ( $\mu_{eff}$ ) and Curie constant values of MIL-100(Cr) and MIL-101( $\text{Al}_{0.8}\text{Cr}_{0.2}$ ) from SQUID and EPR measurements.

MOFs	Measurement	$\theta_p$ (K)	$\mu_{eff}$ ( $\mu_B/\text{f.u.}$ )	$C$
MIL-101(Cr)	SQUID	-82	5.43	3.69
	EPR	-70	-	-
MIL-100 ( $\text{Al}_{0.8}\text{Cr}_{0.2}$ )	SQUID	-87	3.14	1.23
	EPR	-85	-	-

TABLE 6.2: Comparison of magnetization values for the MIL-101(Cr) and MIL-100( $\text{Al}_{0.8}\text{Cr}_{0.2}$ ) MOFs found from  $M$ - $T$  and  $M$ - $H$  curves at the 5 K, 25 K, 35 K and 100 K temperatures

MOFs	$H$ (T)	$M$ (emu/g)				
		at 5 K	at 25 K	at 35 K	at 100 K	300 K
MIL-101(Cr)	( $M$ - $H$ )7 T	4.54	3.12	-	1.81	-
	( $M$ - $H$ )0.5 T	0.44	0.23	-	0.12	-
	( $M$ - $T$ )0.5 T	0.44	0.23	0.21	0.13	0.06
MIL-100 ( $\text{Al}_{0.8}\text{Cr}_{0.2}$ )	( $M$ - $H$ )7 T	4.95	-	1.47	-	-
	( $M$ - $H$ )0.5 T	0.59	-	0.12	-	-
	( $M$ - $T$ ) 0.5 T	0.59	0.16	0.12	0.06	0.00

we can estimate  $J_0 = -11.4 \text{ cm}^{-1}$  for MIL-101(Cr) from the susceptibility data at  $T > \sim 15 \text{ K}$ . Here, we assumed  $J_0 \gg J_1$  as we could not determine  $J_1$  from the magnetization measurements. According to Honda *et al.* [13] the steep drop in  $\chi^{-1}$  at low temperatures  $T < \sim 15 \text{ K}$  can be associated with the inter-trimer interaction and provides a lower limit for a second Curie temperature-like parameter  $\theta_p > -6 \text{ K}$  (Figure 6.4) where

$$\theta'_p = \frac{nJ_{in}}{4k_B} \quad (6.7)$$

In the case of MIL-101(Cr) with its supertetrahedral structure of the connected Cr(III) trimers [3]  $n = 3$  provides  $|J_0| > |J_{in}|$  ( $J_{in} = -5.6 \text{ cm}^{-1}$ ).

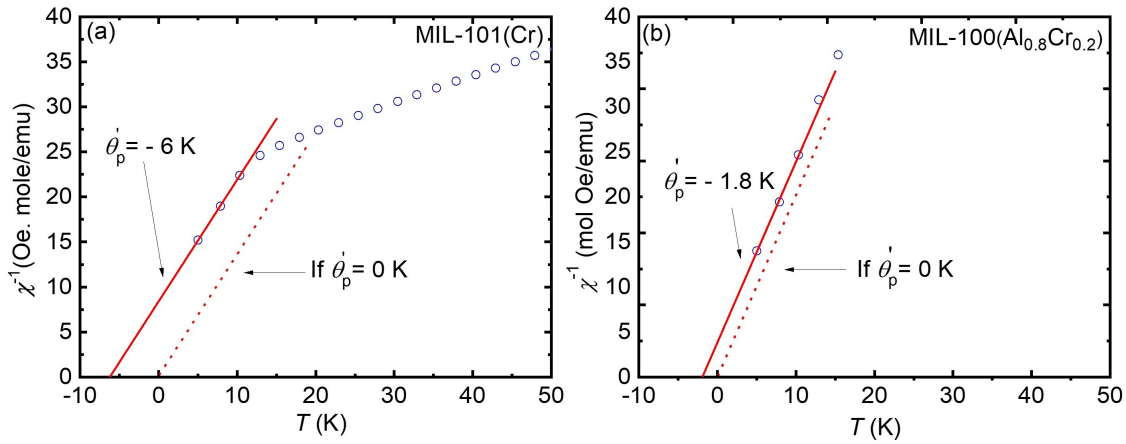


FIGURE 6.4: C-W fit on the temperature-dependent reciprocal of the magnetic susceptibility of (a) MIL-101(Cr) and (b) MIL-100( $\text{Al}_{0.8}\text{Cr}_{0.2}$ ) below  $T < 15 \text{ K}$ .

In the case of MIL-100( $\text{Al}_{0.8}\text{Cr}_{0.2}$ ), the  $\chi^{-1}$  temperature-dependence does not give an indication of the presence of Cr(III) trimers but displays a rather unspecific response of one or several AFM coupled spin systems. Assuming again a further contribution dominating the magnetization data at  $T < 30 \text{ K}$  and applying eqn.6.4, we can roughly estimate the lower limit for a second Curie temperature like parameter  $\theta'_p > -1.8 \text{ K}$  (Figure 6.4). The small limit  $|\theta'_p|$  might indicate a very weak inter-trimer exchange between various  $\text{Al(III)}_{3-x}\text{Cr(III)}_x$  units or just a simple paramagnetic contribution due to isolated Cr(III) ions.

### 6.3 EPR spectroscopy results

Figure 6.5 illustrates a series of temperature-dependent X-band EPR data of MIL-100(Cr) and MIL-100( $\text{Al}_{0.8}\text{Cr}_{0.2}$ ) materials. For comparison with magnetization data, the temperature-dependent EPR intensities  $I_{EPR}$ , which are proportional to the magnetic susceptibilities ( $\chi \propto I_{EPR}$ ) were extracted from the temperature-dependent X-band spectra (Figure 6.5) as derived by full double

integration of the corresponding spectra. The insets of Figure 6.6 show their corresponding inverse intensity  $I_{EPR}^{-1}$  as a function of temperature and fitted using C-W law, eqn. 6.4. The EPR intensities provide  $\theta_p = -70$  K and  $-85$  K for MIL-101(Cr) and MIL-100( $Al_{0.8}Cr_{0.2}$ ), respectively, from the C-W fit, which is in reasonable agreement with the  $\theta_p$  values found from the magnetization susceptibility data and once again suggest the existence of antiferromagnetic interactions in both materials.

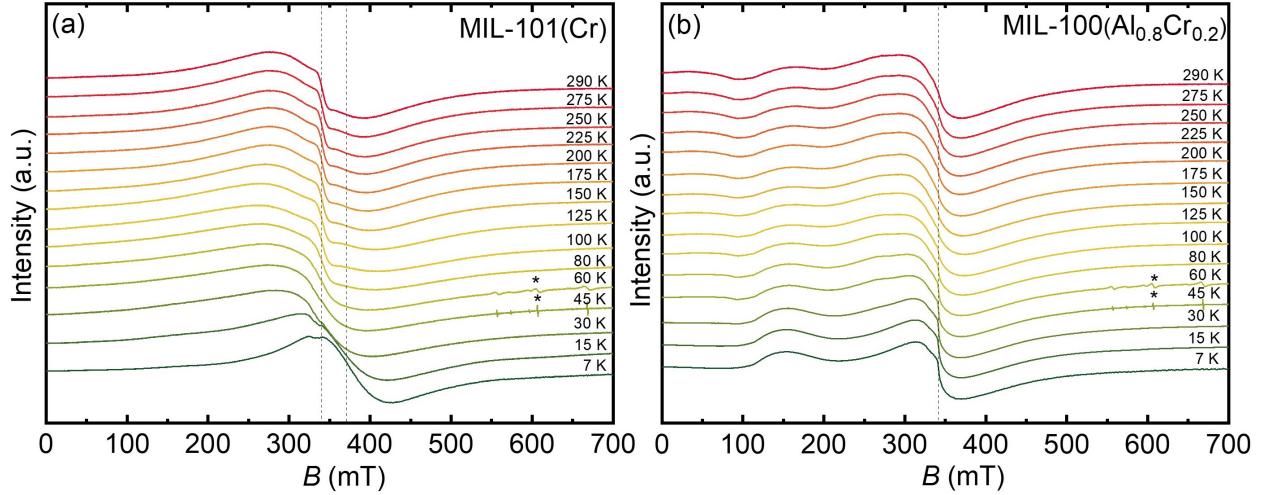


FIGURE 6.5: Temperature-dependent X-band EPR data of (a) MIL-101(Cr) and (b) MIL-100( $Al_{0.8}Cr_{0.2}$ ) at temperature ranging from  $T = 7$  K to  $T = 290$  K (\*-corresponds to the gaseous oxygen in the cryostat).

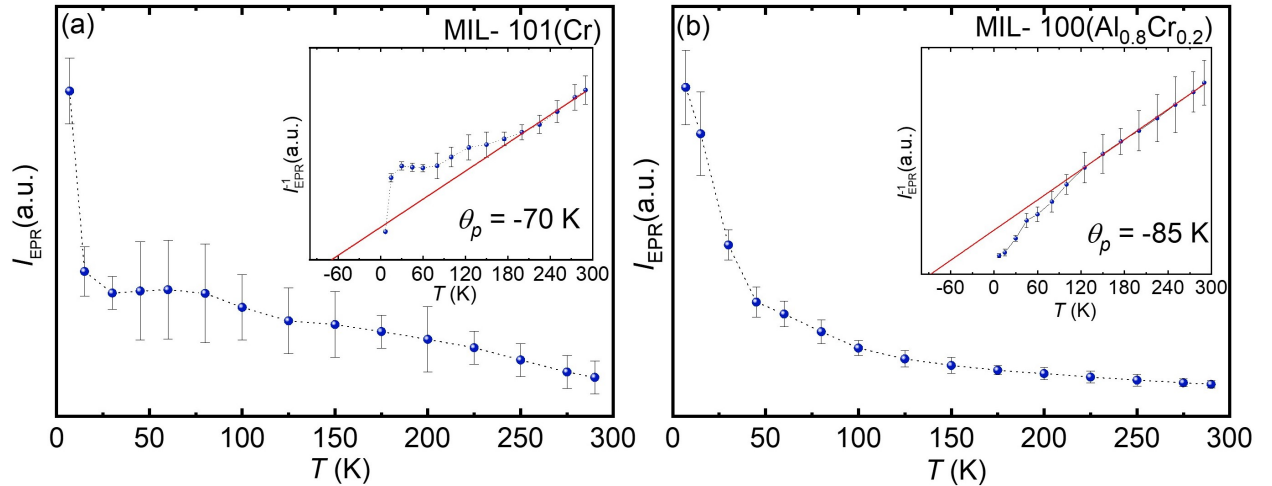


FIGURE 6.6: EPR Intensities ( $I_{EPR}$ ) belong to Cr(III) spectra of (a) MIL-101(Cr), and (b) MIL-100( $Al_{0.8}Cr_{0.2}$ ) extracted from temperature-dependent X-band EPR data. (Inset: Corresponding C-W fit of  $I_{EPR}^{-1}$  as a function of temperature.)

Figure 6.7 shows the multi-frequency EPR spectra of MIL-101(Cr) and MIL-100( $Al_{0.8}Cr_{0.2}$ ) MOFs at room and low temperatures. Unlike MIL-100( $Al_{0.8}Cr_{0.2}$ ), a significant shift in the  $g$ -value

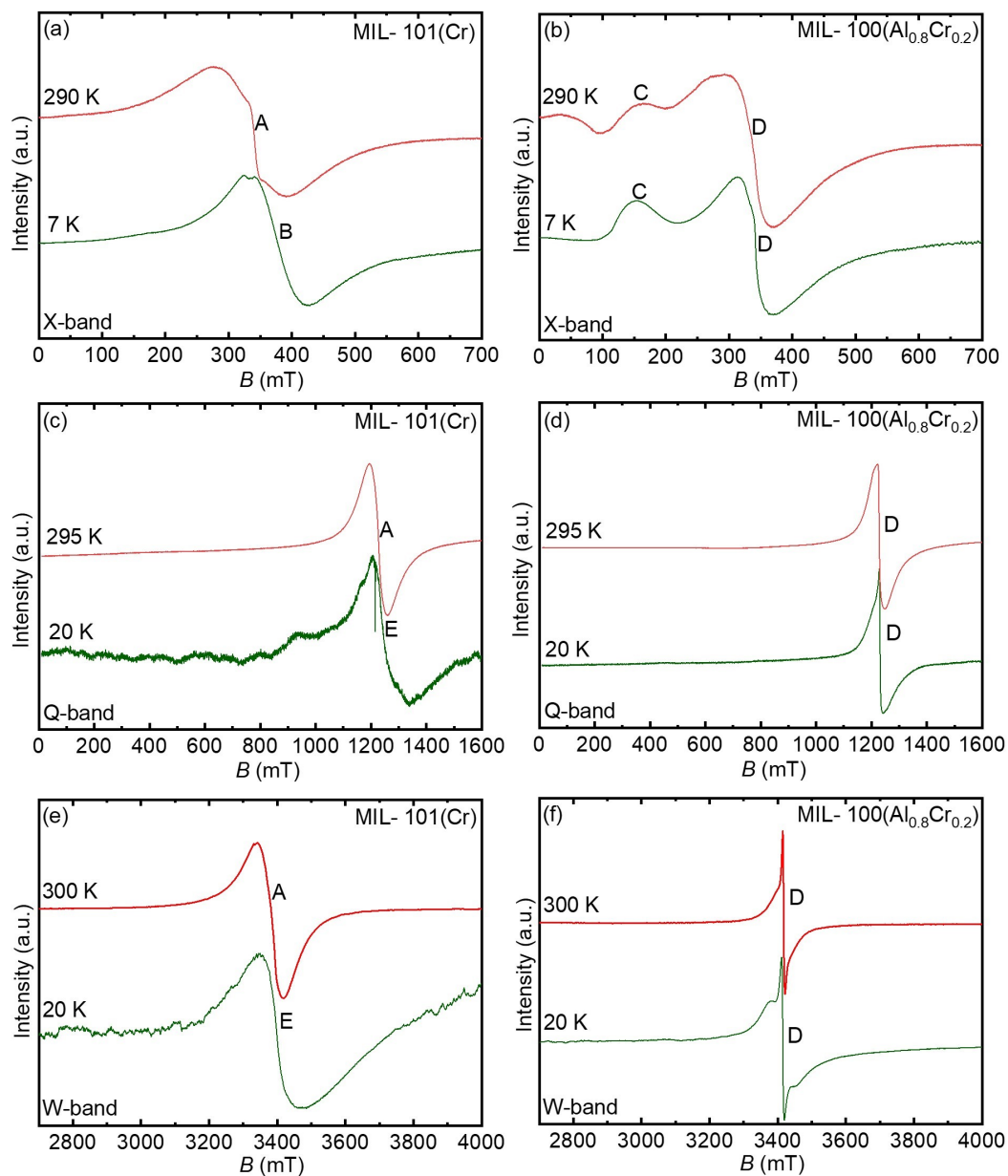


FIGURE 6.7: (a & b) X-band, (c & d) Q-band and (e & f) W-band EPR spectra of MIL-101(Cr) and MIL-100( $\text{Al}_{0.8}\text{Cr}_{0.2}$ ) MOFs, respectively. ( $g$ -values of the corresponding signals:  $g_A = 1.979$ ,  $g_B = 1.779$ ,  $g_C = 5.5 - 4.0$ ,  $g_D = 1.973$  and  $g_E = 1.945$ )

of the major signal A with  $g_A = 1.979$  at 290 K towards smaller  $g$ -values of  $g_E = 1.945$  (signal E at 20 K) and  $g_B = 1.779$  (signal B at 7 K) is observed for MIL-101(Cr).

The change in  $g$  as a function of temperature for MIL-101(Cr) is given in Figure 6.8a together with that of MIL-100( $\text{Al}_{0.8}\text{Cr}_{0.2}$ ) for comparison. We have to note that typical  $g$ -values for both isolated and coupled Cr(III) ions are in the range of  $g = 1.97 - 1.98$  [29]. Honda *et al.* [13] discussed a comparable anomalous  $g$ -shift for Cr(III)<sub>3</sub> trimers in Cr-acetate and Cr-propionate. Such signals with characteristic  $g$ -shifts at low temperatures have also been reported for AFM coupled Cr(III)<sub>3</sub> trimers in other matrices [14, 30] and were assigned to their ground state with the total spin  $S_T = 1/2$  [13, 14, 30].

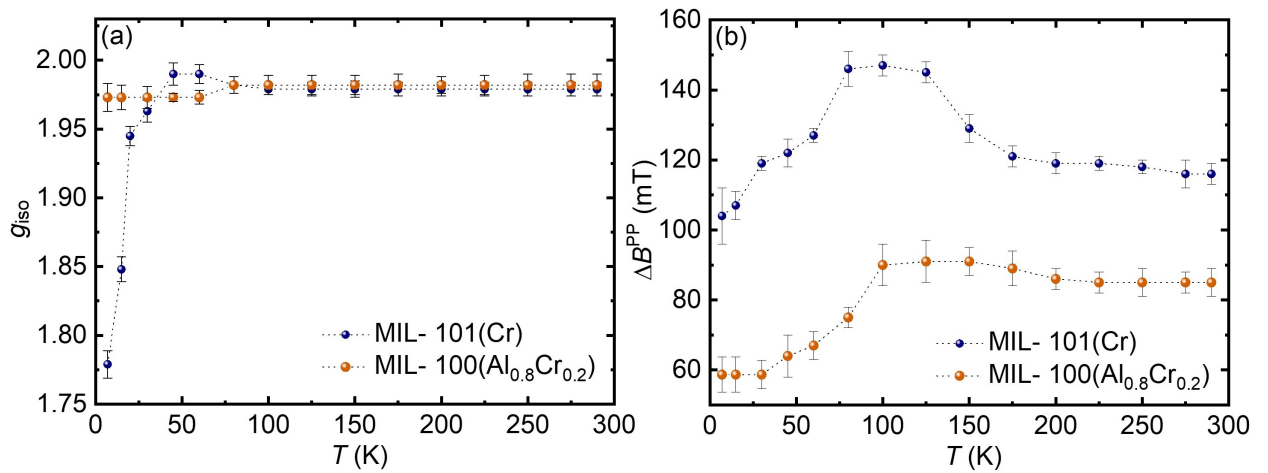


FIGURE 6.8: Temperature-dependent (a)  $g_{iso}$  trend, and (b) peak to peak width ( $\Delta B_{pp}$ ) of MIL-101(Cr) and MIL-100( $\text{Al}_{0.8}\text{Cr}_{0.2}$ ) extracted from the X-band temperature-dependent spectra.

The effective  $g$ -value of this doublet ground state is approximated by [13, 14, 30]

$$g_{eff} \approx g_A \sqrt{1 - \frac{48d^2}{(16J_1^2 + 48d^2) - (\mu_B B g_A)^2}} \quad (6.8)$$

Here,  $d = D_{12,z} + D_{23,z} + D_{13,z}$  is the asymmetric exchange parameter of the trimer according to the D-M interaction and  $\sqrt{16J_1^2 + 48d^2}$  corresponds to the splitting between the  $S_T = 1/2$  ground state and the first excited state of the trimer having likewise  $S_T = 1/2$ . As  $J_1$  is not known for MIL-101(Cr), we cannot derive the value of  $d$  from our experimental results. However, the observed characteristic  $g$ -shift of the doublet ground state at  $T < 30$  K can be considered as a signature for AFM coupled Cr(III)<sub>3</sub> trimers. On the other hand, the almost isotropic EPR signal at higher temperatures is less indicative of AFM coupling as all total spin levels  $S_T = 1/2, 3/2, 9/2$  will be more populated depending on the temperature and degeneracy.

The X-band EPR spectrum of MIL-100( $\text{Al}_{0.8}\text{Cr}_{0.2}$ ) (Figure 6.7a) appears to be more complex

as at least two signals C and D having  $g_C = 4.0 - 5.5$  and,  $g_D = 1.973$ , respectively can be discerned in the whole temperature range (Figure 6.5b). However, besides some decrease in the line-widths towards lower temperatures, (Figure 6.8b) the spectra reveal no characteristic temperature-dependence of the  $g$  values of signals C and, in particular of signal D even at  $T = 7$  K (Figure 6.8a). In addition, the line-width of signal D is significantly smaller than that of signal A in MIL-101(Cr) (Figure 6.8b). Therefore, we can exclude the formation of AFM coupled Cr(III)<sub>3</sub> trimers for MIL-100(Al<sub>0.8</sub>Cr<sub>0.2</sub>).

EPR spectra comparable to those of MIL-100(Al<sub>0.8</sub>Cr<sub>0.2</sub>) have been reported for Cr(III) doped phosphate glasses [29] and microporous materials such as silica and various zeolite type frameworks [31], and the signals C and D have been identified there. Signal C is assigned to isolated high-spin Cr(III) ions with  $S = 3/2$  in a highly distorted octahedral oxygen ion coordination. This gives rise to large variations in the  $E_{ZFS}/D_{ZFS}$  ratios ( $0 < E_{ZFS}/D_{ZFS} < 1/3$ ) leading for  $D_{ZFS} > \mu_B B g_C$  to  $g$ -values between 4.0 - 5.5. This condition is often met for X-band EPR spectroscopy but may not hold any longer at higher fields[31]. Therefore only a single line at  $g = 1.97 - 1.98$  is observed in the Q- and W-band spectra in Figures 6.7d and 6.7f. The presence of isolated Cr(III) species is supported by the most likely paramagnetic response in the low-temperature magnetization data of MIL-100(Al<sub>0.8</sub>Cr<sub>0.2</sub>) (Figure 6.2b). According to previous assignments, signal D is caused either by AFM exchanged coupled Cr(III)<sub>2</sub> pairs [29] or Cr(III)<sub>x</sub>O<sub>y</sub> clusters[31]. Therefore, it seems to be justified to assign signals C and D to Al(III)<sub>2</sub>Cr(III)<sub>1</sub> and Al(III)<sub>1</sub>Cr(III)<sub>2</sub> units in MIL-100(Al<sub>0.8</sub>Cr<sub>0.2</sub>). Similar mixed metal ion trimers have been identified in MOF MIL-100(Al<sub>3-x</sub>Fe<sub>x</sub>)[8].

## 6.4 Conclusion

Magnetization and EPR measurements confirm the formation of AFM coupled Cr(III)<sub>3</sub> trimers in the MOF MIL-101(Cr), having an exchange coupling constant  $J_0 = -11.4 \text{ cm}^{-1}$ . The trimers in the supertetrahedral building units of the MIL-101(Cr) framework are weakly coupled, as indicated by the determined small inter-trimer exchange interaction. The doublet total spin ground state of the Cr(III)<sub>3</sub> trimers reveals D-M interaction leading to a characteristic shift of its  $g$ -value shift at low temperatures. Although the magnetically diluted MOF MIL-100(Al<sub>0.8</sub>Cr<sub>0.2</sub>) displays AFM properties likewise the temperature-independent  $g$ -values of the Cr(III) EPR signals indicate that Cr(III)<sub>3</sub> trimers are not formed, and the Cr(III) ions are dispersed over the framework. We suggest that Cr(III) is incorporated as paramagnetic Al(III)<sub>2</sub>Cr(III)<sub>1</sub> and AFM coupled Al(III)<sub>1</sub>Cr(III)<sub>2</sub>

trimeric metal ion units into the MIL-100 framework though we cannot completely exclude the formation of minor isolated and clustered extra-framework chromium species.

## 6.5 Experimental Details

Metal-organic frameworks MIL-101(Cr) and MIL-100(Al<sub>0.8</sub>Cr<sub>0.2</sub>) were purchased from commercial MOF seller 'Materials Center, Technische Universität Dresden'. In MIL-100(Al/Cr), 20% Cr has been incorporated on Al sites within the frameworks. All the experiments mentioned above were done on the as-synthesized MIL-101(Cr) and MIL-100(Al<sub>0.8</sub>Cr<sub>0.2</sub>) MOFs.

The magnetization measurements were performed using a SQUID magnetometer (Quantum Design MPMS XL). Hysteresis loops at several temperatures between  $\leq 7$  T as well as the temperature-dependence at 0.5 T in the temperature range of 4 K to 300 K, were measured.

Continuous wave (cw) X-band ( $\sim 9.5$  GHz) EPR spectra were measured at a temperature ranging from  $T = 7$  K to  $T = 290$  K by means of a Bruker EMXmicro spectrometer fitted with a Bruker ER4119HS cylindrical cavity using a He cryostat ESR900, Oxford instruments. In all X-band experiments, the microwave (mW) power was set to 2 mW, the modulation frequency was kept as 100 kHz, and the modulation amplitude was maintained at 10 G to acquire a spectrum without any line shape distortion and saturation. Cw Q-band ( $\sim 34$  GHz) EPR spectra were performed using Bruker EMX 10-40 spectrometer fitted with cylindrical cavity and an Oxford Instruments CF935 cryostat at  $T = 20$  K and 295 K. In Q-band, the experimental parameters, the mW power, modulation frequency and modulation amplitude were set to 1.8 mW, 100 kHz and 20 G, respectively. Unlike X- and Q-band EPR spectrometers, the high magnetic field of W-band ( $\sim 95$  GHz) EPR requires a superconducting magnet (Bruker 6T SC) and measured using an Eleksys E600 spectrometer equipped with a Bruker E600-1021H TeraFlex resonator, and the spectra were recorded at  $T = 20$  K and 300 K. For W-band experiments, the microwave power kept as either 5  $\mu$ W or 50  $\mu$ W depending on the signal quality. The EPR intensities of the X-band signals ranging from  $T = 7$  K to  $T = 280$  K (Figure 6.6) were extracted by taking double integration of the full EPR spectrum.



# Bibliography

- (1) Espallargas, G. M.; Coronado, E. *Chem. Soc. Rev.* **2018**, *47*, 533–557.
- (2) Zhong, G.; Liu, D.; Zhang, J. *Cryst. Growth Des.* **2018**, *18*, 7730–7744.
- (3) Van de Voorde, B.; Bueken, B.; Denayer, J.; De Vos, D. *Chem. Soc. Rev.* **2014**, *43*, 5766–5788.
- (4) D'Amore, M.; Civalleri, B.; Bush, I. J.; Albanese, E.; Ferrabone, M. *J. Phys. Chem. C* **2019**, *123*, 28677–28687.
- (5) Steenhaut, T.; Filinchuk, Y.; Hermans, S. *Journal of Materials Chemistry A* **2021**, *9*, 21483–21509.
- (6) Celeste, A.; Paolone, A.; Itié, J.-P.; Borondics, F.; Joseph, B.; Grad, O.; Blanita, G.; Zlotea, C.; Capitani, F. *Journal of the American Chemical Society* **2020**, *142*, 15012–15019.
- (7) Rivera-Torrente, M.; Pletcher, P. D.; Jongkind, M. K.; Nikolopoulos, N.; Weckhuysen, B. M. *ACS Catalysis* **2019**, *9*, 3059–3069.
- (8) Mali, G.; Mazaj, M.; Aron, I.; Hanel, D.; Aron, D.; Jaglii, Z. *J. Phys. Chem. Lett.* **2019**, *10*, 1464–1470.
- (9) Giménez-Marqués, M.; Santiago-Portillo, A.; Navalón, S.; Álvaro, M.; Briois, V.; Nouar, F.; Garcia, H.; Serre, C. *Journal of Materials Chemistry A* **2019**, *7*, 20285–20292.
- (10) Liang, H.; Liu, R.; An, X.; Hu, C.; Zhang, X.; Liu, H. *Chemical Engineering Journal* **2021**, *414*, 128669.
- (11) Ferrer, S.; Lloret, F.; Pardo, E.; Clemente-Juan, J. M.; Liu-González, M.; Garca-Granda, S. *Inorg. Chem.* **2012**, *51*, 985–1001.
- (12) Tsukerblat, B.; Kuyavskaya, B. Y.; Belinskii, M.; Ablov, A.; Novotortsev, V.; Kalinnikov, V. *Theor. Chim. Acta.* **1975**, *38*, 131–138.
- (13) Honda, M.; Morita, M.; Date, M. *J. Phys. Soc. Jpn.* **1992**, *61*, 3773–3785.
- (14) Vlachos, A.; Psycharis, V.; Raptopoulou, C. P.; Lalioti, N.; Sanakis, Y.; Diamantopoulos, G.; Fardis, M.; Karayanni, M.; Papavassiliou, G.; Terzis, A. *Inorganica Chim. Acta.* **2004**, *357*, 3162–3172.

- (15) Figuerola, A.; Tangoulis, V.; Ribas, J.; Hartl, H.; Brüdgam, I.; Maestro, M.; Diaz, C. *Inorg. Chem.* **2007**, *46*, 11017–11024.
- (16) Mendt, M.; Vervoorts, P.; Schneemann, A.; Fischer, R. A.; Pöppl, A. *J. Phys. Chem. C* **2019**, *123*, 2940–2952.
- (17) Mendt, M.; Barth, B.; Hartmann, M.; Pöppl, A. *J. Chem. Phys.* **2017**, *147*, 224701.
- (18) Polyukhov, D. M.; Krause, S.; Bon, V.; Poryvaev, A. S.; Kaskel, S.; Fedin, M. V. *J. Phys. Chem. Lett.* **2020**, *11*, 5856–5862.
- (19) Wittmann, T.; Mondal, A.; Tschense, C. B.; Wittmann, J. J.; Klimm, O.; Siegel, R.; Corzilius, B.; Weber, B.; Kaupp, M.; Senker, J. *J. Am. Chem. Soc.* **2018**, *140*, 2135–2144.
- (20) Thangavel, K.; Bruzzese, P. C.; Mendt, M.; Folli, A.; Knippen, K.; Volkmer, D.; Murphy, D. M.; Pöppl, A. *Physical Chemistry Chemical Physics* **2023**, DOI: 10.1039/D3CP01449E.
- (21) Thangavel, K.; Walenszus, F.; Mendt, M.; Bon, V.; Kaskel, S.; Pöppl, A. *The Journal of Physical Chemistry C* **2023**, DOI: 10.1021/acs.jpcc.2c08905.
- (22) Bitzer, J.; Otterbach, S.; Thangavel, K.; Kultaeva, A.; Schmid, R.; Pöppl, A.; Kleist, W. *Chem. Eur. J.* **2020**, *26*, 5667–5675.
- (23) Thangavel, K.; Mendt, M.; Garai, B.; Folli, A.; Bon, V.; Murphy, D. M.; Kaskel, S.; Pöppl, A. *AIP Advances* **2023**, *13*, 015019.
- (24) Pöppl, A.; Kunz, S.; Himsl, D.; Hartmann, M. *The Journal of Physical Chemistry C* **2008**, *112*, 2678–2684.
- (25) Kultaeva, A.; Biktagirov, T.; Neugebauer, P.; Bamberger, H.; Bergmann, J.; van Slageren, J.; Krautscheid, H.; Pöppl, A. *J. Phys. Chem. C* **2018**, *122*, 26642–26651.
- (26) Thangavel, K.; Folli, A.; Ziese, M.; Hausdorf, S.; Kaskel, S.; Murphy, M. D.; Pöppl, A. *Scipost Physics Proc.* **2023**, *11*, 016.
- (27) Rivera-Torrente, M.; Mandemaker, L. D.; Filez, M.; Delen, G.; Seoane, B.; Meirer, F.; Weckhuysen, B. M. *Chemical Society Reviews* **2020**, *49*, 6694–6732.
- (28) J. Miyake, *S. J. Phys. Soc. Jpn.* **1992**, *61*, 983–988.
- (29) Landry, R.; Fournier, J.; Young, C. J. *J. Chem. Phys.* **1967**, *46*, 1285–1290.
- (30) Psycharis, V.; Raptopoulou, C. P.; Boudalis, A. K.; Sanakis, Y.; Fardis, M.; Diamantopoulos, G.; Papavassiliou, G. *Eur. J. Inorg. Chem.* **2006**, *2006*, 3710–3723.
- (31) Weckhuysen, B. M.; Schoonheydt, R. A.; Mabbs, F. E.; Collison, D. *J. chem. Soc., Faraday Trans.* **1996**, *92*, 2431–2436.

## Chapter 7

# Conclusion

Electron Paramagnetic Resonance (EPR) spectroscopy is a crucial and indispensable tool for comprehending various properties exhibited by materials, particularly through the analysis of their magnetic signatures. However, despite its potential, EPR spectroscopy remains underutilized, especially in the context of Metal-Organic Frameworks (MOFs). This thesis serves to address this research gap by demonstrating the application of EPR spectroscopy to investigate magnetic MOF materials. The objective is to gain a profound understanding of the characteristics of paramagnetic sites, local electronic structures, magnetic interactions, guest-host framework interactions, as well as gas adsorption properties. The findings from this doctoral program provide valuable insights into these areas of interest and contribute significantly to the field. In light of the aims of this study, a succinct summary of the accomplished research outcomes is presented below.

Chapter 1, titled "Introduction," extensively discusses the significance of EPR spectroscopy in the context of MOF materials. It aims to establish the conceptual framework for the thesis work by highlighting the areas where significant developments can be made in research. Various topics and research areas that can benefit from the application of EPR spectroscopy are considered and discussed in detail. Chapter 2, titled "Materials and Methods," selectively discusses the principles and themes of EPR spectroscopy based on the concepts encountered during the PhD work. The chapter also provides a comprehensive description of the MOF materials that were analyzed in the study. Furthermore, the chapter includes an extensive review of the utilization of EPR spectroscopy in the field of MOF science. The chapter also presents an overview of EPR theory, with a particular focus on bimetallic and high-spin species, which are featured in subsequent chapters (Chapters 3-6). Additionally, the chapter outlines other characterization techniques, including PXRD, SQUID, and quantum chemical calculations. These complementary techniques provide additional insights and information that enhance the understanding of the MOF materials alongside the information provided by EPR spectroscopy.

The thesis encompasses a range of significant research findings from different MOF materials, which are summarized as follows:

1. **Chapter 3:** *In situ* EPR spectroscopy is a valuable tool for studying phase transformations in DUT-49 (Cu) induced by xenon and ethylene adsorption and desorption. It detects structural changes in the Cu(II) - Cu(II) paddlewheel (PW) units of the MOF, which are associated with the *op*  $\leftrightarrow$  *cp* phase transformation. The ZFS of the  $S = 1$  state of the copper dimer in the PW unit provides crucial information. The ZFS can be influenced by small structural changes in the PW unit due to framework phase transformations or by coordination of additional molecules to the cupric ions at their CUS sites, as observed with ethylene adsorption. In cases where PXRD measurements are not feasible, *in situ* EPR proves helpful and reveals structural details inaccessible by adsorption isotherm measurements, as demonstrated with xenon adsorption/desorption on DUT-49(Cu). Importantly, the AFM-coupled copper dimers with their ZFS in the excited  $S = 1$  spin state serve as sensitive magnetic probes for detecting even subtle structural changes in the PW units of MOF frameworks. EPR spectroscopy, as a complementary technique, offers a localized approach to explore phase transformations in MOFs containing Cu(II) - Cu(II) PW units, alongside more conventional methods like diffraction and adsorption isotherm measurements.
2. **Chapter 4: DUT-49(M,M):** EPR spectroscopy investigations have revealed the presence of antiferromagnetic coupling in the Cu(II)-Cu(II) and Mn(II)-Mn(II) transition metal dimers, within the paddle wheel units of MOFs DUT-49(Cu) and DUT-49(Mn) respectively. Additionally, monomeric paramagnetic species of Cu(II) and Mn(II) have been observed, indicating the presence of defective paddle wheel units with a missing metal ion. In the case of the mixed metal ion MOF, DUT-49(Cu<sub>0.7</sub>Zn<sub>0.3</sub>), the formation of binuclear paramagnetic Cu(II)-Zn(II) dimers has been confirmed alongside the antiferromagnetic coupled Cu(II)-Cu(II) dimers in the paddlewheel units. The EPR spectra obtained for MOF DUT-49(Cu<sub>0.5</sub>Mn<sub>0.5</sub>) are more complex but have provided unambiguous identification of Cu(II)-Cu(II) dimers. Furthermore, the spectra indicate the presence of Mn(II)-Mn(II) dimers as well as antiferromagnetic coupled Cu(II)-Mn(II) dimers. These results confirm the complete post-synthetic modified (PSM) ion exchange of Co(II) in the DUT-49 framework, wherein other divalent transition metal ions such as Cu(II), Zn(II), and Mn(II) replace Co(II) through the magnetic coupling of the divalent metal centers. Overall, EPR spectroscopy has provided valuable insights into the magnetic properties and metal coordination states within the paddle wheel units of MOFs. The observation of different metal dimers and paramagnetic species contributes to a better understanding of the structural features and ion exchange in these materials. **ZnCuBTC:** EPR confirms successful incorporation of 5 % Zn(II) on Cu(II) sites in CuBTC MOF. CW EPR shows post-exchange modification, while pulse ENDOR reveals hf coupling

between framework protons and Cu(II) ions. In conclusion, EPR confirms PSM feasibility in PW-based MOFs through metal center coupling. **FeCuBTC:** Thorough characterization and comparison with other Fe- and Cu-containing materials were crucial to confirm the formation of a phase-pure FeCuBTC material. EPR spectra provided supporting evidence for the presence of bimetallic paddlewheel units in FeCuBTC. EPR is an excellent choice to verify PSM ion exchange when paramagnetic ions are involved in the SBU of MOF materials.

- Chapter 5:** EPR spectroscopy and quantum chemical calculations were utilized to investigate the geometric and electronic structure of Ni(II)-NO moieties in the Ni(II)-MFU-4l-NO<sub>2</sub> MOF material. W-band CW-EPR identified five-coordinated Ni(II) species at the peripheral sites of the parent Ni-MFU-4l-NO<sub>2</sub> MOF, in agreement with DFT calculations. Also, in Ni(II)-MFU-4l-NO<sub>2</sub> MOF, as another example, EPR successfully verified the PSM ion exchange. These divalent nickel centers capture gaseous NO, forming mononitrosyl complexes with electron spin  $S = 1/2$ , which can be clearly identified through CW X-band EPR measurements. ENDOR studies and DFT/CASSCF calculations provided insights into the Ni(II)-NO bond and Ni-N<sub>f</sub> bond nature. The bonding mechanism involves spin pairing  $\text{NO}\uparrow + \text{Ni(II)}\uparrow\uparrow \rightarrow [\uparrow\text{Ni(II)}(\uparrow\downarrow)\text{NO}]$ , facilitated by the overlap of antibonding  $\pi^*$  nitrogen and nickel  $3d_{x^2-y^2}$  orbitals. These findings underscore the power of advanced EPR techniques combined with quantum chemical calculations in elucidating the intricate electronic structure of open-shell species within metal-organic frameworks.
- Chapter 6:** Magnetization and EPR measurements confirm the presence of antiferromagnetically coupled Cr(III)<sub>3</sub> trimers in the MIL-101(Cr) MOF, with an exchange coupling constant of  $J_0 = -11.4 \text{ cm}^{-1}$ . The weak inter-trimer exchange interaction suggests a weak coupling between the trimers in the MIL-101(Cr) framework. The low-temperature  $g$ -value shift of the Cr(III)<sub>3</sub> trimers indicates a ground state with a doublet total spin and D-M interaction. In contrast, the magnetically diluted MOF MIL-100(Al<sub>0.8</sub>Cr<sub>0.2</sub>) displays AFM properties, but the temperature-independent  $g$ -values of the Cr(III) EPR signals suggest that Cr(III)<sub>3</sub> trimers are not formed. Instead, it is suggested that Cr(III) is incorporated as paramagnetic Al(III)<sub>2</sub>Cr(III)<sub>1</sub> and AFM coupled Al(III)<sub>1</sub>Cr(III)<sub>2</sub> trimeric metal ion units within the MIL-100 framework, with the possibility of minor isolated and clustered extra-framework chromium species.

## Chapter 8

# Publications and Miscellaneous

### Publication and Book chapter associated with the doctoral period

Publications	Contributions of author
1) Bitzer, J.; Otterbach, S.; <b>Thangavel, K.</b> ; Kultaeva, A.; Schmid, R.; Pöppl, A.; Kleist, W. "Experimental Evidence for the Incorporation of Two Metals at Equivalent Lattice Positions in MixedMetal MetalOrganic Frameworks". <i>Chem. Eur. J.</i> <b>2020</b> , 26, 5667.	All acquisition of EPR spectra and processing, simulation, analysis and visualization of EPR data. Manuscript preparation (EPR part).
2) Bracci, M.; Bruzzese P. C.; Famulari, A.; Fioco, D.; Guidetti, A.; Liao Y.- K.; Podvorica, L.; Rezayi, S. F.; Serra, I.; <b>Thangavel, K.</b> "Paramagnetic Species in Catalysis Research: A Unified Approach Towards (the role of EPR in) Heterogeneous, Homogeneous and Enzyme Catalysis". <i>RSC: Electron Paramagnetic Resonance: Volume 27</i> ; Chechik, Victor; Murphy, D. M.; Bode, Bela E, Ed.; Royal Society of Chemistry: London, <b>2020</b> ; pp. 1-46.	Manuscript preparation - MOF portion
3) <b>Thangavel, K.</b> ; Morozkin, A.V.; Murthy, V.R.K.; Rayaprol, S.; Pöppl, A.; Nirmala, R. "Inverse Magnetocaloric Effect and the Magnetostructural transition in Pr <sub>0.15</sub> Ca <sub>0.85</sub> MnO <sub>3</sub> manganites". <i>IEEE Trans: on Magn.</i> <b>2021</b> , 58(2), 25000806	Sample preparation, structural and magnetic properties - analysis, EPR measurements & analysis and manuscript preparation
4) Yan, Y.; Zhang, N.; Tauche, L., M.; <b>Thangavel, K.</b> ; Pöppl, A.; Krautscheid, H. "Direct Synthesis of a Stable Radical Doped Electrically Conductive Coordination Polymer". <i>Inorg. Chem. Front.</i> <b>2022</b> , 9, 5016-5023	EPR experiments and analysis

<p>5) Cornelio, J.; Lee, S. J.; Zhou, T-Y.; Alkas, A.; <b>Thangavel, K.</b>; Pöpl, A.; Telfer, S. "Photoinduced Electron Transfer in Multicomponent Truxene-Quinoxaline Metal-Organic Frameworks". <i>Chem. Mater.</i> <b>2022</b>, <i>34</i>, 18, 8437-8445</p>	EPR experiments and analysis
<p>6) <b>Thangavel, K.</b>; Mendt, M.; Garai, B.; Folli, A.; Bon, V.; Murphy, D. M.; Kaskel, S.; Pöpl, A. "Magnetic coupling of divalent metal centers in postsynthetic metal exchanged bimetallic DUT-49 MOFs by EPR spectroscopy". <i>AIP Adv.</i> <b>2023</b>, <i>13</i>(1), 015019.</p>	Acquisition of EPR spectra, processing, simulation, analysis and visualization of EPR data, manuscript preparation.
<p>7) <b>Thangavel, K.</b>; Walenszus, F.; Mendt, M.; Bon, V.; Kaskel, S.; Pöpl, A. "Monitoring the Local Structure and Magnetic Properties of the Dinuclear Cu<sub>2</sub>-Paddle Wheel Nodes in the Mesoporous MetalOrganic Framework, DUT-49 (Cu), upon Adsorption-Induced Breathing Transitions". <i>J. Phys. Chem. C.</i>, <b>2023</b>, <i>127</i>, 17, 82178234</p>	Acquisition of <i>in situ</i> EPR spectra, processing, simulation, analysis and visualization of EPR data, manuscript preparation.
<p>8) <b>Thangavel, K.</b>; Bruzzese, P. C.; Mendt, M.; Folli, A.; Knippen, K.; Volkmer, D.; Murphy, D. M.; Pöpl, A. "Unveiling the atomistic and electronic structure of Ni(II)-NO adduct in a MOF-based catalyst by EPR spectroscopy and quantum chemical modelling". <i>Phys. Chem. Chem. Phys.</i>, <b>2023</b>, <i>25</i>, 15702-15714</p>	Acquisition of EPR spectra, processing, simulation, analysis and visualization of EPR data, manuscript preparation.
<p>9) <b>Thangavel, K.</b>; Folli, A.; Ziese, M.; Hausdorf, S.; Kaskel, S.; Murphy, D. M.; Pöpl, A. "EPR and SQUID interrogations of Cr (III) trimer complexes in the MIL-101 and bimetallic MIL-100 Metal Organic Frameworks". <i>SciPost Phys. Proc.</i> <b>2023</b>, <i>11</i>, 016</p>	Acquisition of EPR spectra, processing, simulation, analysis and visualization of EPR data, manuscript preparation.
<p>10) <b>Thangavel, K.</b>; Folli, A.; Fischer, M.; Hartmann, M.; Murphy, D. M.; Pöpl, A. "Utilizing EPR Investigations to Interrogate the Liquid Adsorption Properties of Bimetallic MIL-53(Al/Cr) MOF Files". - Accepted in <i>RSC advances</i></p>	Acquisition of EPR spectra, processing, simulation, analysis and manuscript preparation.
<p>11) <b>Thangavel, K.</b>; Bühlman, W.; Pöpl, A. " Post synthetic metal exchanged Zn incorporated HKUST-1 MOF by EPR". - Manuscript under preparation</p>	Acquisition of EPR spectra, processing, simulation, analysis and manuscript preparation.

## Collaborations and foreign contributions to the thesis

1. DUT-49 MOFs Synthesis - Dr. Francesco Walenszus from the group of Prof. Dr. Stefan Kaskel (Department of Inorganic Chemistry, TU Dresden).
2. PXRD experiments of DUT-49(Cu) - Dr. Francesco Walenszus, Dr. Volodymyr Bon (Department of Inorganic Chemistry, TU Dresden).
3. Bimetallic DUT-49 synthesis - Dr. Bikash Garai from the group of Prof. Dr. Stefan Kaskel (Department of Inorganic Chemistry, TU Dresden).
4. MFU-4l:NO<sub>2</sub> MOF synthesis - Dr. Katharina Kanippen from the group of Prof. Dr. Dirk Volkmer (Department of Physics, University of Augsburg).
5. MIL-100 and MIL-101 MOFs synthesis - Dr. Steffen Hausdorf from the group of Prof. Dr. Stefan Kaskel (Department of Inorganic Chemistry, TU Dresden).
6. FeCuBTC MOF synthesis - Group of Prof. Wolfgang Kleist (Faculty of Chemistry and biochemistry, Ruhr University Bochum).
7. ZnCuBTC MOF synthesis - Dr. Winfried Böhlmann (University of Leipzig).
8. MIL-53 MOF synthesis - Dr. Marcus Fischer from the group of Prof. Dr. Martin Hartmann (FAU, Erlangen).
9. SQUID magnetometry measurements - Prof. Dr. Michael Ziese (Leipzig University).
10. PrCaMnO<sub>3</sub> manganite - PXRD, SEM, EDAX, and Seebeck coefficient experiments were performed in India by the author (Department of Physics, IIT Madras, India).
11. Dr. Matthias Mendt assisted with *in situ* EPR experiments, NO adsorption and analysis; Dr. Andrea Folli assisted with W-band experiments and analysis; and Dr. Paolo Cleto Bruzzese helped with pulse EPR data simulation of MFU-4l MOF and performed quantum chemical calculations



## Chapter 9

# CV and Miscellaneous

### Outreach activities

1. Knowledge for Change: A decade of Citizen Science (2020-2030) in support of the SDGs conference. A video about Citizen Social Science - Place: Berlin, Germany [Youtube link](#)
2. Participating Falling Walls Lab competition and talking on What what your research will break and how - Place: Leipzig, Germany [Youtube link](#)
3. Magnetism as Art Showcase - Finalist - Place: Minneapolis, USA (Virtual) [Showcase link](#)

### Magnetism as Art finalist -Second prize(MMM 2022 )



FIGURE 9.1: It is the SEM image (polygon shaped) of a paddle wheel-based bimetallic ZnCuBTC metal-organic framework containing an antiferromagnetically coupled  $S = 1$  spin state Cu(II)-Cu(II) dimers - portrayed as a **Coral reef - Underwater artwork**

## Kavipriya Thangavel

✉ ThangavelK@cardiff.ac.uk

🐦 Twitter

🌐 LinkedIn

👤 Google Scholar

🌐 PARACAT project(MSCA)

🌐 Cardiff group



An enthusiastic and recognized researcher with a demonstrated history of 5+ years of experience in various scientific research with strong international collaborations via Marie Skłodowska Curie actions fellowship. A well-trained experimentalist and competent in EPR and SQUID magnetometry measurements and analysis. A metal-organic frameworks specialist with expertise in investigating liquid adsorption, gas adsorption, inter- & intra-molecular coupling and guest-host framework interactions studies. An 'out of box' thinker and an excellent team player, motivated to be a part of the EPR community.

### Education

- Jun 2019 - Jun 2023

📖 **Ph.D. (Physics & Chemistry), Joint doctoral program** b/w Cardiff (Chemistry) and Leipzig (Physics) Universities  
 Thesis title: *Elucidation of the role of paramagnetic valence states of transition metal ions in bimetallic MOF catalysts.* **Supervisors:** Prof. Andreas Pöpl and Prof. Damien Murphy
- Aug 2016 - Aug 2017

📖 **M.Phil. (Physics)**, University of Madras, India  
 Thesis title: *Effect of spin interactions on the Landé splitting factor in NiFe<sub>2</sub>O<sub>4</sub> inverse spinel.*
- Jul 2014 - Apr 2016

📖 **M.Sc. (Physics)**, Bharathiar University, India.  
 Thesis title: *"Microwave Assisted Combustion Synthesis of BaFe<sub>12</sub>O<sub>19</sub> and Its Magnetic Properties"*.

### Work experience

- Dec 2022 - Jun 2023

📖 **Deutsche Forschungsgemeinschaft (DFG)**, Researcher on the project FOR 2433 - MOF switches, Felix Bloch Institute for Solid State Physics, University of Leipzig, Germany
- Jun 2019 - Dec 2022

📖 **Marie Skłodowska-Curie program**, Joint agreement between Leipzig (Germany) and Cardiff (UK) Universities via European Union's H2020 program - PARACAT, Grant No. 813209.
- Apr 2018 - Jun 2019

📖 **Junior Research Fellow (JRF)**, Department of Physics, Indian Institute of Technology Madras (IITM), Chennai, India

### Skills

- Technical

📖 MATLAB, EasySpin for EPR data simulation, MS Office, Origin, L<sup>A</sup>T<sub>E</sub>X.
- Experiments


📖 EPR spectroscopy, SQUID magnetometry, XRD, SEM, FT-IR.
- Teaching

📖 Physics practical for Undergraduate students at Leipzig University and guided for understanding the structural & magnetic properties of superconductors for the school kids in IIT Madras.
- Miscellaneous







📖 Academic research, teaching, article writing, publishing, international collaborations, networking, excellent communication, independence of research ideas and travelling.
- Conferences and Workshops

📖 More than 15 international conferences were attended (10 countries) with oral and poster presentations.

## Skills (continued)

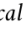

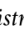

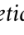
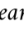
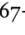
Languages  English and Tamil (reading, writing and speaking competencies) and Malayalam (reading and writing).

## Awards and Achievements


- 2022  **Finalist in 'Magnetism as Art Showcase' competition**, MMM 2022, Minneapolis, USA
- 2019  **Marie Skłodowska-Curie Fellowship**, European Union Horizon 2020 program.
- 2018  **Junior Research Fellowship**, IIT Madras, India
- 2017  **First rank holder in M.Phil- Physics**, University of Madras, India
- 2016  **Cleared Tamil Nadu State Eligibility Test for Lectureship (TNSET 2016)**, Tamilnadu, India
- 2015  **Summer Internship at IGCAR - National level write up**, IGCAR, India

## Research Publications




### Journal Articles

- 1 **K. Thangavel**, W. Bühlman, and A. Pöpl, "Post synthetic metal exchanged zn incorporated hku-1 mof by epr spectroscopy," *Manusript under preparation*,
- 2 **K. Thangavel**, A. Folli, M. Hartman, D. Murphy, and A. Pöpl, "Liquid phase adsorption in bimetallic mil-53(al/cr) mof," *Manusript under preparation*,
- 3 **K. Thangavel**, P. C. Bruzzese, M. Mendt, *et al.*, "Unveiling the atomistic and electronic structure of niii-no adduct in a mof-based catalyst by epr spectroscopy and quantum chemical modelling," *Physical Chemistry Chemical Physics*, 2023.  DOI: 10.1039/D3CP01449E.
- 4 **K. Thangavel**, M. Mendt, B. Garai, *et al.*, "Magnetic coupling of divalent metal centers in postsynthetic metal exchanged bimetallic dut-49 mofs by epr spectroscopy," *AIP Advances*, vol. 13, no. 1, p. 015 019, 2023.  DOI: 10.1063/9.0000532.
- 5 **K. Thangavel**, F. Walenzus, M. Mendt, V. Bon, S. Kaskel, and A. Pöpl, "Monitoring the local structure and magnetic properties of the dinuclear cu2-paddle wheel nodes in the mesoporous metal-organic framework, dut-49 (cu), upon adsorption-induced breathing transitions," *The Journal of Physical Chemistry C*, 2023.  DOI: 10.1021/acs.jpcc.2c08905.
- 6 J. Cornelio, S. J. Lee, T.-Y. Zhou, *et al.*, "Photoinduced electron transfer in multicomponent truxene-quinoxaline metal-organic frameworks," *Chemistry of Materials*, vol. 34, no. 18, pp. 8437-8445, 2022.  DOI: 10.1021/acs.chemmater.2c022202.
- 7 **K. Thangavel**, A. Morozkin, V. Murthy, S. Rayaprol, A. Pöpl, and R. Nirmala, "Inverse magnetocaloric effect and the magnetostructural transition in pr<sub>0.15</sub>ca<sub>0.18</sub>mno<sub>3</sub> manganite," *IEEE Transactions on Magnetics*, vol. 58, no. 2, pp. 1-6, 2021.  DOI: 10.1109/TMAG.2021.3092644.
- 8 J. Bitzer, S. Otterbach, **K. Thangavel**, *et al.*, "Experimental evidence for the incorporation of two metals at equivalent lattice positions in mixed-metal metal-organic frameworks," *Chemistry - A European journal*, vol. 26, no. 25, pp. 5667-5675, 2020.  DOI: 10.1002/chem.201905596.
- 9 Y. Yan, N. Zhang, L. M. Tauche, **K. Thangavel**, A. Pöpl, and H. " Krautscheid, "Direct synthesis of a stable radical doped electrically conductive coordination polyme," *Chem. Eur. J.*, vol. 26, no. 25, pp. 5667-5675, 2020.  DOI: 10.1002/chem.201905596.

### Books and Chapters








- 1 M. Bracci, P. C. Bruzzese, A. Famulari, *et al.*, *Paramagnetic species in catalysis research: a unified approach towards (the role of EPR in) heterogeneous, homogeneous and enzyme catalysis*. The Royal Society of Chemistry, 2021, vol. 27, pp. 1–46, ISBN: 978-1-83916-171-1.  DOI: 10.1039/9781839162534-00001.

### Conference Proceedings

- 1 **K. Thangavel**, A. Folli, M. Ziese, *et al.*, “Epr and squid interrogations of cr(iii) trimer complexes in the mil-101(cr) and bimetallic mil-100(al/cr) mofs,” vol. 11, *Scipost*, 2023, p. 016.  DOI: 10.21468/SciPostPhysProc.11.016.
- 2 **K. Thangavel**, S. K. Balu, and C. Venkateswaran, “Effect of spin interactions on the landé splitting factor in nife<sub>2</sub>o<sub>4</sub> inverse spinel,” vol. 1942, *AIP*, 2018, p. 130 027.  DOI: 10.1063/1.5029097.
- 3 **K. Thangavel** and R. Nirmala, “Magnetic, magnetocaloric and electrical transport properties of electron-doped manganite eu<sub>0.15</sub>ca<sub>0.15</sub>mno<sub>3</sub>,” vol. 2265, *AIP*, 2018, p. 030 507.  DOI: 10.1063/5.0016696.



### Oral Presentations

---

- 2023  Adsorption of NO on Ni(II)-based MFU-4l Catalyst MOF Evidenced by EPR Spectroscopy and Quantum Chemical Modeling, RSC EPR 2023, Leeds, UK
- 2022  Monitoring the Local Structure, magnetic, Gas and Liquid Adsorption Properties of the Cr(III), Mn(III), Ni(II) and Cu(II) based MOFs by EPR Spectroscopy , EPR in Catalysis, Athens, Greece
- 2021  Investigations on Metal Organic Frameworks to Elucidate the Gas and Liquid Adsorption Properties, Chemistry at the surface conference, Baveno, Italy
  -  EPR investigation on Cu(II) pairs in DUT-49(Cu) MOF to elucidate the magnetic coupling and Xenon adsorption (in situ) properties, RSC EPR 2021, Cardiff, UK (Virtual)
  -  UV-Vis spectroscopy on Metal-Organic Frameworks, Virtual, Zaragoza, Spain
- 2020  Elucidation of the Role of Paramagnetic Valence States of High Spin Transition Metal Ions in FeCuBTC and MIL -100 Bimetallic MOFs, Winter School, Cardiff, UK
- 2019  Elucidation of the role of Paramagnetic valence States of High Spin Transition Metal Ions in Bimetallic MIL-100 and MIL-101 MOF Catalysts, PARACAT summer school, Antwerp, Belgium

### References

---

- Prof. Andreas Pöpl**  E-mail - poepl@physik.uni-leipzig.de, University of Leipzig, Germany.
- Prof. Damien Murphy**  E-mail - murphydm@cardiff.ac.uk, Cardiff University, Great Britain.

# List of Abbreviations

AFM	Antiferromagnetic
AO	Atomic orbital
BDC	Benzenedicarboxylate
BTC	Benzenetricarboxylate
CAS	Complete active space
CIDEP	Chemically induced dynamic electron polarization
<i>cp</i>	Closed pore
CUS	Coordinatively unsaturated metal site
CW	Continuous wave
C-W	Curie-Weiss
DFT	Density functional theory
D-M	Dzyaloshinsky-Moriya
DQ	Double quantum
DUT	Dresden University of Technology
EM	Electro magnetic
ENDOR	Electron nuclear double resonance
EPR	Electron paramagnetic resonance
ESE	Electron spin echo
ESEEM	Electron spin echo envelope modulation
ESR	Electron spin resonance
EZ	Electron Zeeman
FCC	Field cooled cooling
FCW	Field cooled warming
fs	Fine structure
FWHM	Full width at half maximum
H <sub>4</sub> BBCDC	([1,1-biphenyl]-4,4-diyl)bis(9H-carbazole-3,6-dicarboxylic acid)
HFEPR	High frequency electron paramagnetic resonance
HFI	Hyperfine interaction

---

<b>HKUST</b>	<b>Hong Kong University of Science and Technology</b>
<b>HOMO</b>	<b>Highest occupied canonical molecular orbital</b>
<b>HYSCORE</b>	<b>Hyperfine sublevel correlation</b>
<b>LCMT</b>	<b>Ligand-metal charge transfer</b>
<i>lp</i>	<b>Large pore</b>
<b>MFU</b>	<b>Metal Organic Framework Ulm University</b>
<b>MIL</b>	<b>Materials of Institut Lavoisier</b>
<b>MO</b>	<b>Molecular orbital</b>
<b>MOF</b>	<b>Metal organic framework</b>
<b>MUF</b>	<b>Massey University framework</b>
<b>MW</b>	<b>Microwave</b>
<b>NGA</b>	<b>Negative gas adsorption</b>
<b>NMR</b>	<b>Nuclear magnetic resonance</b>
<i>np</i>	<b>narrow pore</b>
<b>NQI</b>	<b>Nuclear quadrupole interaction</b>
<b>NZ</b>	<b>Nuclear Zeeman</b>
<b>PSM</b>	<b>Post-synthetic modification</b>
<i>pp</i>	<b>Peak-to-peak</b>
<b>PW</b>	<b>Paddle wheel</b>
<b>PXRD</b>	<b>Powder X-ray diffraction</b>
<b>RF</b>	<b>Radio frequency</b>
<b>SBU</b>	<b>Secondary building unit</b>
<b>SCF</b>	<b>Self-consistent field</b>
<b>SEM</b>	<b>Scanning electron microscopy</b>
<b>SQUID</b>	<b>Superconducting quantum interference device</b>
<b>XRD</b>	<b>X-ray diffraction</b>
<b>ZFC</b>	<b>Zero field cooling</b>
<b>ZFS</b>	<b>Zero field splitting</b>

# List of Symbols

$A, A_i$	hyperfine interaction tensor/principal value
$a_{iso}$	isotropic hyperfine interaction value
$B$	pseudo secular hyperfine interaction constant
$\vec{B}$	external magnetic field vector/magnitude
$B_1$	magnitude of oscillating magnetic field perpendicular to $\vec{B}$
$C$	Curie constant
$\chi$	magnetic susceptibility
$D, D$	ZFS tensor, axial part of ZFS
$\delta B^{pp}$	peak-to-peak EPR linewidth
$E_A$	activation energy
$\eta$	nuclear quadrupole interaction asymmetry parameter
$g, g, g_i$	g-tensor/factor/principal value
$g_e$	free electron g-value
$g_n$	nuclear g-factor
$\hat{H}$	spin Hamiltonian
$h$	Planck constant
$\hat{I}, I_i$	nuclear spin vector operator and its component
$2J$	isotropic coupling constant
$k_B$	Bohr magneton
$\lambda$	spin orbit coupling constant
$m_I$	nuclear magnetic quantum number
$m_s$	magnetic quantum number
$\mu_B$	Bohr magneton
$\mu_{eff}$	effective magnetic moment
$\mu_n$	nuclear magneton
$M$	Magnetization
$\nu_l$	nuclear larmor frequency
$\rho$	hyperfine interaction asymmetry parameter

---

$P$	Pressure
$p/p_0$	relative pressure
$Q$	nuclear quadrupole interaction tensor
$Q_c$	quadrupole coupling constant
$S, \hat{S}, S_i$	electron spin, electron spin vector operator and its component
$\theta_p$	paramagnetic Curie temperature
$T$	dipolar hyperfine interaction tensor
$T$	temperature or dipolar hyperfine interaction constant
$t, t_1, t_2$	time constants in pulse sequences
$\tau$	lifetime decay rate or time constant in pulse sequences